

# CMS Draft Analysis Note

*The content of this note is intended for CMS internal use and distribution only*

2020/01/28

Archive Hash: efd4f33

Archive Date: 2020/01/24

## Common analysis object definitions and trigger efficiencies for the $H \rightarrow WW$ analysis with full Run-II data

Alicia Calderon, Jonatan Piedra, Pedro Fernandez, Cedric Prieels<sup>1</sup>,  
Xavier Janssen, Davide Di Croce, Tomas Kello<sup>2</sup>,  
V. Ciulli, Piergiulio Lenzi, Lorenzo Viliani<sup>3</sup>,  
Arun Kumar, Sarah Freed, Karl Ecklund<sup>4</sup>,  
Amandeep Kaur, S. Beri<sup>5</sup>,  
P. Chen, Pei-Rong Yu, K.F. Chen<sup>6</sup>,  
Adrian Alvarez Fernandez, I. Josa Mutuberria<sup>7</sup>, and  
Dennis Roy<sup>8</sup>

<sup>1</sup> Instituto de Fisica de Cantabria (CSIC - University of Cantabria), Spain.

<sup>2</sup> University of Antwerpen, Belgium.

<sup>3</sup> University and INFN Firenze, Italy.

<sup>4</sup> Rice University, USA.

<sup>5</sup> Panjab University, Chandigarh, India.

<sup>6</sup> National Taiwan University.

<sup>7</sup> Centro de Investigaciones Energeticas Medioambientales Tecnologicas

<sup>8</sup> RWTH Aachen University, Germany

## Abstract

Descriptions are presented for the definition, reconstruction, efficiencies and systematics of the objects used in the  $H \rightarrow WW$  Run-II analysis for  $35.9 \text{ fb}^{-1}$  integrated luminosity for 2016,  $41.86 \text{ fb}^{-1}$  for 2017 and  $58.83 \text{ fb}^{-1}$  for 2018. Electrons, muons, jets, and missing transverse momenta are basic elements of the event reconstruction for the analysis. Measurements of the single and double lepton efficiencies are fulfilled to be used for the  $H \rightarrow WW$  Run 2 analysis.

This box is only visible in draft mode. Please make sure the values below make sense.

PDFAuthor:

HWW working group

PDFTitle:

Common analysis object definitions and trigger efficiencies for the H  
rightarrow WW analysis with full Run-II data

PDFSubject:

CMS

PDFKeywords:

CMS, physics, your topics

Please also verify that the abstract does not use any user defined symbols

DRAFT

## 1 Contents

2	1	Introduction . . . . .	3
3	2	Changes w.r.t AN-19-105 . . . . .	3
4	3	Muons . . . . .	4
5	3.1	Muon Reconstruction and Selection . . . . .	4
6	3.2	Muon Working Point Optimization . . . . .	4
7	3.3	Muon ID and Isolation Efficiencies from Tag and Probe Method . . . . .	5
8	3.4	Systematic uncertainties of the method . . . . .	7
9	3.5	Muon momentum scale and resolution . . . . .	22
10	4	Electrons . . . . .	25
11	4.1	Electron Reconstruction and Selection . . . . .	25
12	4.2	Variables used for electron Id . . . . .	25
13	4.3	Electron Id in HWW . . . . .	27
14	4.4	Electron Id/Iso Efficiencies from Tag & Probe Method . . . . .	30
15	4.5	Systematics for TnP Studies . . . . .	34
16	4.6	Results from Tag & Probe . . . . .	38
17	5	Lepton trigger efficiencies . . . . .	44
18	5.1	Introduction . . . . .	44
19	5.2	Lepton trigger definitions for run period 2016 . . . . .	44
20	5.3	Lepton trigger definitions for run period 2017 . . . . .	51
21	5.4	Lepton trigger definitions for run period 2018 . . . . .	62
22	5.5	DZ Trigger Efficiencies results . . . . .	66
23	5.6	Systematics . . . . .	69
24	6	Fake lepton background estimation . . . . .	82
25	6.1	Introduction . . . . .	82
26	6.2	Lepton fake rate estimation in a dijet control region . . . . .	82
27	6.3	Lepton prompt rate estimation in a Z-enriched control region . . . . .	85
28	6.4	Data-driven validation of background modelling . . . . .	86
29	6.5	Flavour composition . . . . .	87
30	6.6	Systematic uncertainties . . . . .	88
31	7	Jets . . . . .	107
32	7.1	Jet reconstruction . . . . .	107
33	7.2	Jet selection . . . . .	107
34	7.3	L1 Prefire corrections . . . . .	107
35	7.4	Uncertainties . . . . .	107
36	8	Missing Transverse Energy . . . . .	114
37	8.1	MET reconstruction . . . . .	114
38	8.2	MET filter . . . . .	114
39	8.3	MET uncertainties . . . . .	114
40	9	Drell-Yan multivariate discriminants . . . . .	116
41	9.1	DNN Training . . . . .	117
42	9.2	DYMVA <sub>DNN</sub> discriminator . . . . .	118
43	9.3	BDT training . . . . .	134

44	10	Tau embedded samples . . . . .	139
45	10.1	Introduction . . . . .	139
46	10.2	Scale factors . . . . .	139
47	10.3	Interference with other MC samples . . . . .	140
48	10.4	Uncertainties . . . . .	140
49	10.5	Control regions . . . . .	140
50	11	B-Tagging . . . . .	148
51	11.1	B tagging algorithms performance . . . . .	148
52	11.2	Scale factors . . . . .	150

DRAFT

## 53 1 Introduction

54 This note describes the physics objects reconstruction and selection for the  $H \rightarrow WW$  Run-II  
55 analysis, together with the reconstruction efficiencies and evaluation of their performances.  
56 The objects include electrons, muons, jets, and missing transverse momentum. Measurements  
57 of the trigger efficiencies for the single and double lepton trigger paths are also presented. The  
58 fake lepton background affecting the analysis is estimated. All the results are based on the  
59  $35.9 \text{ fb}^{-1}$  integrated luminosity for 2016,  $41.86 \text{ fb}^{-1}$  for 2017 and  $59.7 \text{ fb}^{-1}$  for 2018.

## 60 2 Changes w.r.t AN-19-105

- 61 Trigger efficiencies for electron triggers were recomputed for electron triggers for  
62 the year 2017 and 2018 with MVA selections and the trigger efficiency comparison  
63 plots of cut based tight id vs MVA WP has been added .
- 64 Separate study is performed with MVA methods namely Boosted Decision Tree(BDT)  
65 and Deep Neural Network(DNN) to recover as much signal as possible while reject-  
66 ing the Drell-Yan backgrounds in HWW . Detailed section containing this study has  
67 been added to this note .
- 68 Another section , Tau embedded samples has been introduced in this note. In  $H \rightarrow$   
69 WW these embedded samples can be used to estimate the DY background in  $e\mu$  final  
70 state channels. This section includes the details of recomputation of scale factors for  
71 the embedded samples and a few distributions showing the effect of using embed-  
72 ded samples to describe the DY background which eventually results in lowering  
73 the uncertainties .

DRAFT

---

### 74 3 Muons

75 Editors: Pedro Manteca, Alicia Calderon, Adrian Alvarez

76 **3.1 Muon Reconstruction and Selection**

77 The Muon POG only provides reference efficiencies [1] for standard selections [2]. The muon  
78 identification currently used in the HWW analysis is based upon the recommendation from the  
79 Muon POG group for the Tight selection, accessible in Ref. [2] with extra cuts on the  $d_{xy}$  and  $d_z$   
80 variables.

81 A muon is labeled as "TightHWW" if:

- 82 •  $p_T > 10 \text{ GeV}$ ,
- 83 •  $|\eta| < 2.4$ ,
- 84 • it is identified like a standard Tight Muon using the Muon POG selections [2],
- 85 •  $|d_{xy}| < 0.01 \text{ cm}$  for  $p_T < 20 \text{ GeV}$  and  $|d_{xy}| < 0.02 \text{ cm}$  for  $p_T > 20 \text{ GeV}$ , where  $d_{xy}$  is  
86 the impact parameter w.r.t. the primary vertex,
- 87 •  $|d_z| < 0.1 \text{ cm}$ , where  $d_z$  is the longitudinal distance of the tracker track w.r.t. the  
88 primary vertex.

89  
90 For the muon isolation criteria we are using the recommended Muon POG tight PF-based com-  
91 bined relative isolation with  $\Delta\beta$  correction in a cone size of  $\Delta R < 0.4$  [2]:

$$ISO = \left( \sum p_T(\text{ch.had from PV}) + \max(0, \sum Et(\text{neut.had}) + \sum Et(\text{phot}) - 0.5 \times \sum p_T(\text{ch.had from PU})) \right) / p_T(\mu) \quad (1)$$

$$ISO_{tight} < 0.15.$$

92 For the study of Fakes we are using the recommended very loose selection on relative PF isola-  
93 tion:

$$ISO_{fake} < 0.40. \quad (2)$$

94 **3.2 Muon Working Point Optimization**

95 The choice of the muon selection described in the previous section is the result of a study with  
96 different working points. For that study we use a 94X MC sample of the signal, as well as 94X  
97 samples of the backgrounds (WW, DY,  $t\bar{t}$ , single top and W+jets). We filter the events in these  
98 samples by requiring the following:

- 99 • Two leptons with opposite charges and opposite flavour ( $e\mu$  selection),
- 100 •  $p_{T1} > 25 \text{ GeV}$ ,
- 101 •  $p_{T2} > 20 \text{ GeV}$  for the high  $p_{T2}$  region and  $10 < p_{T2} < 20 \text{ GeV}$  for the low  $p_{T2}$  region,
- 102 • no third lepton with  $p_{T3} > 10 \text{ GeV}$ ,
- 103 •  $m_{ll} > 12 \text{ GeV}$ ,
- 104 •  $p_{Tll} > 12 \text{ GeV}$ ,

- 105 • no jet with  $p_{Tj} > 20$  and btag CSVV2  $> 0.5803$  (top quark veto),
- 106 • PF and mp MET  $> 20$  GeV
- 107 •  $m_{th} > 60$  GeV,
- 108 •  $m_{tw2} > 30$  GeV

109 After this selection we count the number of signal  $S$  and background  $B$  events in which the  
 110 muon passes the four different working point requirements. We then compute the signal sig-  
 111 nificance  $S/\sqrt{S+B}$  for each of the working points that we consider. Those working points  
 112 are the standard Muon POG definitions of Tight Muon ID and Medium Muon ID [2], and those  
 113 two working points with additional cuts in the impact parameter  $IP$  variables,  $d_{xy}$  and  $d_z$ , which  
 114 are written in section 3.1.

Table 1: Signal significance for each of the muon working points in the 0 jets channel.

Muon working point	$S / \sqrt{S+B}$ $p_{T2}^T > 20$ GeV	$S / \sqrt{S+B}$ $10 < p_{T2}^T < 20$ GeV
Medium Muon	1.96	1.50
Tight Muon	2.02	2.17
Medium Muon + IP cuts	2.03	2.26
Tight Muon + IP cuts	2.02	2.28

Table 2: Signal significance for each of the muon working points in the 1 jet channel.

Muon working point	$S / \sqrt{S+B}$ $p_{T2}^T > 20$ GeV	$S / \sqrt{S+B}$ $10 < p_{T2}^T < 20$ GeV
Medium Muon	1.13	0.72
Tight Muon	1.15	0.91
Medium Muon + IP cuts	1.15	0.96
Tight Muon + IP cuts	1.15	0.95

115 For the high  $p_{T2}$  case very similar values have been extracted from the four IDs, but for the  
 116 low  $p_{T2}$  case, where the non-prompt contribution is much larger, the working points with ad-  
 117 ditional IP cuts are the best choices in terms of the signal significance. The same conclusion is  
 118 obtained for both the 0-jet bin and the 1-jet categories. For the analysis we chose the Tight ID  
 119 plus IP cuts selection.

### 120 3.3 Muon ID and Isolation Efficiencies from Tag and Probe Method

121 The muon ID and Isolation efficiency is studied and compared to the prediction of MC in order  
 122 to understand if a correction is needed.

<sup>123</sup> Results are based on full Run2016, Run2017, and Run2018 with Golden json files. The considered datasets for both data and Monte-Carlo are listed in Table 3, Table 4, and Table 5 respectively.

Table 3: List of data and Monte-Carlo samples used for 2016.

Stream	Run and reconstruction version
SingleMuon	Run2016B-07Aug17_ver2-v1
	Run2016C-07Aug17-v1
	Run2016D-07Aug17-v1
	Run2016E-07Aug17-v1
	Run2016F-07Aug17-v1
	Run2016G-07Aug17-v1
	Run2016H-07Aug17-v1
Monte-Carlo	DYJetsToLL_M-50_TuneCP5_13TeV-madgraphMLM-pythia8/RunIIBAutumn18DRPremix-102X_upgrade2018_realistic_v15-v1

Table 4: List of data and Monte-Carlo samples used for 2017.

Stream	Run and reconstruction version
SingleMuon	Run2017B-17Nov2017-v1
	Run2017C-17Nov2017-v1
	Run2017D-17Nov2017-v1
	Run2017E-17Nov2017-v1
	Run2017F-17Nov2017-v1
Monte-Carlo	DYJetsToLL_M-50_TuneCP5_13TeV-madgraphMLM-pythia8/RunIIFall17DRPremix-RECOSIMstep_94X_mc2017_realistic_v10-v1

Table 5: List of data and Monte-Carlo samples used for 2018.

Stream	Run and reconstruction version
SingleMuon	Run2018A-17Sep2018-v2
	Run2018B-17Sep2018-v1
	Run2018C-17Sep2018-v1
	Run2018D-PromptReco-v2
Monte-Carlo	DYJetsToLL_M-50_TuneCP5_13TeV-madgraphMLM-pythia8/RunIIBAutumn18DRPremix-102X_upgrade2018_realistic_v15-v1

<sup>126</sup> The muon efficiency is obtained as following:

$$\epsilon_{\mu} = \epsilon_{\text{trk}} \times \epsilon_{\text{TightHWW}} \times \epsilon_{ISO_{tight}}, \quad (3)$$

<sup>127</sup> where  $\epsilon_{\text{trk}}$  is the tracker (TRK) muon efficiency,  $\epsilon_{\text{TightHWW}}$  is the "TightHWW" muon efficiency under the assumption that the muon passes the TRK selections, discussed at Section 3.1, and  $\epsilon_{ISO_{tight}}$  is the efficiency of the isolation criteria under the assumption that the muon passes the "TightHWW" selections.

<sup>131</sup> The tracking efficiency  $\epsilon_{\text{trk}}$  is computed by the Tracking POG and its scale factor is very close to 1 for  $p_T > 20$  GeV/c [1]. The muon ID "TightHWW" and isolation efficiencies are computed using tag and probe.

<sup>134</sup> We determined the muon ID and isolation efficiencies using the tag-and-probe method [3]. For such studies, we used the officially supported package, under "PhysicsTools/TagAndProbe" [4].  
<sup>135</sup> The tag muon is obtained by applying all the kinematic "TIGHT" selections, listed at Muon

<sup>137</sup> POG twiki page [2], we also require  $p_T > 29$  GeV and  $Rel.Comb.Isolation(dB, dR = 0.4) < 0.2$ .  
<sup>138</sup> Additionally, the tag muon is required to match to the trigger: HLT\_IsoMu27 for data, which  
<sup>139</sup> is the lowest unprescaled and isolated single muon trigger, to exclude efficiency correlations  
<sup>140</sup> with the trigger. The probe muon definition varies according to the selection criterion we want  
<sup>141</sup> to test. Finally, one probe muon per tag is required.

142

<sup>143</sup> Concerning the fits, we use the sum of two voigtians to fit the signal and CMSshape to fit the  
<sup>144</sup> background. The considered Z mass window where the dimuon mass is fitted is [70-130] GeV  
<sup>145</sup> for ID efficiencies and [77-130] GeV for ISO efficiencies, and the number of mass bins is 40.

<sup>146</sup> The "TightHWW" selection is loose and  $\epsilon_{\text{TightHWW}}$  is around 95 – 99% in almost all bins of  $p_T$   
<sup>147</sup> and  $\eta$ .

<sup>148</sup> In Tables 6, we present the muon ID "TightHWW" scale-factors in  $p_T$  and  $\eta$  bins for 2016 com-  
<sup>149</sup> puted by the ratio of data and MC efficiencies. In MC we perform a weight pile-up reweighting  
<sup>150</sup> on the number of vertices in Data.

<sup>151</sup> In Tables 8, we present the muon ISO "Tight iso" scale-factors in  $p_T$  and  $\eta$  bins for 2016 com-  
<sup>152</sup> puted by the ratio of data and MC efficiencies.

<sup>153</sup> In Tables 10, we present the muon ID "TightHWW" scale-factors in  $p_T$  and  $\eta$  bins for 2017 com-  
<sup>154</sup> puted by the ratio of data and MC efficiencies. In MC we perform a weight pile-up reweighting  
<sup>155</sup> on the number of vertices in Data.

<sup>156</sup> In Tables 12, we present the muon ISO "Tight iso" scale-factors in  $p_T$  and  $\eta$  bins for 2017 com-  
<sup>157</sup> puted by the ratio of data and MC efficiencies.

<sup>158</sup> In Tables 14, we present the muon ID "TightHWW" scale-factors in  $p_T$  and  $\eta$  bins for 2018 com-  
<sup>159</sup> puted by the ratio of data and MC efficiencies. In MC we perform a weight pile-up reweighting  
<sup>160</sup> on the number of vertices in Data.

<sup>161</sup> In Tables 16, we present the muon ISO "Tight iso" scale-factors in  $p_T$  and  $\eta$  bins for 2018 com-  
<sup>162</sup> puted by the ratio of data and MC efficiencies.

<sup>163</sup> The isolation efficiency is calculated on top of the "TightHWW" muon ID selections, that is  
<sup>164</sup> why the total SFs for muon "TightHWW" + tight Isolation, which will be used during the  
<sup>165</sup> calculation of the Higgs efficiency in MC are defined by the following formula:

$$SFs = SFs(\text{"TightHWW"}) \cdot SFs(\text{ISO}). \quad (4)$$

<sup>166</sup> Some fits for 2017 are shown for those bins where a deviation of scale factor from unity is seen,  
<sup>167</sup> in Figure 1 for TightHWW ID  $10 < p_T < 15$  GeV,  $-2.1 < \eta < -1.6$ . In Figure 2 for TightHWW  
<sup>168</sup> ID  $15 < p_T < 20$  GeV,  $0.2 < \eta < 0.3$ . In Figure 3 for TightHWW ID  $100 < p_T < 200$  GeV,  
<sup>169</sup>  $2.1 < \eta < 2.4$ . In Figure 4 for TightHWW ID  $100 < p_T < 200$  GeV,  $-0.3 < \eta < -0.8$ . In  
<sup>170</sup> Figure 5 for Tight ISO / TightHWW ID  $10 < p_T < 15$  GeV,  $-0.2 < \eta < 0.2$ . In Figure 6 for  
<sup>171</sup> Tight ISO / TightHWW ID  $10 < p_T < 15$  GeV,  $-0.8 < \eta < -0.3$ . In Figure 7 for Tight ISO /  
<sup>172</sup> TightHWW ID  $15 < p_T < 20$  GeV,  $1.2 < \eta < 1.6$ . Similar features have been seen for 2016 and  
<sup>173</sup> 2018.

### <sup>174</sup> 3.4 Systematic uncertainties of the method

<sup>175</sup> Four variations are considered with respect to the nominal Tag-and-Probe parameters described  
<sup>176</sup> in the previous section.

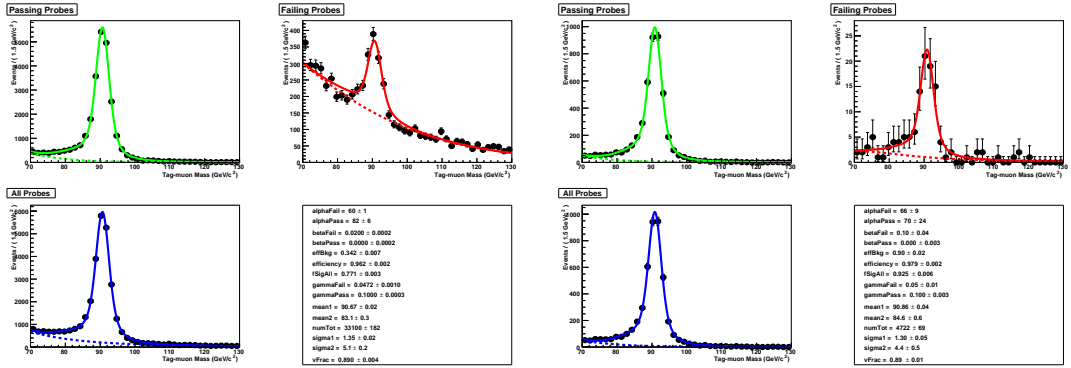


Figure 1: Fit performance for TightHWW ID,  $10 < p_T < 15 \text{ GeV}$   $-1.6 < \eta < -2.1$  for DATA (left) and Montecarlo (right)

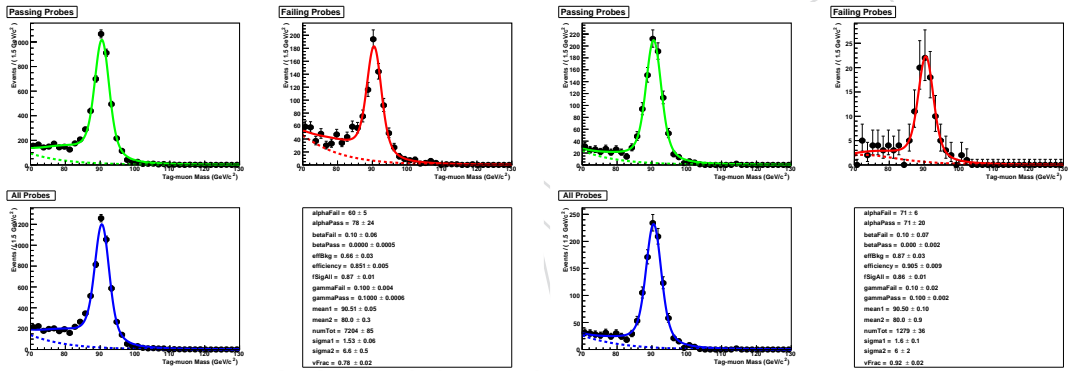


Figure 2: Fit performance for TightHWW ID,  $10 < p_T < 15 \text{ GeV}$   $0.2 < \eta < 0.3$  for DATA (left) and Montecarlo (right)

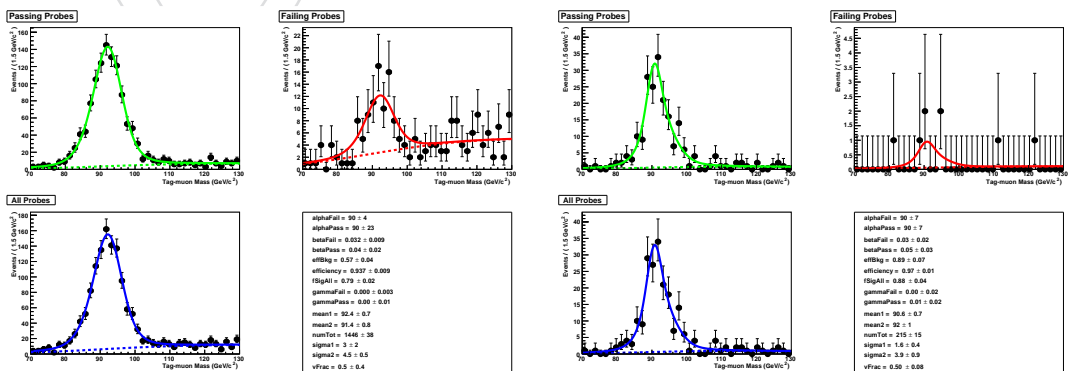


Figure 3: Fit performance for TightHWW ID,  $100 < p_T < 200 \text{ GeV}$   $2.1 < \eta < 2.4$  for DATA (left) and Montecarlo (right)

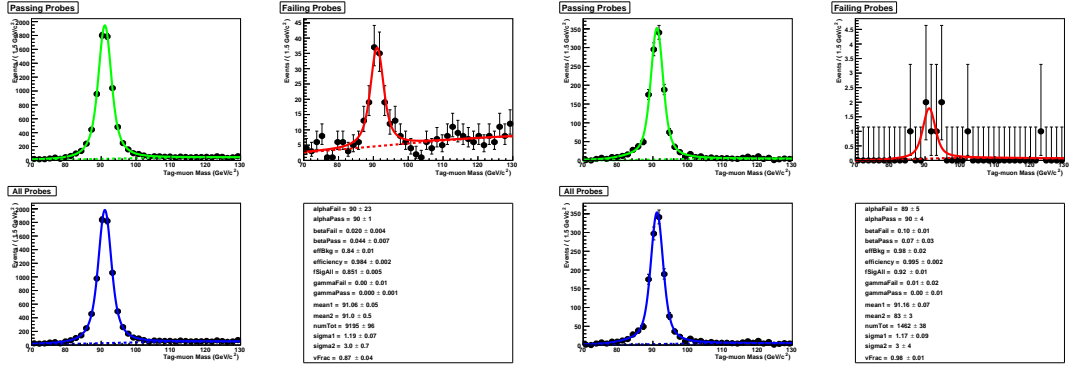


Figure 5: Fit performance for Tight ISO / TightHWW ID,  $10 < p_T < 15 \text{ GeV}$   $-0.2 < \eta < 0.2$  for DATA (left) and Montecarlo (right)

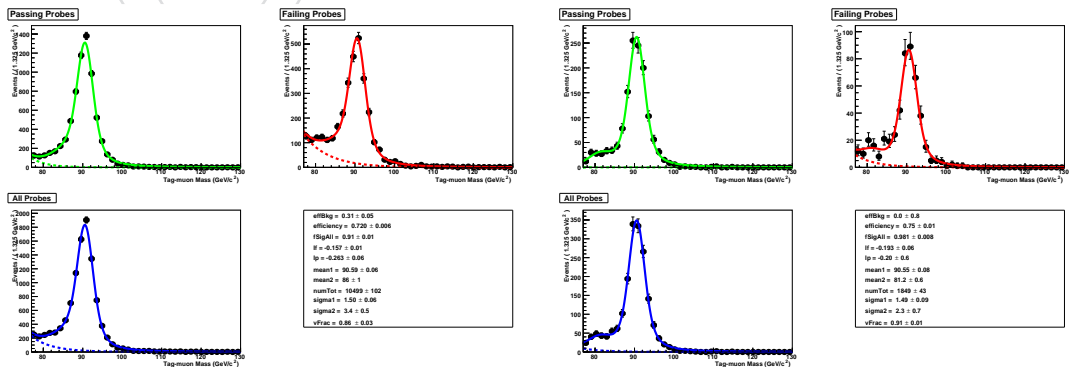


Figure 6: Fit performance for Tight ISO / TightHWW ID,  $10 < p_T < 15 \text{ GeV}$   $-0.8 < \eta < -0.3$  for DATA (left) and Montecarlo (right)

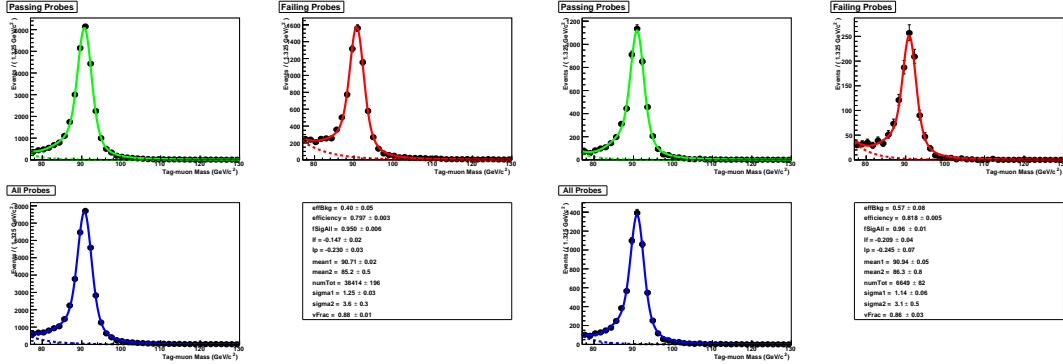


Figure 7: Fit performance for Tight ISO / TightHWW ID,  $15 < p_T < 20 \text{ GeV}$   $1.2 < \eta < 1.6$  for DATA (left) and Montecarlo (right)

- 177 First, the isolation of the tag muon is moved from  $\text{Rel.Comb.Isolation}(dB, dR = 0.4) < 0.2$  to  
 178  $\text{Rel.Comb.Isolation}(dB, dR = 0.4) < 0.3$  and  $\text{Rel.Comb.Isolation}(dB, dR = 0.4) < 0.1$ .  
 179 Second, the signal fit function is changed from two Voigtians to a single Voigtian.  
 180 Third, the number of mass bins where the fit is done is moved from 40 to 50 and 30.  
 181 Finally, we shift the mass range up and down. For ID is the shifted from [70-130] GeV to [75,140]  
 182 GeV and [65,120] GeV, while for ISO it is shifted from [77,130] GeV to [80,140] GeV and [70,120]  
 183 GeV.  
 184 Notice that these variations are the same as the Muon POG used for computing the official 2017  
 185 scale factors.  
 186 Once all the efficiencies have been computed for data and simulation, we estimate the errUp  
 187 (errDown) taking the systematic variation maximizing up (down) error on scale factors per bin.  
 188 Then, the systematic uncertainty is computed as:

$$Syst = \sqrt{\text{errUp}^2 + \text{errDown}^2} \quad (5)$$

- 189 The muon ID "TightHWW" and Isolation scale factors with statistical and systematic uncer-  
 190 tainties are available in this GitHub repository [5].  
 191 In Tables 7, we present the total muon ID "TightHWW" uncertainties on the scale-factors in  $p_T$   
 192 and  $\eta$  bins for 2016.  
 193 In Tables 9, we present the muon ISO "Tight iso" uncertainties on scale-factors in  $p_T$  and  $\eta$  bins  
 194 computed for 2016.  
 195 In Tables 11, we present the total muon ID "TightHWW" uncertainties on the scale-factors in  
 196  $p_T$  and  $\eta$  bins for 2017.  
 197 In Tables 13, we present the muon ISO "Tight iso" uncertainties on scale-factors in  $p_T$  and  $\eta$   
 198 bins computed for 2017.  
 199 In Tables 15, we present the total muon ID "TightHWW" uncertainties on the scale-factors in  
 200  $p_T$  and  $\eta$  bins for 2018.  
 201 In Tables 17, we present the muon ISO "Tight iso" uncertainties on scale-factors in  $p_T$  and  $\eta$   
 202 bins computed for 2018.

Table 6: Muon ID ("TightHWW") Scale-Factors for full Run 2016 Legacy Rereco.

$p_T/\eta$	-2.4:-2.1	-2.1:-1.6	-1.6:-1.2	-1.2:-0.8	-0.8:-0.3	-0.3:-0.2	-0.2:0.0	0.0:0.2	0.2:0.3	0.3:0.8	0.8:1.2	1.2:1.6	1.6:2.1	2.1:2.4
10:15	0.9995	1.0016	0.9985	0.9907	0.9844	1.0183	1.0089	1.0089	1.0265	0.9862	0.9808	0.9882	0.9927	0.9972
15:20	0.9805	0.9870	0.9950	0.9867	0.9935	0.9686	0.9927	0.9927	0.9771	0.9924	0.9826	0.9986	0.9912	0.9797
20:25	0.9756	0.9829	0.9949	0.9823	0.9914	0.9712	0.9906	0.9910	0.9590	0.9917	0.9776	0.9927	0.9873	0.9822
25:30	0.9793	0.9850	0.9942	0.9794	0.9912	0.9659	0.9899	0.9886	0.9610	0.9899	0.9784	0.9932	0.9874	0.9805
30:40	0.9773	0.9828	0.9947	0.9782	0.9891	0.9685	0.9903	0.9883	0.9614	0.9887	0.9770	0.9940	0.9876	0.9828
40:60	0.9766	0.9851	0.9957	0.9796	0.9908	0.9713	0.9911	0.9894	0.9638	0.9898	0.9786	0.9945	0.9871	0.9774
60:100	0.9618	0.9794	0.9963	0.9773	0.9917	0.9597	0.9914	0.9886	0.9655	0.9883	0.9764	0.9948	0.9858	0.9796
100:200	0.9803	0.9743	0.9831	0.9740	0.9949	0.9634	0.9954	0.9814	0.9482	0.9870	0.9732	0.9962	0.9782	0.9895
Color Definition														
Scale Factors	0.99-1.01	0.98-0.99	1.01-1.02	0.97-0.98	1.02-1.03	0.96-0.97	0.95-0.96	< 0.95						

Table 7: Muon ID (“TightHWW”) total uncertainty on Scale-Factors for full Run 2016 Legacy Rereco.

$p_T/\eta$	-2.4:-2.1	-2.1:-1.6	-1.6:-1.2	-1.2:-0.8	-0.8:-0.3	-0.3:-0.2	-0.2:0.0	0.0:0.2	0.2:0.3	0.3:0.8	0.8:1.2	1.2:1.6	1.6:2.1	2.1:2.4
10:15	0.015	0.008	0.010	0.011	0.009	0.05	0.02	0.02	0.06	0.010	0.009	0.010	0.008	0.013
15:20	0.013	0.006	0.007	0.007	0.006	0.019	0.007	0.007	0.02	0.006	0.007	0.006	0.006	0.009
20:25	0.010	0.005	0.008	0.006	0.010	0.012	0.009	0.009	0.013	0.010	0.009	0.006	0.005	0.008
25:30	0.008	0.005	0.006	0.006	0.006	0.008	0.006	0.006	0.008	0.006	0.006	0.006	0.005	0.007
30:40	0.008	0.005	0.005	0.005	0.005	0.006	0.005	0.005	0.005	0.006	0.005	0.005	0.005	0.009
40:60	0.007	0.005	0.005	0.005	0.005	0.006	0.005	0.005	0.006	0.006	0.005	0.005	0.005	0.008
60:100	0.011	0.006	0.005	0.005	0.011	0.010	0.006	0.006	0.016	0.005	0.006	0.005	0.006	0.012
100:200	0.04	0.013	0.006	0.011	0.008	0.05	0.05	0.011	0.011	0.05	0.006	0.011	0.009	0.014
Total uncertainty	0.000-0.005	0.005-0.01	0.010-0.02	0.02-0.035	0.035-0.05	> 0.05								

Color Definition

Table 8: Muon ISO / Muon ID ("TightHWW") Scale-Factors for full Run 2016 Legacy Rereco.

$p_T/\eta$	-2.4:-2.1	-2.1:-1.6	-1.6:-1.2	-1.2:-0.8	-0.8:-0.3	-0.3:-0.2	-0.2:-0.0	0.0:0.2	0.2:0.3	0.3:0.8	0.8:1.2	1.2:1.6	1.6:2.1	2.1:2.4
10:15	0.9650	0.9640	0.9596	0.9719	0.9620	0.9507	0.9648	0.9648	0.9745	0.9668	0.9605	0.9679	0.9602	0.9492
15:20	0.9670	0.9780	0.9753	0.9660	0.9737	0.9945	0.9652	0.9652	0.9830	0.9842	0.9880	0.9648	0.9702	0.9610
20:25	0.9789	0.9889	0.9832	0.9905	0.9795	0.9784	0.9691	0.9925	0.9830	0.9915	0.9854	0.9856	0.9821	0.9797
25:30	0.9905	0.9927	0.9921	0.9911	0.9934	0.9928	0.9886	0.9961	0.9930	0.9988	1.0009	0.9901	0.9910	0.9871
30:40	0.9971	0.9973	0.9951	0.9947	0.9939	0.9956	0.9930	0.9936	0.9943	0.9979	0.9976	0.9932	0.9954	0.9927
40:60	0.9990	0.9975	0.9972	0.9971	0.9958	0.9956	0.9955	0.9955	0.9973	0.9979	0.9976	0.9964	0.9971	0.9971
60:100	0.9999	0.9990	0.9980	0.9996	0.9986	0.9969	0.9989	0.9980	0.9971	1.0004	0.9986	1.0001	0.9980	1.0038
100:200	0.9966	1.0003	1.0017	1.0018	1.0033	0.9980	1.0051	0.9931	1.0020	1.0085	0.9994	0.9967	1.0066	1.0048

Color Definition

Scale Factors	0.99-1.01	0.98-0.99	0.97-0.98	0.96-0.97	0.95-0.96	< 0.95
---------------	-----------	-----------	-----------	-----------	-----------	--------

Table 9: Muon ISO / Muon ID (“TightHWW”) total uncertainty on Scale-Factors for full Run 2016 Legacy Rereco.

$p_T/\eta$	-2.4:-2.1	-2.1:-1.6	-1.6:-1.2	-1.2:-0.8	-0.8:-0.3	-0.3:-0.2	-0.2:0.0	0.0:0.2	0.2:0.3	0.3:0.8	0.8:1.2	1.2:1.6	1.6:2.1	2.1:2.4
10:15	0.017	0.014	0.019	0.02	0.03	0.06	0.06	0.06	0.06	0.03	0.02	0.018	0.014	0.017
15:20	0.009	0.008	0.010	0.012	0.012	0.04	0.018	0.018	0.04	0.013	0.013	0.010	0.007	0.010
20:25	0.006	0.004	0.005	0.007	0.006	0.015	0.010	0.011	0.016	0.007	0.007	0.006	0.004	0.006
25:30	0.004	0.002	0.003	0.004	0.003	0.008	0.005	0.005	0.008	0.003	0.004	0.003	0.003	0.004
30:40	0.0014	0.0009	0.0011	0.0012	0.0011	0.002	0.0017	0.0018	0.002	0.0010	0.0013	0.0011	0.0010	0.0013
40:60	0.0007	0.0004	0.0005	0.0005	0.0005	0.0011	0.0008	0.0008	0.0009	0.0005	0.0005	0.0005	0.0004	0.0007
60:100	0.002	0.0011	0.0013	0.0012	0.0013	0.002	0.002	0.003	0.003	0.0012	0.0013	0.0013	0.0011	0.002
100:200	0.007	0.006	0.004	0.004	0.005	0.004	0.007	0.003	0.008	0.005	0.005	0.007	0.010	
Total uncertainty	0.000-0.005	0.005-0.01	0.010-0.02	0.02-0.035	0.035-0.05	> 0.05								

Color Definition

Table 10: Muon ID ("TightHWW") Scale-Factors for full Run 2017.

$p_T/\eta$	-2.4:-2.1	-2.1:-1.6	-1.6:-1.2	-1.2:-0.8	-0.8:-0.3	-0.3:-0.2	-0.2:-0.0	0.0:0.2	0.2:0.3	0.3:0.8	0.8:1.2	1.2:1.6	1.6:2.1	2.1:2.4
10:15	0.9880	0.9827	0.9981	0.9961	1.0018	1.0099	1.0129	1.0129	1.0193	0.9893	0.9767	0.9978	0.9901	0.9852
15:20	0.9735	0.9831	0.9955	0.9849	0.9995	0.9582	0.9932	0.9932	0.9400	0.9891	0.9813	0.9970	0.9899	0.9807
20:25	0.9737	0.9839	0.9976	0.9863	0.9940	0.9561	0.9936	0.9963	0.9757	0.9915	0.9800	0.9975	0.9892	0.9771
25:30	0.9741	0.9819	0.9975	0.9852	0.9931	0.9580	0.9936	0.9952	0.9619	0.9914	0.9790	0.9979	0.9905	0.9826
30:40	0.9719	0.9794	0.9973	0.9842	0.9935	0.9570	0.9932	0.9942	0.9635	0.9921	0.9781	0.9972	0.9900	0.9815
40:60	0.9709	0.9815	0.9979	0.9849	0.9941	0.9556	0.9945	0.9953	0.9636	0.9924	0.9790	0.9966	0.9896	0.9800
60:100	0.9622	0.9779	0.9959	0.9842	0.9935	0.9525	0.9938	0.9944	0.9563	0.9918	0.9747	0.9967	0.9868	0.9887
100:200	0.9649	0.9732	0.9899	0.9851	0.9884	0.9645	1.0060	0.9953	0.9831	0.9872	0.9738	0.9981	0.9868	0.9635

Color Definition

Scale Factors	0.99-1.01	0.98-0.99	0.97-0.98	0.96-0.97	0.95-0.96	< 0.95
---------------	-----------	-----------	-----------	-----------	-----------	--------

Table 11: Muon ID ("TightHW $\tau\tau$ ") total uncertainty on Scale-Factors for full Run 2017.

$p_T/\eta$	-2.4:-2.1	-2.1:-1.6	-1.6:-1.2	-1.2:-0.8	-0.8:-0.3	-0.3:-0.2	-0.2:0.0	0.0:0.2	0.2:0.3	0.3:0.8	0.8:1.2	1.2:1.6	1.6:2.1	2.1:2.4
10:15	0.010	0.007	0.008	0.012	0.010	0.05	0.016	0.016	0.06	0.011	0.012	0.008	0.007	0.009
15:20	0.008	0.006	0.006	0.008	0.005	0.02	0.007	0.007	0.02	0.007	0.007	0.006	0.006	0.007
20:25	0.006	0.005	0.006	0.007	0.008	0.012	0.007	0.008	0.014	0.008	0.008	0.007	0.005	0.007
25:30	0.006	0.006	0.005	0.005	0.005	0.009	0.006	0.006	0.008	0.005	0.005	0.005	0.007	0.006
30:40	0.006	0.005	0.005	0.005	0.005	0.006	0.005	0.005	0.005	0.006	0.005	0.005	0.005	0.005
40:60	0.005	0.005	0.005	0.005	0.005	0.006	0.005	0.005	0.012	0.005	0.008	0.005	0.005	0.005
60:100	0.008	0.006	0.011	0.007	0.005	0.010	0.006	0.006	0.011	0.005	0.006	0.005	0.006	0.008
100:200	0.05	0.014	0.006	0.012	0.007	0.04	0.014	0.011	0.05	0.006	0.014	0.009	0.013	0.03
Total uncertainty	0.000-0.005	0.005-0.01	0.010-0.02	0.02-0.035	0.035-0.05	> 0.05								

Color Definition

Table 12: Muon ISO / Muon ID ("TightHWW") Scale-Factors for full Run 2017.

$p_T/\eta$	-2.4:-2.1	-2.1:-1.6	-1.6:-1.2	-1.2:-0.8	-0.8:-0.3	-0.3:-0.2	-0.2:0.0	0.0:0.2	0.2:0.3	0.3:0.8	0.8:1.2	1.2:1.6	1.6:2.1	2.1:2.4
10:15	0.9808	1.0062	0.9758	0.9868	0.9564	0.9705	0.92208	0.9790	0.9952	0.9885	0.9992	0.9919	0.9825	
15:20	0.9863	1.0046	0.9902	0.9974	0.9901	0.9939	0.9806	0.9806	1.0073	1.0037	0.9744	0.9747	0.9902	0.9838
20:25	0.9876	0.9903	0.9826	0.9883	0.9965	0.9850	0.9893	0.9869	0.9873	0.9896	1.0004	0.9862	0.9993	0.9915
25:30	0.9941	0.9956	0.9903	0.9868	0.9944	0.9907	0.9988	0.9911	0.9964	0.9960	0.9919	0.9912	0.9972	0.9914
30:40	0.9964	0.9980	0.9937	0.9922	0.9958	0.9925	0.9956	0.9959	0.9961	0.9976	0.9963	0.9930	0.9962	0.9944
40:60	0.9991	0.9990	0.9965	0.9964	0.9966	0.9967	0.9977	0.9992	0.9989	0.9990	0.9978	0.9965	0.9986	0.9981
60:100	0.9962	1.0001	0.9990	1.0009	0.9971	1.0016	0.9985	0.9992	1.0002	1.0011	0.9988	0.9993	0.9995	1.0008
100:200	0.9947	1.0028	1.0001	1.0056	1.0006	0.9972	0.9958	1.0000	0.9978	0.9996	0.9980	1.0019	1.0000	0.9977

Color Definition

Scale Factors	0.99-1.01	0.98-0.99	0.97-0.98	0.96-0.97	0.95-0.96	< 0.95
---------------	-----------	-----------	-----------	-----------	-----------	--------

Table 13: Muon ISO / Muon ID ("TightHWW") total uncertainty on Scale-Factors for full Run 2017.

$p_T/\eta$	-2.4:-2.1	-2.1:-1.6	-1.6:-1.2	-1.2:-0.8	-0.8:-0.3	-0.3:-0.2	-0.2:0.0	0.0:0.2	0.2:0.3	0.3:0.8	0.8:1.2	1.2:1.6	1.6:2.1	2.1:2.4
10:15	0.017	0.017	0.02	0.03	0.03	0.06	0.06	0.06	0.06	0.03	0.03	0.02	0.015	0.017
15:20	0.010	0.010	0.015	0.017	0.016	0.04	0.02	0.02	0.04	0.016	0.016	0.013	0.009	0.011
20:25	0.008	0.007	0.009	0.010	0.009	0.018	0.012	0.018	0.009	0.009	0.010	0.009	0.007	0.008
25:30	0.006	0.006	0.006	0.007	0.006	0.010	0.007	0.010	0.006	0.006	0.007	0.006	0.006	0.006
30:40	0.005	0.005	0.005	0.005	0.005	0.006	0.005	0.005	0.005	0.005	0.005	0.005	0.005	0.005
40:60	0.005	0.005	0.005	0.005	0.005	0.005	0.005	0.005	0.005	0.005	0.005	0.005	0.005	0.005
60:100	0.005	0.005	0.005	0.005	0.005	0.006	0.005	0.006	0.005	0.005	0.005	0.005	0.005	0.006
100:200	0.008	0.007	0.007	0.008	0.006	0.009	0.007	0.008	0.006	0.006	0.006	0.008	0.009	0.010
Total uncertainty	0.000-0.005	0.005-0.01	0.010-0.02	0.02-0.035	0.035-0.05	> 0.05								

Color Definition

Table 14: Muon ID ("TightHWW") Scale-Factors for full Run 2018.

$p_T/\eta$	-2.4:-2.1	-2.1:-1.6	-1.6:-1.2	-1.2:-0.8	-0.8:-0.3	-0.3:-0.2	-0.2:-0.0	0.0:0.2	0.2:0.3	0.3:0.8	0.8:1.2	1.2:1.6	1.6:2.1	2.1:2.4
10:15	0.9686	0.9806	0.9996	0.9801	0.9975	0.9895	1.0053	1.0053	0.9446	0.9908	0.9763	0.9984	0.9967	0.9726
15:20	0.9683	0.9817	0.9974	0.9836	0.9951	0.9513	0.9925	0.9925	0.9678	0.9678	0.9901	0.9849	0.9945	0.9888
20:25	0.9681	0.9826	0.9979	0.9874	0.9963	0.9670	0.9936	0.9986	0.9725	0.9921	0.9835	0.9967	0.9899	0.9786
25:30	0.9679	0.9821	0.9977	0.9858	0.9960	0.9779	0.9943	0.9918	0.9795	0.9941	0.9804	0.9964	0.9890	0.9742
30:40	0.9688	0.9789	0.9970	0.9848	0.9956	0.9778	0.9933	0.9946	0.9740	0.9930	0.9814	0.9957	0.9885	0.9749
40:60	0.9672	0.9802	0.9967	0.9856	0.9964	0.9752	0.9950	0.9952	0.9743	0.9943	0.9821	0.9958	0.9875	0.9761
60:100	0.9652	0.9756	0.9959	0.9835	0.9957	0.9725	0.9919	0.9946	0.9760	0.9931	0.9803	0.9945	0.9853	0.9702
100:200	0.9500	0.9750	0.9944	0.9839	0.9976	0.9688	0.9984	0.9890	0.9460	0.9925	0.9778	0.9954	0.9780	0.9881

Scale Factors	0.99-1.01	0.98-0.99	0.97-0.98	0.96-0.97	0.95-0.96	< 0.95
Color Definition						

Table 15: Muon ID ("TightHW $\tau\tau$ ") total uncertainty on Scale-Factors for full Run 2018.

$p_T/\eta$	-2.4:-2.1	-2.1:-1.6	-1.6:-1.2	-1.2:-0.8	-0.8:-0.3	-0.3:-0.2	-0.2:0.0	0.0:0.2	0.2:0.3	0.3:0.8	0.8:1.2	1.2:1.6	1.6:2.1	2.1:2.4
10:15	0.009	0.007	0.008	0.009	0.010	0.04	0.02	0.02	0.04	0.008	0.011	0.010	0.007	0.010
15:20	0.007	0.006	0.007	0.006	0.006	0.016	0.007	0.007	0.017	0.006	0.006	0.006	0.006	0.007
20:25	0.006	0.005	0.006	0.008	0.008	0.011	0.008	0.008	0.011	0.008	0.006	0.007	0.005	0.006
25:30	0.005	0.007	0.005	0.005	0.006	0.007	0.006	0.006	0.005	0.008	0.005	0.005	0.005	0.007
30:40	0.005	0.005	0.005	0.005	0.005	0.005	0.005	0.005	0.005	0.005	0.005	0.005	0.005	0.005
40:60	0.005	0.005	0.005	0.005	0.005	0.006	0.005	0.005	0.005	0.005	0.005	0.005	0.005	0.005
60:100	0.007	0.005	0.005	0.005	0.005	0.008	0.005	0.005	0.009	0.005	0.006	0.005	0.005	0.007
100:200	0.04	0.010	0.007	0.010	0.007	0.03	0.010	0.009	0.04	0.006	0.011	0.007	0.011	0.03
Total uncertainty	0.000-0.005	0.005-0.01	0.010-0.02	0.02-0.035	0.035-0.05	> 0.05								

Color Definition

Table 16: Muon ISO / Muon ID ("TightHWW") Scale-Factors for full Run 2018.

$p_T/\eta$	-2.4:-2.1	-2.1:-1.6	-1.6:-1.2	-1.2:-0.8	-0.8:-0.3	-0.3:-0.2	-0.2:0.0	0.0:0.2	0.2:0.3	0.3:0.8	0.8:1.2	1.2:1.6	1.6:2.1	2.1:2.4
10:15	1.1308	1.0907	1.0156	0.9654	0.9618	0.9595	1.0022	1.0022	0.9491	0.9796	0.9731	1.0091	1.0746	1.1053
15:20	1.0856	1.0669	1.0211	0.9886	0.9744	0.9716	0.9803	0.9803	0.9866	0.9904	0.9951	1.0140	1.0501	1.0877
20:25	1.0610	1.048	1.0082	0.9898	0.9834	0.9838	0.9855	0.9863	0.9790	0.9969	0.9851	1.0074	1.0407	1.0674
25:30	1.0394	1.0303	1.0082	0.9887	0.9880	0.9886	0.9853	0.9889	0.9874	0.9915	0.9931	1.0064	1.0307	1.0463
30:40	1.0239	1.0184	1.0037	0.9920	0.9926	0.9897	0.9908	0.9917	0.9930	0.9971	0.9957	1.0022	1.0159	1.0259
40:60	1.0121	1.0093	1.0021	0.9969	0.9967	0.9958	0.9957	0.9962	0.9966	0.9982	0.9978	1.0013	1.0079	1.0113
60:100	1.0056	1.0040	0.9996	0.9992	0.9983	0.9962	0.9971	0.9978	0.9991	1.0003	0.9988	1.0011	1.0043	1.0044
100:200	0.9954	1.0020	0.9995	1.0034	0.9993	0.9977	1.0057	0.9999	1.0092	1.0019	1.0011	1.0057	1.0049	0.9944

Color Definition

Scale Factors	0.99-1.01	0.98-0.99, 1.01-1.02	0.97-0.98, 1.02-1.03	0.96-0.97, 1.03-1.04	0.95-0.96, 1.04-1.05	< 0.95, > 1.05
---------------	-----------	----------------------	----------------------	----------------------	----------------------	----------------

203 The trigger muon efficiency will be discussed in Section 5.

### 204 3.5 Muon momentum scale and resolution

205 To eliminate a possible bias in the muon momentum originated from detector misalignment,  
 206 software reconstruction or uncertainties in the magnetic field, we apply the corrections devel-  
 207 oped by the Rochester group [6, 7]. These corrections are derived from a sample of  $Z/\gamma^* \rightarrow \mu\mu$   
 208 events, in bins of charge,  $\eta$ , and  $\phi$  of the muons. They are based on the comparison of the po-  
 209 sition of the peak in the  $\mu^+\mu^-$  invariant mass distributions with the  $Z$  mass PDG value. Both  
 210 data and MC samples are corrected with this method, which also provides an estimation of the  
 211 associated systematic uncertainty. Looking at the relative uncertainty of the correction factor  
 212 we can consider an uncertainty of 0.2% in the muon momentum for all three years. Differences  
 213 between the peak position of corrected data and corrected MC are also of this amount.

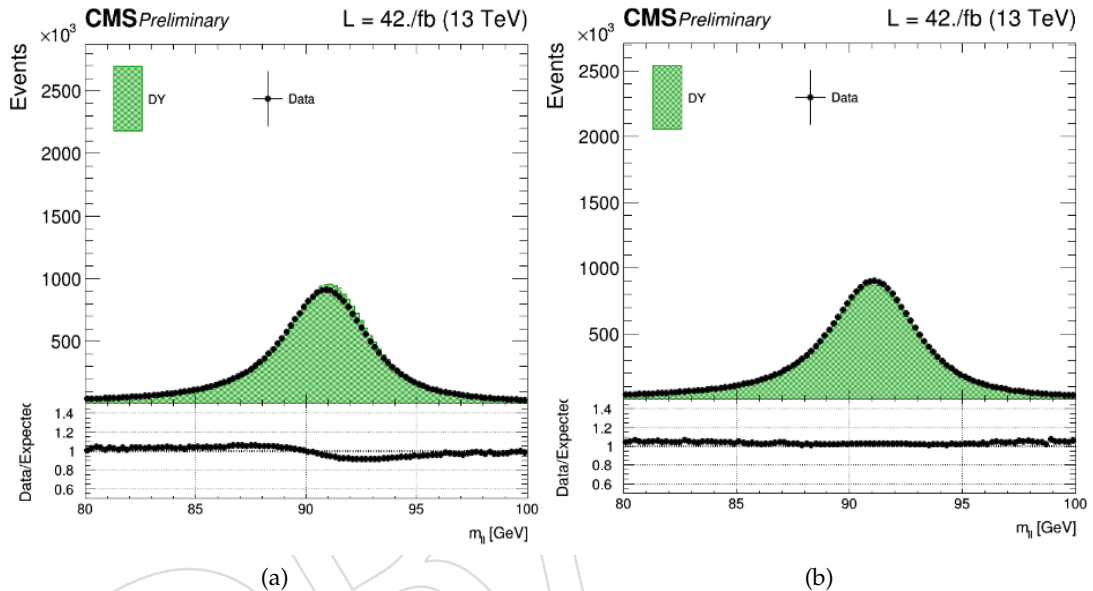


Figure 8: Comparison of the data/MC agreement in the DY control region before (a) and after (b) applying the Rochester corrections to 2017 data and MC. The wiggle around the  $Z$  mass peak is flattened with the changes, which improves the agreement.

Table 17: Muon ISO / Muon ID (“TightHWW”) total uncertainty on Scale-Factors for full Run 2018.

Color Definition														
Total uncertainty														
$p_T/\eta$	-2.4:-2.1	-2.1:-1.6	-1.6:-1.2	-1.2:-0.8	-0.8:-0.3	-0.3:-0.2	-0.2:-0.0	0.0:0.2	0.2:0.3	0.3:0.8	0.8:1.2	1.2:1.6	1.6:2.1	2.1:2.4
10:15	0.017	0.014	0.018	0.02	0.03	0.09	0.05	0.05	0.08	0.02	0.03	0.019	0.015	0.016
15:20	0.009	0.008	0.010	0.011	0.011	0.03	0.015	0.015	0.03	0.011	0.012	0.010	0.008	0.010
20:25	0.006	0.004	0.005	0.006	0.006	0.013	0.009	0.009	0.013	0.006	0.006	0.004	0.004	0.006
25:30	0.003	0.003	0.003	0.003	0.006	0.006	0.004	0.004	0.006	0.003	0.003	0.002	0.003	0.003
30:40	0.0011	0.0010	0.0010	0.0009	0.0008	0.0018	0.0012	0.0011	0.0019	0.0008	0.0010	0.0010	0.0009	0.0012
40:60	0.0007	0.0004	0.0005	0.0004	0.0004	0.0015	0.0015	0.0006	0.0005	0.0004	0.0004	0.0004	0.0004	0.0007
60:100	0.002	0.0014	0.0012	0.0013	0.0002	0.0016	0.0016	0.003	0.0016	0.0010	0.0012	0.0013	0.0014	0.0019
100:200	0.006	0.006	0.005	0.004	0.003	0.007	0.007	0.005	0.008	0.003	0.004	0.005	0.005	0.008

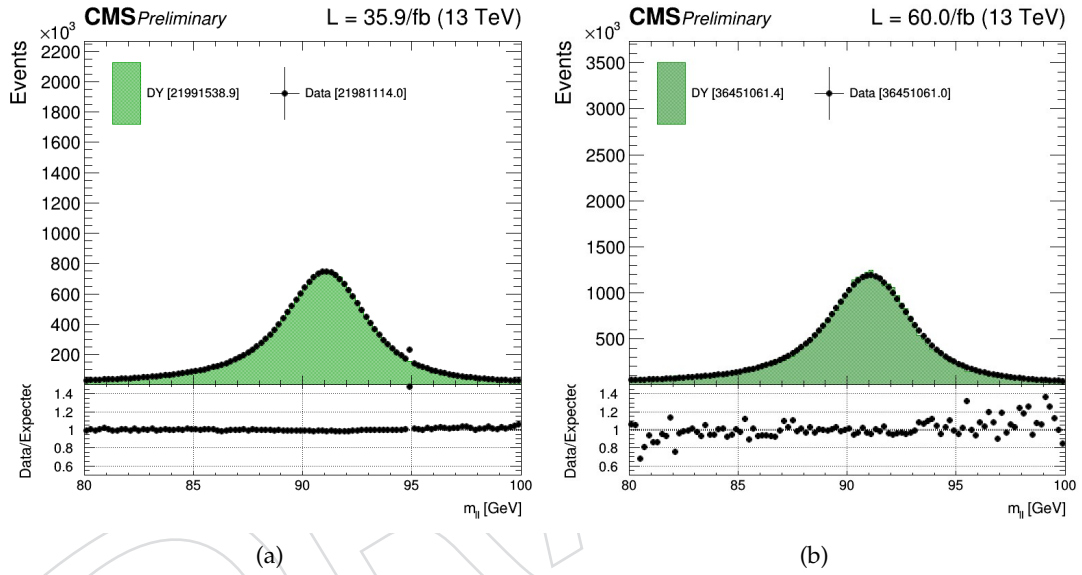


Figure 9: This is the comparison of the data/MC agreement in the DY control region for 2016 (a) and 2018 (b) after applying the Rochester corrections. Same as for 2017, the wiggle around the Z mass peak is flattened.

## 214 4 Electrons

215 Editors: A. Kumar, P. Chen, P. Yu

### 216 4.1 Electron Reconstruction and Selection

217 Several strategies are used in CMS to identify prompt isolated electrons (signal), and to separate  
 218 them from background sources, mainly originating from photon conversions, jets misidentified  
 219 as electrons, or electrons from semileptonic decays of  $b$  and  $c$  quarks. Simple and robust algo-  
 220 rithms have been developed to apply sequential selections on a set of discriminants. Simulated  
 221 samples are used to test different electron ids and evaluate corresponding efficiencies.

### 222 4.2 Variables used for electron Id

223 Variables that provide discriminating power are grouped into three main categories:

- 224 • **Calorimetric observables:** Used to separate genuine electrons (signal electrons or  
 225 electrons from photon conversions) from misidentified electrons (jets with large elec-  
 226 tromagnetic components), based on the transverse shape of electromagnetic show-  
 227 ers in the ECAL and exploiting the fact that electromagnetic showers are narrower  
 228 than hadronic showers. The energy fractions deposited in the HCAL (expected to  
 229 be small, as electromagnetic showers are essentially fully contained in the ECAL), as  
 230 well the energy deposited in the preshower in the endcaps are also used.

- 231 • **hOverE ( $\frac{H}{E}$ ):** Ratio of energy deposited in HCAL to ECAL
- 232 • **ooEmoop ( $\frac{1}{E_{SC}} - \frac{1}{p}$ ):**  $E_{SC}$  is the supercluster energy and  $p$  is the track mo-  
 233 mentum at the point of closest approach to the primary vertex
- 234 • **sigmaIetaIeta ( $\sigma_{\eta\eta}$ ):** The weighted cluster RMS along  $\eta$  inside 5x5 region  
 235 of supercluster
- 236 • **dEtaInSeed ( $\Delta\eta$ ):**  $\eta$  difference between supercluster and position of inner  
 237 track extrapolated from interaction vertex.
- 238 • **dPhiIn ( $\Delta\phi$ ):**  $\phi$  difference between supercluster and position of inner  
 239 track extrapolated from interaction vertex.
- 240 • **sigmaIphiIphi ( $\sigma_{\phi\phi}$ ):** The weighted cluster RMS along  $\eta$  inside 5x5 re-  
 241 gion of supercluster.
- 242 • **circularity:**  $1 - E^{1\times 5} / E^{5\times 5}$ ,  $E^{n\times m}$  is the sum of cluster energies of  $n$  cells  
 243 ( $\phi$ )  $\times$   $m$  cells ( $\eta$ ) region.
- 244 • **R9:**  $1 - E^{3\times 3} / E_{SC}$
- 245 • **supercluster  $\eta$  width**
- 246 • **supercluster  $\phi$  width**
- 247 • **JSC:**  $\eta$  of supercluster.
- 248 •  **$\Delta\eta_{seed,track}$ :** The seed cluster  $\eta$  - track  $\eta$  position at the point of closest  
 249 approach to the seed cluster, extrapolated from the outermost track state.
- 250 •  **$E_{ES}/E_{SC,raw}$ :**  $E_{ES}$  is the energy from preshower,  $E_{SC,raw}$  is the sum of clus-  
 251 ter energies without any corrections.
- 252 •  **$E_{SC}/p$ :** The supercluster energy over track momentum at the point of clos-  
 253 est approach to the beamspot.
- 254 •  **$E_{Cluster}/p$ :** The electron cluster energy/track momentum at the point of  
 255 closest approach to the electron cluster, extrapolated from the outermost  
 256 track state.

- 257     • **fbrem:** The brem fraction from the gsf fit, (Track momentum in - Track  
258       momentum out) / Track momentum in.
- 259     • **Isolation variables:** A significant fraction of background to isolated primary elec-  
260       trons is due to misidentified jets or to genuine electrons within a jet resulting from  
261       semileptonic decays of  $b$  or  $c$  quarks. In both cases, the electron candidates have  
262       significant energy flow near their trajectories, and requiring electrons to be isolated  
263       from such nearby activity greatly reduces these sources of background.
- 264       • **relIsoWithEA:** PF based isolation defined in a cone size of 0.3 around the  
265       electron direction, relative to electron  $p_T$
- 266     • **Tracking quality variable:**
- 267       • **Expected inner hits:** The number of pixel layers without corresponding  
268       hits in the trajectory of a reconstructed gsfTrack.
- 269       • **Number of matched track hits:** The number of tracker layers with hit in  
270       the trajectory of track.
- 271       • **kfchi2:** The  $\chi^2$  value calculated from the reconstructed track and corre-  
272       sponding hits.
- 273       • **Number of matched gsfTrack hits:** The  $\chi^2$  value calculated from the re-  
274       constructed gsfTrack and corresponding hits.
- 275       • **gsfchi2:** The number of tracker layers with hit in the trajectory of gsf-  
276       Track.
- 277     • **Conversion rejection variables:** Used to reject secondary electrons produced from  
278       photon conversions. To reject this background, CMS algorithms exploit the pattern  
279       of track hits. When photon conversions take place inside the volume of the tracker,  
280       the first hit on electron tracks from the converted photons is often not located in the  
281       innermost layer of the tracker, and missing hits are therefore present in that region.  
282       For prompt electrons, whose trajectories start from the beamline, no missing hits are  
283       expected in the inner layers. Also the impact parameter of the electron is required to  
284       be small for the electron to be originated from the vertex of interest
- 285       • **Conversion veto:** Check if a given electron candidate matches to at least  
286       one conversion candidate in the collection which also passes the selection  
287       cuts.
- 288       • Transverse (**d0**) and longitudinal (**dz**) impact parameter
- 289       • **Probability of conversion vertex fit** ( $P_{conversion}$ )
- 290     A set of selections is applied on the variables defined above to separate the real electrons from  
291       fakes. A set of cuts on various variables for achieving a particular signal efficiency is called  
292       "Working Point(WP)". And such type of ID is called "cut-based id". EGamma Physics Object  
293       Group (EGM POG) provides four such working points. The cuts are different for electrons in  
294       the ECAL barrel or in the endcap. These are defined below:
- 295       • **Tight WP :** This corresponds to an average 70% selection efficiency for electrons with  
296        $p_T > 20$  GeV. This working point is used where backgrounds are very large. The  
297        $H \rightarrow WW$  analysis has large backgrounds like  $W + jets$ , where the second lepton is  
298       fake. So, in this analysis we use Tight WP for electrons. On the top of that, we apply  
299       more cuts to make the electron id selection *Trigger safe*.
- 300       • **Medium WP :** Here, the average efficiency is about 80% for electrons with  $p_T > 20$   
301       GeV. This is also a good starting point for measurements of  $W$  and  $Z$  cross-sections.
- 302       • **Loose WP :** This working point is used only for very clean final states. The average

303 efficiency is about 90%.

- 304 • **Veto WP** : Generally, this is not used for signal selection. However, it is found to  
 305 be useful for extra lepton veto counting of electrons. The average efficiency is about  
 306 95%.

307 The cuts which go inside these working points depend on various factors including the running  
 308 conditions. So, every time the conditions change, the cuts have to be tuned again.

309 Another set of selection come from the MVA approach, a single discriminator variable,  $MVA_{min}$ ,  
 310 is computed based on multiple variables of the electron object and provides separation between  
 311 the signal and backgrounds on the basis of Boosted Decision Tree (BDT) algorithm. One can  
 312 then cut on discriminator value or use the distribution of the values for a shape based statistical  
 313 analysis. Two WPs of 80% and 90% signal efficiency from General Purpose MVA is given by the  
 314 EGM POG. As for the variables used in the MVA training, they are summarized on Table 18.

Table 18: The variables used in the MVA training.

MVA variables
$\sigma_{\eta\eta}$
$\sigma_{\phi\phi}$
circularity
R9
supercluster $\eta$ width
supercluster $\phi$ width
$hOverE \left( \frac{H}{E} \right)$
Number of matched track hits
Number of matched gsfTrack hits
kfchi2
gsfchi2
fbrem
Expected inner hits
$P_{conversion}$
$E_{SC}/p$
$E_{Cluster}/p$
$\text{ooEmoop} \left( \frac{1}{E_{SC}} - \frac{1}{p} \right)$
dEtaIn ( $\Delta\eta$ )
dPhiIn ( $\Delta\phi$ )
$\Delta\eta_{seed,track}$
$\rho$
pfPhotonIso
pfChargedHadIso
pfNeutralHadIso
$E_{ES}/E_{SC,raw}$

### 315 4.3 Electron Id in HWW

- 316 In  $H \rightarrow WW$ , we define the “**loose**” electron as the denominator in fake rate calculation, as for  
 317 the numerator, which is applied on the top of the “**loose**” electron, the “**tight**” definition are  
 318 defined and tested in the Id performance study.
- 319 In 2016, the “**loose**” electron is defined from the basis of the official cut-based “Trigger Save”

of electron Id given on Table 19. There are some identification and detector-based isolation requirements at HLT level from electron triggers. The extra cuts like the expected missing inner hits,  $d0$  and  $dz$ , are summarized on Table 20. The “**Tight**” electron are chosen from six different definitions with performance study. These six working points are derived from the cut-based Id and the MVA Id. For cut-based Ids, we have two working points. The `cut_WP_Tight80X` WP consists of the official cut-based “Tight WP”, expected missing inner hits,  $d0$  and  $dz$  selection. Another WP with additional triple charge agreement is defined as `cut_WP_Tight80X_SS` Id. The rest four working points are based on the official MVA Id. Given no suggested isolation cut value from the EGamma POG, the cut values used in 2015/2016 cut-based Id (see Table 21 and Table 22) used to mix with the 80% and 90% MVA WPs. We then have `mva_80p_Iso2015`, `mva_80p_Iso2015`, `mva_90p_Iso2015` and `mva_90p_Iso2016` as the MVA-based WPs. Detailed cut values are concluded on Table 23.

Table 19: List of HLT safe selection.

Id Variable	Cut (EB)	Cut (EE)
<code>full15x5_sigmaIetaIeta &lt;</code>	0.011	0.031
<code>abs(dEtaInSeed) &lt;</code>	0.004	-
<code>abs(dPhiIn) &lt;</code>	0.020	-
<code>hOverE &lt;</code>	0.060	0.065
<code>ooEmooP &lt;</code>	0.013	0.013
<code>ecalPFClusterIso &lt;</code>	0.160	0.120
<code>hcalPFClusterIso &lt;</code>	0.120	0.120
<code>trackIso &lt;</code>	0.08	0.08
<code>GsfTrack <math>\chi^2/NDOF &lt;</math></code>	-	3.0

Table 20: Additional cuts applied in the loose definition for electron in  $H \rightarrow WW$  analysis.

Id Variable	Cut (EB)	Cut (EE)
Expected Missing Inner Hits $\leq$	1	1
<code>abs(d0) &lt;</code>	0.05	0.1
<code>abs(dz) &lt;</code>	0.1	0.2

Table 21: Cut-Based Tight id for Barrel ( $|\eta_{supercluster}| \leq 1.479$ ) and for Endcap ( $1.479 < |\eta_{supercluster}| < 2.5$ )

Id Variable	Cut (EB)	Cut (EE)
<code>full15x5_sigmaIetaIeta &lt;</code>	0.00998	0.0292
<code>abs(dEtaInSeed) &lt;</code>	0.00308	0.00605
<code>abs(dPhiIn) &lt;</code>	0.0816	0.0394
<code>hOverE &lt;</code>	0.0414	0.0641
<code>relIsoWithEA &lt;</code>	0.0588	0.0571
<code>ooEmooP &lt;</code>	0.0129	0.0129
<code>abs(d0) &lt;</code>	0.05	0.1
<code>abs(dz) &lt;</code>	0.1	0.2
<code>expectedMissingInnerHits &lt;</code>	1	1
<code>passConversionVeto</code>	True	True

In 2017 and 2018, we define the “**loose**” electron from the basis of the official “Medium” of electron Id, with additional calorimetric observable requirements and  $dxy$  and  $dz$  cuts, the whole selections are summarized on Table 24. As for the numerator, which is applied on the

Table 22: The combined isolation cut used for electron in H $\rightarrow$ WW analysis

Isolation cut value	Endcap	Barrel
2015	<0.0646	<0.0354
2016	<0.0571	<0.05880

Table 23: Four working points are based on the official MVA Id with mixing the isolation cut value from the EGamma POG 2015/2016 cut-based Id.

MVA Id	MVA working point	combined isolation
mva_80p_Iso2015	MVA_min cut (80% signal eff)	2015
mva_80p_Iso2016	MVA_min cut (80% signal eff)	2016
mva_90p_Iso2015	MVA_min cut (90% signal eff)	2015
mva_90p_Iso2016	MVA_min cut (90% signal eff)	2016

335 top of the “**loose**” electron, four “**tight**” definition are defined and also tested in the Id perfor-  
 336 mance study. These four working points are come from the official MVA Id, mva\_80p\_noIso,  
 337 mva\_80p\_Iso, mva\_90p\_noIso and mva\_90p\_Iso as the tested WPs. Different from 2016, we  
 338 will choose one WP from these four candidates.

Table 24: List of “Loose” selection for 2017 and 2018.

Id Variable	Cut (EB)	Cut (EE)
cutBasedElectronID-Fall17-94X-V1-Medium	YES	YES
$\sigma_{\eta\eta}$ <	–	0.03
$\frac{ \eta }{E_{\text{SC}}} - \frac{1}{p} <$	–	0.014
$\text{abs}(dx) <$	0.05	0.1
$\text{abs}(dz) <$	0.1	0.2

### 339 4.3.1 Id performance study for 2017 and 2018

340 To choose the best electron “**tight**” working point from four candidates, the performance study  
 341 is needed and expected to show two important features, signal efficiency and background re-  
 342 jection, the definitions are listed below:

- 343 • **Signal efficiency** :  $P(\text{passing “tight” candidate} | \text{passing loose event selection})$
- 344 • **Background rejection** :  $1 - P(\text{passing “tight” candidate} | \text{passing loose event selec-} \\ 345 \text{tion})$

346 The whole performance study is based on pure MC samples, the ggH sample is used to cal-  
 347 culate signal efficiency, W + jet, TTTToSemiLepton and WW are used to estimate background  
 348 rejection, the details of datasets are listed on the Table 25. Before showing the signal efficiency  
 349 and background rejection, events are categorized into ee case and em case, then pass a series  
 350 of selections, which include the basic kinematic thresholds and loose electron filters. To fo-  
 351 cus on the electron objects, there are additional muon selections applied in em case, the whole  
 352 selections are listed on Table 26.

353 In Fig. 10 and Fig. 11, the triangle markers show the performances of four candidates in ee  
 354 and em case. The X-axis is background rejection and the Y-axis is signal efficiency. In gen-  
 355 eral, the mva\_90p\_Iso and mva\_90p\_noIso has better signal efficiency than mva\_80p\_Iso and  
 356 mva\_80p\_noIso as expected. In ee case, the working points with isolation variables training,  
 357 mva\_80p\_Iso and mva\_90p\_Iso, show higher background rejection than other two without  
 358 isolation variable training. In em case, mva\_90p\_Iso and mva\_90p\_noIso show higher sig-  
 359 nal efficiency than other two, and mva\_80p\_Iso and mva\_80p\_noIso do better in background

Table 25: List of MC samples used in electron identification.

Sample	DAS name	Xsec [pb]
$ggH$	/GluGluHToWWTto2L2Nu_M125_13TeV_powheg_pythia8/ ddicroce-GluGluHToWWTto2L2Nu_M125_13TeV_powheg -pythia8_nAOD_private- 60fc7d9153a3c626dca414ab6cce3b8f/USER	0.9913
$W + jet$	/WJetsToLNu_TuneCP5_13TeV-madgraphMLM-pythia8/ RunIIFall17NanoAOD-PU2017_12Apr2018_94X_mc2017 _realistic_v14-v2/NANOAODSIM	61526.7
$T\bar{T} To SemiLepton$	/TTToSemiLeptonic_TuneCP5_PSweights _13TeV-powheg-pythia8/RunIIFall17NanoAOD-PU2017 _12Apr2018_94X_mc2017_realistic_v14-v1 /NANOAODSIM	364.35
WW	/WW_TuneCP5_13TeV-pythia8/ RunIIFall17NanoAOD-PU2017_12Apr2018_94X _mc2017_realistic_v14-v1/NANOAODSIM	114.726

Table 26: List of selections in electron identification.

Selection
Allow extra leptons than the leading lepton pair
$m_{ll} > 12$ GeV, MET $> 20$ GeV
Leading lepton $p_T > 25$ GeV
$p_T > 13$ (muon) / $15$ (electron) GeV for the second lepton
Tight Muon selection (only for em event)
Electron loose working point

- rejection. Judge from getting higher background rejection, but not losing too much signal efficiency, then the `mva_90p_Iso` is best candidate so far.
- In order not to miss any improvement space, the isolation cut value scanning based on `mva_90p_noIso` is performed as cross markers in Fig. 12 and Fig. 13, the legend in the lower left shows that the isolation threshold choosing based on `mva_90p_noIso`, the signal efficiency and background rejection expected. From the curve consisted by cross markers, it shows the significant improvement on background rejection with proper isolation threshold, but the performance still can not achieve to `mva_90p_Iso` candidate. According to the result of whole performance study, the `mva_90p_Iso` is chosen, then in order to drop more fake in some of channels, the `Electron_pfRelIso03_all` should be lower than 0.06 threshold in both barrel and endcap. The table 27 shows the definition of “Tight” electron for 2017 and 2018.

Table 27: List of “Tight” selection for 2017 and 2018.

Id Variable	Cut (EB)	Cut (EE)
<code>mvaEleID-Fall17-iso-V1-wp90</code>	YES	YES
<code>abs(pfRelIso03_all) &lt;</code>	0.06	0.06

#### 4.4 Electron Id/Iso Efficiencies from Tag & Probe Method

- One of the well established data-driven approach for measuring the particle efficiencies is the so called Tag and Probe method. The Tag and probe method uses a known mass resonance (e.g.  $J/\Psi$ ,  $\epsilon$ ,  $Z$ ) to select particles of the desired type, and probe the efficiency of a particular selection criterion on these particles. In general the “tag” is an object that passes a set of very

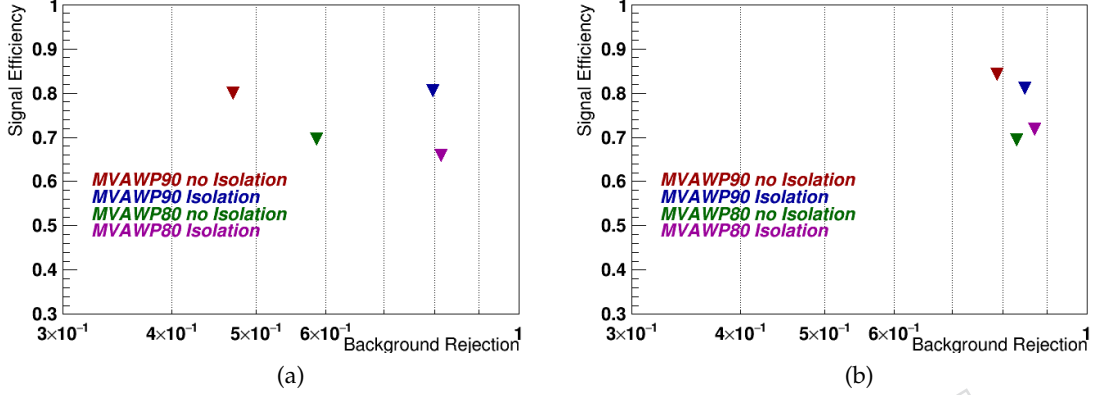


Figure 10: The performance, signal efficiency(Y-axis) and background rejection(X-axis), of four electron tight candidates for barrel(left) and endcap(right) in  $ee$  case. The working points `mva_80p_Iso` and `mva_90p_Iso` show higher background rejection than other two, the `mva_90p_Iso` has better signal efficiency than `mva_80p_Iso` as expected.

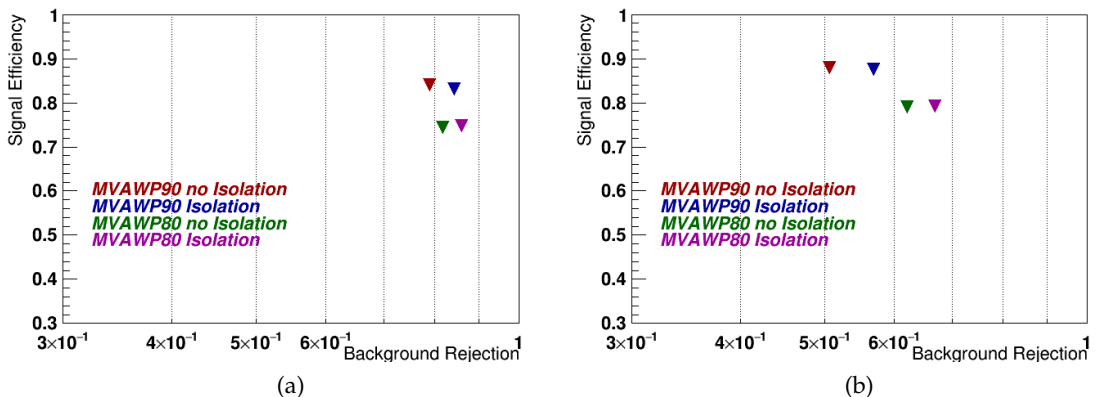


Figure 11: The performance, signal efficiency(Y-axis) and background rejection(X-axis), of four electron tight candidates for barrel(left) and endcap(right) in  $em$  case. The working points `mva_90p_Iso` and `mva_90p_noIso` show higher signal efficiency than other two, and `mva_80p_Iso` and `mva_80p_noIso` do better in background rejection.

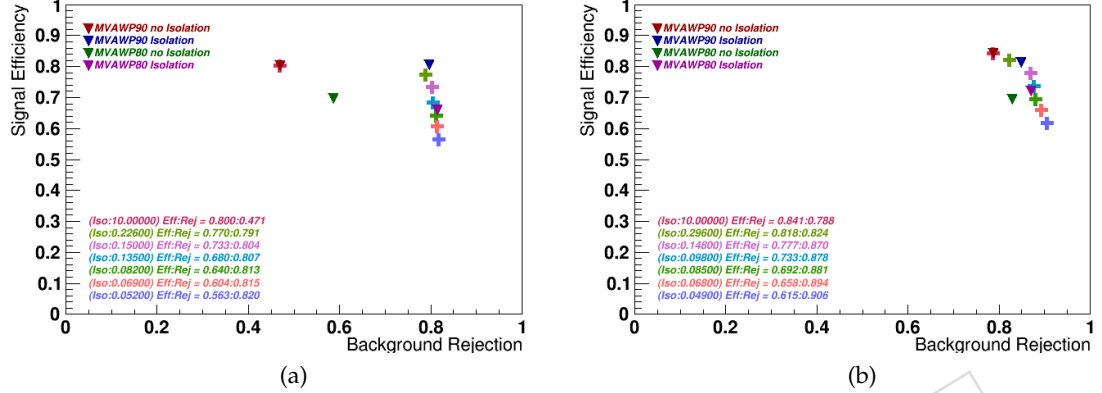


Figure 12: The performance, signal efficiency(Y-axis) and background rejection(X-axis), of four electron tight candidates for barrel(left) and endcap(right) in  $ee$  case. The cross markers show the performance of isolation threshold scanning based on mva\\_90p\\_noIso.

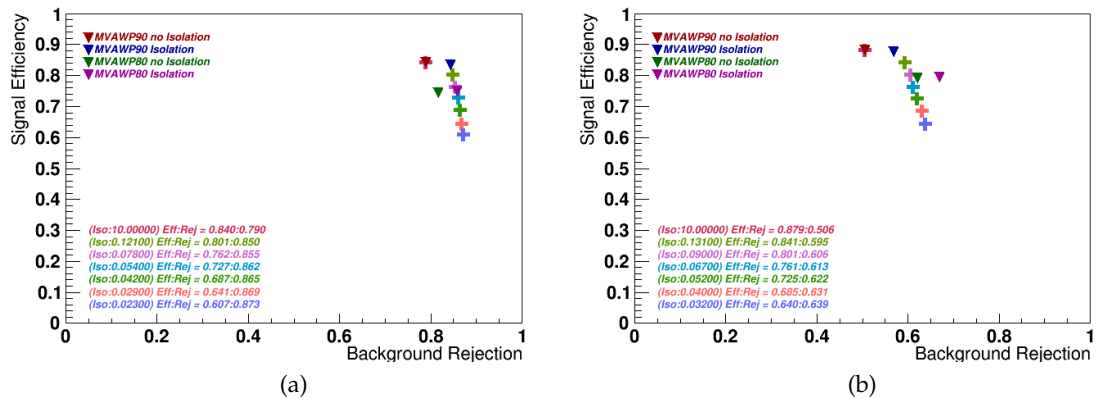


Figure 13: The performance, signal efficiency(Y-axis) and background rejection(X-axis), of four electron tight candidates for barrel(left) and endcap(right) in  $em$  case. The cross markers show the performance of isolation threshold scanning based on mva\\_90p\\_noIso.

376 tight selection criteria designed to isolate the required particle type. Tags are often referred  
 377 to as a “golden” electrons or muons and the fake rate for passing tag selection criteria should  
 378 be very small. A generic set of the desired particle type (i.e. with potentially very loose se-  
 379 lection criteria) known as “probes” is selected by pairing these objects with tags such that the  
 380 invariant mass of the combination is consistent with the mass of the resonance. Combinatoric  
 381 backgrounds may be eliminated through any of a variety of background subtraction methods  
 382 such as fitting, or sideband subtraction. The definition of the probe objects depend on the  
 383 specifics of the selection criterion being examined.

384 The simple expression to get the efficiency as a function of  $p_T$  and  $\eta$  is given below:

$$385 \quad \varepsilon(p_T, \eta) = \frac{N_{\text{Pass}}^{\text{Probes}}}{N_{\text{Pass}}^{\text{Probes}} + N_{\text{Fail}}^{\text{Probes}}}$$

#### 386 4.4.1 Tag & Probe Methodology

387 This method is used here to get the Identification efficiency of electrons. In this case, the Tag is a  
 388 well identified and isolated electron which also made to pass an electron Trigger to increase the  
 389 purity. Once the Tag electron is selected then we look for another object which is reconstructed  
 390 as electron. After passing some kinematical selection, we get the total probe selection. The in-  
 391 variant mass of the pair is then reconstructed from Tag and Probe electron and a Z boson mass  
 392 window is imposed. After that, we ask the Probe to pass the Id working point to be checked  
 393 and compute the efficiency. This is done for both data and MC. Once we get the efficiency  
 394 for both data and MC then we compute the scale factors, which are the ratio of efficiencies of  
 395 Data and MC. These scale factors are used then in the analysis to scale the MC to correct the  
 396 difference in efficiencies between data and MC. The Pile-Up reweighting is also applied on MC  
 397 during the computation of efficiencies. A MC truth matching has also been applied in case of  
 398 the computation using simulation. There are basically two methods to estimate the efficiencies.  
 399 One is the *Counting Method* and the other is the *Fitting Method*. The counting method is used  
 400 when there is less background. We are computing efficiencies with loose Z mass window and  
 401 hence there is a possibility of background contamination under the Z peak. Hence, proper han-  
 402 dling of background becomes important. In order to take into account the effect of background,  
 403 the Fitting method has been used to estimate the efficiency.

404 The Fitting functions and example fits are shown in Section 4.4.3. All the samples and selection  
 405 criteria and described in Tables 28,29,30,31, 32, 33 and 34. ReReco datasets (for 2017B to 2017F),  
 406 have been used with full luminsity of 2017  $42.6 \text{ fb}^{-1}$ . Madgraph Drell-Yan MC sample is used  
 407 as a default one ( $\bar{48}\text{M}$  events). For computation of systematics, DY sample with MCNLO gen-  
 408 erator has been used which has  $28\text{M}$  events and this sample in next-to-leading order.

Table 28: Data Sample used for TnP Studies for 2016.

/SingleElectron/Run2016B-23Sep2016-v3/MINIAOD
/SingleElectron/Run2016C-23Sep2016-v1/MINIAOD
/SingleElectron/Run2016D-23Sep2016-v1/MINIAOD
/SingleElectron/Run2016E-23Sep2016-v1/MINIAOD
/SingleElectron/Run2016F-23Sep2016-v1/MINIAOD
/SingleElectron/Run2016G-23Sep2016-v1/MINIAOD
/SingleElectron/Run2016H-PromptReco-v3/MINIAOD

409 Tag & Probe pairs are then selected using Z mass window of 60 to 120 GeV. Only one Tag &  
 410 Probe per event is chosen. If there exist more than one pair then the one whose invariant mass

Table 29: Data Sample used for TnP Studies for 2017.

/SingleElectron/Run2017B-31Mar2018-v1/MINIAOD
/SingleElectron/Run2017C-31Mar2018-v1/MINIAOD
/SingleElectron/Run2017D-31Mar2018-v1/MINIAOD
/SingleElectron/Run2017E-31Mar2018-v1/MINIAOD
/SingleElectron/Run2017F-31Mar2018-v1/MINIAOD

Table 30: Data Sample used for TnP Studies for 2018.

/EGamma/Run2018A-17Sep2018-v2/AOD
/EGamma/Run2018B-17Sep2018-v1/AOD
/EGamma/Run2018C-17Sep2018-v1/AOD
/EGamma/Run2018D-PromptReco-v2/AOD

411 closer to Z pole mass has been selected.

#### 412 4.4.2 Bin Scheme

413 As mentioned before, efficiencies have been computed as a function of  $p_T$  and  $\eta$  of electron. A  
 414 special bin of Barrel-Endcap transition region has been kept because the efficiencies here are  
 415 usually low and fitting also do not perform well.  $p_T$  bins = (10, 20, 35, 50, 90, 150, 500)  
 416  $|\eta|$  bins = (-2.5, -2.0, -1.566, -1.4442, -0.8, 0.0, 0.8, 1.4442, 1.566, 2.0, 2.5)  
 417 Since, we have enough large dataset in 2016, so the  $p_T$  bins have been extended to 500 GeV and  
 418 high  $p_T$  bins have been divided more.

#### 419 4.4.3 Tag & Probe Fits

420 As mentioned above, we have used a fitting method to estimate the efficiencies. For signal  
 421 fitting, MC templates are derived from the simulated sample in the Z mass range 60 to 120  
 422 GeV in  $p_T$  and  $\eta$  bins. The MC Templates are then smeared using Gaussian function. For the  
 423 background fitting, the CMSShape function has been used. This function is a combination of  
 424 an exponential function and an error function. The exponential decay distribution becomes  
 425 active at high mass beyond the Z peak and the error function takes over at low masses due to  
 426 threshold effect. Other signal and background fitting functions were also tried for systematic  
 427 studies. This will be explained later in Section 4.5.

428 In 2016, Using `mva_90p_Iso2016` as example, Figs. 14,15 shows the fits for low  $p_T$  bin and  
 429 high  $p_T$  bin.

430 In 2017, Using `mva_90p_Iso` and datasets RunC+D as example, Figs. 16,17 shows the fits for  
 431 low  $p_T$  bin and high  $p_T$  bin.

432 In 2018, Using `mva_90p_Iso` as example, Figs. 18,19 shows the fits for low  $p_T$  bin and high  $p_T$   
 433 bin.

### 434 4.5 Systematics for TnP Studies

435 We studied all the possible sources of uncertainties which can affect the electron efficiencies.  
 436 All the sources of systematic uncertainties and their methods of computation are described in  
 437 this section. Most of these sources are related to the machinery of Tag & Probe method.

- 438 • **Signal Shape:** We have used the “Fitting Method” to estimate the efficiencies and  
 439 for that we used MC templates along with Gaussian PDF as our signal fitting func-

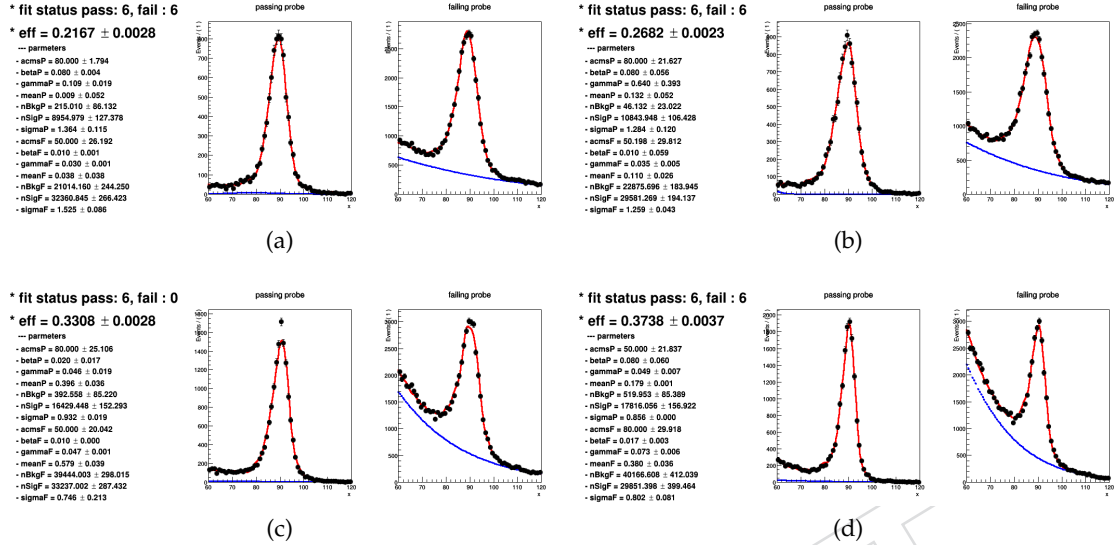


Figure 14: Fits for  $p_T$  bin (10-20) GeV on top from (left to right)  $\eta$  bin (-2.5,-2.0) and (-2.0,-1.566) and on bottom from (left to right)  $\eta$  bin (-1.4442,-0.8) and (-0.8,0.0).  
for 2016 dataset.

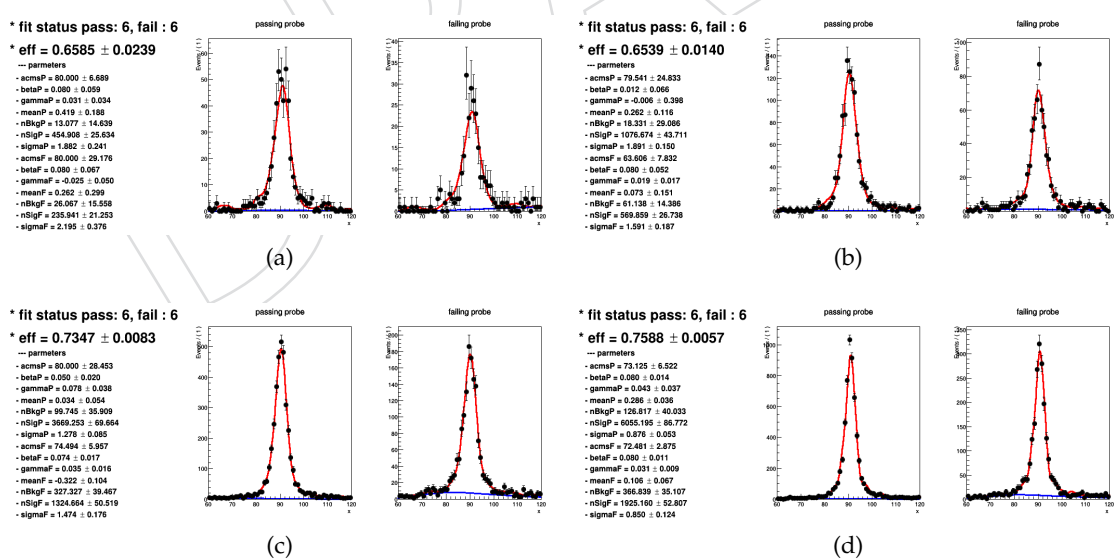


Figure 15: Fits for  $p_T$  bin (150-500) GeV on top from (left to right)  $\eta$  bin (-2.5,-2.0) and (-2.0,-1.566) and on bottom from (left to right)  $\eta$  bin (-1.4442,-0.8) and (-0.8,0.0).  
for 2016 dataset.

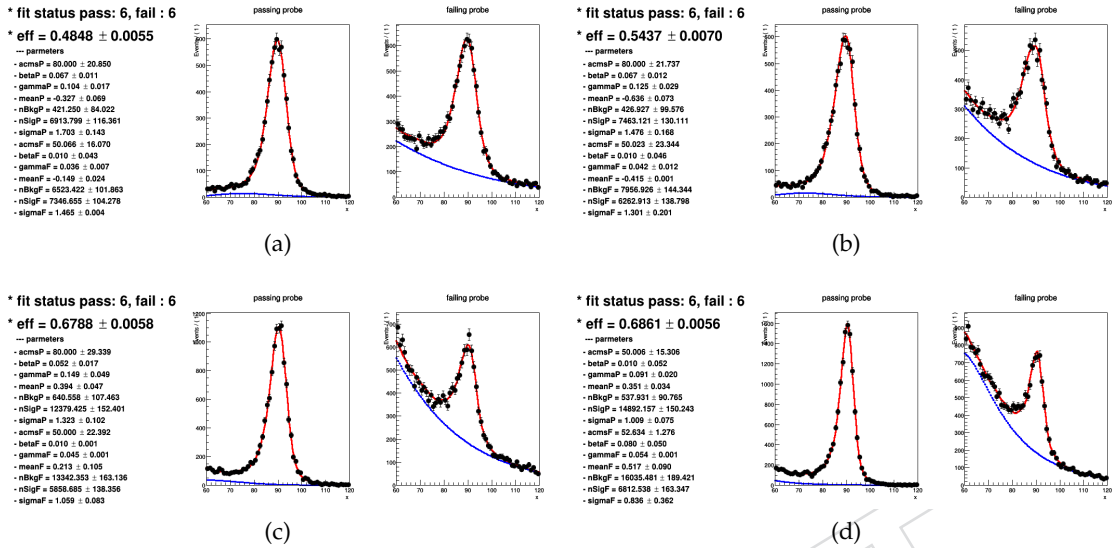


Figure 16: Fits for  $p_T$  bin (10-20) GeV on top from (left to right)  $\eta$  bin (-2.5,-2.0) and (-2.0,-1.566) and on bottom from (left to right)  $\eta$  bin (-1.4442,-0.8) and (-0.8,0.0).  
for 2017 Run C+D dataset.

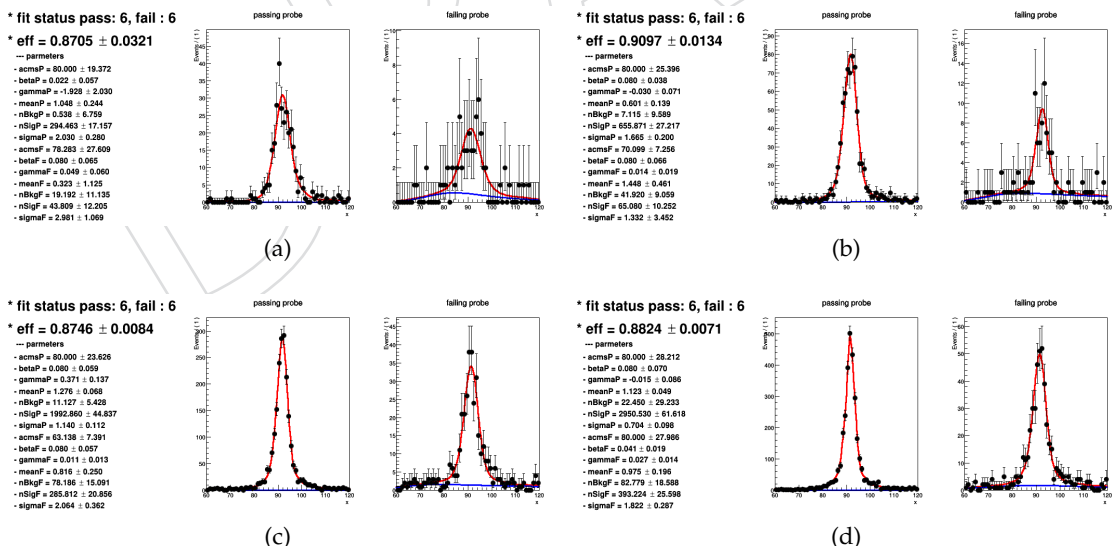


Figure 17: Fits for  $p_T$  bin (150-500) GeV on top from (left to right)  $\eta$  bin (-2.5,-2.0) and (-2.0,-1.566) and on bottom from (left to right)  $\eta$  bin (-1.4442,-0.8) and (-0.8,0.0).  
for 2017 Run C+D dataset.

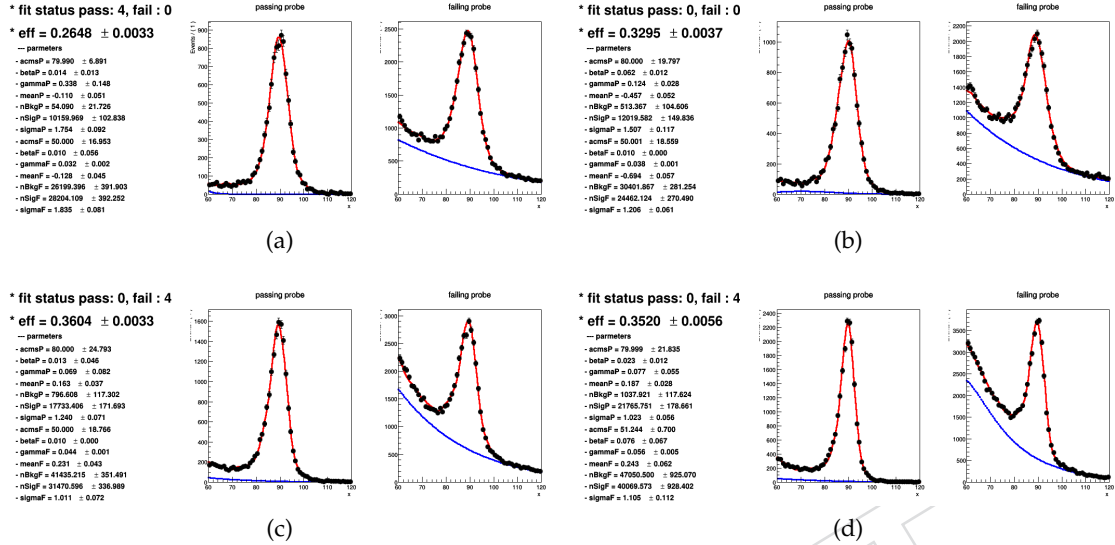


Figure 18: Fits for  $p_T$  bin (10-20) GeV on top from (left to right)  $\eta$  bin (-2.5,-2.0) and (-2.0,-1.566) and on bottom from (left to right)  $\eta$  bin (-1.4442,-0.8) and (-0.8,0.0).  
for 2018 dataset.

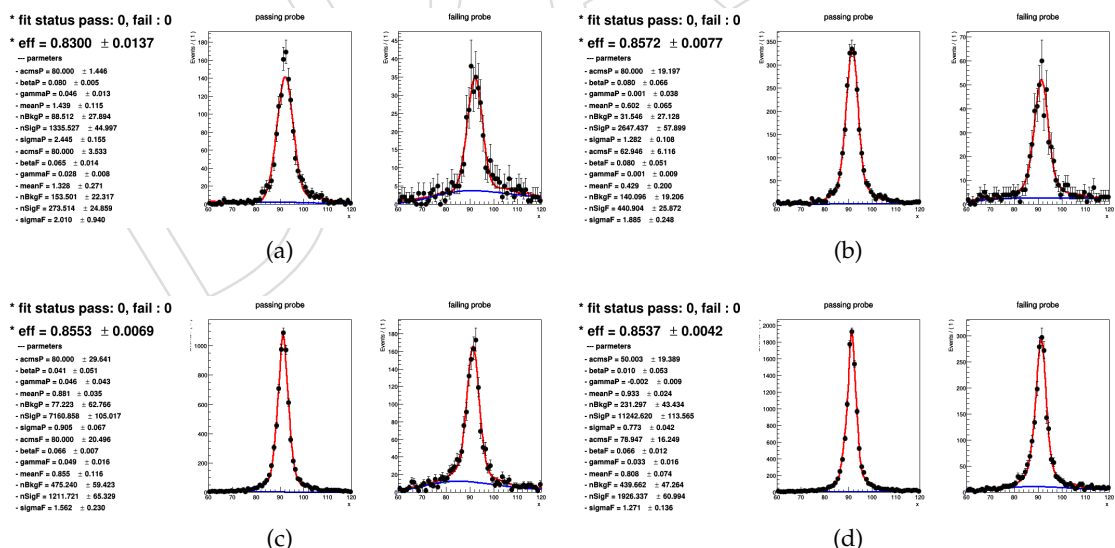


Figure 19: Fits for  $p_T$  bin (150-500) GeV on top from (left to right)  $\eta$  bin (-2.5,-2.0) and (-2.0,-1.566) and on bottom from (left to right)  $\eta$  bin (-1.4442,-0.8) and (-0.8,0.0).  
for 2018 dataset.

Table 31: Summer16 MC samples used for TnP studies for 2016. Suffix: *RunIISummer16MiniAODv2-PUMoriond17\_80X\_mcRun2\_asymptotic\_2016\_TrancheIV\_v6\_ext1-v2/MINIAODSIM*

Sample
/DYJetsToLL_M-50_TuneCUETP8M1_13TeV-amcatnloFXFX-pythia8
/DYJetsToLL_M-50_TuneCUETP8M1_13TeV-madgraphMLM-pythia8

Table 32: Fall17 MC samples used for TnP studies for 2017. Suffix: *RunIIFall17MiniAODv2-PU2017\_12Apr2018\_94X\_mc2017\_realistic\_v14\_ext1-v1/MINIAODSIM*

Sample
/DYJetsToLL_M-50_TuneCP5_13TeV-amcatnloFXFX-pythia8-ext1
/DYJetsToLL_M-50_TuneCP5_13TeV-madgraphMLM-pythia8

440      We have checked the variation of the efficiencies by changing the fitting function  
 441      to “Crystal-Ball” function.

- 442      • **Background Shape:** For the background fitting, CMSShape function has been used  
 443      as described above. For studying the effect of changing the background fitting we  
 444      have used “Exponential” function. This is also an important source of systematics.
- 445      • **NLO vs LO MC Sample:** The effect of this uncertainty is minimal and is covered  
 446      by the larger statistical uncertainty. We have used an LO DY madgraph sample  
 447      as our default sample for efficiencies calculation and NLO MC@NLO sample for  
 448      systematics.
- 449      • **Tag Selection :** We change the selection on Tag, non-trigger MVA id applied on the  
 450      top of Tight Id and the  $p_T$  cut is changed from 30 to 33 GeV and then check the  
 451      variation in efficiencies.

## 452      4.6 Results from Tag & Probe

453      In this section, various distributions will be shown for data efficiencies and scale factors with  
 454      their uncertainties.

455      For 2016, in Fig. 20, data efficiencies are shown in upper part of the canvas and bottom part  
 456      shows the scale factor as a function of  $p_T$  for various  $\eta$  bins and vice-versa. The total systematic  
 457      uncertainties are shown on the Fig. 26.

458      For 2017, in Fig. 21, 22, 23 and 24, data efficiencies are shown in upper part of the canvas and  
 459      bottom part shows the scale factor as a function of  $p_T$  for various  $\eta$  bins and vice-versa. The  
 460      total systematic uncertainties are shown on the Fig. 27.

461      For 2018, in Fig. 25, data efficiencies are shown in upper part of the canvas and bottom part  
 462      shows the scale factor as a function of  $p_T$  for various  $\eta$  bins and vice-versa. The total systematic  
 463      uncertainties are shown on the Fig. 28.

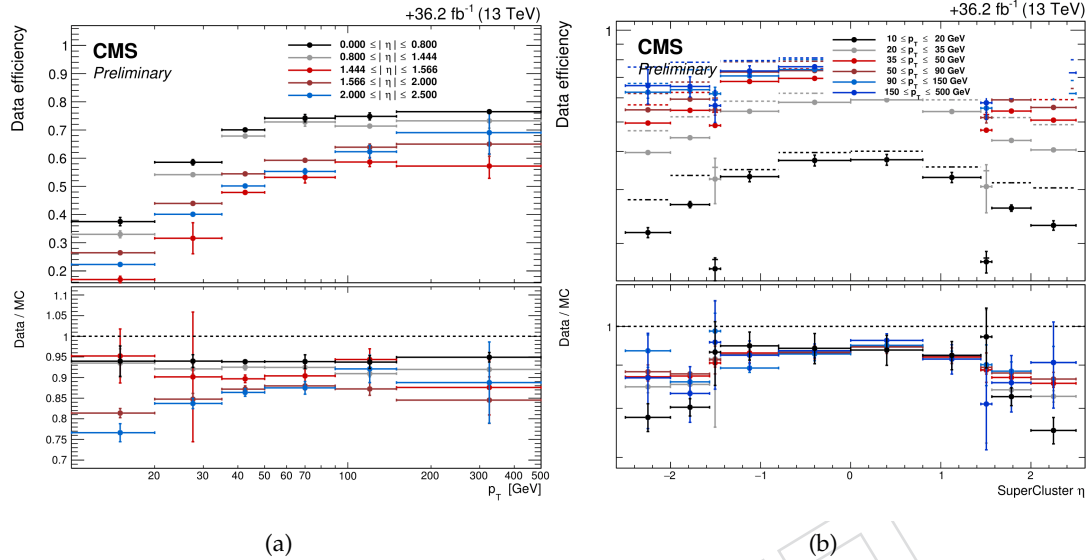


Figure 20: Efficiencies for Electrons cut based on mva\_90p\_Iso2016 cuts. Efficiencies for 2016 dataset are shown in upper half of the plots and scale factors in lower half.

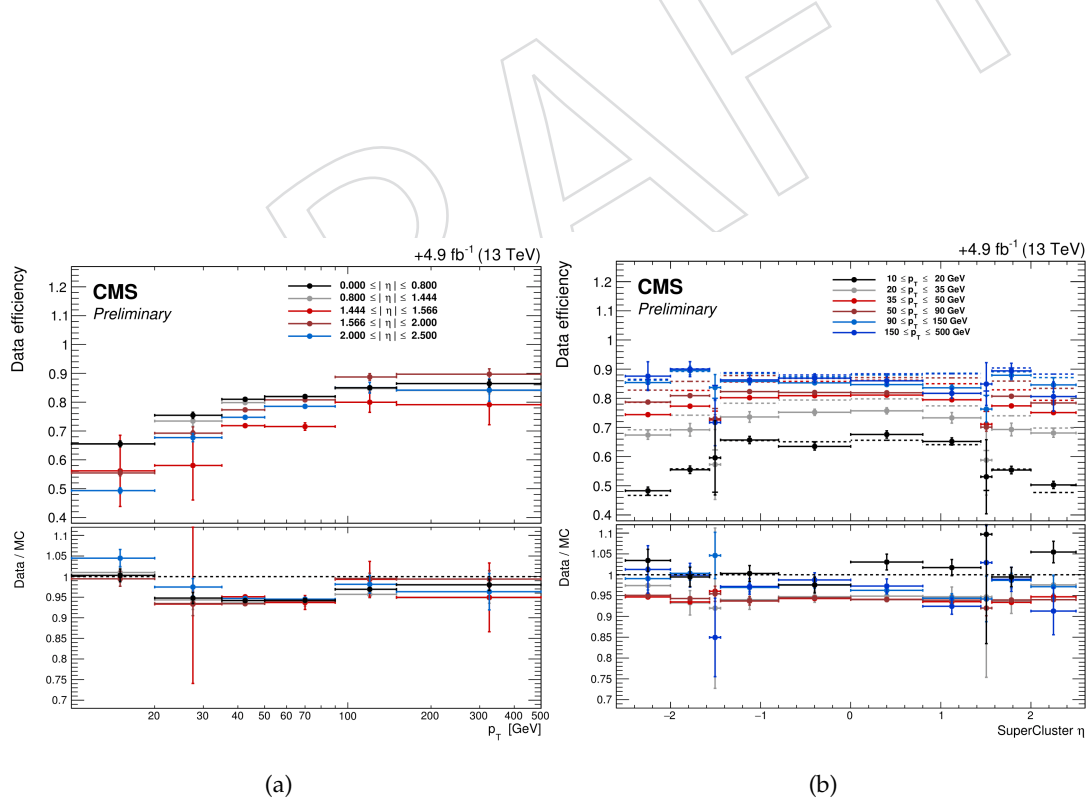


Figure 21: Efficiencies for Electrons cut based on mva\_90p\_Iso cuts. Efficiencies for RunB dataset are shown in upper half of the plots and scale factors in lower half.

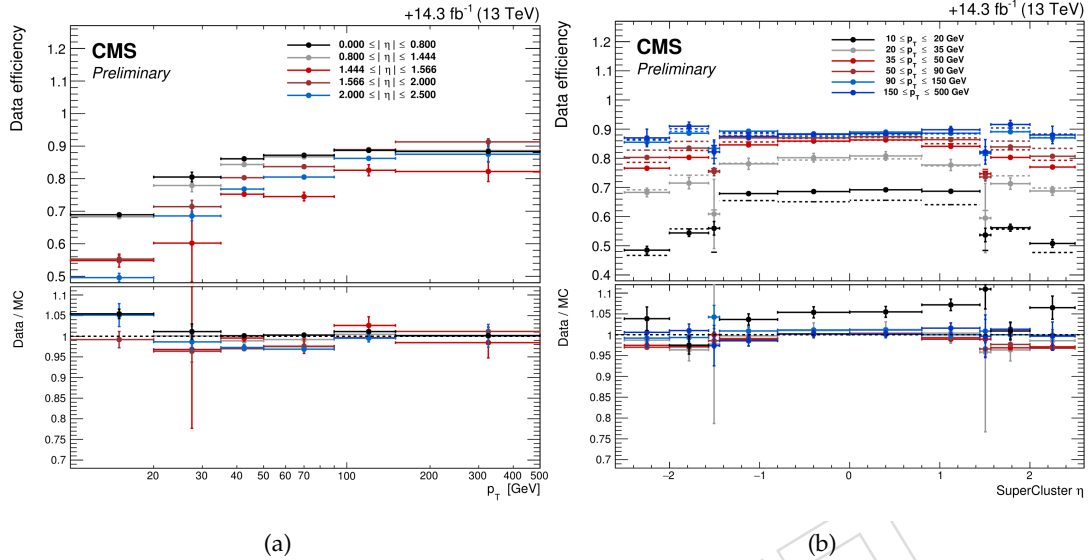


Figure 22: Efficiencies for Electrons cut based on mva\_90p\_Iso cuts. Efficiencies for RunC+D datasets are shown in upper half of the plots and scale factors in lower half.

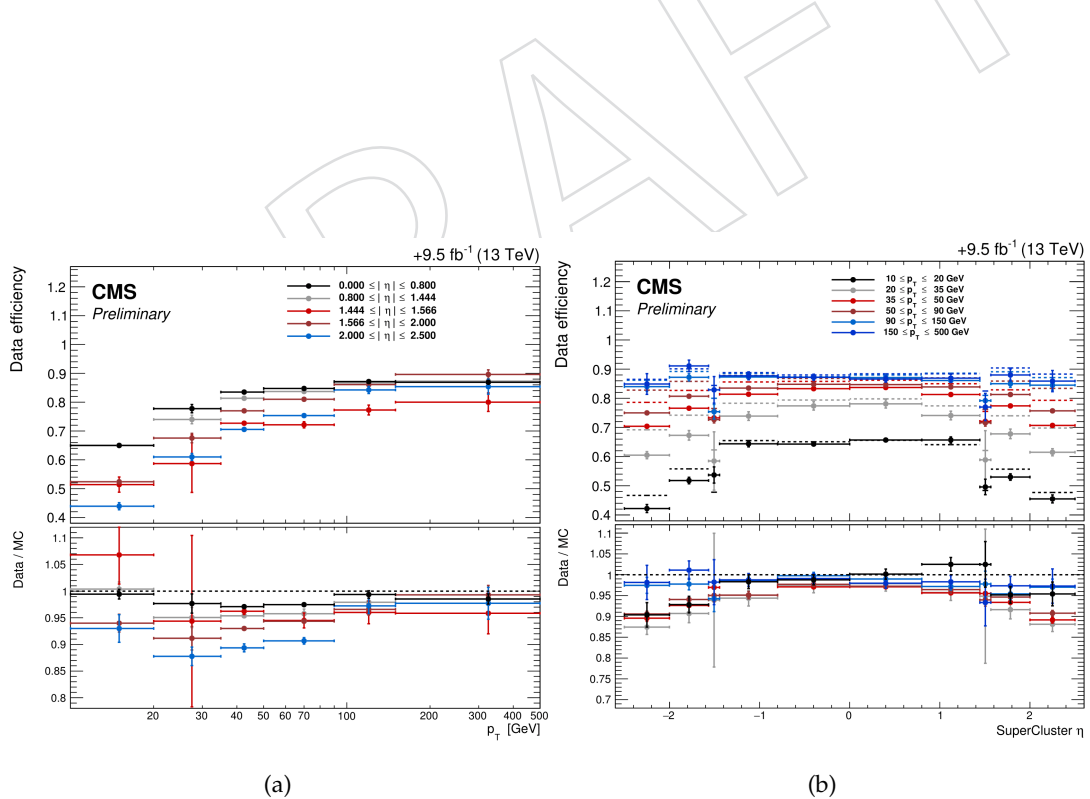


Figure 23: Efficiencies for Electrons cut based on mva\_90p\_Iso cuts. Efficiencies for RunE dataset are shown in upper half of the plots and scale factors in lower half.

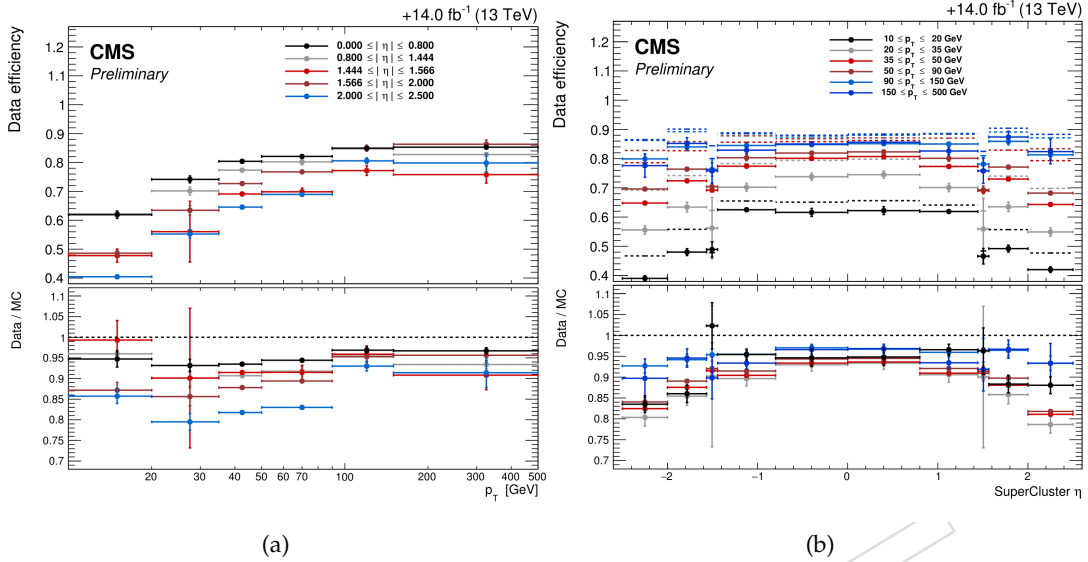


Figure 24: Efficiencies for Electrons cut based on mva\_90p\_Iso cuts. Efficiencies for RunF dataset are shown in upper half of the plots and scale factors in lower half.

Figure 25: Efficiencies for Electrons cut based on mva\_90p\_Iso cuts. Efficiencies for 2018 dataset are shown in upper half of the plots and scale factors in lower half.

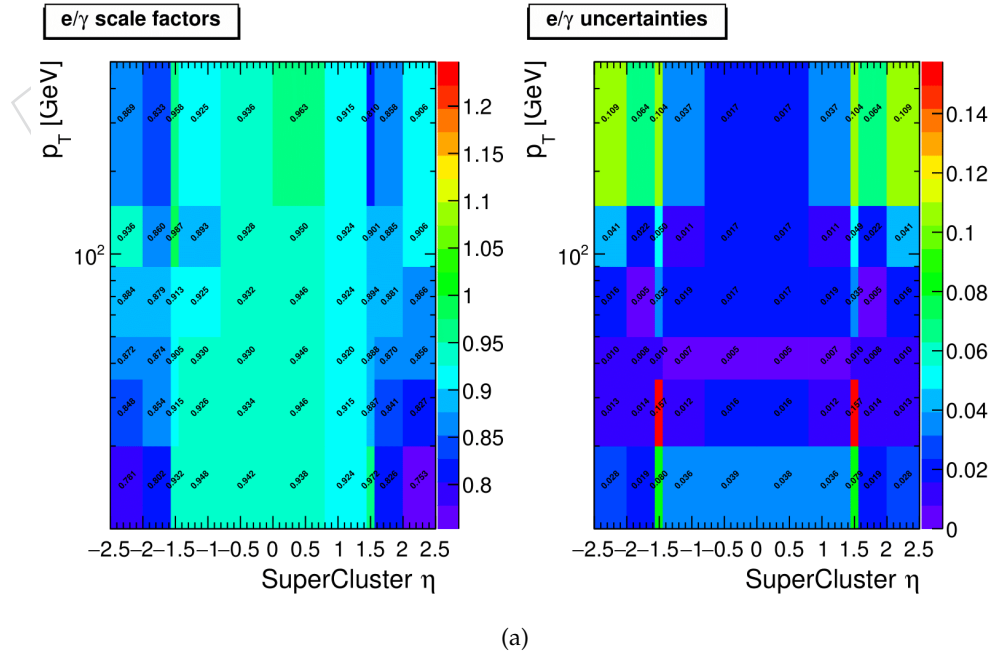


Figure 26: Electron scale factor and uncertainty in 2D with 2016 datasets.

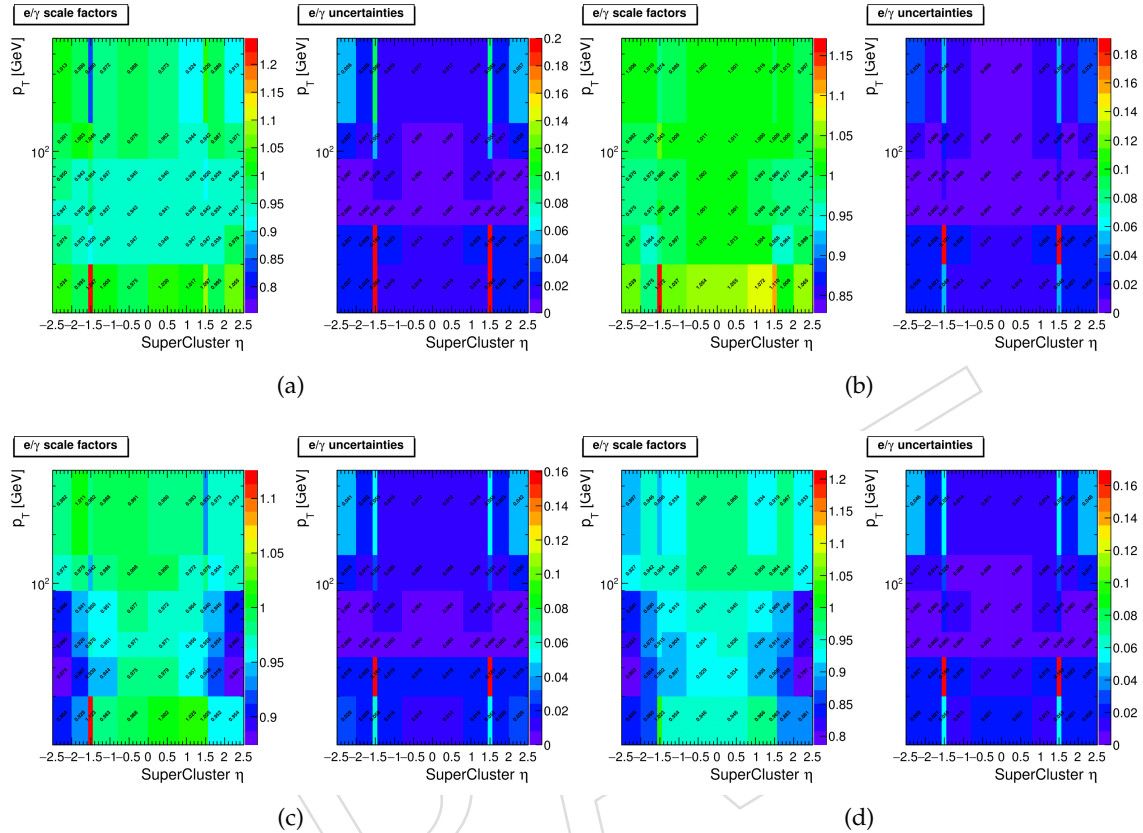


Figure 27: Electron scale factor and uncertainty in 2D with 2017 datasets (a) Run B (b) Run C+D (c) Run E (d) Run F.

Figure 28: Electron scale factor and uncertainty in 2D with 2018 datasets.

Table 33: Fall17 MC samples used for TnP studies for 2018.

Sample
/DYToEE_M-50_NNPDF31_TuneCP5_13TeV-powheg-pythia8
/DYJetsToLL_M-50_TuneCP5_13TeV-madgraphMLM-pythia8

Table 34: Tag &amp; Probe Selection

Selection	Tag	Probe
$p_T >$	30 GeV	10 GeV
$ \eta_{SC}  <$	2.17	2.5
Id	“tight” electron	“tight” + “loose” electron
Trigger	HLT_Ele27_eta2p1_WPTight_Gsf_v*	-

## 464 5 Lepton trigger efficiencies

465 Editors: Amandeep Kaur, Arun Kumar, D. Di Croce

### 466 5.1 Introduction

467 The trigger efficiency calculation for entire Run 2 is presented in this section. In the  $H \rightarrow WW$   
 468 analysis, final states with 2 leptons (electrons or muons) are studied, therefore a combination  
 469 of both single and double lepton triggers are used. For the calculation of the trigger efficiency  
 470 we are using the tag-and-probe method. Tag and Probe pair is required to pass the di-lepton  
 471 mass window 60 GeV to 120 GeV in order to select events with  $Z$  boson. In order to make  
 472 a pass probe collection, probes are required to match the trigger object corresponding to the  
 473 the last filter of HLT path.  $\Delta R < 0.1$  is used to match the trigger object to probe. Then  
 474 trigger efficiency is defined as the ratio of events with passing probes to all probes. The trigger  
 475 efficiency is calculated in data and applied to the data directly without MC corrections.

### 476 5.2 Lepton trigger definitions for run period 2016

477 Table 35 shows all the triggers used in the analysis for 2016 dataset.

Table 35: Triggers for Signal Selection

Data Set	Run range	HLT path
SingleMuon	[273158,284044]	HLT_IsoMu24_v* HLT_IsoTkMu24_v*
SingleElectron	[273158,284044]	HLT_Ele27_WPTight_Gsf_v* HLT_Ele25_eta2p1_WPTight_Gsf_v*
DoubleMuon	[273158,281612]	HLT_Mu17_TrkIsoVVL_Mu8_TrkIsoVVL_v* HLT_Mu17_TrkIsoVVL_TkMu8_TrkIsoVVL_v*
	[281613,284044]	HLT_Mu17_TrkIsoVVL_Mu8_TrkIsoVVL_DZ_v* HLT_Mu17_TrkIsoVVL_TkMu8_TrkIsoVVL_DZ_v*
DoubleEG	[273158,284044]	HLT_Ele23_Ele12_CaloIdL_TrackIdL_IsoVL_DZ_v*
MuonEG	[273158,278272]	HLT_Mu23_TrkIsoVVL_Ele12_CaloIdL_TrackIdL_IsoVL_v* HLT_Mu8_TrkIsoVVL_Ele23_CaloIdL_TrackIdL_IsoVL_v*
	[278273,284044]	HLT_Mu12_TrkIsoVVL_Ele23_CaloIdL_TrackIdL_IsoVL_DZ_v* HLT_Mu23_TrkIsoVVL_Ele12_CaloIdL_TrackIdL_IsoVL_DZ_v*

#### 478 5.2.1 Tag and Probe Studies

479 CMSSW\_9\_4\_10 has been used. Datasets used are mentioned in Table 36. The JSON used is  
 480 Cert\_271036-284044\_13TeV\_23Sep2016ReReco\_Collisions16\_JSON.txt, which correspond to the  
 481 integrated luminosity of  $35.92 \text{ fb}^{-1}$ .

Table 36: Datasets used for the computation of lepton trigger efficiencies

DataSets
/SingleElectron/Run2016(B to H)-17Jul2018-v*/MINIAOD
/SingleMuon/Run2016(B to H)-17Jul2018-v*/MINIAOD

482 The selection for the tag and probe pair is given below.

#### 483 Tag Selection

484

- tag is required to pass the POG defined cut based “tight” identification and isolation criteria. For electrons the definition of identification working point is given here [?]. For muons here [2].
- $p_T > 35(30)$  GeV for  $e(\mu)$ .
- tag lepton should be matched to HLT\_Ele27\_WPTight\_Gsf and HLT\_IsoMu24 for  $e$  and  $\mu$  respectively.

#### 491 Probe Selection

- probe is required to pass the HWW specific identification criteria. The working points are defined in Section 3.1 and 4

495 Trigger efficiency is computed as a function of  $p_T$  and  $\eta$  of probe as there is always a turn-on in  
 496 efficiency with respect to  $p_T$ ,  $\eta$  binning is required to take into account the different response  
 497 from various parts of detector.

498 The binning used for various triggers is the following.  $p_T$  binning depends on the trigger  
 499 threshold.

500  **$\eta$  bins for  $e$**  : -2.5, -2.1, -1.6, -1.4, -0.8, 0, 0.8, 1.4, 1.6, 2.1, 2.5

501  **$\eta$  bins for  $\mu$**  : -2.4, -2.1, -1.6, -1.2, -0.8, -0.3, -0.2, 0.2, 0.3, 0.8, 1.2, 1.6, 2.1, 2.4

502

#### 503 $p_T$ bins

- Ele23 : 0,23,24,25,26,30,35,40,45,50,100
- Ele12 : 0,12,13,15,18,22,30,35,40,50,100
- Ele25 : 0,25,26,27,29,31,34,37,40,50,100
- Ele27 : 0,27,28,29,30,32,35,40,45,50,100
- Mu17 : 0,10,15,16,17,18,19,20,25,30,40,60,100,200
- Mu8 : 0,10,13,16,20,25,30,40,60,100,200
- Mu24 : 0,10,22,23,24,25,26,30,40,60,100,200
- Mu12 : 0,10,11,12,13,14,15,20,25,30,35,40,45,50,60,100,200
- Mu23 : 0,10,21,22,23,24,25,26,30,40,60,100,200

514 Double lepton HLT paths needs two leptons to pass them and hence two parts. Each part of the  
 515 path is called “leg”. Trigger efficiencies are computed for each “leg” of the HLT path. Then the  
 516 efficiencies of each leg is combined according to the type of event we have. We use the counting  
 517 method to estimate the efficiency. No fitting has been performed as with the tight selection, the  
 518 background contamination under Z peak is very low.

#### 519 5.2.2 Results

520 Efficiencies are computed for each Era (2016B to 2016H) in order to check the differences be-  
 521 cause of change in run conditions and efficiency plots are with era distribution 2016BCDEF and  
 522 2016GH.

523 To compute the trigger efficiency of  $\mu$  leg in mixed Mu-EG triggers, since the  $\mu$  leg is not the  
 524 same as one of the legs of double muon triggers so we need to emulate the HLT selection.  
 525 SingleMu PD has been used to measure the efficiencies. Tag is required to pass the condi-

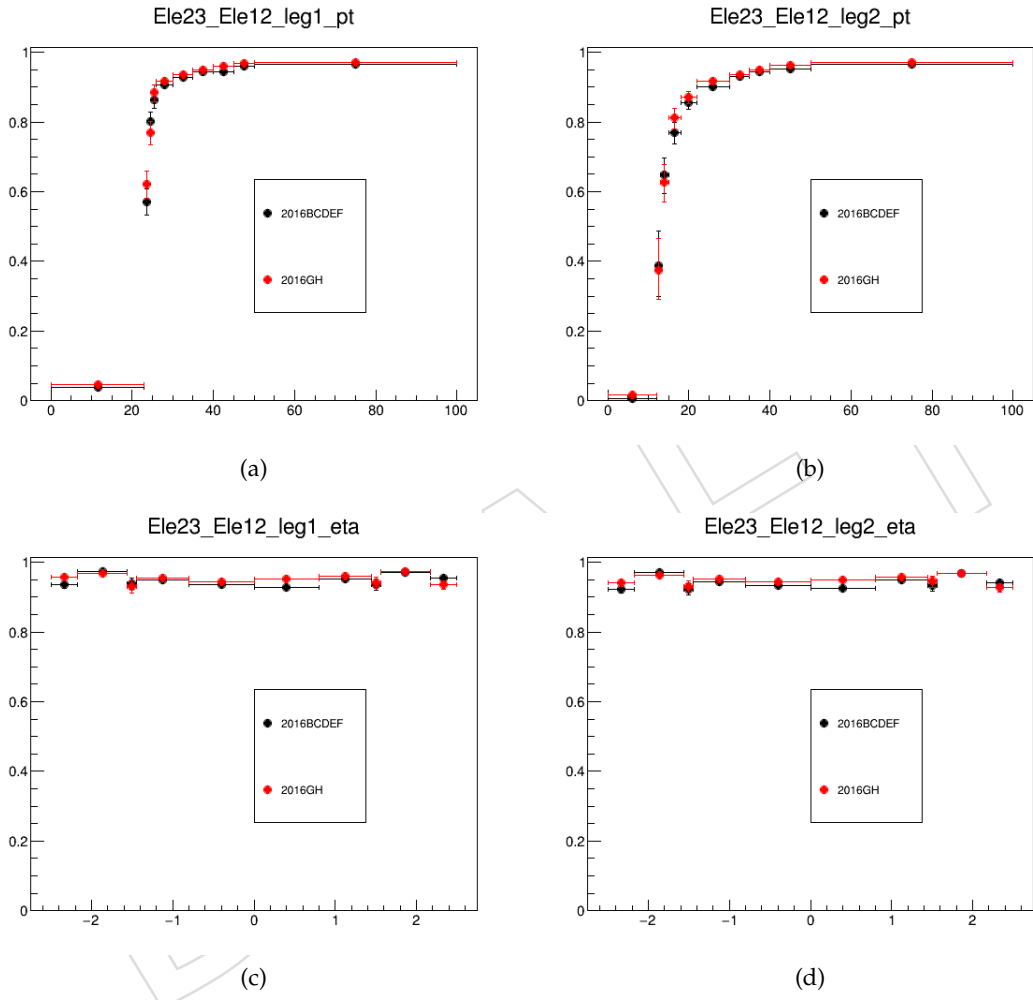


Figure 29: Trigger efficiency as a function of  $p_T$  (top) and  $\eta$  (bottom) for Leg1 (left) and Leg2 (right) of HLT\_Ele23\_Ele12\_CaloIdL\_TrackIdL\_IsoVL\_DZ\_v\*. Efficiencies are separated for DATA in run period 2016BCDEF , 2016GH.

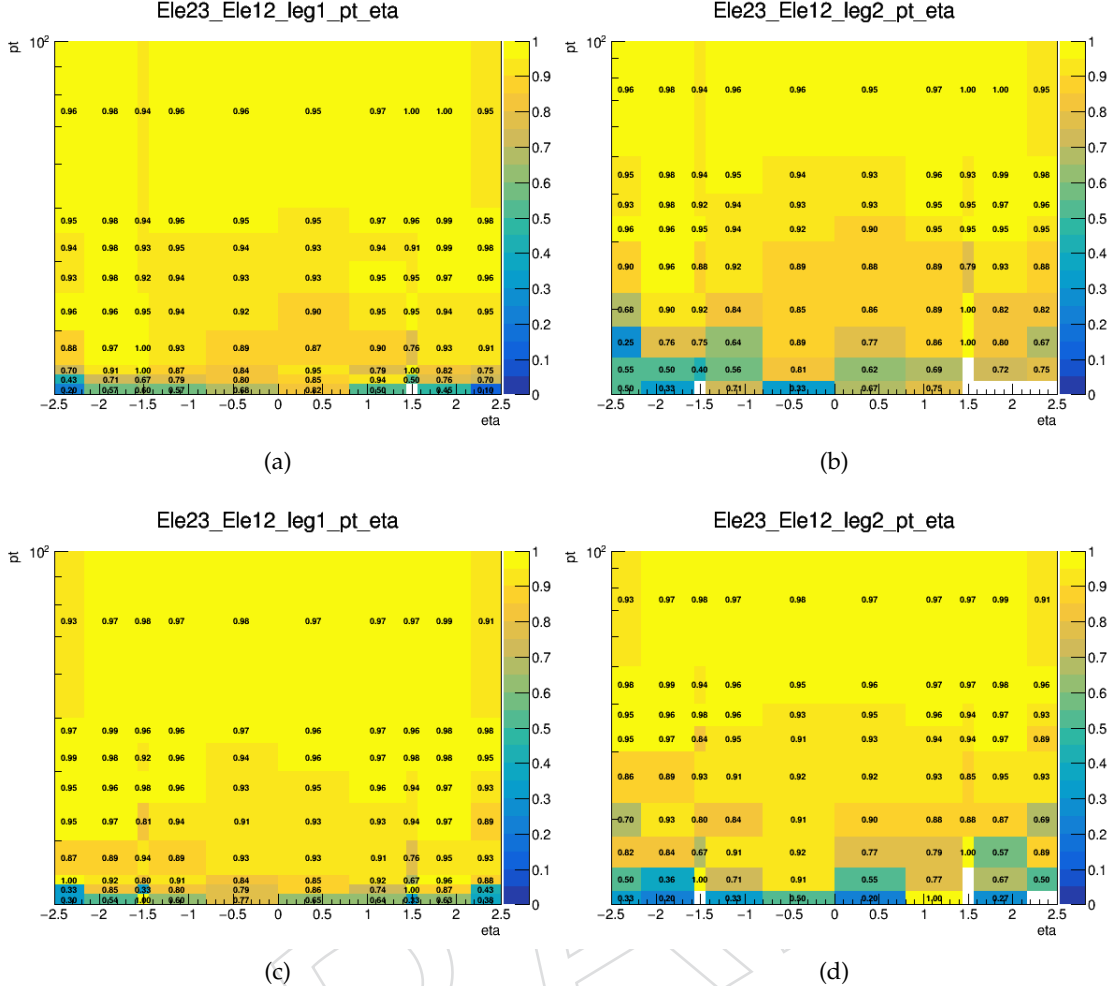


Figure 30: 2D plots (top) 2016BCDEF and (bottom) 2016GH run period for Leg1 (left) and Leg2 (right) of HLT\_Ele23\_Ele12\_CaloIdL\_TrackIdL\_IsoVL\_DZ\_v\*.

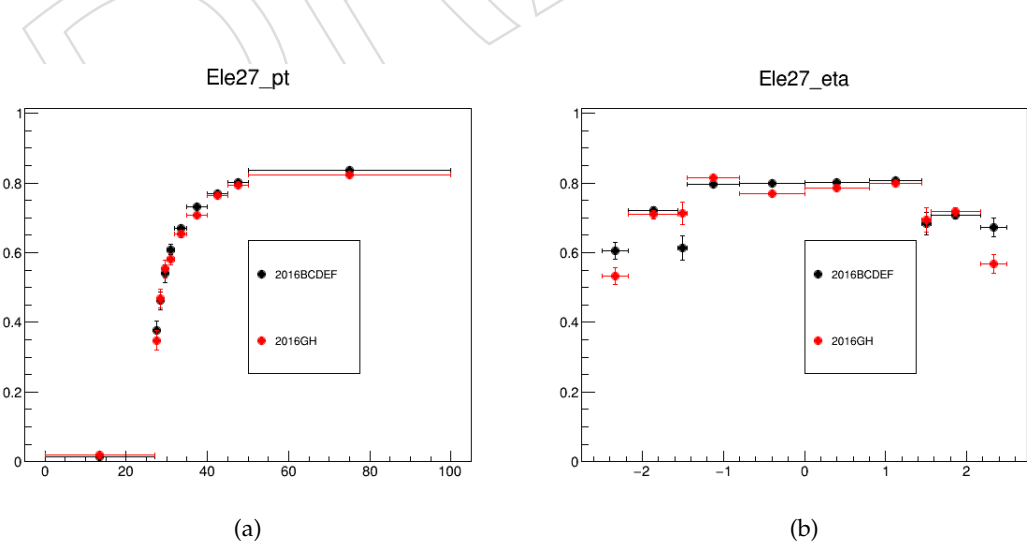


Figure 31: Trigger efficiency as a function of  $p_T$  (left) and  $\eta$  (right) for HLT\_Ele27\_WPTight\_Gsf\_v\*. Efficiencies are separated for DATA in run period 2016BCDEF and 2016GH.

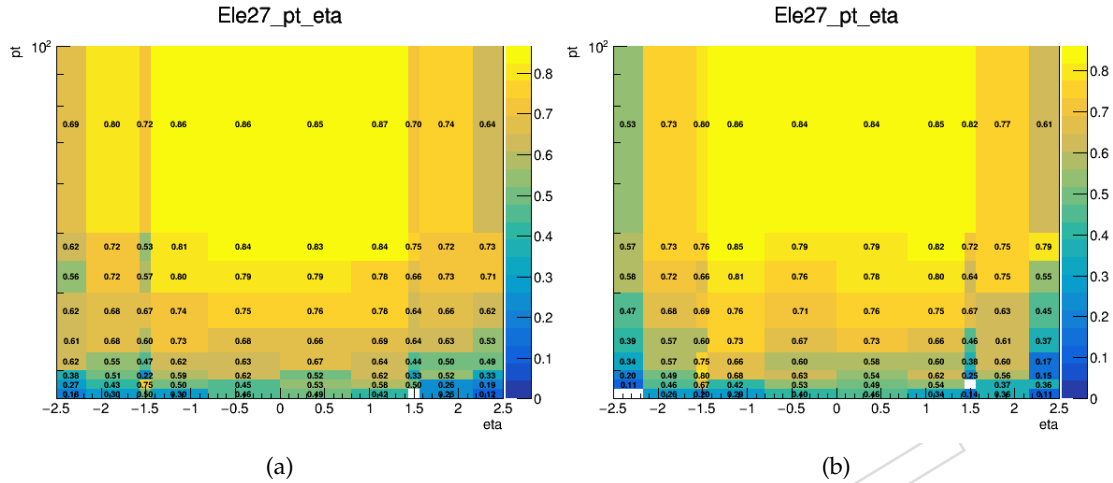


Figure 32: 2D plot (top) for 2016BCDEF and (bottom) 2016GH run period for HLT\_Ele27\_WPTight\_Gsf\_v\*.

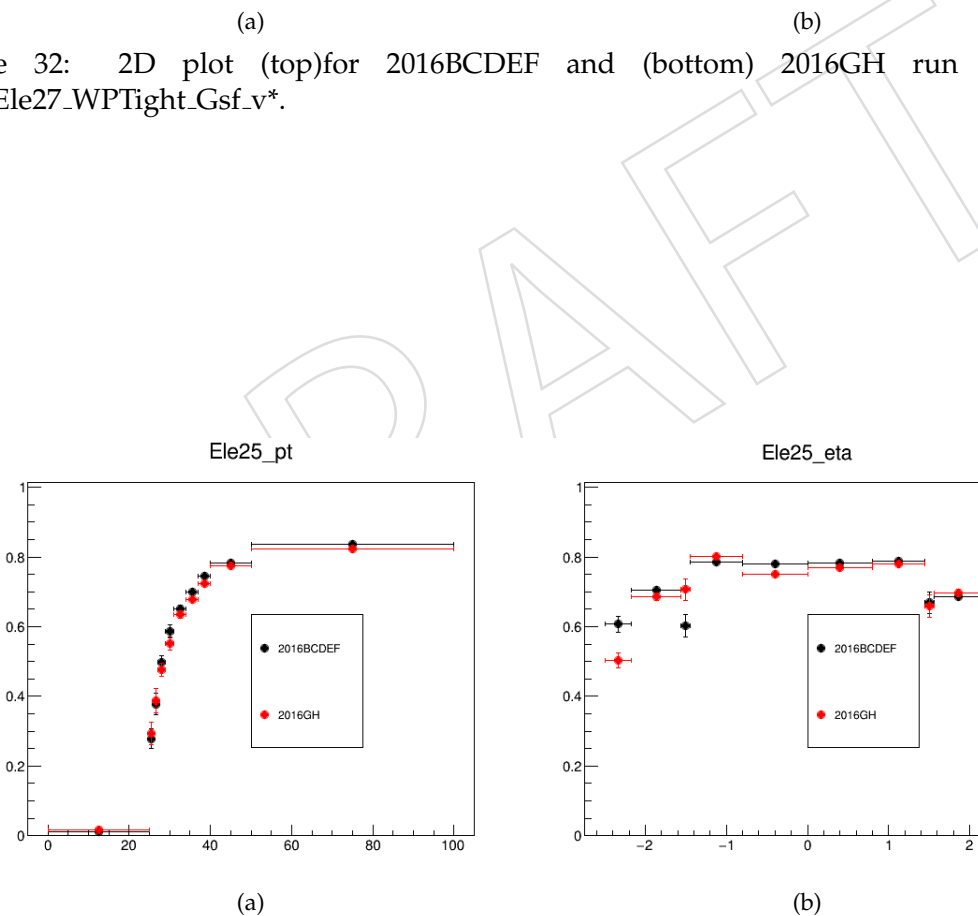


Figure 33: Trigger efficiency as a function of  $p_T$  (left) and  $\eta$  (right) for HLT\_Ele25\_eta2p1\_WPTight\_Gsf\_v\*. Efficiencies are separated for DATA in run period 2016BCDEF and 2016GH .

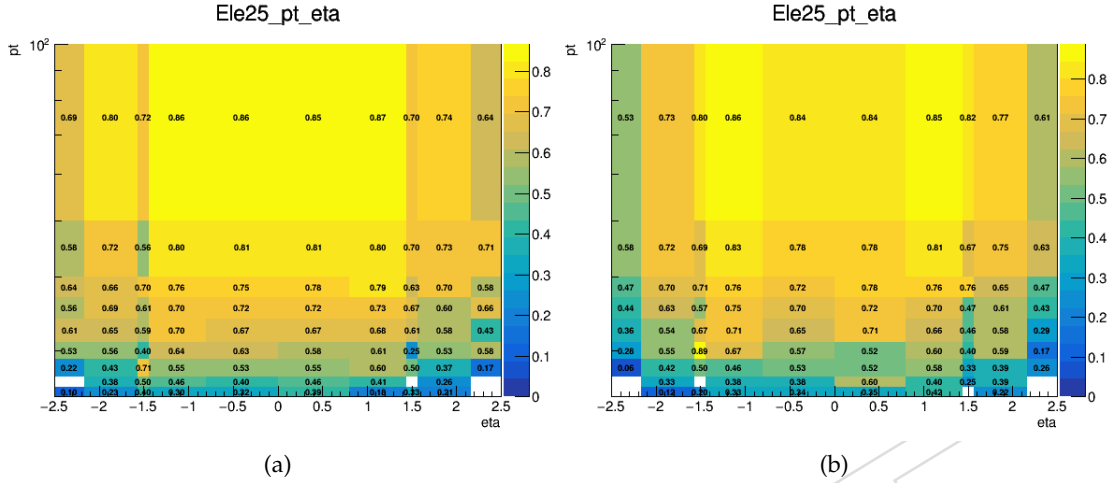


Figure 34: 2D plot (top) for 2016BCDEF and (bottom) 2016GH run period for HLT\_Ele25\_eta2p1\_WPTight\_Gsf\_v\*.

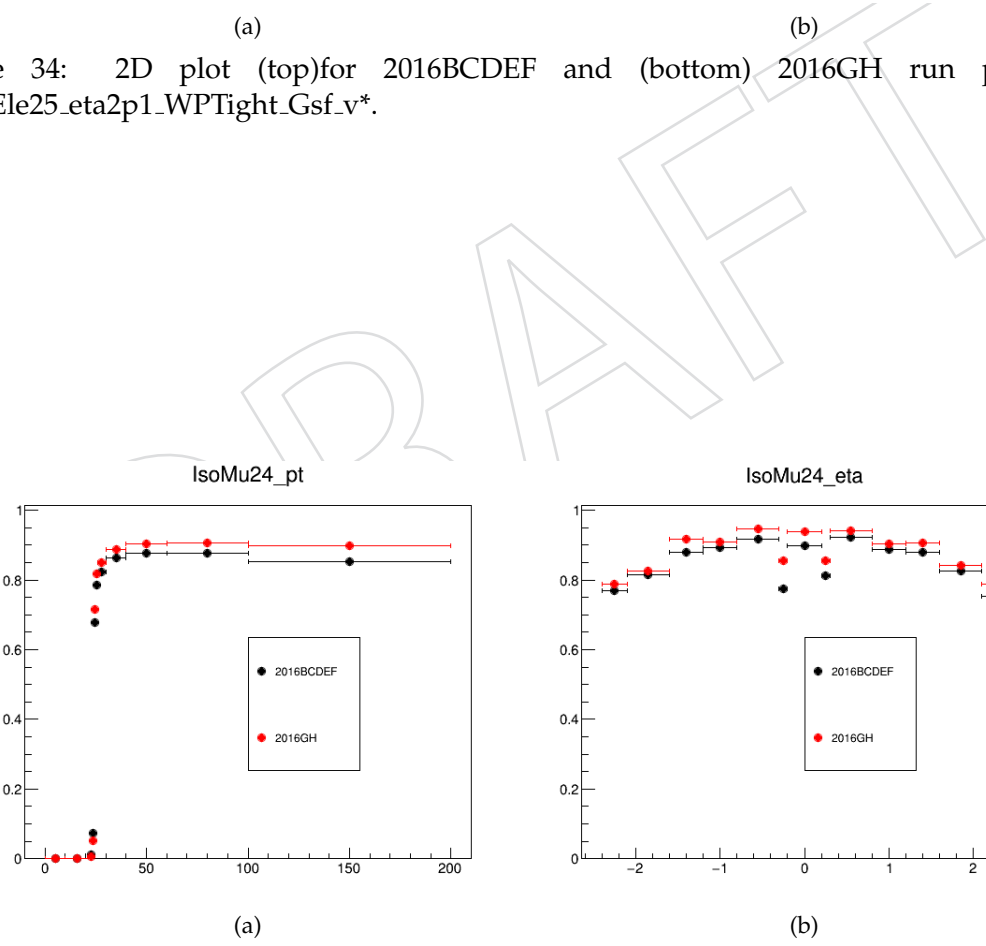


Figure 35: Trigger efficiency as a function of  $p_T$  (left) and  $\eta$  (right) for HLT\_IsoMu24\_v\*. Efficiencies are separated for DATA in run period 2016BCDEF and 2016GH.

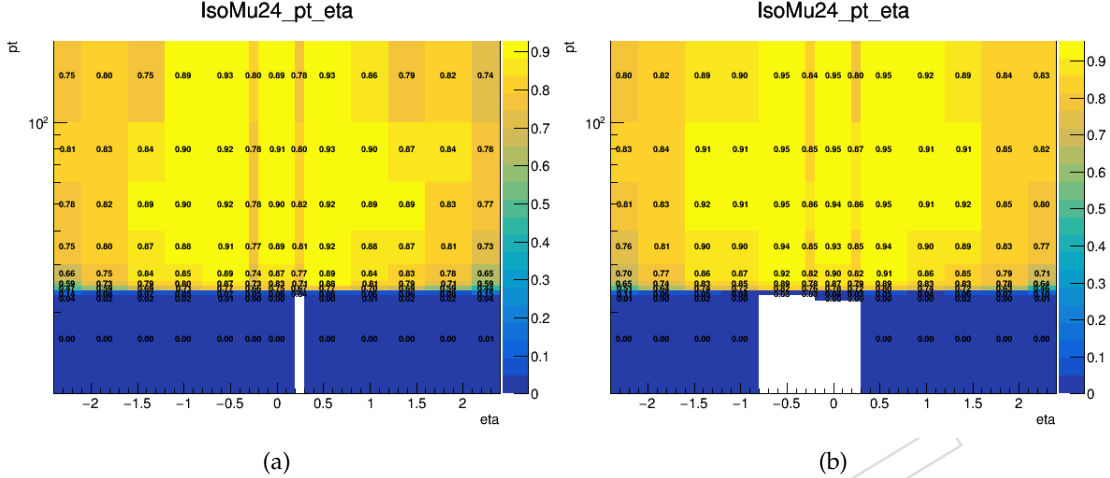


Figure 36: 2D plot for HLT\_IsoMu24\_v\*. Efficiencies are separated for DATA in run period 2016BCDEF and 2016GH.

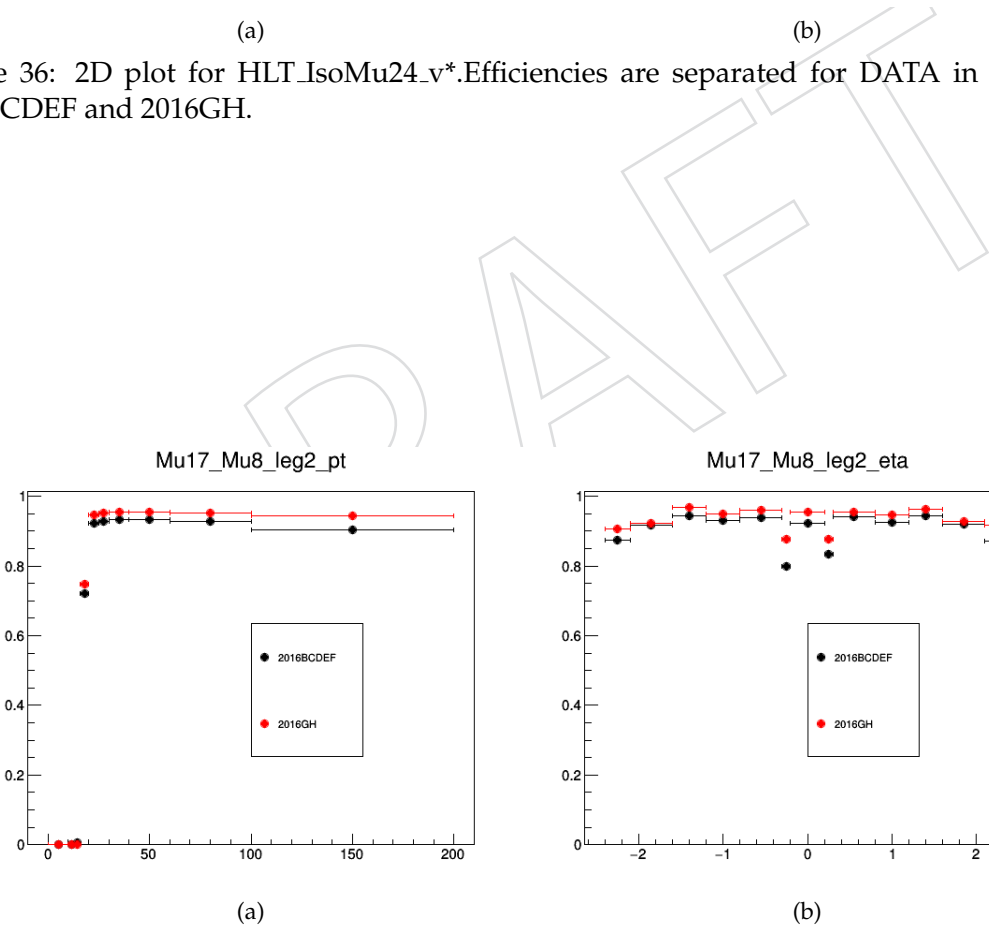
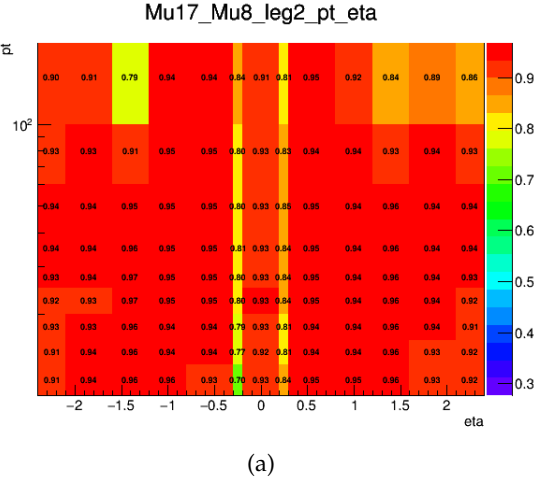


Figure 37: Trigger efficiency as a function of  $p_T$  (left) and  $\eta$  (right) for Leg2 of HLT\_Mu17\_TrkIsoVVL\_Mu8\_TrkIsoVVL\_DZ\_v\*. Efficiencies are separated for DATA in run period 2016BCDEF and 2016GH.



(a)

Figure 38: 2D plot for Leg2 of HLT\_Mu17\_TrkIsoVVL\_Mu8\_TrkIsoVVL\_DZ\_v\*.

tions as mentioned above. Probes are required to match to the filter of subleading leg of HLT\_Mu17\_Mu8 having same selection as muon leg of cross triggers at HLT ( $\Delta R < 0.1$ ). A cut of  $p_T > 12$  GeV and 23 GeV are applied to emulate trigger threshold of  $\mu$  leg Mu12 and Mu23 respectively of cross triggers. Since, the L1T seed triggers are also different between Double muon trigger and cross trigger so following L1T quality criteria has also been imposed.

- $12 \geq \text{L1-muon quality} \leq 15$
- $\text{L1 } \mu p_T \geq 20 \parallel \text{L1 } \mu p_T \geq 23$  (For Mu23 Leg of cross-trigger)
- $\text{L1 } \mu p_T \geq 5 \parallel \text{L1 } \mu p_T \geq 7$  (For Mu12 Leg of cross-trigger)

HLT\_Mu8\_Ele23 was available during run range [273158,278272] only and for run > 278272 HLT\_Mu12\_Ele23 has been used .

The efficiencies of the cross-trigger for Mu23 and Mu12 legs are shown in Figure 39.

For electron legs of the cross-triggers, we used the efficiencies of legs of double electron triggers.

### 5.3 Lepton trigger definitions for run period 2017

Table 37 shows all the triggers used in the analysis.

Table 37: Triggers for Signal Selection

Data Set	Run range	HLT path
SingleMuon	[297046,306462]	HLT_IsoMu27_v*
DoubleMuon	[297046,299329]	HLT_Mu17_TrkIsoVVL_Mu8_TrkIsoVVL_DZ_v*
	[299368,306462]	HLT_Mu17_TrkIsoVVL_Mu8_TrkIsoVVL_DZ_Mass8_v*
EGamma	[297046,306462]	HLT_Ele35_WPTight_Gsf_v* HLT_Ele23_Ele12_CaloIdL_TrackIdL_IsoVL_v*
MuonEG	[297046,306462]	HLT_Mu12_TrkIsoVVL_Ele23_CaloIdL_TrackIdL_IsoVL_DZ_v*
	[297046,299329]	HLT_Mu23_TrkIsoVVL_Ele12_CaloIdL_TrackIdL_IsoVL_DZ_v*
	[299368,306462]	HLT_Mu23_TrkIsoVVL_Ele12_CaloIdL_TrackIdL_IsoVL_v*

#### 5.3.1 Tag and Probe Studies

CMSSW\_9\_4\_9 has been used. Datasets used are mentioned in Table 38. The JSON used is Cert\_294927-306462\_13TeV\_EOY2017ReReco\_Collisions17\_JSON.txt, which correspond to the integrated luminosity of  $42 \text{ fb}^{-1}$ .

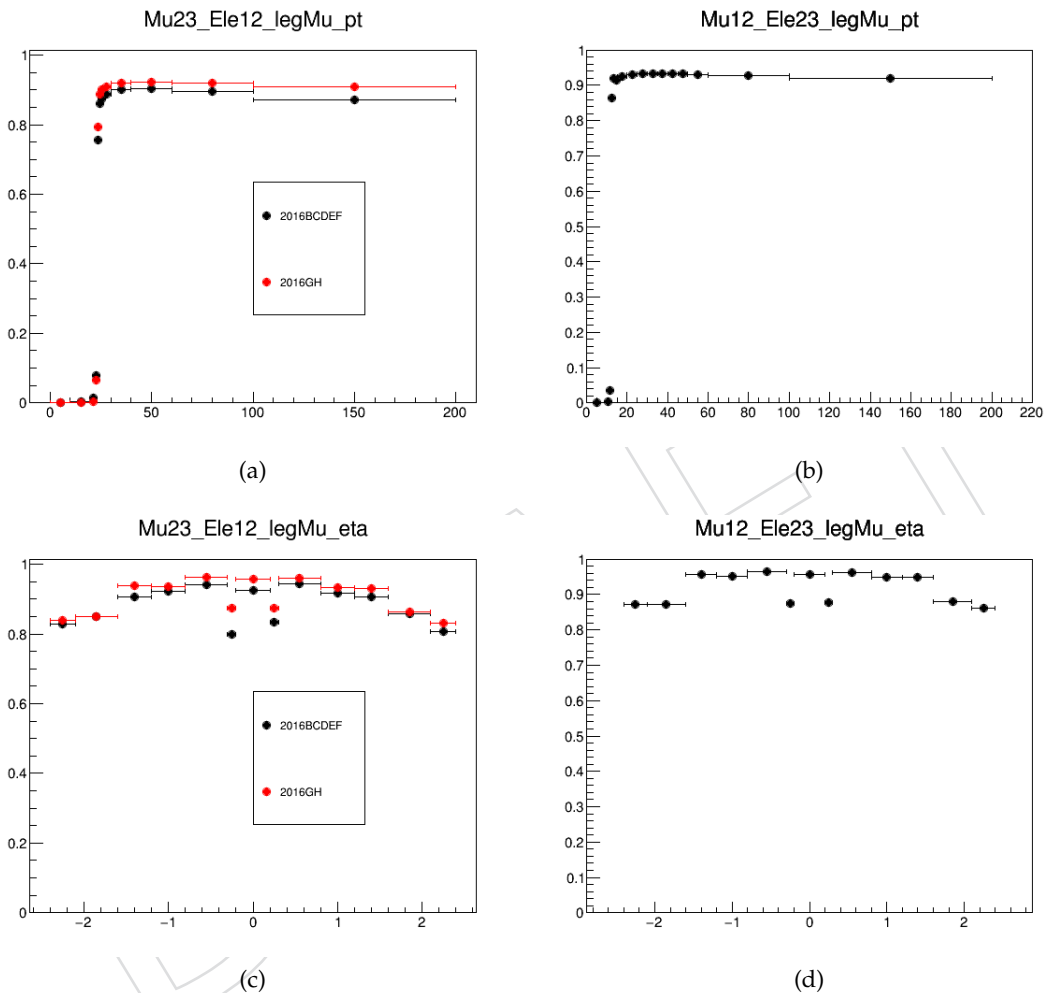


Figure 39: Trigger efficiency as a function of  $p_T$  (top) and  $\eta$  (bottom) for Muon legs of cross-triggers Mu23(left) and Mu12(right). Efficiencies are separated for DATA in run period 2016BCDEF and 2016GH for Mu23 whereas HLT\_Mu12\_Ele23 is considered for 2016FGH run period.

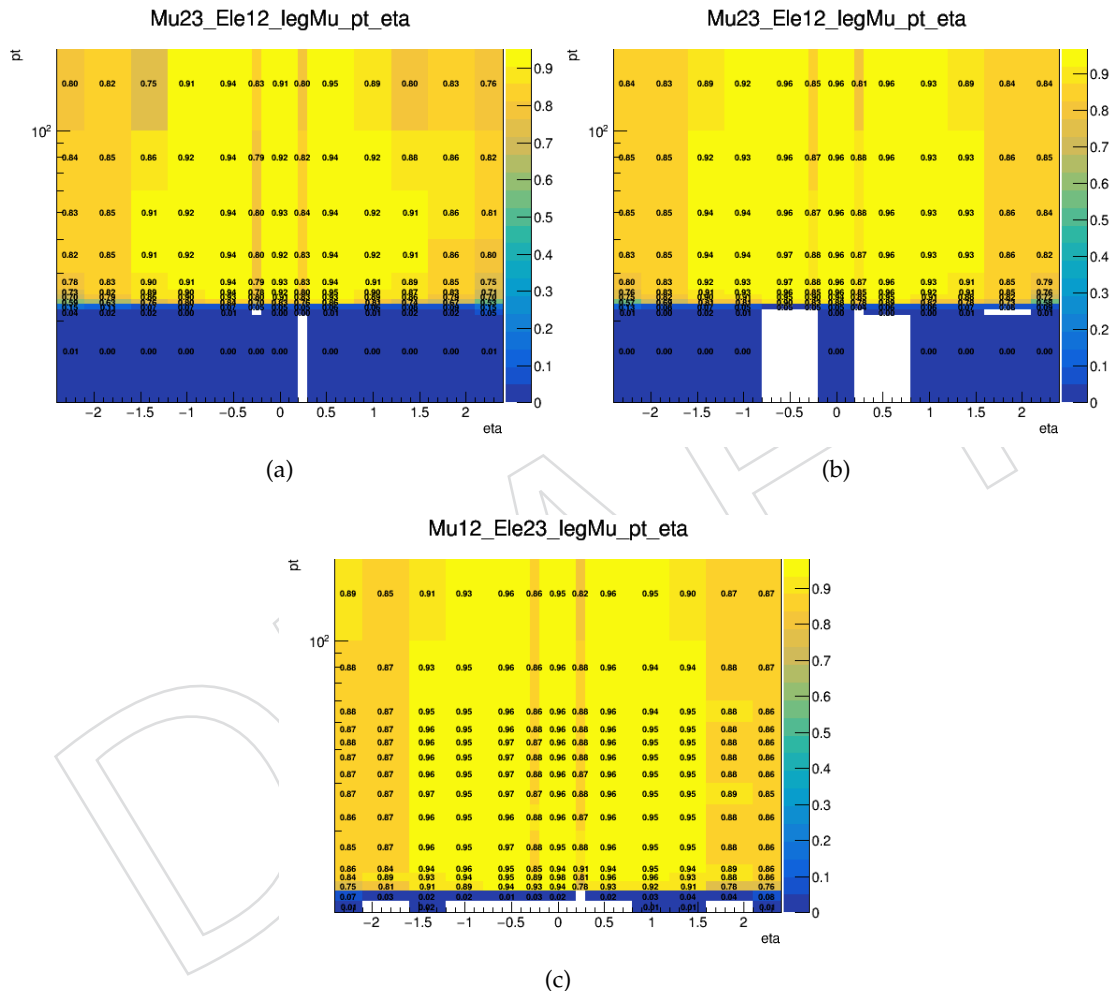


Figure 40: 2D plot for Muon legs of cross-triggers Mu23(top) and Mu12(bottom).

Table 38: Datasets used for the computation of lepton trigger efficiencies

DataSets
/SingleElectron/Run2017(B-to-F)-31Mar2018-v1/MINIAOD
/SingleMuon/Run2017(B-to-F)-31Mar2018-v1/MINIAOD

544 The selection for the tag and probe pair is given below.

#### 545 Tag Selection

546

- 547 • tag is required to pass the POG defined cut based “tight” identification and isolation  
548 criteria. For electrons the definition of identification working point is given here [?]  
549 ]. For muons here [2].
- 550 •  $p_T > 40(30)$  GeV for  $e(\mu)$ .
- 551 • tag lepton should be matched to HLT\_Ele35\_WPTight\_Gsf and HLT\_IsoMu27 for  $e$   
552 and  $\mu$  respectively.

#### 553 Probe Selection

554

- 555 • probe is required to pass the HWW specific identification criteria. The working  
556 points are defined in Section 3.1 and 4

557 Trigger efficiency is computed as a function of  $p_T$  and  $\eta$  of probe as there is always a turn-on in  
558 efficiency with respect to  $p_T$ ,  $\eta$  binning is required to take into account the different response  
559 from various parts of detector.

560 The binning used for various triggers is the following.  $p_T$  binning depends on the trigger  
561 threshold.

562  **$\eta$  bins for  $e$**  : -2.5, -2.1, -1.6, -1.4, -0.8, 0, 0.8, 1.4, 1.6, 2.1, 2.5

563  **$\eta$  bins for  $\mu$**  : -2.4, -2.1, -1.6, -1.2, -0.8, -0.3, -0.2, 0.2, 0.3, 0.8, 1.2, 1.6, 2.1, 2.4

564

#### 565 $p_T$ bins

566

- 567 • Ele23 : 0,10,20,21,22,23,24,25,26,30,35,40,45,50,60,100,200
- 568 • Ele12 : 0,10,11,12,13,14,15,20,25,30,35,40,45,50,60,100,200
- 569 • Ele35 : 0,10,20,30,32,33,34,35,36,37,38,40,45,50,60,100,200
- 570 • Mu17 : 0,10,15,16,17,18,19,20,22,25,30,35,40,45,50,60,100,200
- 571 • Mu8 : 0,6,7,8,9,10,12,15,20,25,30,35,40,45,50,60,100,200
- 572 • Mu27 : 0,10,20,23,25,26,27,28,29,30,35,40,45,50,60,100,200
- 573 • Mu12 : 0,10,11,12,13,14,15,20,25,30,35,40,45,50,60,100,200
- 574 • Mu23 : 0,10,20,21,22,23,24,25,26,30,35,40,45,50,60,100,200

575 Double lepton HLT paths needs two leptons to pass them and hence two parts. Each part of the  
576 path is called “leg”. Trigger efficiencies are computed for each “leg” of the HLT path. Then the  
577 efficiencies of each leg is combined according to the type of event we have. We use the counting

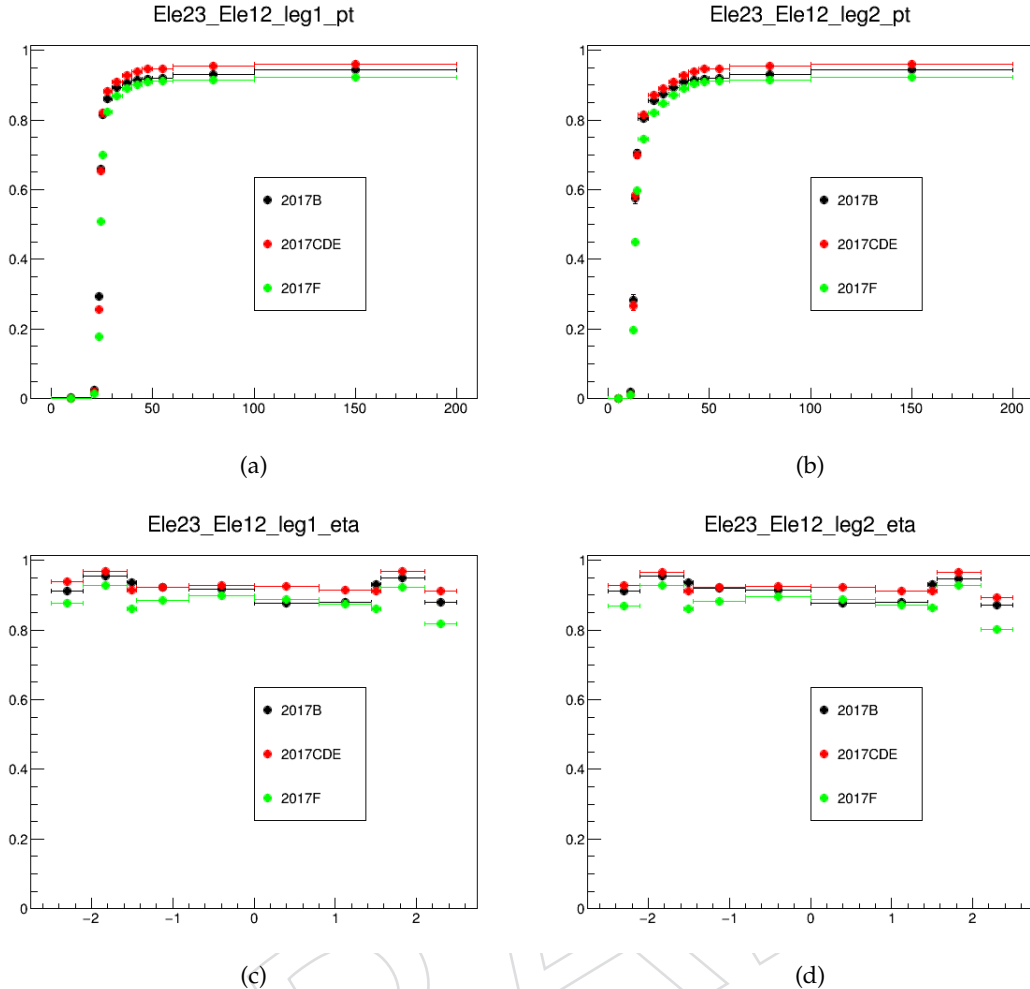


Figure 41: Trigger efficiency as a function of  $p_T$  (top) and  $\eta$  (bottom) for Leg1 (left) and Leg2 (right) of HLT\_Ele23\_Ele12\_CaloIdL\_TrackIdL\_IsoVL\_DZ\_v\*. Efficiencies are separated for DATA in run period 2017 B , 2017 CDE and 2017 F.

578 method to estimate the efficiency. No fitting has been performed as with the tight selection, the  
579 background contamination under Z peak is very low.

### 580 5.3.2 Results

581 Efficiencies are computed for each Era (2017B to 2017F) in order to check the differences because  
582 of change in run conditions.

583 In an another study , trigger efficiencies has been measured with MVA selections accquired for  
584 the tag electron , the comaprison of tight selection and MVA is shown in Figure 45

585 To compute the trigger efficiency of  $\mu$  leg in mixed Mu-EG triggers, since the  $\mu$  leg is not the  
586 same as one of the legs of double muon triggers so we need to emulate the HLT selection.  
587 SingleMu PD has been used to measure the efficiencies. Tag is required to pass the condi-  
588 tions as mentioned above. Probes are required to match to the filter of subleading leg of  
589 HLT\_Mu17\_Mu8 having same selection as muon leg of cross triggers at HLT ( $\Delta R < 0.1$ ). A  
590 cut of  $p_T > 12$  GeV and 23 GeV are applied to emulate trigger threshold of  $\mu$  leg Mu12 and  
591 Mu23 respectively of cross triggers. Since, the L1T seed triggers are also different between  
592 Double muon trigger and cross trigger so following L1T quality criteria has also been imposed.

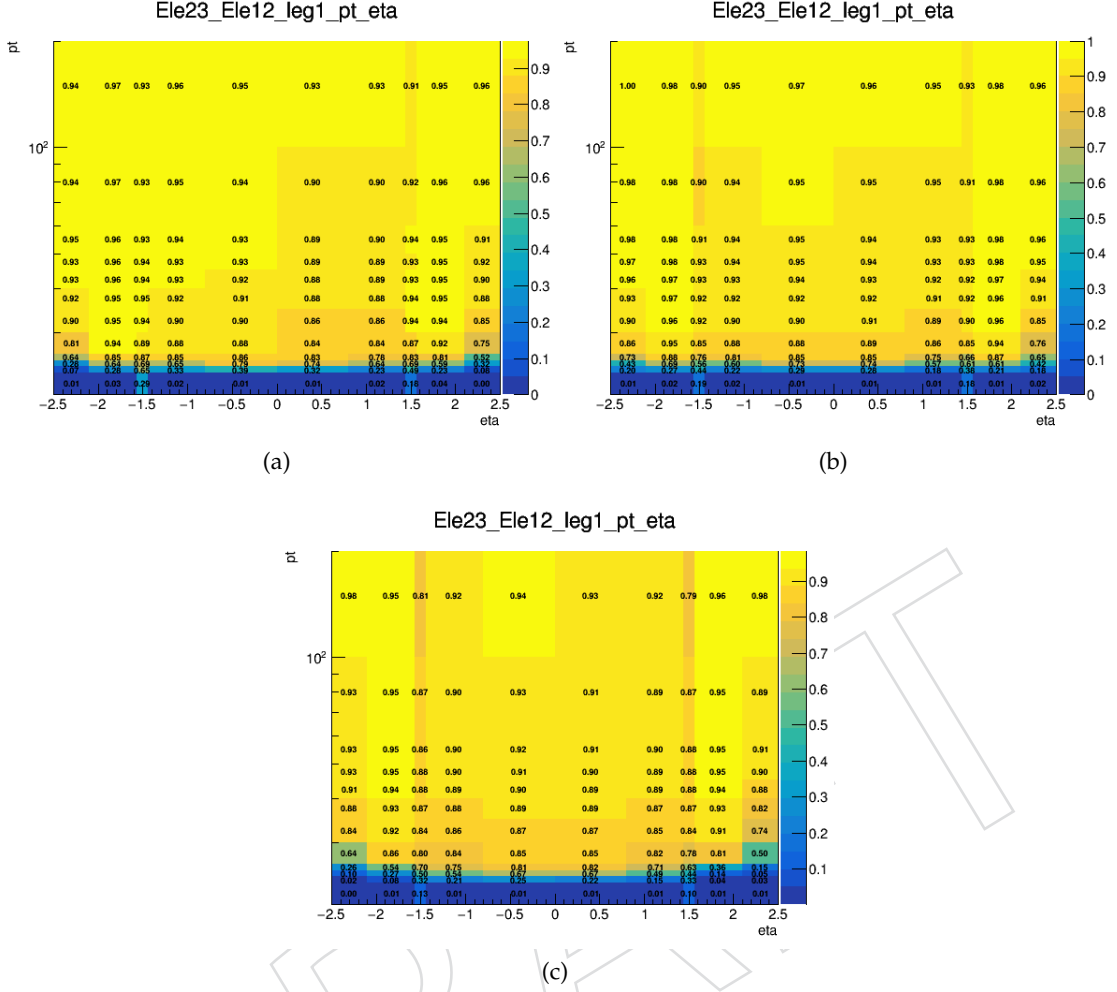


Figure 42: 2D plots for HLT\_Ele23\_Ele12\_CaloIdL\_TrackIdL\_IsoVL\_DZ\_v\*. Efficiencies are separated for DATA in run period 2017 B , 2017 CDE and 2017 F.

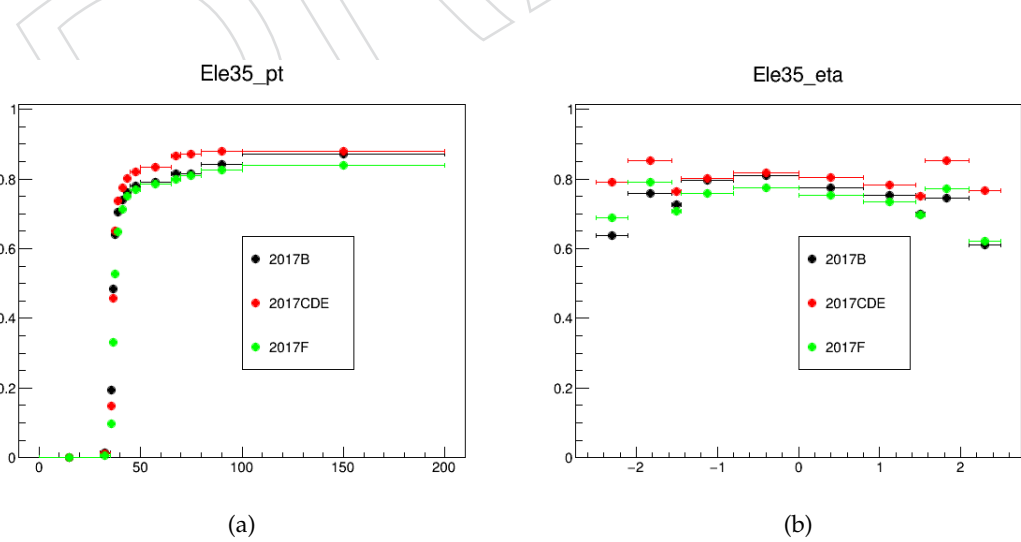


Figure 43: Trigger efficiency as a function of  $p_T$  (left) and  $\eta$  (right) for HLT\_Ele35\_WPTight\_Gsf\_v\*. Efficiencies are separated for DATA in run period 2017 B , 2017 CDE and 2017 F.

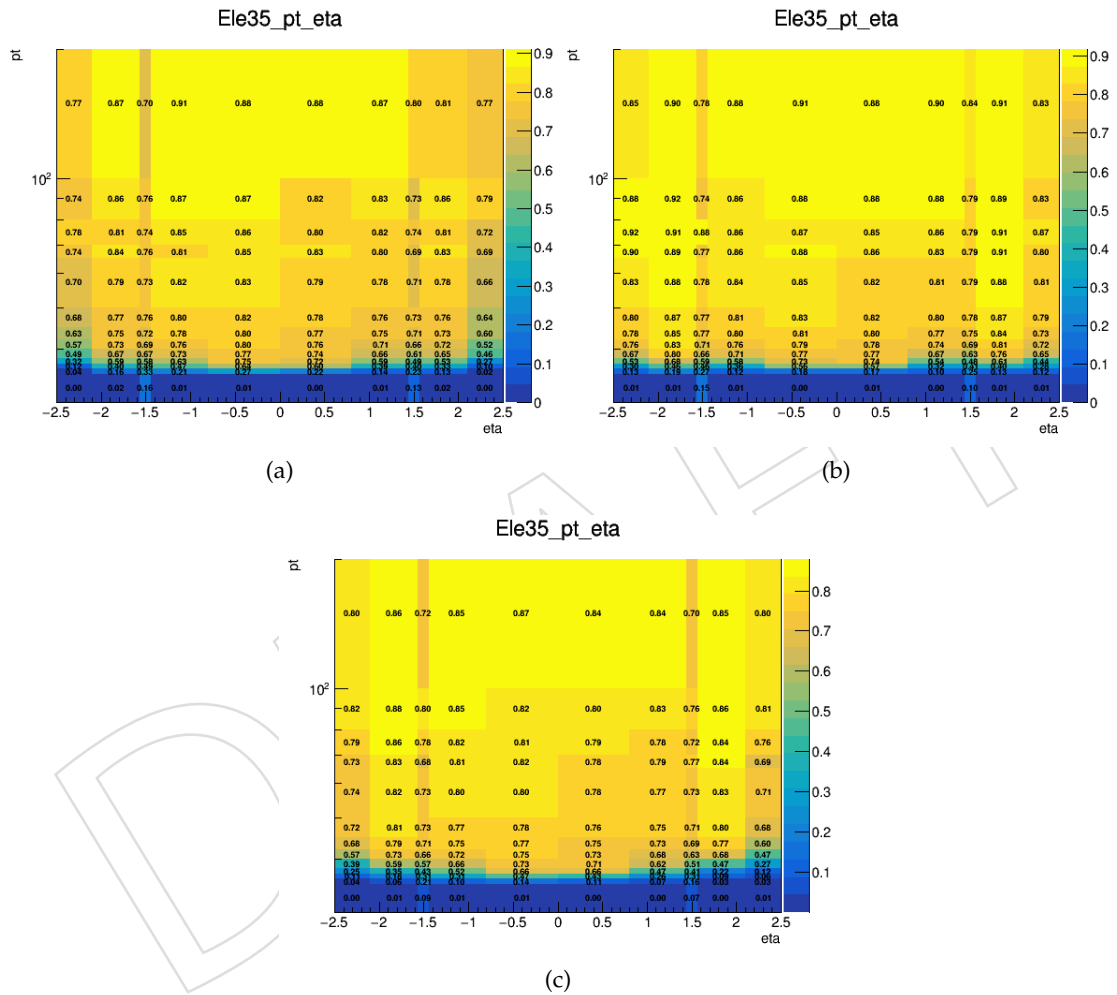


Figure 44: 2D plots for HLT\_Ele35\_WPTight\_Gsf\_v\*. Efficiencies are separated for DATA in run period 2017 B , 2017 CDE and 2017 F.

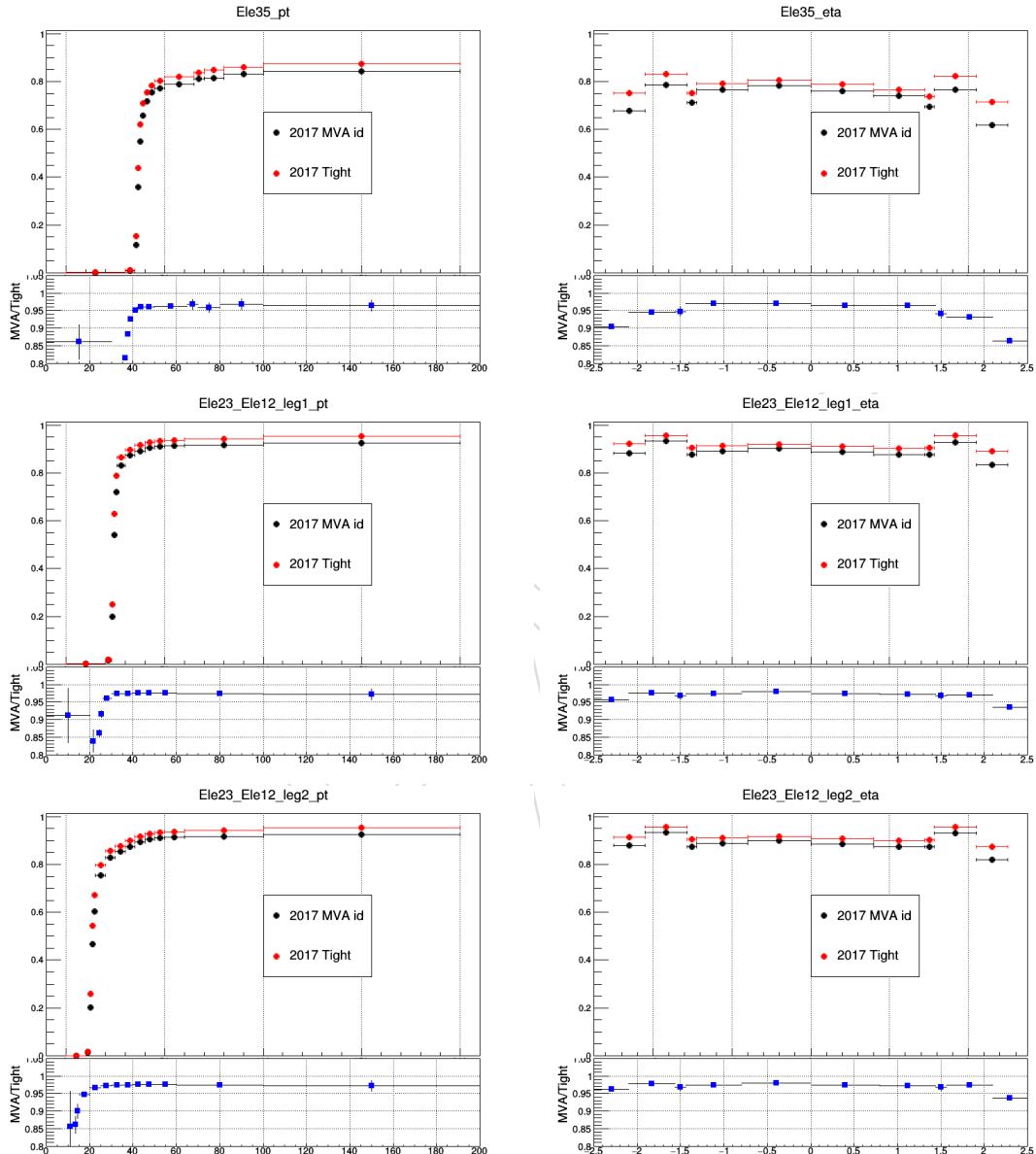


Figure 45: MVA vs Tight id comparison of trigger efficiency as a function of  $p_T$  (left) and  $\eta$  (right) for electron triggers for the run period 2017.

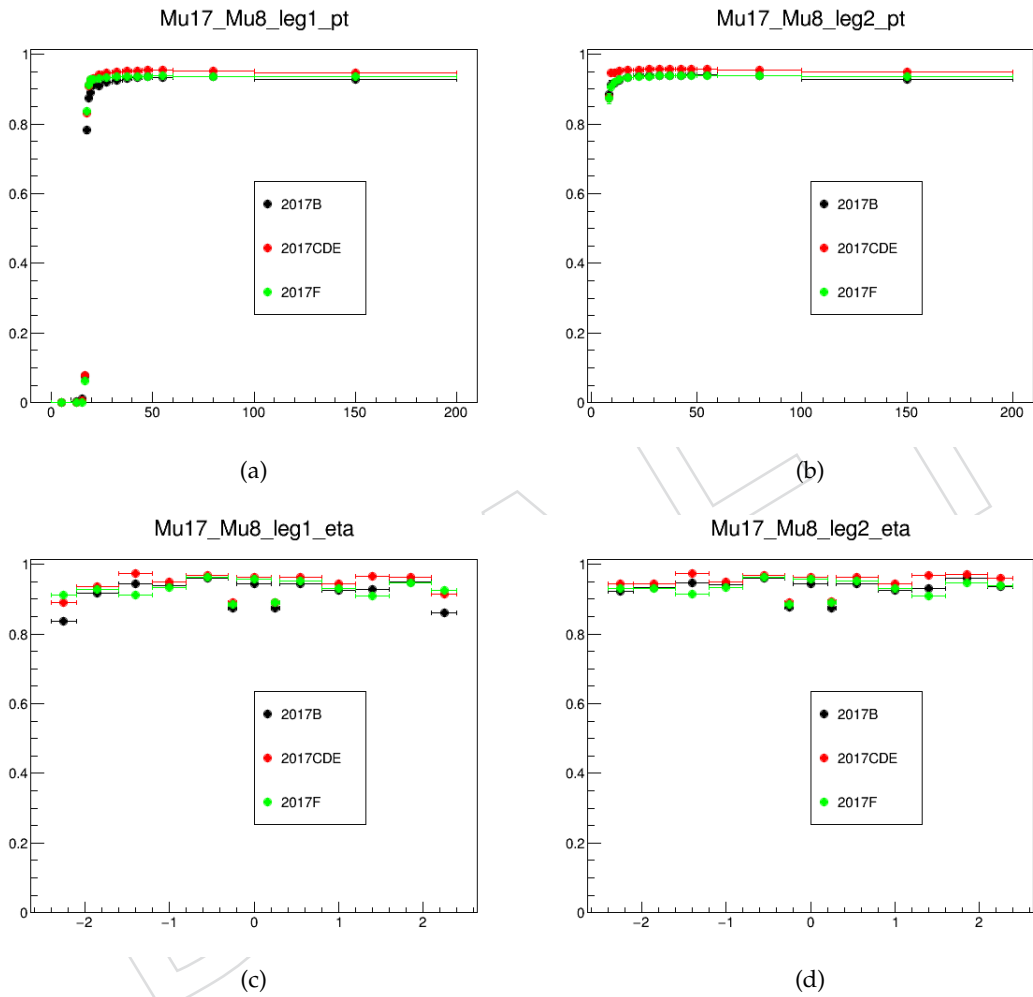


Figure 46: Trigger efficiency as a function of  $p_T$  (top) and  $\eta$  (bottom) for Leg1 (left) and Leg2 (right) of HLT\_Mu17\_TrkIsoVVL\_Mu8\_TrkIsoVVL\_DZ\_v\*. Efficiencies are separated for run period 2017B, 2017CDE and 2017F.

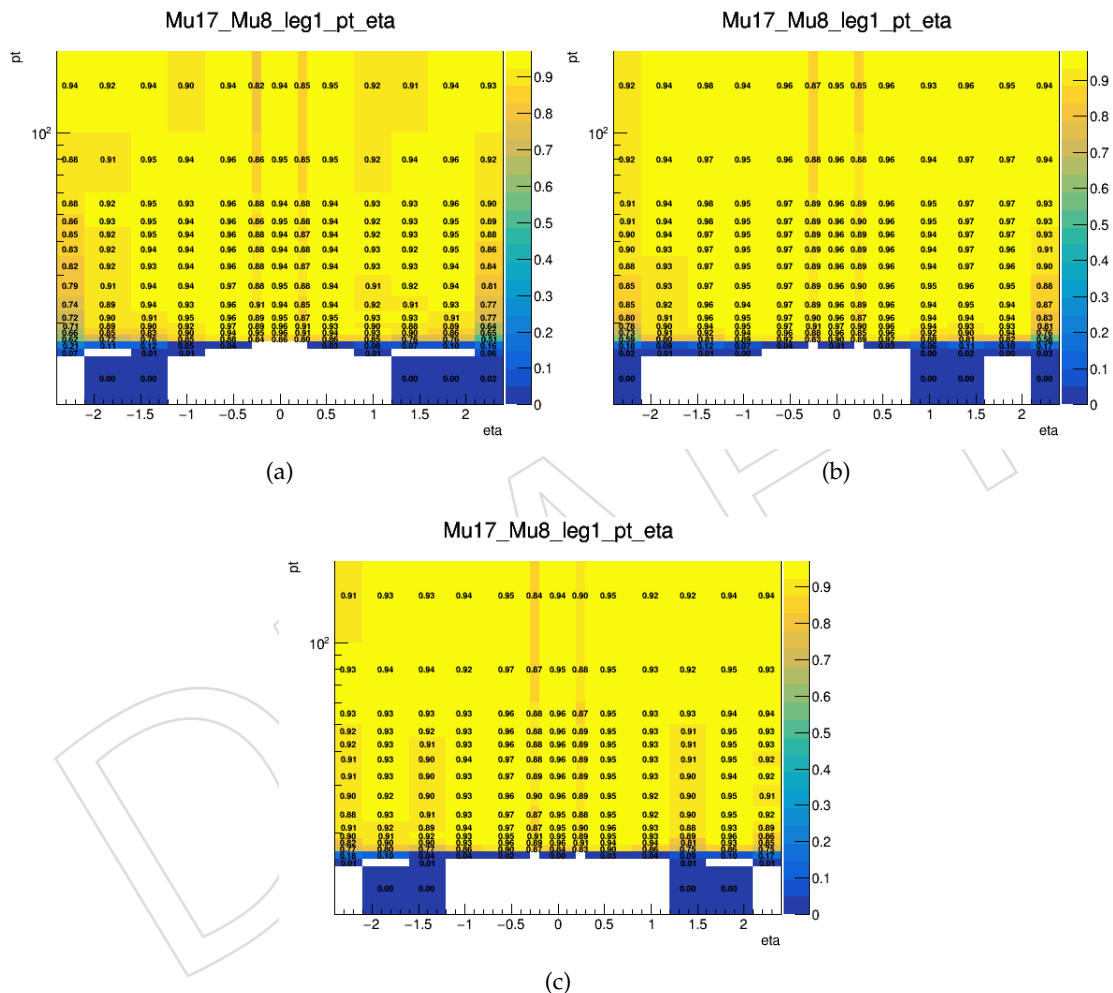


Figure 47: 2D plots for Mu17 of HLT\_Mu17\_TrkIsoVVL\_Mu8\_TrkIsoVVL\_DZ\_v\*.

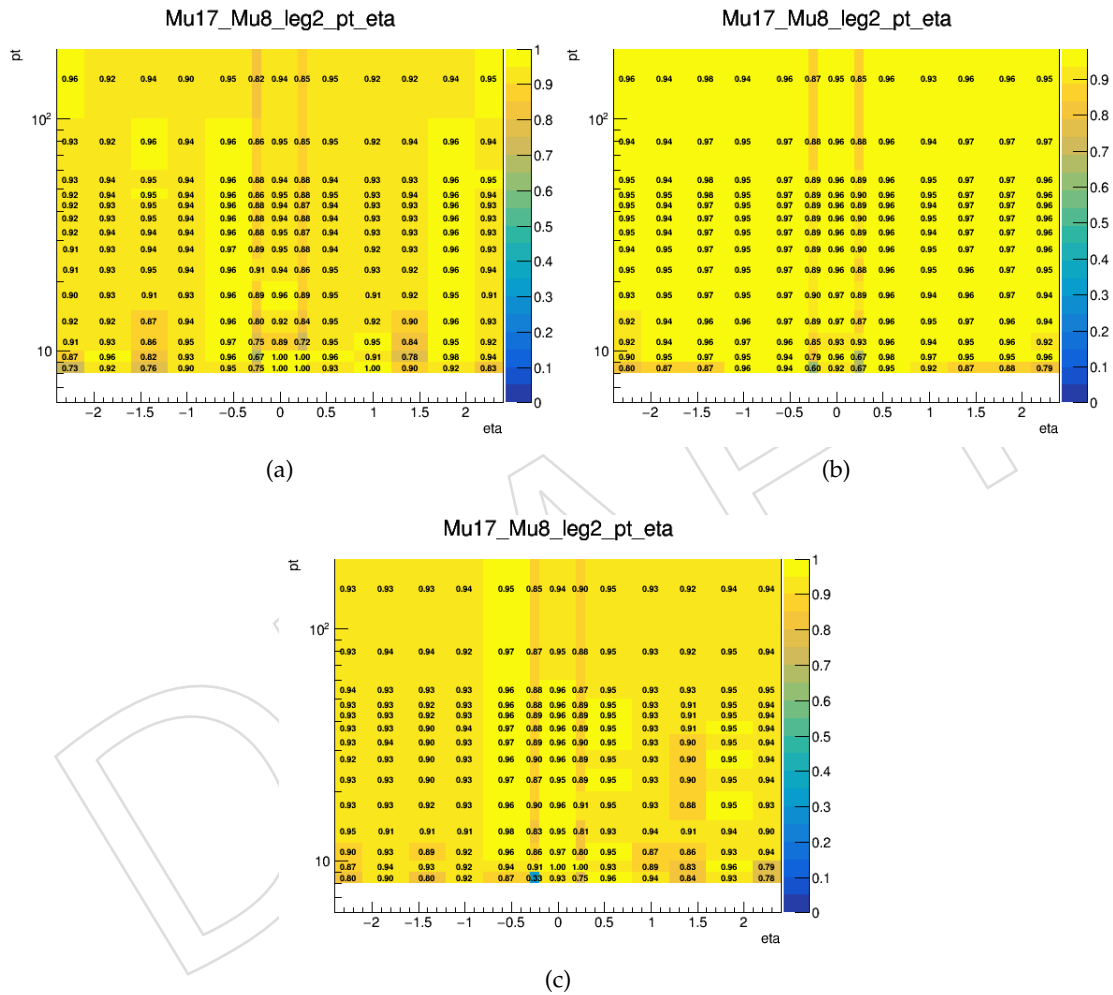


Figure 48: 2D plots for Mu8 of HLT\_Mu17\_TrkIsoVVL\_Mu8\_TrkIsoVVL\_DZ\_v\*.

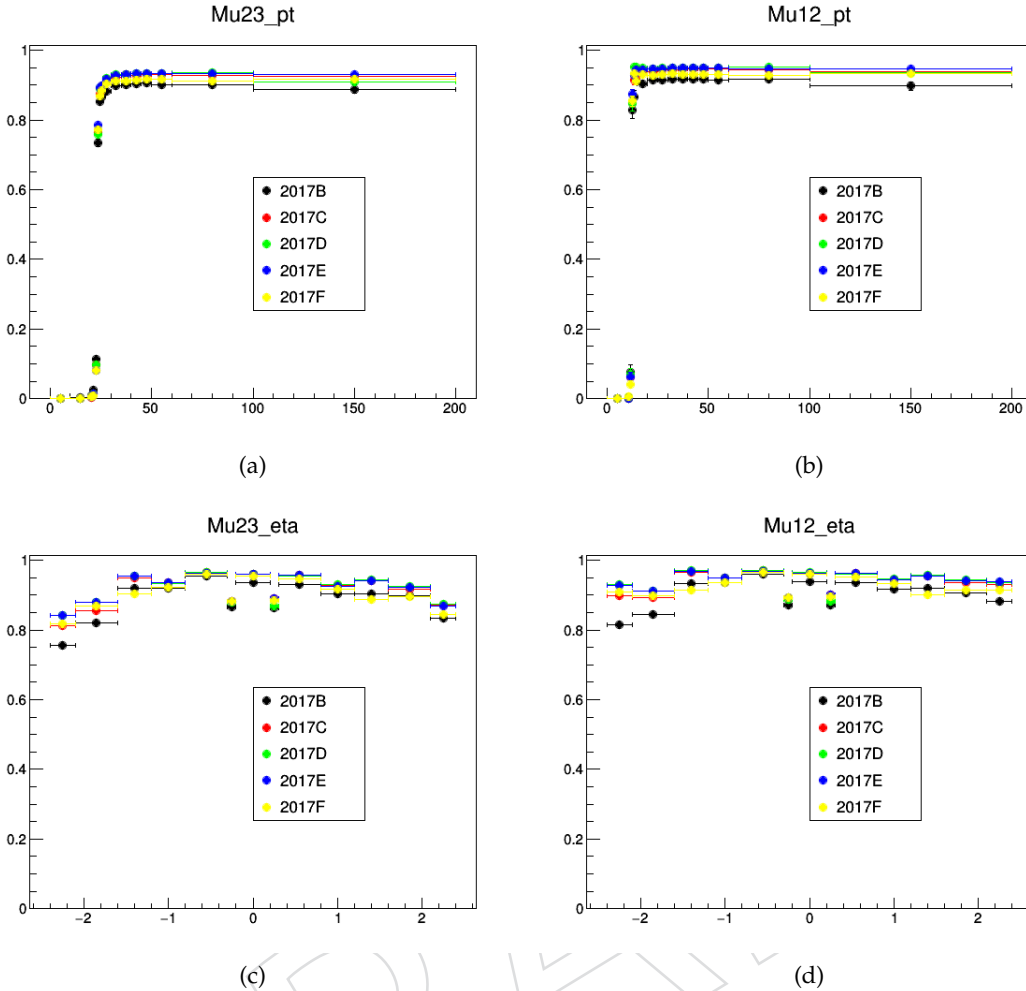


Figure 49: Trigger efficiency as a function of  $p_T$  (top) and  $\eta$  (bottom) for Muon legs of cross-triggers Mu23(left) and Mu12(right).Efficiencies are separated for DATA in run period 2017 B , 2017 CDE and 2017 F.

- $12 \geq \text{L1-muon quality} \leq 15$
- $\text{L1 } \mu p_T \geq 20 \parallel \text{L1 } \mu p_T \geq 23$  (For Mu23 Leg of cross-trigger)
- $\text{L1 } \mu p_T \geq 5 \parallel \text{L1 } \mu p_T \geq 7$  (For Mu12 Leg of cross-trigger)

596 The efficiencies of the cross-trigger legs are shown in Figure 49.

597 For electron legs of the cross-triggers, we used the efficiencies of legs of double electron triggers.

## 598 5.4 Lepton trigger definitions for run period 2018

599 Table 39 shows all the triggers used in the analysis.

### 600 5.4.1 Tag and Probe Studies

601 CMSSW\_10\_2\_11 has been used. Datasets used are mentioned in Table 40. The JSON used  
 602 is Cert\_314472-325175\_13TeV\_PromptReco\_collisions18\_JSON.txt, which correspond to the inte-  
 603 grated luminosity of  $59.7 \text{ fb}^{-1}$ .

604 The selection for the tag and probe pair is given below.

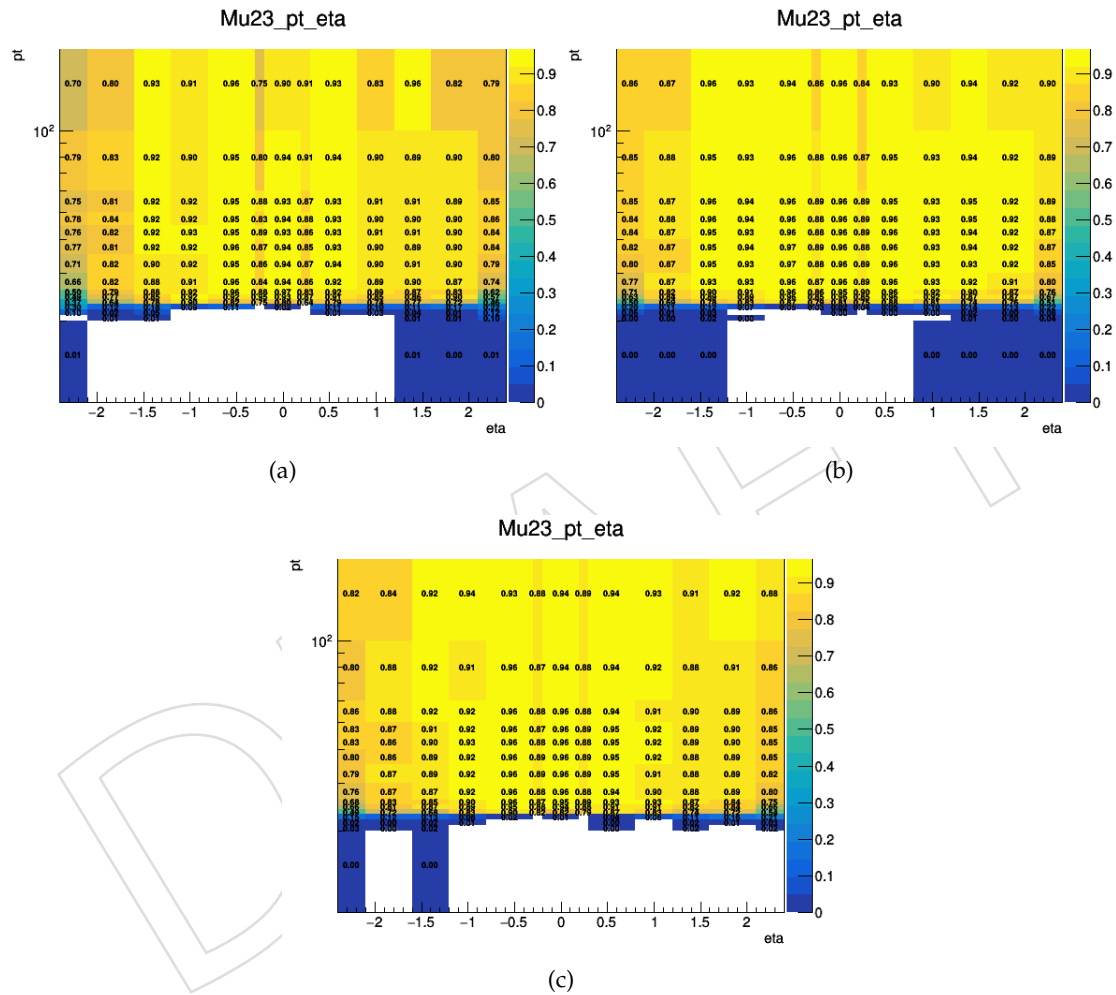


Figure 50: 2D plots for Mu23 leg of HLT\_Mu23\_Ele12 . Efficiencies are separated for DATA in run period 2017 B , 2017 CDE and 2017 F.

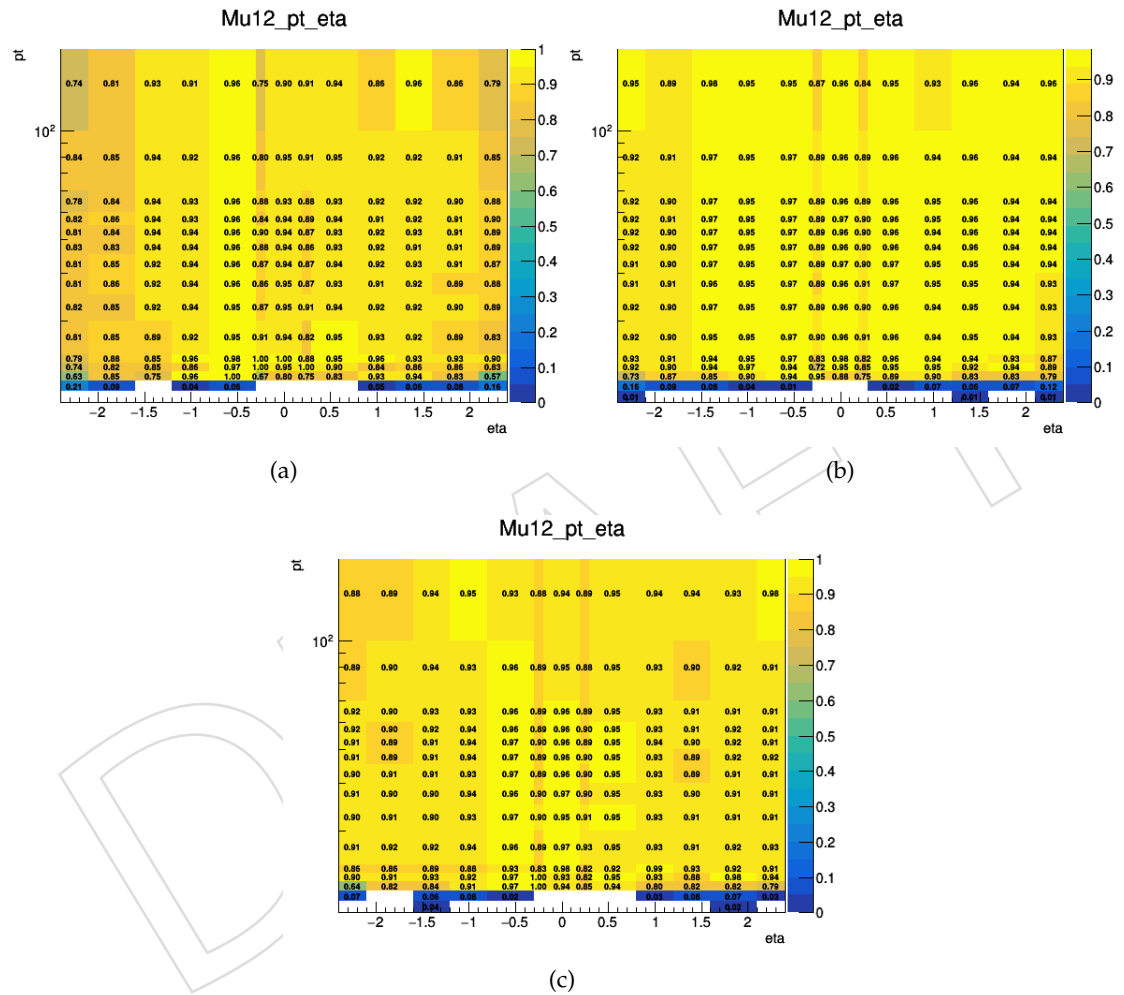


Figure 51: 2D plots for Mu12 leg of HLT\_Mu12\_Ele23. Efficiencies are separated for DATA in run period 2017 B , 2017 CDE and 2017 F.

Table 39: Triggers for Signal Selection

Data Set	Run range	HLT path
SingleMuon	[315252,325172]	HLT_IsoMu24_v* HLT_Mu50_v*
	[314859,325175]	HLT_IsoMu27_v*
DoubleMuon	[315252,325172]	HLT_Mu17_TrkIsoVVL_Mu8_TrkIsoVVL_DZ_Mass3p8_v* HLT_Mu17_TrkIsoVVL_Mu8_TrkIsoVVL_DZ_Mass8_v*
EGamma	[315252,325172]	HLT_Ele32_WPTight_Gsf_v* HLT_Ele35_WPTight_Gsf_v* HLT_Ele23_Ele12_CaloIdL_TrackIdL_IsoVL_v*
MuonEG	[315252,325172]	HLT_Mu12_TrkIsoVVL_Ele23_CaloIdL_TrackIdL_IsoVL_DZ_v* HLT_Mu23_TrkIsoVVL_Ele12_CaloIdL_TrackIdL_IsoVL_DZ_v*

Table 40: Datasets used for the computation of lepton trigger efficiencies

DataSets
/EGamma/Run2018(A to D)-17Sep2018-v2/MINIAOD
/SingleMuon/Run2018(A to D)-17Sep2018-v2/MINIAOD

## 605 Tag Selection

606

- 607 • tag is required to pass the POG defined cut based “tight” identification and isolation  
608 criteria. For electrons the definition of identification working point is given here [?]  
609 ]. For muons here [2].
- 610 •  $p_T > 40(30)$  GeV for  $e(\mu)$ .
- 611 • tag lepton should be matched to HLT\_Ele35\_WPTight\_Gsf and HLT\_IsoMu24 for  $e$   
612 and  $\mu$  respectively.

## 613 Probe Selection

614

- 615 • probe is required to pass the HWW specific identification criteria. The working  
616 points are defined in Section 3.1 and 4

617 Trigger efficiency is computed as a function of  $p_T$  and  $\eta$  of probe as there is always a turn-on in  
618 efficiency with respect to  $p_T$ ,  $\eta$  binning is required to take into account the different response  
619 from various parts of detector.

620 The binning used for various triggers is the following.  $p_T$  binning depends on the trigger  
621 threshold.

622  $\eta$  bins for  $e$  : -2.5, -2.1, -1.6, -1.4, -0.8, 0, 0.8, 1.4, 1.6, 2.1, 2.5

623  $\eta$  bins for  $\mu$  : -2.4, -2.1, -1.6, -1.2, -0.8, -0.3, -0.2, 0.2, 0.3, 0.8, 1.2, 1.6, 2.1, 2.4

624

## 625 $p_T$ bins

626

627 • Ele23 : 0,20,23,24,25,26,30,35,40,45,50,60,100,200

628 • Ele12 : 0,10,12,13,14,15,20,25,30,35,40,45,50,60,100,200

- 
- 629     • Ele32 : 0,30,32,33,34,35,36,37,38,40,45,50,60,100,200  
 630     • Ele35 : 0,30,35,36,37,38,40,42,45,50,65,70,80,100,200  
 631     • Mu17 : 0,10,15,16,17,18,19,20,22,25,30,35,40,45,50,60,100,200  
 632     • Mu8 : 0,6,7,8,9,10,12,15,20,25,30,35,40,45,50,60,100,200  
 633     • Mu27 : 0,10,20,23,25,26,27,28,29,30,35,40,45,50,60,100,200  
 634     • Mu12 : 0,10,11,12,13,14,15,20,25,30,35,40,45,50,60,100,200  
 635     • Mu23 : 0,10,20,21,22,23,24,25,26,30,35,40,45,50,60,100,200  
 636     • Mu50 : 0,45,50,51,52,54,56,60,65,75,100,150,200

637 Double lepton HLT paths needs two leptons to pass them and hence two parts. Each part of the  
 638 path is called “leg”. Trigger efficiencies are computed for each “leg” of the HLT path. Then the  
 639 efficiencies of each leg is combined according to the type of event we have. We use the counting  
 640 method to estimate the efficiency. No fitting has been performed as with the tight selection, the  
 641 background contamination under Z peak is very low.

#### 642 5.4.2 Results

643 Efficiencies are computed for each Era (2018A to 2018D) in order to check the differences be-  
 644 cause of change in run conditions.

645 In an another study , trigger efficiencies has been measured with MVA selections acquired for  
 646 the tag electron , the comaprison of tight selection and MVA is shown in Figure 58

647 To compute the trigger efficiency of  $\mu$  leg in mixed Mu-EG triggers, since the  $\mu$  leg is not the  
 648 same as one of the legs of double muon triggers so we need to emulate the HLT selection.  
 649 SingleMu PD has been used to measure the efficiencies. Tag is required to pass the condi-  
 650 tions as mentioned above. Probes are required to match to the filter of subleading leg of  
 651 HLT\_Mu17\_Mu8 having same selection as muon leg of cross triggers at HLT ( $\Delta R < 0.1$ ). A  
 652 cut of  $p_T > 12$  GeV and 23 GeV are applied to emulate trigger threshold of  $\mu$  leg Mu12 and  
 653 Mu23 respectively of cross triggers. Since, the L1T seed triggers are also different between  
 654 Double muon trigger and cross trigger so following L1T quality criteria has also been imposed.

- 655     •  $12 \geq \text{L1-muon quality} \leq 15$   
 656     •  $\text{L1 } \mu p_T \geq 20 \parallel \text{L1 } \mu p_T \geq 23$  (For Mu23 Leg of cross-trigger)  
 657     •  $\text{L1 } \mu p_T \geq 5 \parallel \text{L1 } \mu p_T \geq 7$  (For Mu12 Leg of cross-trigger)

658 The efficiencies of the cross-trigger legs are shown in Figure 67.

659 For electron legs of the cross-triggers, we used the efficiencies of legs of double electron triggers.

#### 660 5.5 DZ Trigger Efficiencies results

661 These efficiencies are simply the ratio between the events that passed the trigger with DZ se-  
 662 lection criteria and without DZ selection. The DZ trigger efficiencies are evaluated in two  
 663 different electron working points: MVA and tight electron identification. The results are shown  
 664 in Fig 68-Fig 73. The efficiencies in function of PU were applied according the Run period in  
 665 Table 35, 37 and 39. However, the DZ efficiencies were not applied for dielectron triggers in  
 666 2017 and 2018, and for Mu-EG in 2018, as the non DZ version of these trigger are unprescaled.  
 667 Moreover the 2017 DZ trigger efficiencies of Mu-EG were applied in function of the lepton  $p_T$ ,  
 668 as this DZ filter is  $p_T$  dependent. The applied efficiencies are summarized in Table 41- 45.

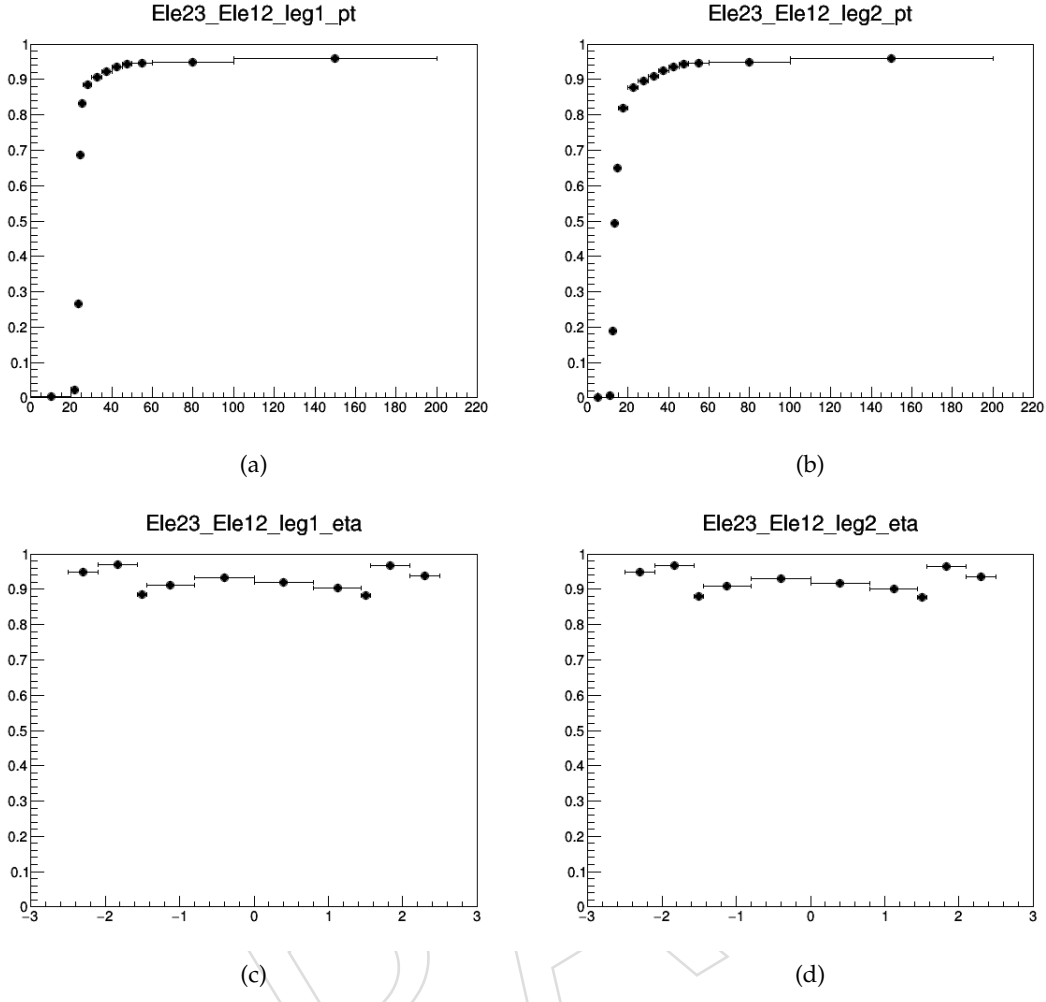


Figure 52: Trigger efficiency as a function of  $p_T$  (top) and  $\eta$  (bottom) for Leg1 (left) and Leg2 (right) of HLT\_Ele23\_Ele12\_CaloIdL\_TrackIdL\_IsoVL\_DZ\_v\*.

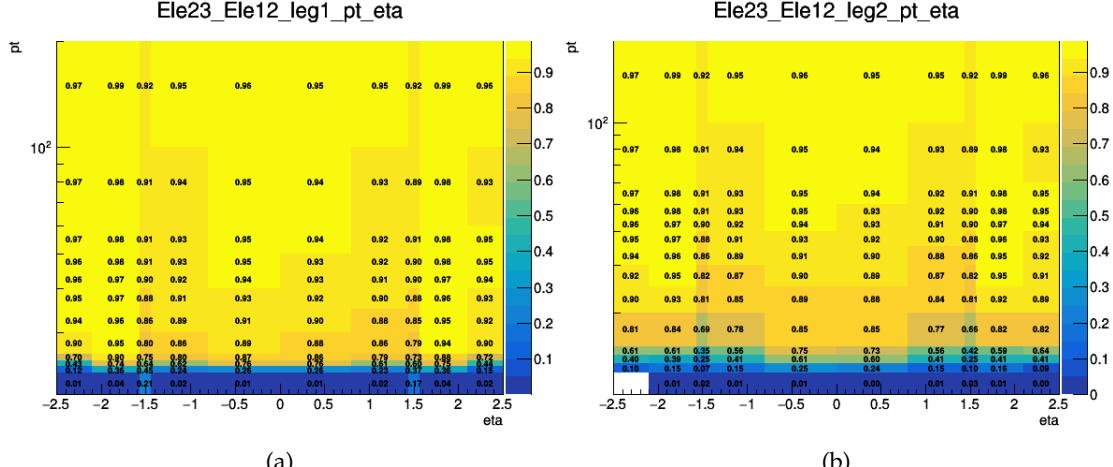


Figure 53: 2D plots (left) for leg1 (right) for leg2 for HLT\_Ele23\_Ele12\_CaloIdL\_TrackIdL\_IsoVL\_DZ\_v\*.

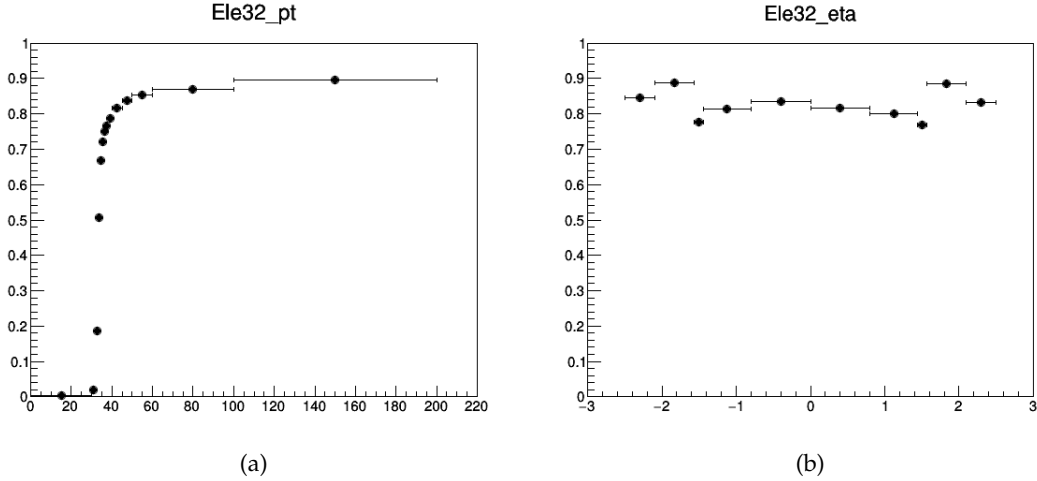


Figure 54: Trigger efficiency as a function of  $p_T$  (left) and  $\eta$  (right) for HLT\_Ele32\_WPTight\_Gsf\_v\*.

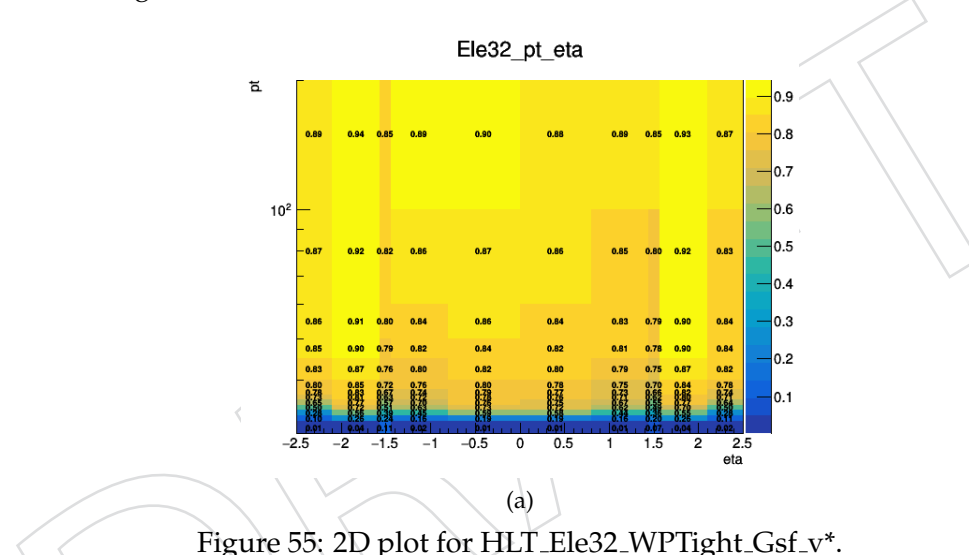


Figure 55: 2D plot for HLT\_Ele32\_WPTight\_Gsf\_v\*.

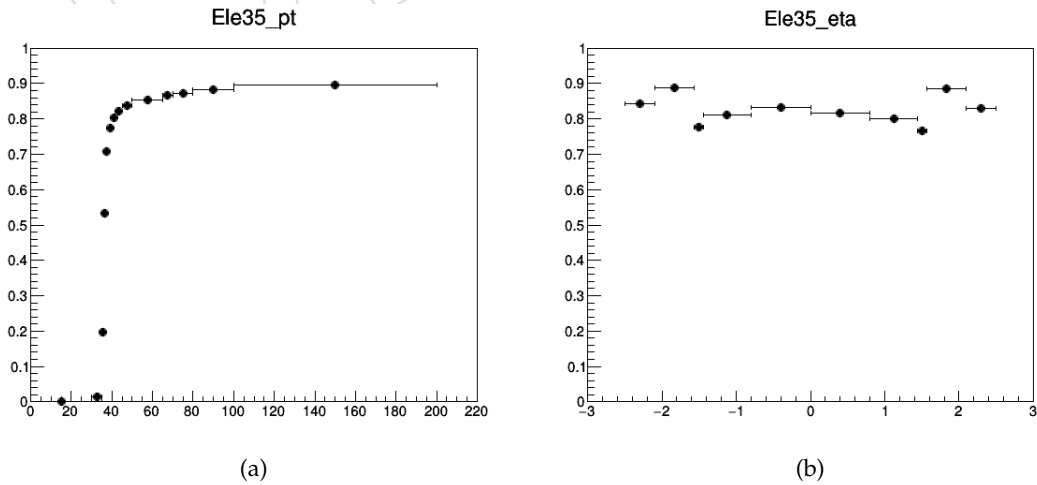


Figure 56: Trigger efficiency as a function of  $p_T$  (left) and  $\eta$  (right) for HLT\_Ele35\_WPTight\_Gsf\_v\*.

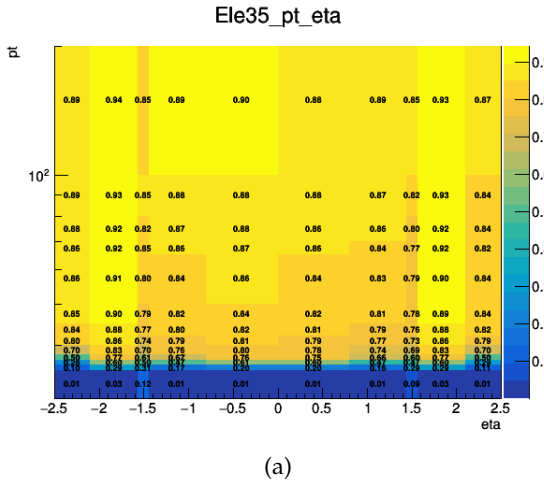


Figure 57: 2D plot for HLT\_Ele35\_WPTight\_Gsf\_v\*.

Table 41: 2016 DZ trigger efficiencies in function of PU

Trigger PU	Absolute value				
	0-20	20-30	30-40	40-50	50-100
DoubleEG (MVA e WP)	$0.9931 \pm 0.0003$	$0.9836 \pm 0.0008$	$0.968 \pm 0.004$	$0.97 \pm 0.02$	
DoubleEG (Tight e WP)	$0.9933 \pm 0.0003$	$0.9836 \pm 0.0009$	$0.966 \pm 0.004$	$0.94 \pm 0.03$	
DoubleMu	$0.9934 \pm 0.0006$	$0.9920 \pm 0.0009$	$0.988 \pm 0.003$	$0.98 \pm 0.01$	
EG-Mu (MVA e WP)	$0.961 \pm 0.001$	$0.947 \pm 0.002$	$0.922 \pm 0.007$	$0.87 \pm 0.05$	
EG-Mu (Tight e WP)	$0.961 \pm 0.001$	$0.947 \pm 0.002$	$0.922 \pm 0.007$	$0.87 \pm 0.05$	
Mu-EG (MVA e WP)	$0.9632 \pm 0.0009$	$0.948 \pm 0.002$	$0.930 \pm 0.007$	$0.91 \pm 0.04$	
Mu-EG (Tight e WP)	$0.9632 \pm 0.0009$	$0.948 \pm 0.002$	$0.930 \pm 0.006$	$0.91 \pm 0.04$	

## 5.6 Systematics

Two sources of systematics are considered :

- variation of tag  $p_T$ . Tag lepton  $p_T$  was varied by 5 GeV up and down and the variation in trigger efficiencies are measured.
- variation of Z mass window. Nominal window is 60 GeV to 120 GeV. The range was changed to 70 GeV to 110 GeV and then the efficiencies are measured.

The uncertainty coming out of these variations was added in quadrature with the statistical uncertainty.

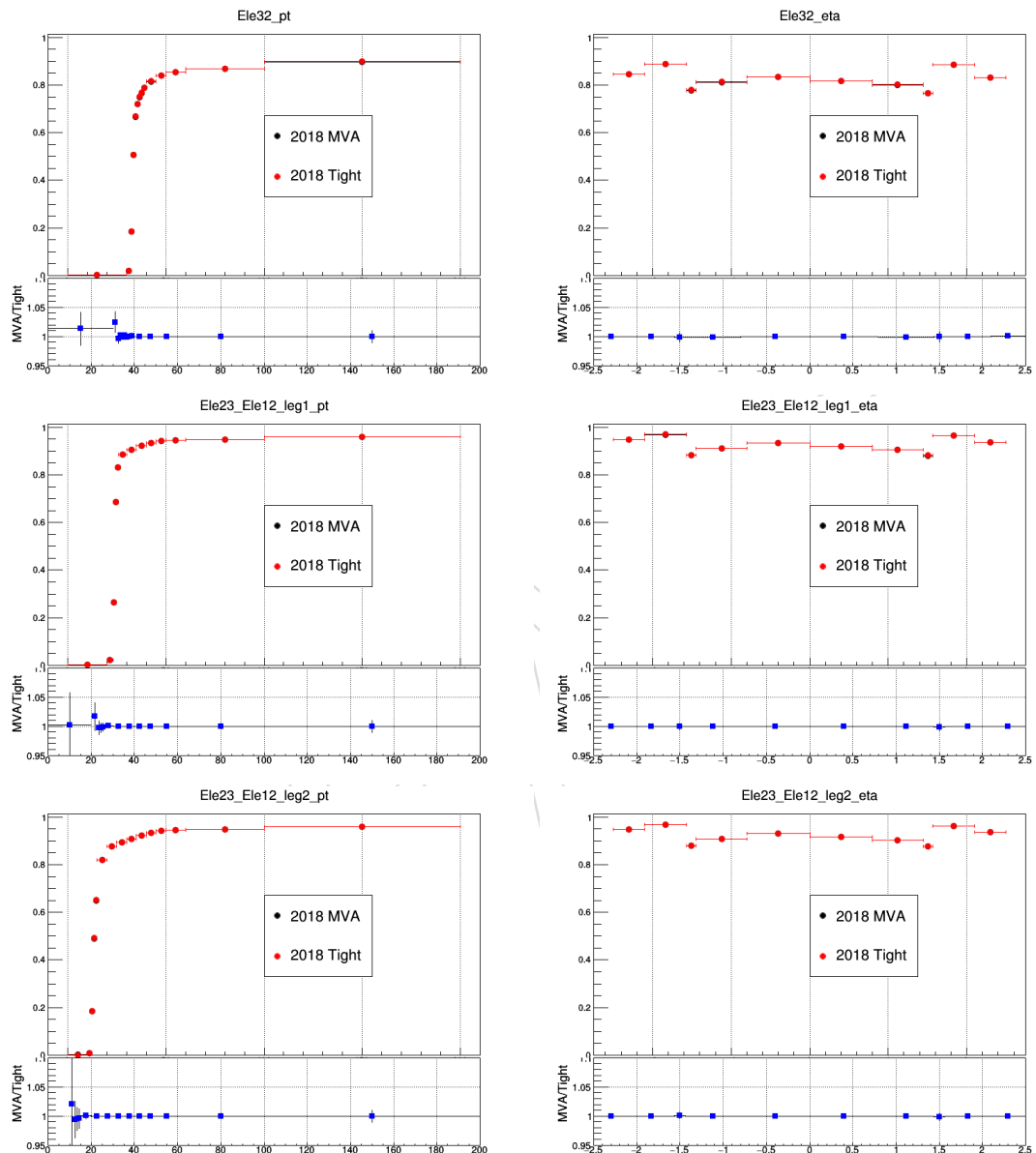


Figure 58: MVA vs Tight id comparison of trigger efficiency as a function of  $p_T$  (left) and  $\eta$  (right) for electron triggers for the run period 2018.

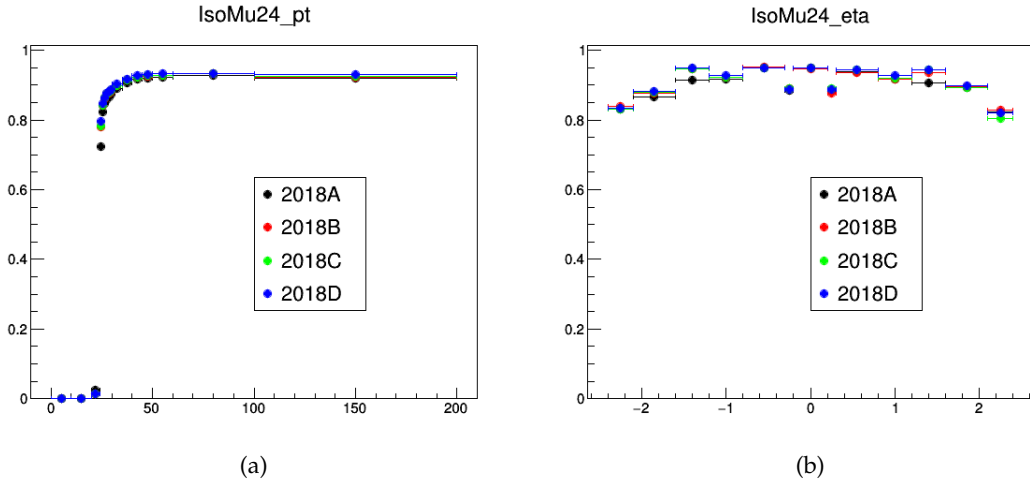


Figure 59: Trigger efficiency as a function of  $p_T$  (left) and  $\eta$  (right) for HLT\_IsoMu24\_v\*. Efficiencies are separated per data taking Era.

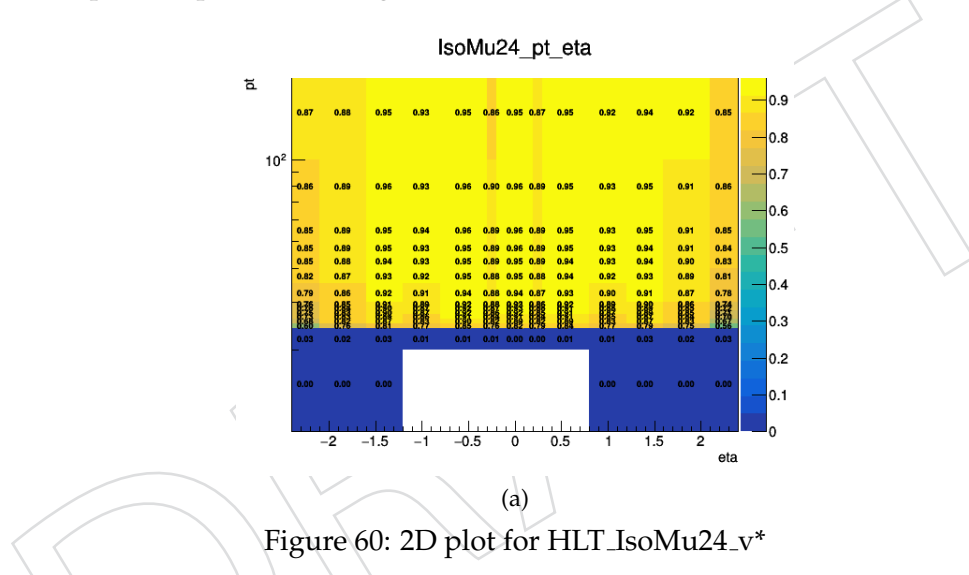


Figure 60: 2D plot for HLT\_IsoMu24\_v\*

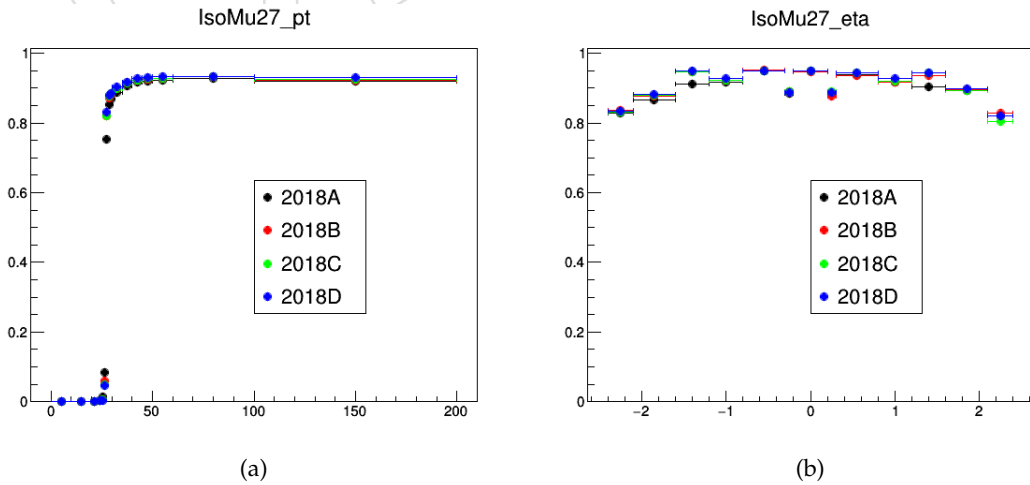
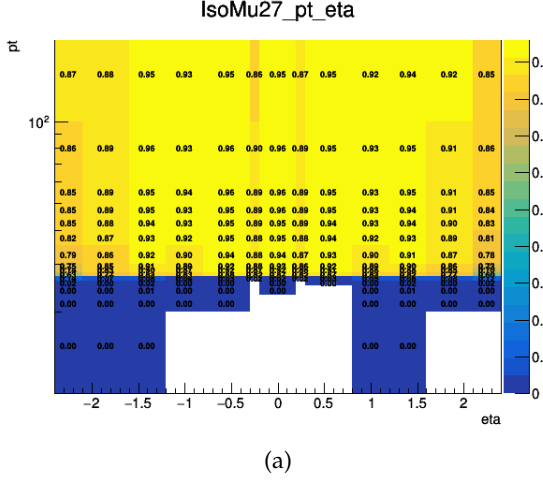
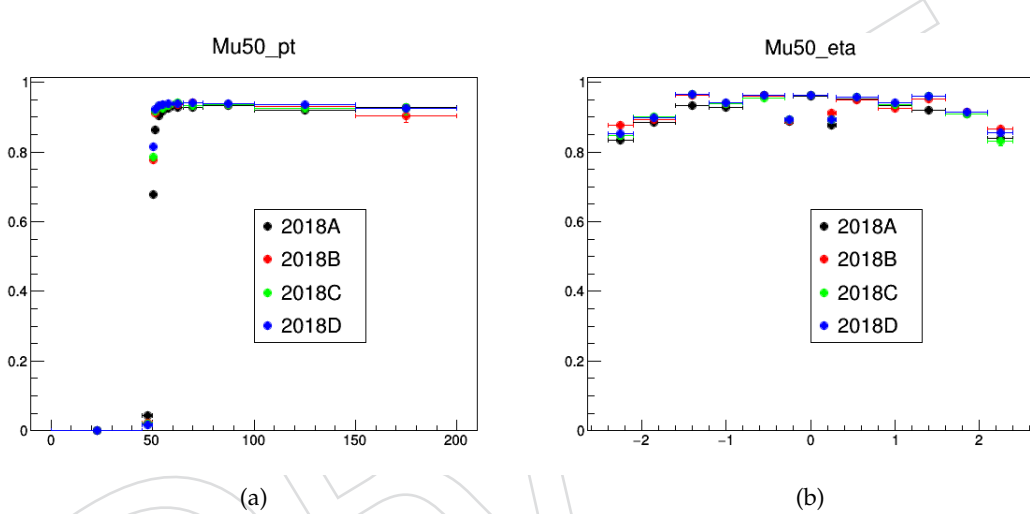
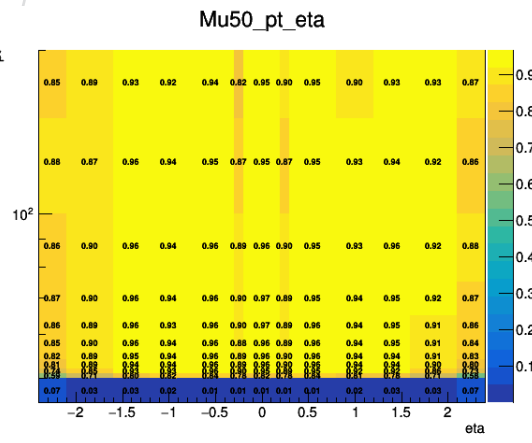


Figure 61: Trigger efficiency as a function of  $p_T$  (left) and  $\eta$  (right) for HLT\_IsoMu27\_v\*. Efficiencies are separated per data taking Era.



(a)

Figure 62: 2D plot for HLT\_IsoMu27\_v\*

Figure 63: Trigger efficiency as a function of  $p_T$  (left) and  $\eta$  (right) for HLT\_Mu50\_v\*. Efficiencies are separated per data taking Era.

(a)

Figure 64: 2D plot for HLT\_Mu50\_v\*

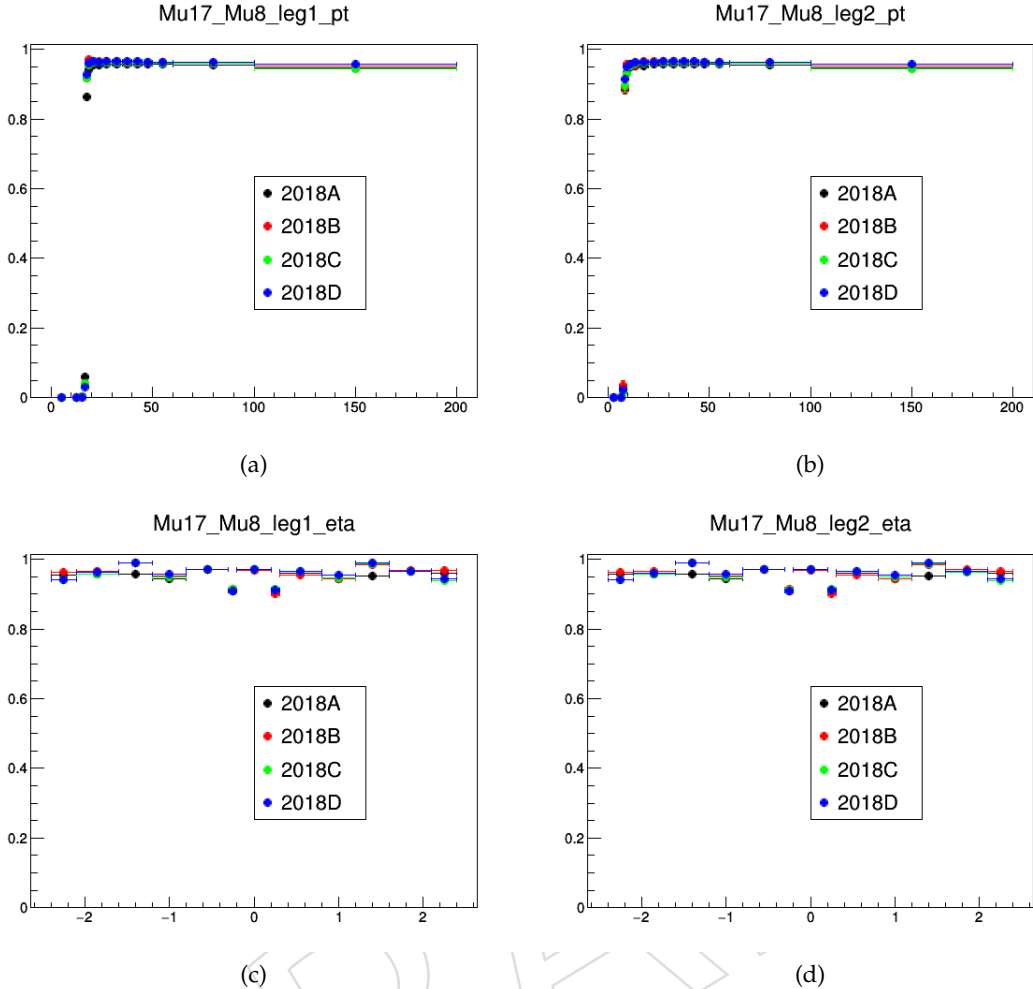


Figure 65: Trigger efficiency as a function of  $p_T$  (top) and  $\eta$  (bottom) for Leg1 (left) and Leg2 (right) of HLT\_Mu17\_TrkIsoVVL\_Mu8\_TrkIsoVVL\_DZ\_v\*. Efficiencies are separated per data taking Era.

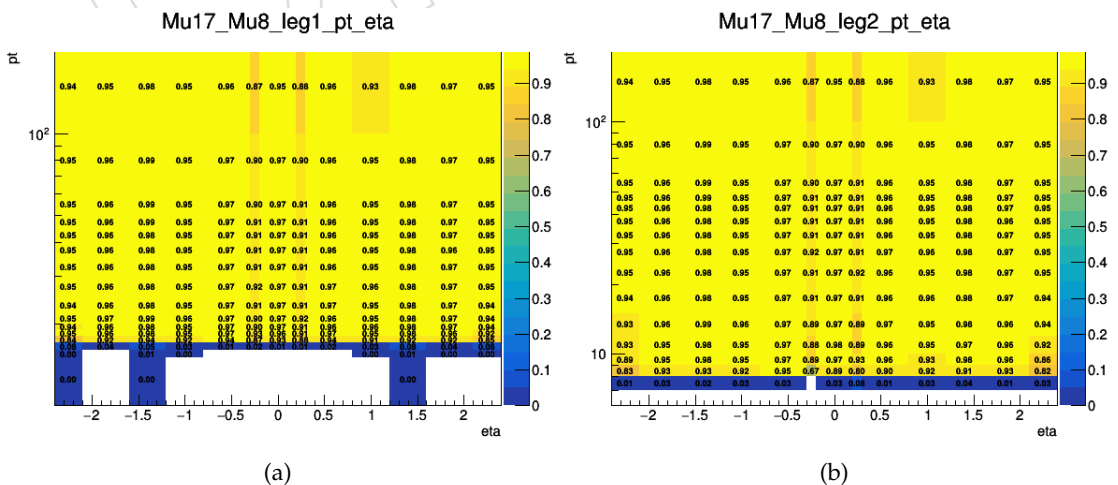


Figure 66: 2D plots for Leg1 (left) and Leg2 (right) of HLT\_Mu17\_TrkIsoVVL\_Mu8\_TrkIsoVVL\_DZ\_v\*.

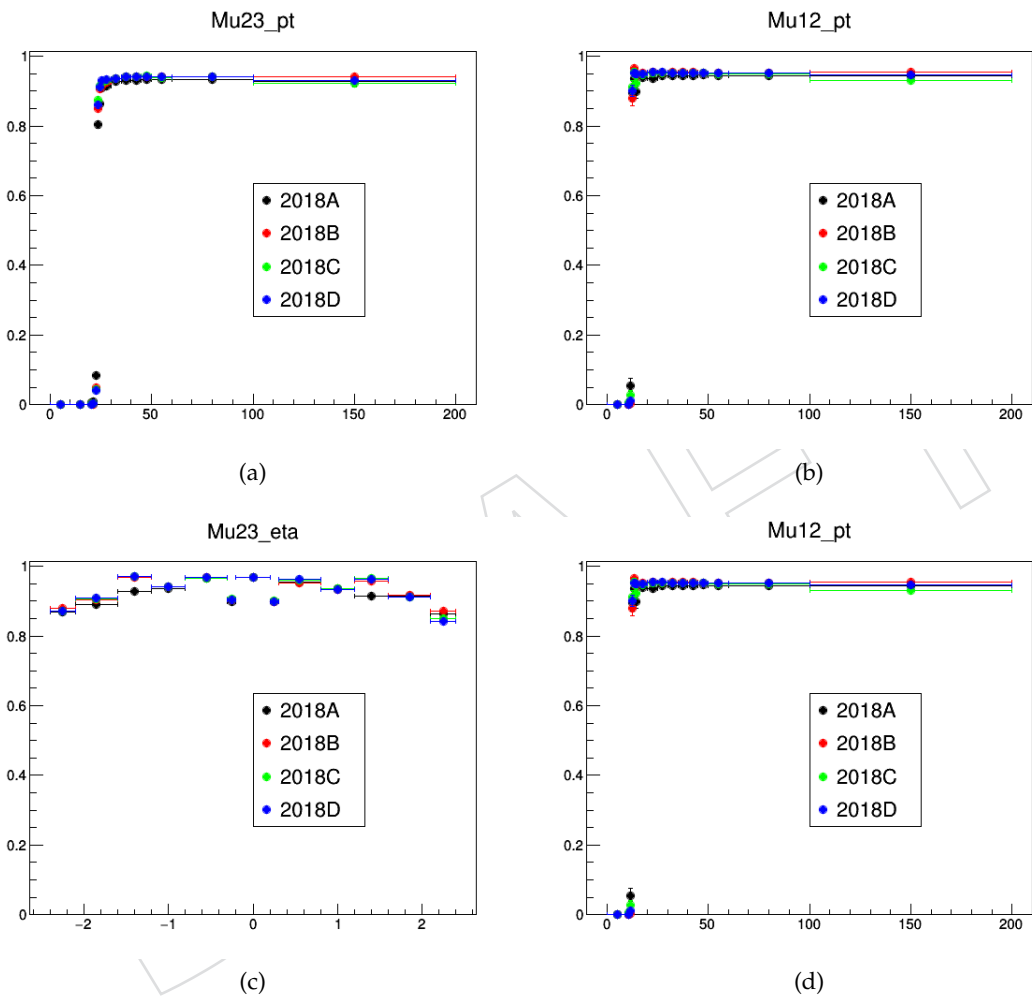


Figure 67: Trigger efficiency as a function of  $p_T$  (top) and  $\eta$  (bottom) for Muon legs of cross-triggers Mu23(left) and Mu12(right). Efficiencies are separated per data taking Era.

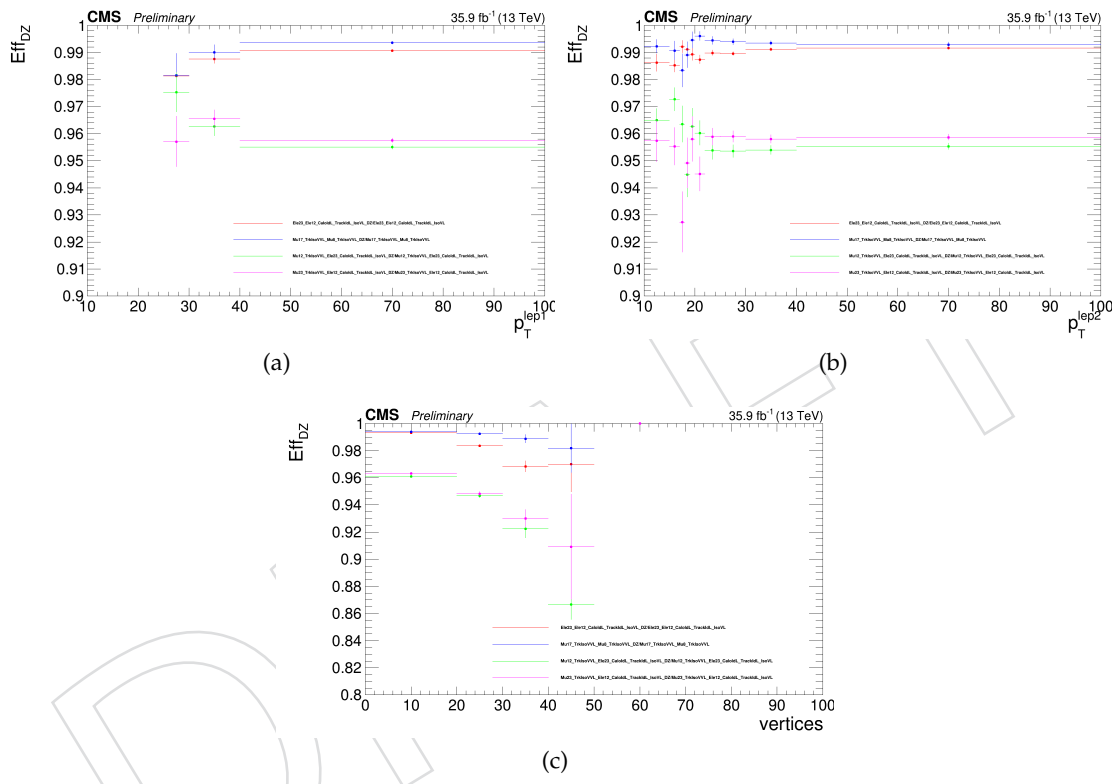


Figure 68: 2016 DZ trigger efficiencies for MVA electron working point in function of leading lepton  $p_T$  (left), trailing lepton  $p_T$  (right) and in function of number of primary vertices (bottom). In red for dielectron, in blue for dimuon, in green for EG-Mu and in pink Mu-EG triggers.

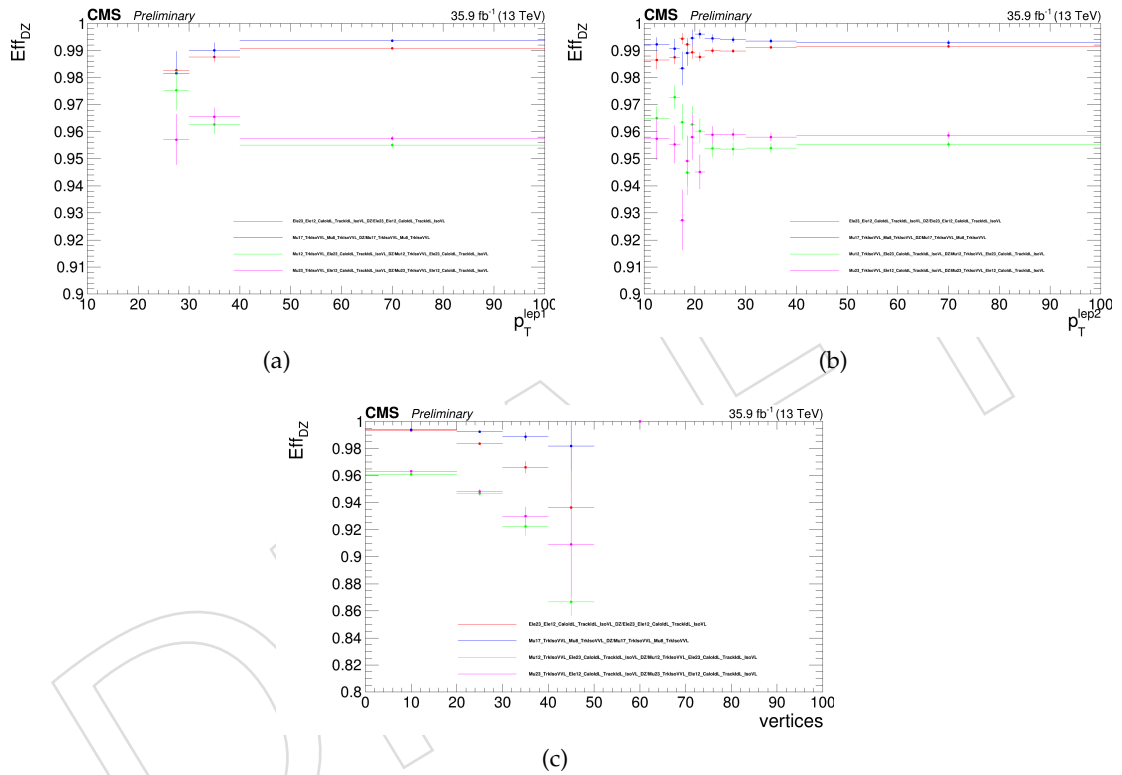


Figure 69: 2016 DZ trigger efficiencies for tight electron working point in function of leading lepton  $p_{\text{T}}$  (left), trailing lepton  $p_{\text{T}}$  (right) and in function of number of primary vertices (bottom). In red for dielectron, in blue for dimuon, in green for EG-Mu and in pink Mu-EG triggers.

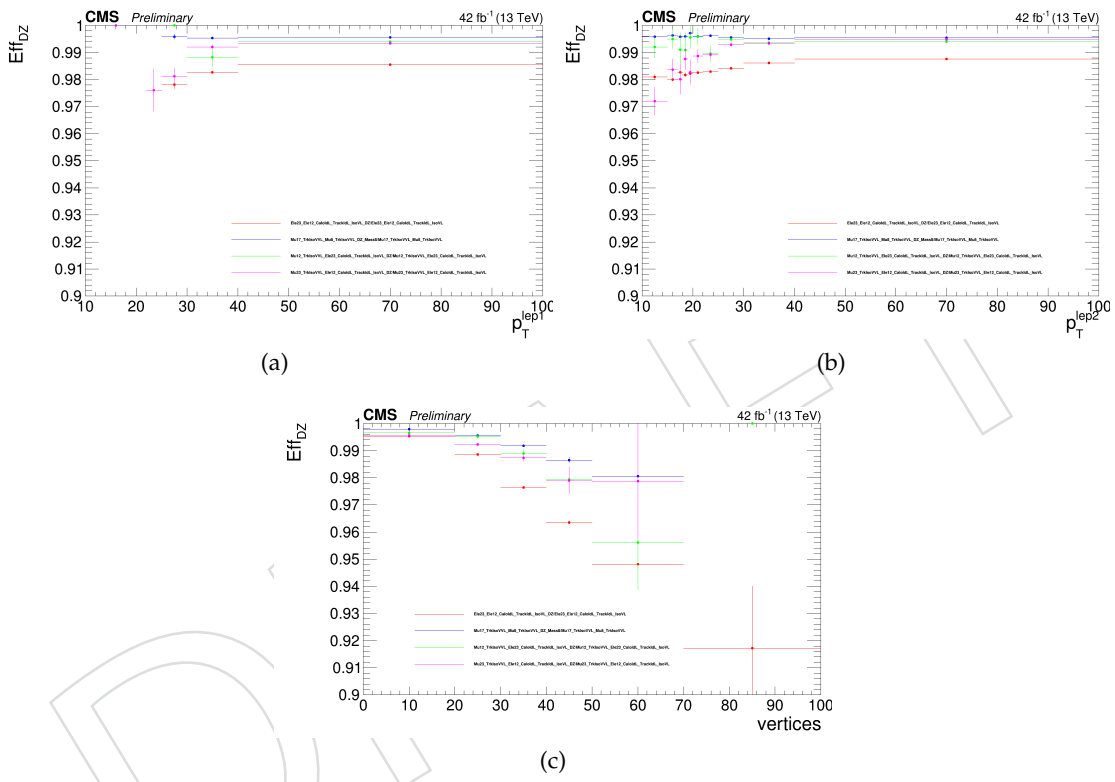


Figure 70: 2017 DZ trigger efficiencies for MVA electron working point in function of leading lepton  $p_{\text{T}}$  (left), trailing lepton  $p_{\text{T}}$  (right) and in function of number of primary vertices (bottom). In red for dielectron, in blue for dimuon, in green for EG-Mu and in pink Mu-EG triggers.

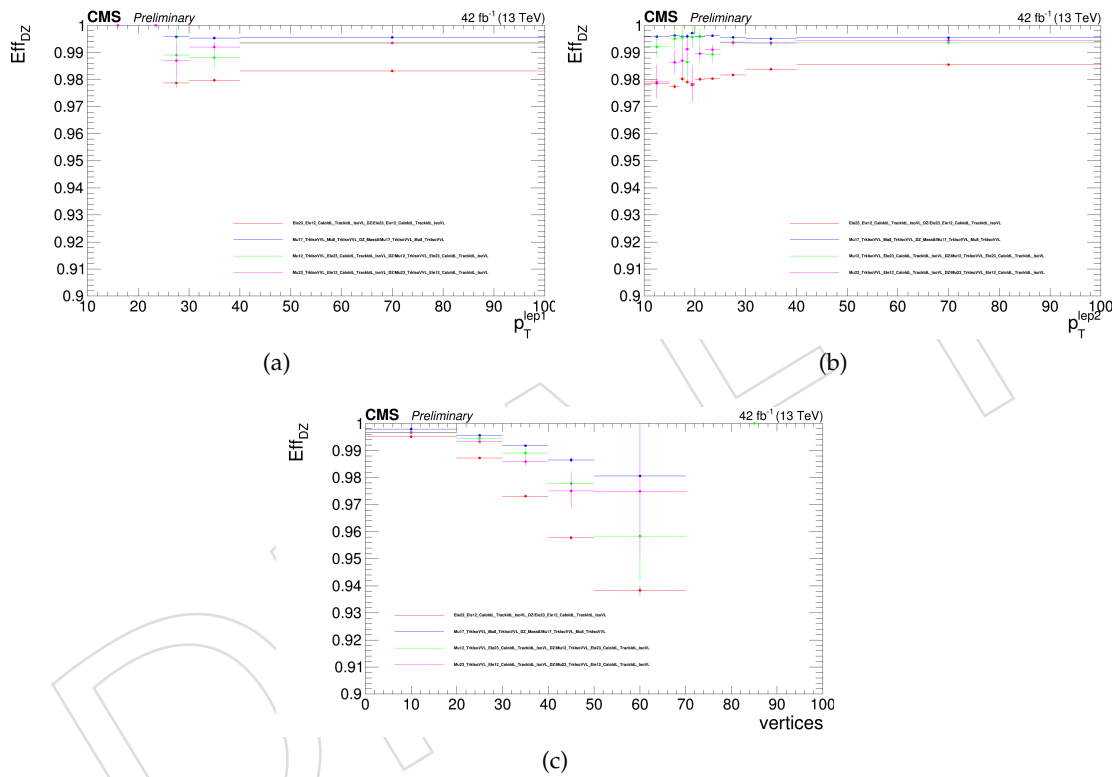


Figure 71: 2017 DZ trigger efficiencies for tight electron working point in function of leading lepton  $p_T$  (left), trailing lepton  $p_T$  (right) and in function of number of primary vertices (bottom). In red for dielectron, in blue for dimuon, in green for EG-Mu and in pink Mu-EG triggers.

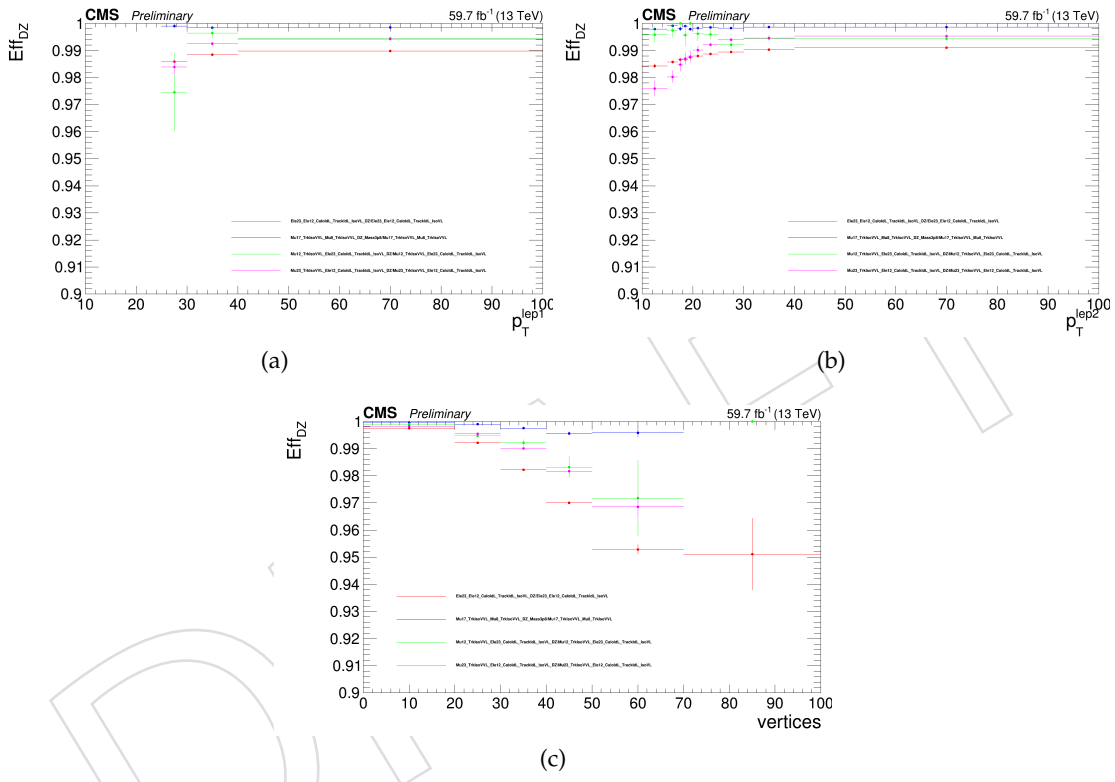


Figure 72: 2018 DZ trigger efficiencies for MVA electron working point in function of leading lepton  $p_{\text{T}}$  (left), trailing lepton  $p_{\text{T}}$  (right) and in function of number of primary vertices (bottom). In red for dielectron, in blue for dimuon, in green for EG-Mu and in pink Mu-EG triggers.

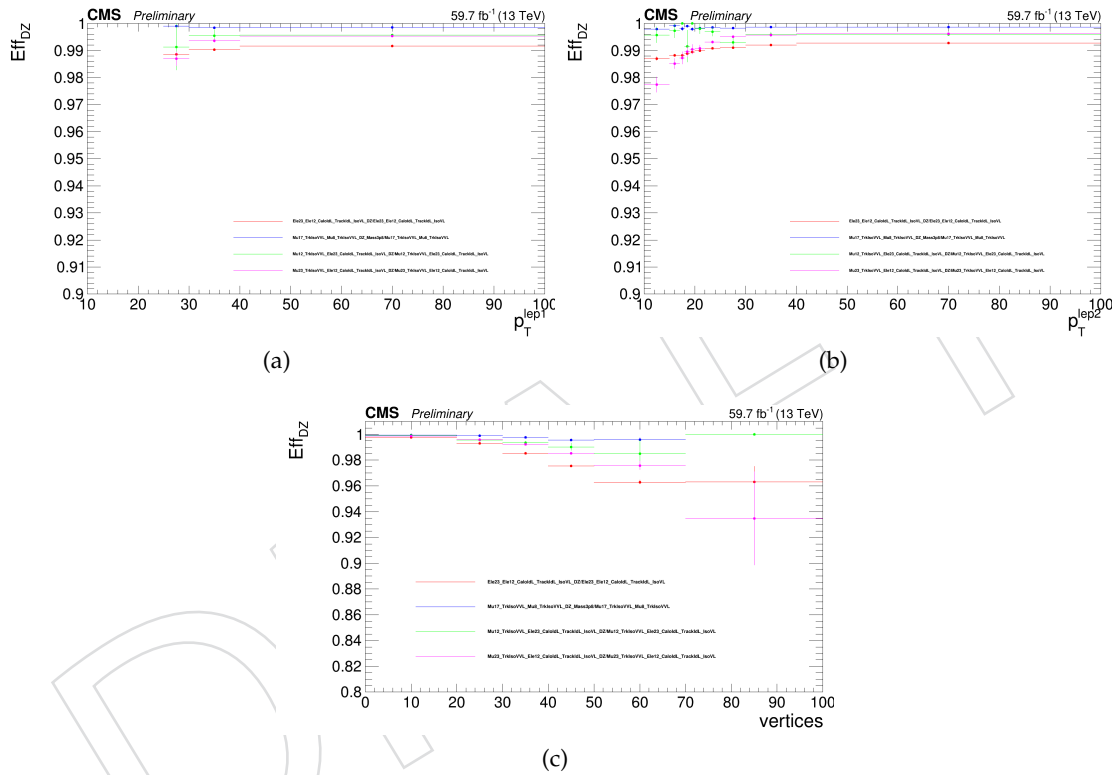


Figure 73: 2018 DZ trigger efficiencies for tight electron working point in function of leading lepton  $p_T$  (left), trailing lepton  $p_T$  (right) and in function of number of primary vertices (bottom). In red for dielectron, in blue for dimuon, in green for EG-Mu and in pink Mu-EG triggers.

Table 42: 2017 DZ trigger efficiencies in function of PU

PU	DoubleMuon	EG-Mu (MVA e WP)	EG-Mu (Tight e WP)
0-20	$0.99797 \pm 0.00003$	$0.9966 \pm 0.0007$	$0.9966 \pm 0.0007$
20-30	$0.99594 \pm 0.00005$	$0.9952 \pm 0.0007$	$0.9952 \pm 0.0007$
30-40	$0.9923 \pm 0.0001$	$0.989 \pm 0.002$	$0.989 \pm 0.002$
40-50	$0.9882 \pm 0.0003$	$0.979 \pm 0.005$	$0.979 \pm 0.005$
50-10	$0.983 \pm 0.001$	$0.96 \pm 0.02$	$0.96 \pm 0.02$

Table 43: 2017 DZ trigger efficiencies in function of PU for MuEG trigger with MVA electron identification

Trigger $p_T$	Absolute value				
	10-22	22-25	25-30	30-40	40-100
10-15	$0.93 \pm 0.04$	$0.96 \pm 0.03$	$0.96 \pm 0.02$	$0.96 \pm 0.02$	$0.980 \pm 0.005$
15-17	$0.93 \pm 0.04$	$0.96 \pm 0.03$	$0.97 \pm 0.02$	$0.97 \pm 0.01$	$0.990 \pm 0.004$
17-18	$0.93 \pm 0.04$	$0.97 \pm 0.03$	$0.99 \pm 0.01$	$0.98 \pm 0.01$	$0.980 \pm 0.007$
18-19	$0.93 \pm 0.04$	$0.97 \pm 0.03$	$0.97 \pm 0.02$	$0.98 \pm 0.01$	$0.994 \pm 0.004$
19-20	$0.93 \pm 0.04$	$0.97 \pm 0.03$	$0.95 \pm 0.02$	$0.98 \pm 0.01$	$0.983 \pm 0.006$
20-22	$0.93 \pm 0.04$	$0.99 \pm 0.01$	$0.97 \pm 0.01$	$0.997 \pm 0.003$	$0.989 \pm 0.003$
22-25		$0.99 \pm 0.01$	$0.986 \pm 0.005$	$0.990 \pm 0.003$	$0.989 \pm 0.002$
25-30			$0.989 \pm 0.004$	$0.993 \pm 0.001$	$0.9929 \pm 0.0009$
30-40				$0.993 \pm 0.001$	$0.9934 \pm 0.0006$
40-100					$0.9948 \pm 0.0004$

Table 44: 2017 DZ trigger efficiencies in function of PU for MuEG trigger with tight electron identification

Table 45: 2018 DZ trigger efficiencies in function of PU

PU	DoubleMuon	EG-Mu (MVA e WP)	EG-Mu (Tight e WP)
0-20	$0.99954 \pm 0.00003$	$0.9991 \pm 0.0004$	$0.9991 \pm 0.0004$
20-30	$0.99903 \pm 0.00004$	$0.9947 \pm 0.0008$	$0.9947 \pm 0.0008$
30-40	$0.99808 \pm 0.00007$	$0.992 \pm 0.001$	$0.992 \pm 0.001$
40-50	$0.9961 \pm 0.0002$	$0.983 \pm 0.004$	$0.983 \pm 0.004$
50-70	$0.9939 \pm 0.0007$	$0.97 \pm 0.01$	$0.97 \pm 0.01$
70-100	$0.994 \pm 0.009$	$0.97 \pm 0.01$	$0.97 \pm 0.01$

## 677 **6 Fake lepton background estimation**

678 Editors: J. Piedra, C. Prieels, I. Josa Mutuberria, A. Álvarez Fernández.

### 679 **6.1 Introduction**

680 The estimation of the fake leptons contribution in the  $H \rightarrow WW$  analysis, the  $WW$  cross section,  
681 and in the search for dark matter in the mono-Higgs channel, is presented. Lepton fake (and  
682 prompt) rates are estimated using a data-driven method, as a function of the lepton  $p_T$  and  $\eta$   
683 in a single lepton triggered sample. Closure tests of the method and systematic uncertainties  
684 associated are also presented.

685 In the dilepton +  $E_T^{\text{miss}}$  analysis, referred to in the following as the  $WW$  selection, the pri-  
686 mary source of background from lepton misidentification in the 0-jet bin category comes from  
687 misidentified  $W+jets$  events while in the 1- and 2-jets categories, semileptonic  $t\bar{t}$  decays are  
688 the main source of lepton misidentification background. QCD multijet and hadronic top back-  
689 grounds (both processes with two fake leptons) are present as well but at a much smaller level.  
690 Events in which  $W$  bosons are produced in association with jets give rise to background to  
691  $WW$  events when a jet is misidentified as a lepton. These events contain a real lepton and real  
692 missing energy from the  $W$  decay. With the jet misidentified as a lepton, the  $W+jets$  events  
693 have therefore two identified leptons, missing energy, and no other significant event charac-  
694 teristics and, as a result, the  $W+jets$  events cannot be readily suppressed by event selection.  
695 This background is particularly important at low  $p_T$  and is thus critical for the low mass Higgs  
696 analysis.

697 The estimation of the fake lepton contribution is based on the ‘fakeable object’ data-driven  
698 method, and provides a measurement of the yield and the kinematic distributions of the non-  
699 prompt background. It is a general technique, applicable to any physics analysis in which  
700 particle level selection criteria are used to suppress background. The method can be used with  
701 any number of final state particles and it is independent of the event selection. The fakeable  
702 object method follows the formulae described in [8, 9].

703 The fundamental idea of the fakeable object method is to select a control sample of events  
704 enriched in the background being estimated, and then use an extrapolation factor to relate  
705 these events to the background in the signal region. The method is data-driven since the control  
706 sample is selected in data, and the extrapolation factor is measured with data as well. For non-  
707 prompt leptons the extrapolation is done in the  $(p_T, \eta)$  phase space of the lepton. The control  
708 sample is defined using a looser lepton definition, chosen such that the rate of misidentification  
709 is increased. The extrapolation factor relates background misidentified with this criteria, to  
710 background misidentified as passing the full particle selection of the signal region.

### 711 **6.2 Lepton fake rate estimation in a dijet control region**

712 The method looks for leptons satisfying loose isolation and identification criteria, which will  
713 pass or fail the tighter lepton requirements of the  $WW$  selection. The ratio of tight over loose  
714 leptons is called the lepton fake rate,  $fr$ . This ratio can be determined from the abundantly  
715 produced QCD or other events as a function of the lepton kinematics. It is assumed that, once  
716 the lepton kinematics are taken into account, the same ‘universal’ fake ratios can be applied to  
717 the other backgrounds to extract the signal. The prompt ratio,  $pr$ , of tight-to-loose leptons for  
718 prompt leptons (usually ignored and assumed to be 1) is also computed and taken into account  
719 in this case.

720 A set of loosely selected lepton-like objects, referred to as the ‘fakeable object’ or ‘denominator’

721 from here on, is defined in a sample of events dominated by dijet (QCD) production.  
 722 To measure the fake rate we count how many fakeable objects pass the full lepton selection of  
 723 the analysis, parametrized as a function of the phase space of the fakeable lepton (bins of  $\eta$  and  
 724  $p_T$ ). The ratio of the fully identified lepton, referred as 'numerator', to the fakeable objects is  
 725 taken as the probability for a fakeable object to mimic a lepton:

$$fr = \frac{\text{number of fully reconstructed leptons}}{\text{number of fakeable objects}} \quad (6)$$

726 The tight (numerator) lepton definition follows the physics object definition of the WW analy-  
 727 sis. The loose (denominator) object definition has a significant impact on the systematic uncer-  
 728 tainty of the method, due to the fact that the sample dependence uncertainties for extrapolating  
 729 in different isolation and lepton quality criteria are typically different. The higher instantan-  
 730 eous luminosity delivered by the LHC leads to tighter selection requirements in the high level  
 731 trigger for electrons, thus limiting our choice of possible denominator object definitions. For  
 732 2016 analysis, we use the loose electron official cut-based Trigger Safe electron Id described in  
 733 Table 19, with the extra requirements of Table 19, with the tight electron definition being de-  
 734 scribed in Table 21. For 2017 and 2018 the loose and tight electron definitions are different, and  
 735 they are written in Table 24 and 27, respectively.

736 For the muons, the loose muon selection requirements differ from the tight selection only in a  
 737 less stringent cut on the relative isolation variable. The complete tight definition was written  
 738 in section 3.1.

- 739 •  $\text{PFrelIso04} < 0.4$  for the muon denominator,
- 740 •  $\text{PFrelIso04} < 0.15$  for the muon numerator .

### 741 6.2.1 Definition of the dijet control region

742 The QCD enriched sample is selected using the single lepton trigger paths listed in Table 46 Due  
 743 to the high instantaneous luminosity achieved by LHC during the Run II, these triggers are  
 744 heavily prescaled. The corresponding integrated luminosity for each of them is also detailed in  
 745 Table 46, along with their  $p_T$  range of application. For 2017 and 2018, we used the low trigger  
 746 path of 8 GeV instead of 12 GeV to avoid the turn-on effect , since we select electrons starting  
 747 from 13 GeV.

Table 46: Single lepton trigger paths used for selecting the enriched QCD sample.

Electron trigger paths	$\mathcal{L}_{\text{int}} [\text{fb}^{-1}]$		
	2016	2017	2018
HLT_Ele8_CaloIdL_TrkIdL_IsoVL_PFJet30 ( $p_T < 25 \text{ GeV}$ )	//	0.00397	0.00641
HLT_Ele12_CaloIdL_TrkIdL_IsoVL_PFJet30 ( $p_T < 25 \text{ GeV}$ )	0.01485	//	//
HLT_Ele23_CaloIdL_TrkIdL_IsoVL_PFJet30 ( $p_T \geq 25 \text{ GeV}$ )	0.06281	0.04347	0.03891
Muon trigger paths	$\mathcal{L}_{\text{int}} [\text{fb}^{-1}]$		
	2016	2017	2018
HLT_Mu8_TrkIsoVVL ( $p_T < 20 \text{ GeV}$ )	0.00780	0.00290	0.00856
HLT_Mu17_TrkIsoVVL ( $p_T \geq 20 \text{ GeV}$ )	0.21675	0.06594	0.04578

748 Events with loose leptons and jets are then selected. Lepton candidates are required to be well  
 749 separated from the highest- $E_T$  jet of the event, with  $\Delta R(\ell, j) > 1$ . Typical values for the jet  $E_T$

750 threshold are in the 25–35 GeV range, but the fake rate is calculated from 15 GeV to 45 GeV for  
 751 both electrons and muons.

The QCD enriched sample still may contain real leptons from W or Z leptonic decays that can bias the lepton fake rate. Leptons from W decays are removed by requiring the event to have Puppi  $E_T^{\text{miss}} < 20 \text{ GeV}$ . The transverse mass variable constructed with the lepton  $p_T$  and the  $E_T^{\text{miss}}$ ,

$$M_T = \sqrt{2 p_T^\ell E_T^{\text{miss}} (1 - \cos(\phi_\ell - \phi_{E_T^{\text{miss}}}))},$$

752 has to be lower than 20 GeV as well. The contamination from Z events is further reduced by  
 753 requiring one and only one lepton in the event.

### 754 6.2.2 Subtraction of the residual contamination from prompt leptons

755 After applying the selections described above, there is still contamination from prompt leptons  
 756 from EWK (W/Z+jets) events. To remove a possible bias in the full lepton selection sample  
 757 (numerator), and to a lesser extent in the denominator sample, the residual EWK contamination  
 758 is estimated from Monte Carlo samples. Using the expected cross section and the effective  
 759 luminosity of the lepton triggers listed in Table 46, the EWK contribution in the denominator  
 760 and numerator samples is subtracted before computing the fake rates.

761 The MC samples used in the following studies are listed in Table 47 (for the year 2016), Table 48  
 762 (for 2017) and Table 49 (for 2018). They are generated with Madgraph and MC@NLO.

Table 47: Simulated W/Z+jets samples used in the fake background studies (2016 MC).

Dataset name
DYJetsToLL_M-10to50-LO
DYJetsToLL_M-50_ext2
WJetsToLNu

762

Table 48: Simulated W/Z+jets samples used in the fake background studies (2017 MC).

Dataset name
DYJetsToLL_M-10to50-LO
DYJetsToLL_M-50
WJetsToLNu-LO

Table 49: Simulated W/Z+jets samples used in the fake background studies (2018 MC).

Dataset name
DYJetsToLL_M-10to50-LO
DYJetsToLL_M-50-LO
WJetsToLNu-LO

763 In Figure 74 we show the relative EWK contamination for the full identification lepton sample  
 764 and for the loose lepton sample for electrons, using a jet  $E_T$  threshold of 35 GeV. In Figure 75  
 765 we show the same relative EWK contamination for the muon numerator and denominator  
 766 samples, using this time a jet  $E_T$  threshold of 25 GeV. The correction is mainly important at  
 767 higher  $p_T$ , where the contribution of real leptons is larger, as expected.

768 In Figures 76 and 77 we show the comparison of the lepton fake rate estimation from data be-  
 769 fore and after removing the EWK contribution estimated from MC in  $p_T$  and  $\eta$  bins, both for

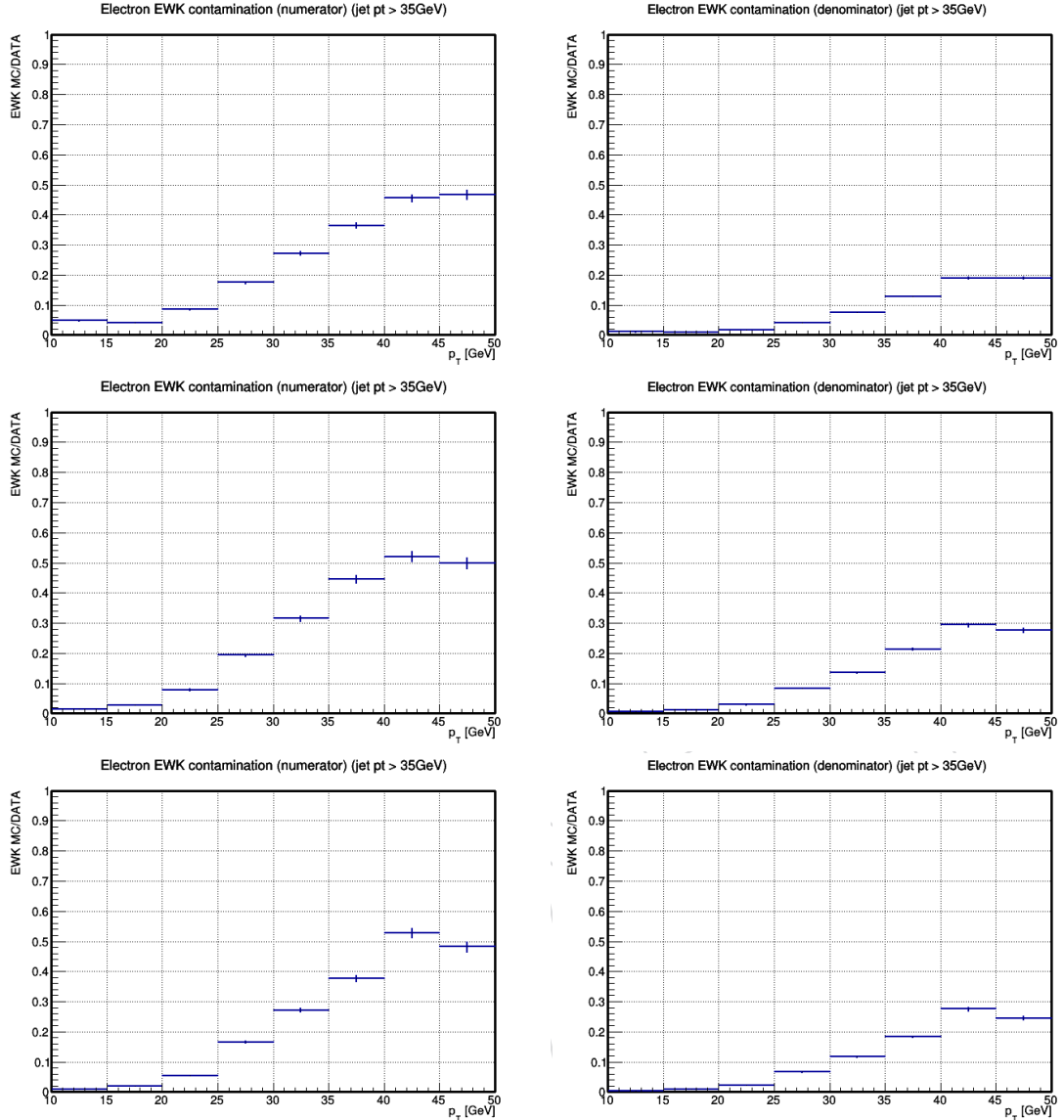


Figure 74: Relative EWK contamination for the full identification lepton sample (left) and for the loose sample (right) in  $p_T$  bins of the electron, from a control region sample obtained with a jet threshold of 35 GeV, and for the full Run II: 2016 (top), 2017 (middle) and 2018 (bottom).

770 electrons (jet  $E_T > 25\text{ GeV}$ ) and for muons (jet  $E_T > 25\text{ GeV}$ ). The subtraction has a significant  
 771 effect for about  $p_T > 20\text{ GeV}$ . These results have been obtained for 2016, 2017 and 2018 inde-  
 772 pendently. In Fig. 78 the results for the three years are drawn together. The jet  $E_T$  thresholds  
 773 for all the WW analysis jet categories are summarized in Table 50.

### 774 6.3 Lepton prompt rate estimation in a Z-enriched control region

775 The use of the prompt rate takes the real lepton contamination in the control sample into ac-  
 776 count. The prompt rate is measured using  $Z \rightarrow \ell\ell$  events from Monte Carlo simulation. The  
 777 prompt rates for both muons and electrons are shown in Figure 79.

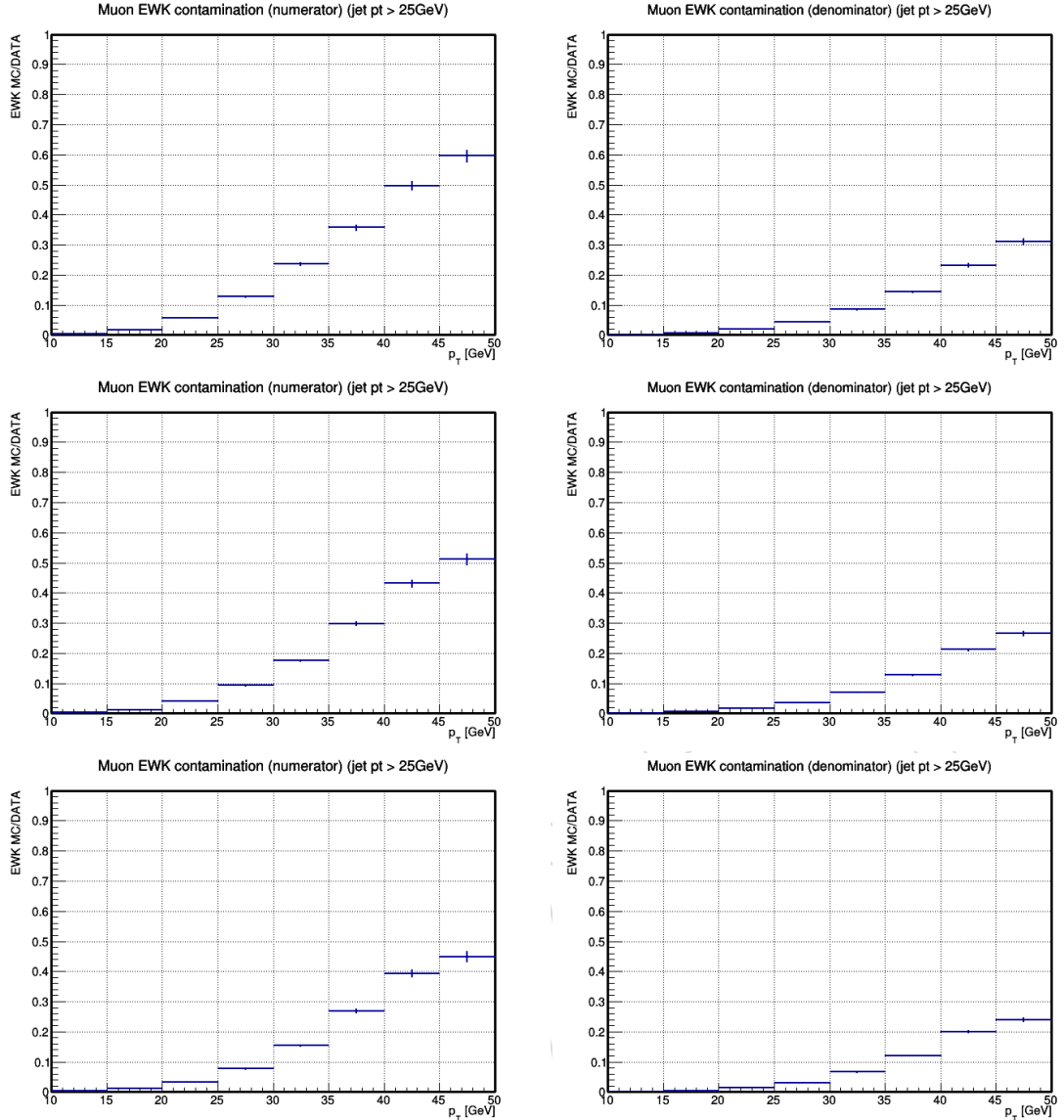


Figure 75: Relative EWK contamination for the full identification lepton sample (left) and for the loose sample (right) in  $p_T$  bins of the muon, from a control region sample obtained with a jet threshold of 25 GeV, and for the full Run II: 2016 (top), 2017 (middle) and 2018 (bottom).

#### 778 6.4 Data-driven validation of background modelling

779 The region obtained by reversing the opposite sign lepton requirement in the WW selection is  
 780 enriched with W+jets events where one of the jets is misidentified as a lepton. The fake rate  
 781 procedure can be applied to this same-sign control region as a data-driven closure test of the  
 782 method. The results of the closure test on same-sign events give reasonable agreement with  
 783 the expectations, as it is shown in Figures 80-83 (for the year 2016), Figures 84-87 (for 2017) and  
 784 Figures 88-91 (for 2018). The plots are divided in two categories, depending on whether or not  
 785 the second lepton  $p_T$  is greater than 20 GeV, since the low  $p_T$  region is also relevant for the  
 786 differential analysis and we want to study it separately.

Table 50: Leading jet  $E_T$  thresholds used for the fake rate determination, in the 0-, 1- and 2-jet categories.

	0-jet bin	1-jet bin	2-jet bin
electrons	35 GeV	35 GeV	35 GeV
muons	20 GeV	25 GeV	35 GeV

## 787 6.5 Flavour composition

788 The sources of fakes for electrons and muons are not the same. We estimate the fake rate using  
 789 a QCD-enriched control region, and if we look at the QCD MC events, the jet associated with  
 790 the fakeable object has a different flavour distribution depending on the lepton. The majority  
 791 of the jets associated with muons come from b quarks, whereas for electrons there are more  
 792 associated jets coming from light quarks and gluons (Fig. 92).

793 We expect that the estimation of the fake rate depends on the associated jet flavour composition,  
 794 and for electrons that will change significantly depending on the selection that we use. Since  
 795 we want to estimate the W+jets contribution using fake rates obtained with QCD, we need to  
 796 look at the flavour distribution in a W+jets control region and check if it is similar to the QCD  
 797 one. We compare the jets associated with electrons, since for muons the b quarks are always  
 798 the main contribution. For the W+jets control region we select events with one tight lepton,  
 799 missing transverse energy and a second lepton that is associated with a jet, using MC truth.  
 800 The result is in Fig. 93(a).

801 Aside from that, it is useful to see if using Z+jets MC events we would obtain a similar jet  
 802 flavour distribution, so we will also use DY MC. For the Z+jets region, three leptons are needed.  
 803 Two of them must be tight, have the same flavour, opposite sign, and a reconstructed mass  
 804 close to the Z mass. The third lepton (an electron) is the fakeable object, close to the jet whose  
 805 flavour we want to obtain. The flavour distribution of the Z+jets control region is in Fig. 93(b).  
 806 The QCD flavour distribution has also been drawn in Fig. 93(c) for comparison.

807 What we can see in Fig. 93 is that there are more b quarks for Z+jets and more c quarks for  
 808 W+jets, so they are not that similar. The distributions when the lepton is tight have a lesser  
 809 light quark component for both cases. In Fig. 94 all of the control regions are represented in the  
 810 same plot, showing the flavour distribution of the jets associated to the loose electrons.

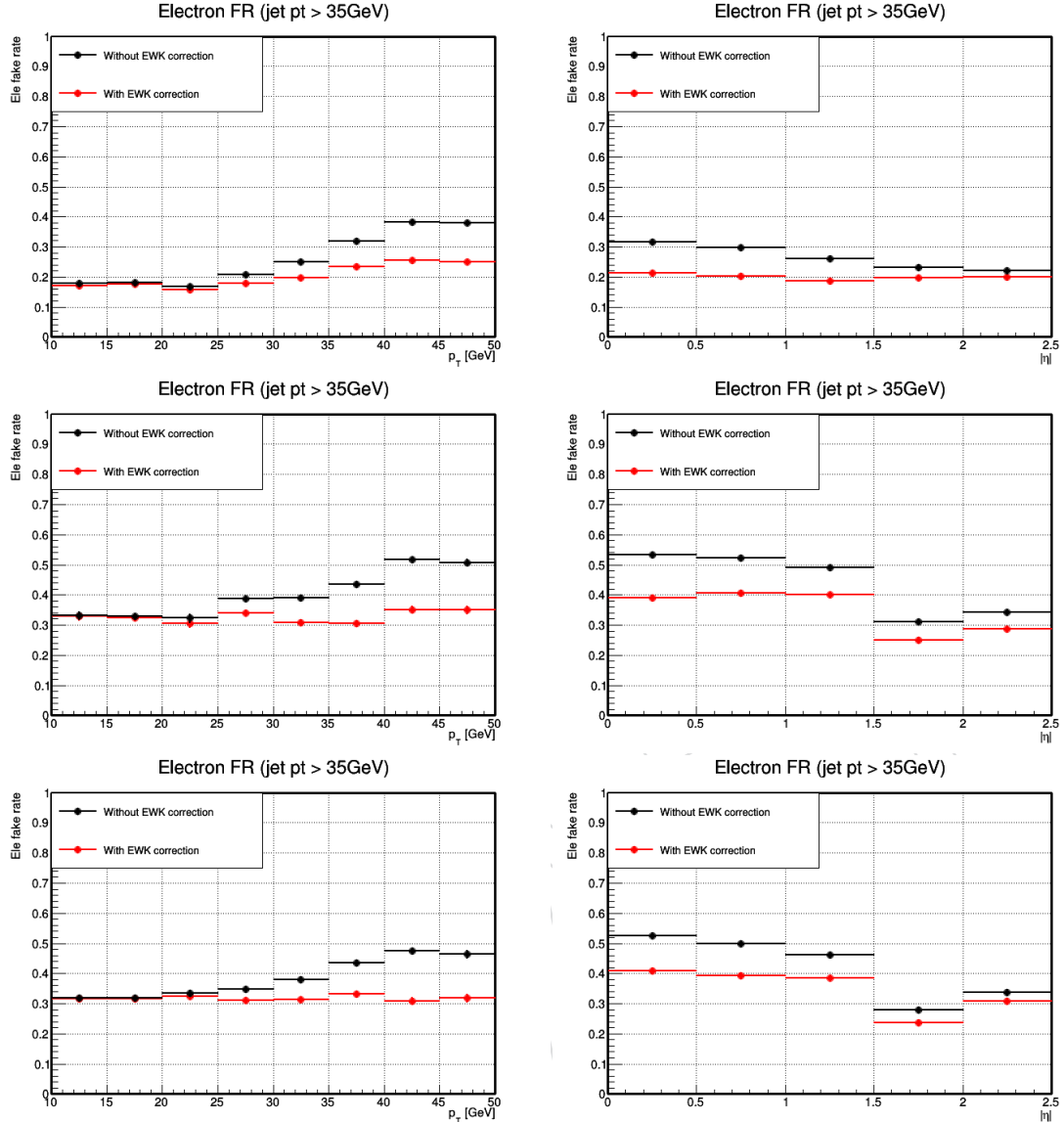


Figure 76: Electron fake rate as a function of the loose lepton  $p_T$  (left) and  $\eta$  (right), before and after EWK correction (in black and red, respectively), from a control region sample obtained with a jet threshold of 35 GeV, and for the full Run II: 2016 (top), 2017 (middle) and 2018 (bottom).

## 6.6 Systematic uncertainties

When extrapolating from reconstructed jets there are two relevant energy scales: the energy of the jet and the energy of the misidentified lepton. A jet with a given energy can be misidentified as lepton with a different energy. For example, 100 GeV jets can be misidentified as 20 GeV electrons, or they can be misidentified as 100 GeV electrons. In general, the rate at which jets are misidentified as leptons depends on both the energy of the initial jet and the energy of the lepton it is misidentified as. The problem with this naive method is that the systematic uncertainty associated with the extrapolation from reconstructed jet to misidentified lepton is large. There are light-quark jets, gluon jets, heavy-flavor jets, etc. Each of these different jet types is expected to have a different fake rate. The fake rate is measured in a control sample with a particular mix of jet types and is only applicable for that specific mixture. For example,

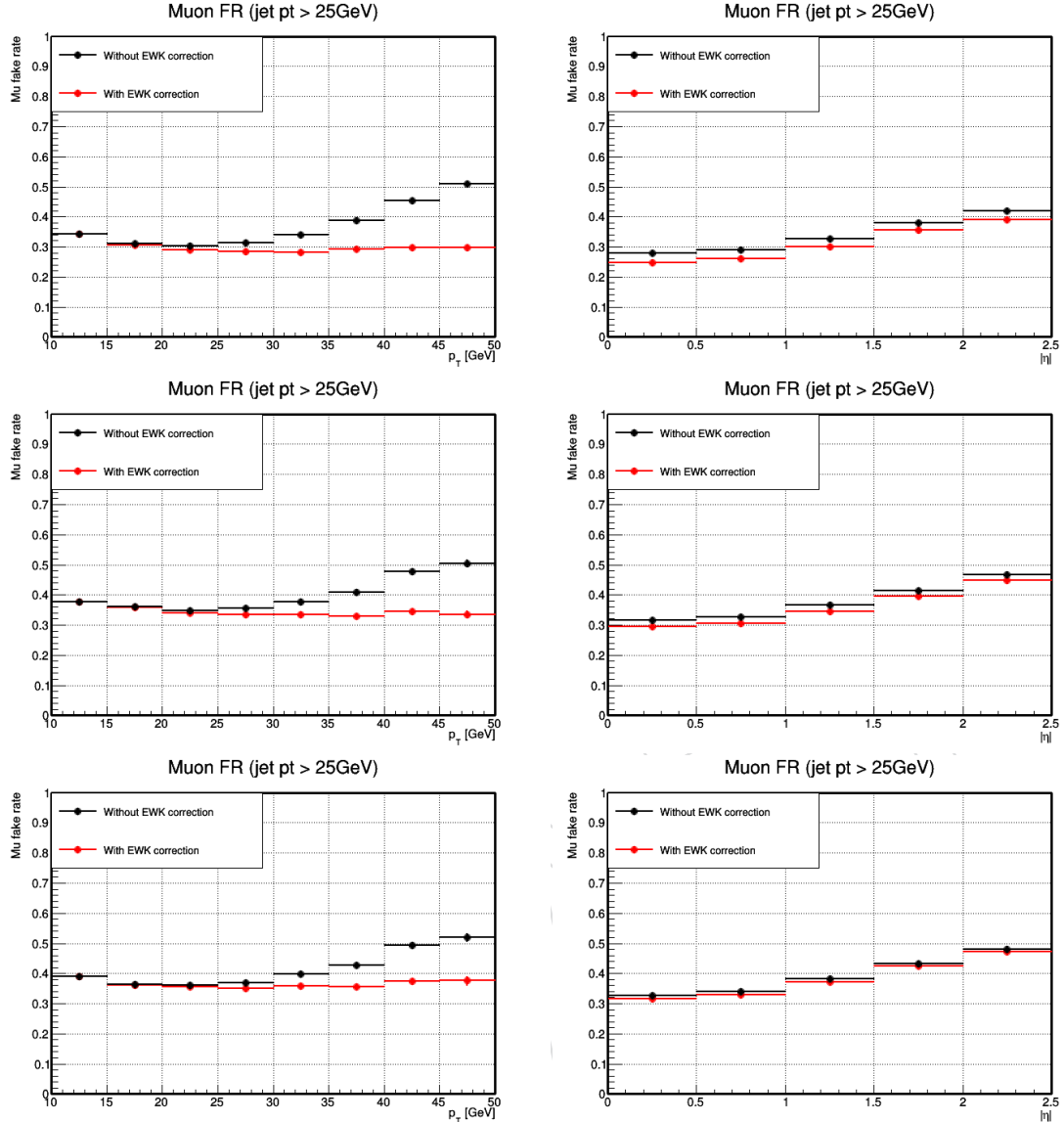


Figure 77: Muon fake rate as a function of the loose lepton  $p_T$  (left) and  $\eta$  (right), before and after EWK correction (in black and red, respectively), from a control region sample obtained with a jet threshold of 25 GeV, and for the full Run II: 2016 (top), 2017 (middle) and 2018 (bottom).

dijet events are dominated by gluon jets. However, the jets in W+jets events tend to be quark-initiated jets.

Several sources can be taken into account for the systematics. The first one is computed by moving the recoiling jet energy by 10 GeV up and down with respect to the nominal value. In case of the 0-jet bin, the nominal values are 20 GeV for muons and 35 GeV for electrons. In the 1-jet bin, since the top contribution starts to be important, and hence we will have more fake contribution from b-quark jets, the nominal values are 25 GeV for muons and 35 GeV for electrons. For the 2-jet bin the nominal values are 35 GeV both for muons and electrons. We estimate the systematics by calculating the fake lepton contribution in a region enriched in WW events. These are the selection criteria we use:

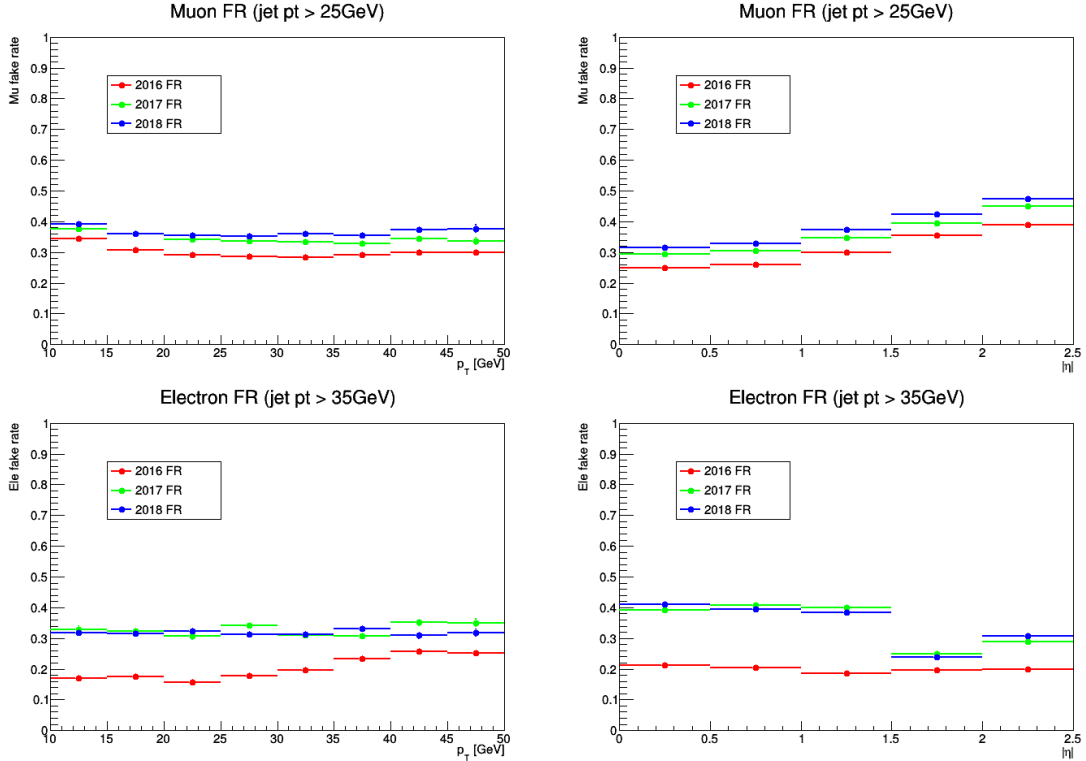


Figure 78: Muon fake rate (top) and electron fake rate (bottom) as a function of the loose lepton  $p_T$  (left) and  $\eta$  (right), obtained for the full Run II.

- Two leptons with opposite sign and same flavour,
- Highest  $p_T$  lepton with  $p_T > 25$  GeV and  $|\eta| < 2.5$ ,
- Second highest  $p_T$  lepton with  $p_T > 20$  GeV and  $|\eta| < 2.5$ ,
- No additional leptons with  $p_T < 10$  GeV,
- MET  $> 20$  GeV,
- $m_{ll} > 20$  GeV,
- $p_{Tll} > 30$  GeV,
- bVeto (no jet with  $p_T > 20$  GeV,  $|\eta| < 2.5$  and  $btagDeepB > 0.1522$ ),
- 0,1 or 2 jets with  $p_T > 30$  GeV for the 0-1- or 2-jet bins,

With this selection we obtain the fake lepton contribution that is summarised in Tables 51-53, with the nominal jet energy thresholds and the up and down variations, adding or subtracting 10 GeV to the nominal value. We move the thresholds independently for electrons and muons. The fake lepton contribution computed with the fake rates varied by their statistical uncertainties is also shown on the table. Using the results of Tables 51-53, the uncertainties are calculated and shown in Tables 54-56.

The total uncertainty in the  $e\mu$  channel does not cover the discrepancies shown in the SS control region. From the same-sign control region we consider a 30% flat error to cover all the uncertainties.

Table 51: Non-prompt leptons data-driven estimation for 2016, (coming from W+jets and QCD events) at WW selection cuts in the  $e\mu$  channel for the 0-,1- and 2-jet categories, showing the up and down jet energy threshold variations, and the statistical error of the lepton fake rate. Errors are statistical only.

	$e\mu$ 0-jet bin	$e\mu$ 1-jet bin	$e\mu$ 2-jet bin
Nominal	$1148 \pm 27$	$769 \pm 24$	$318 \pm 15$
Electron jet $E_T$ up	$1057 \pm 25$	$714 \pm 22$	$295 \pm 14$
Electron jet $E_T$ down	$1185 \pm 27$	$787 \pm 24$	$324 \pm 15$
Electron statistical error up	$1208 \pm 28$	$804 \pm 25$	$334 \pm 16$
Electron statistical error down	$1091 \pm 26$	$736 \pm 23$	$303 \pm 14$
Muon jet $E_T$ up	$1088 \pm 25$	$724 \pm 22$	$298 \pm 14$
Muon jet $E_T$ down	$1168 \pm 28$	$795 \pm 25$	$339 \pm 16$
Muon statistical error up	$1164 \pm 27$	$784 \pm 24$	$326 \pm 15$
Muon statistical error down	$1133 \pm 26$	$754 \pm 23$	$310 \pm 15$

Table 52: Non-prompt leptons data-driven estimation for 2017, (coming from W+jets and QCD events) at WW selection cuts in the  $e\mu$  channel for the 0-,1- and 2-jet categories, showing the up and down jet energy threshold variations, and the statistical error of the lepton fake rate. Errors are statistical only.

	$e\mu$ 0-jet bin	$e\mu$ 1-jet bin	$e\mu$ 2-jet bin
Nominal	$2385 \pm 52$	$2095 \pm 50$	$1032 \pm 35$
Electron jet $E_T$ up	$2433 \pm 53$	$2117 \pm 52$	$1041 \pm 36$
Electron jet $E_T$ down	$2348 \pm 51$	$2069 \pm 49$	$1023 \pm 34$
Electron statistical error up	$2639 \pm 59$	$2303 \pm 57$	$1132 \pm 40$
Electron statistical error down	$2168 \pm 47$	$1918 \pm 45$	$948 \pm 31$
Muon jet $E_T$ up	$2275 \pm 49$	$1993 \pm 47$	$970 \pm 33$
Muon jet $E_T$ down	$2420 \pm 53$	$2170 \pm 52$	$1092 \pm 37$
Muon statistical error up	$2444 \pm 53$	$2161 \pm 52$	$1073 \pm 36$
Muon statistical error down	$2329 \pm 50$	$2033 \pm 49$	$994 \pm 33$

Table 53: Non-prompt leptons data-driven estimation for 2018, (coming from W+jets and QCD events) at WW selection cuts in the  $e\mu$  channel for the 0-,1- and 2-jet categories, showing the up and down jet energy threshold variations, and the statistical error of the lepton fake rate. Errors are statistical only.

	$e\mu$ 0-jet bin	$e\mu$ 1-jet bin	$e\mu$ 2-jet bin
Nominal	$3710 \pm 77$	$3006 \pm 74$	$1314 \pm 57$
Electron jet $E_T$ up	$3782 \pm 80$	$3097 \pm 78$	$1350 \pm 53$
Electron jet $E_T$ down	$3655 \pm 75$	$2957 \pm 72$	$1292 \pm 49$
Electron statistical error up	$4097 \pm 89$	$3321 \pm 87$	$1453 \pm 60$
Electron statistical error down	$3392 \pm 68$	$2752 \pm 65$	$1206 \pm 43$
Muon jet $E_T$ up	$3502 \pm 72$	$2862 \pm 70$	$1234 \pm 48$
Muon jet $E_T$ down	$3772 \pm 78$	$3117 \pm 77$	$1394 \pm 53$
Muon statistical error up	$3811 \pm 79$	$3110 \pm 77$	$1376 \pm 52$
Muon statistical error down	$3617 \pm 74$	$2911 \pm 72$	$1258 \pm 49$

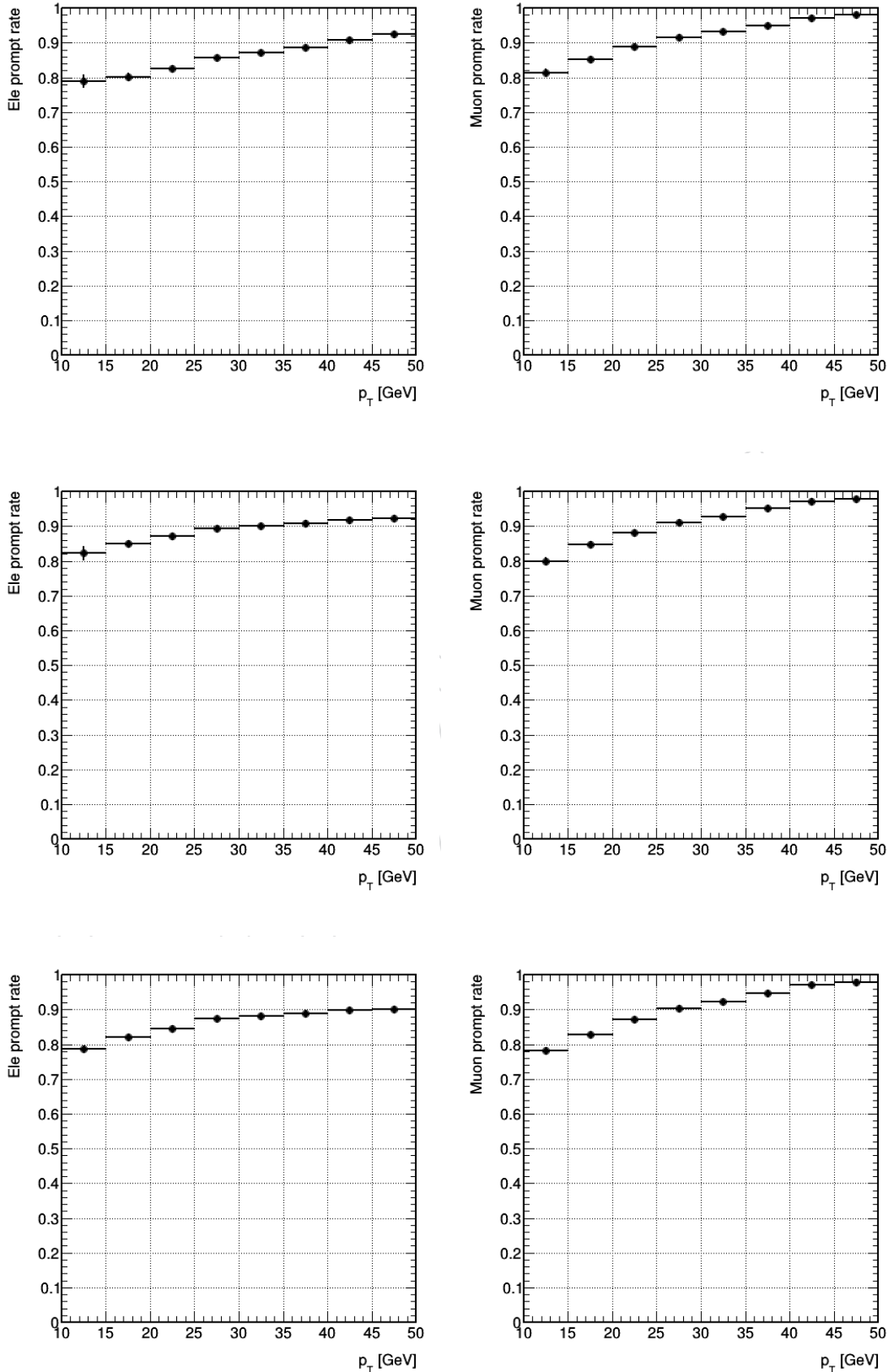


Figure 79: Prompt rate for electrons (left) and muons (right) in  $p_T$  bins, both estimated in Z+jets simulation for the full Run II: 2016 (top), 2017 (middle) and 2018 (bottom). Errors are statistical only.

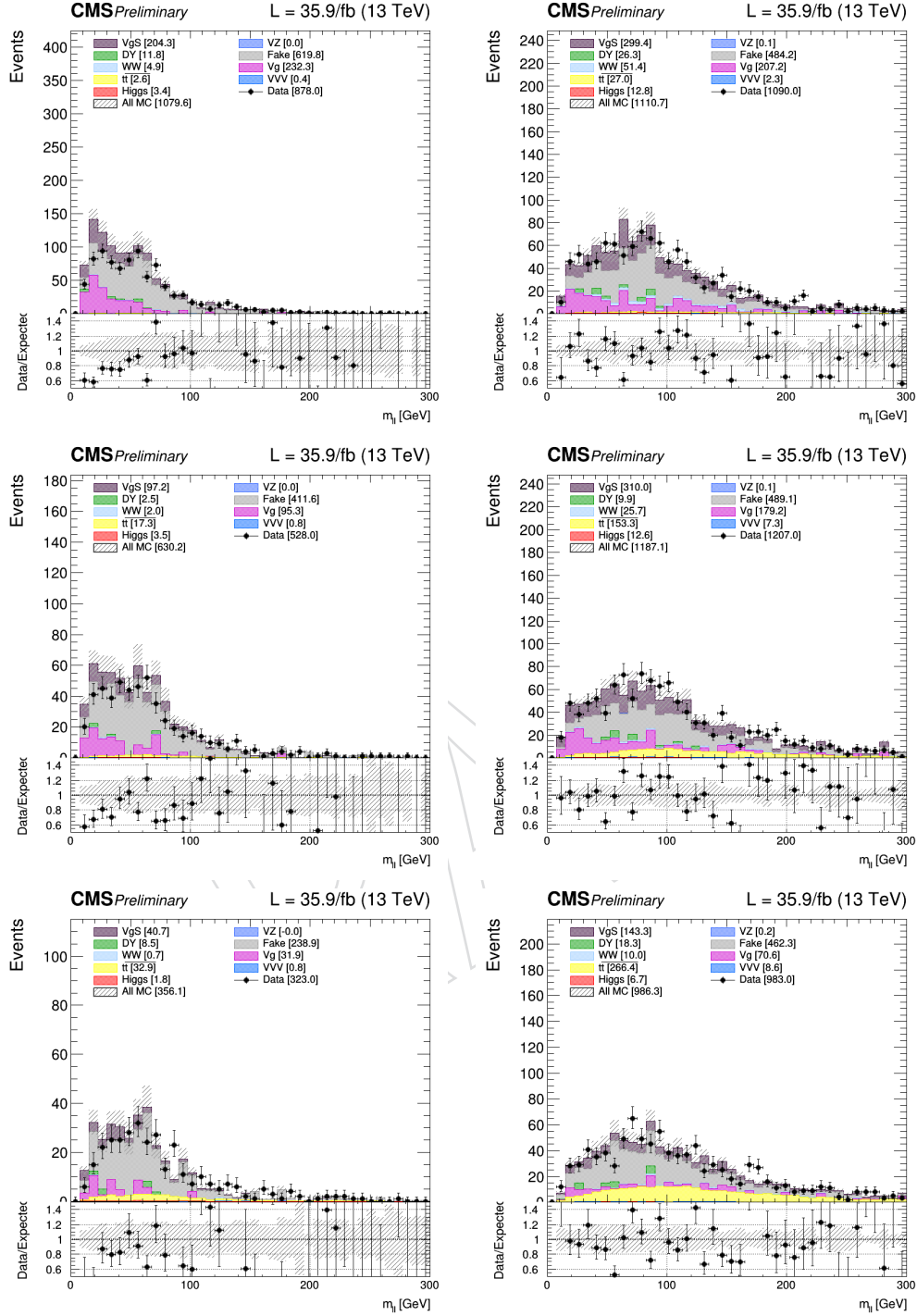


Figure 80: Various distributions at the  $WW$  selection level in the same-sign control region for  $e\mu$  events for the year 2016 and divided into low ( $< 20$  GeV, left) and high ( $\geq 20$  GeV, right) trailing lepton  $p_T$  and jet multiplicity (top: 0j, middle: 1j, bottom:  $\geq 2j$ ). as described in the text. Errors are only statistical.

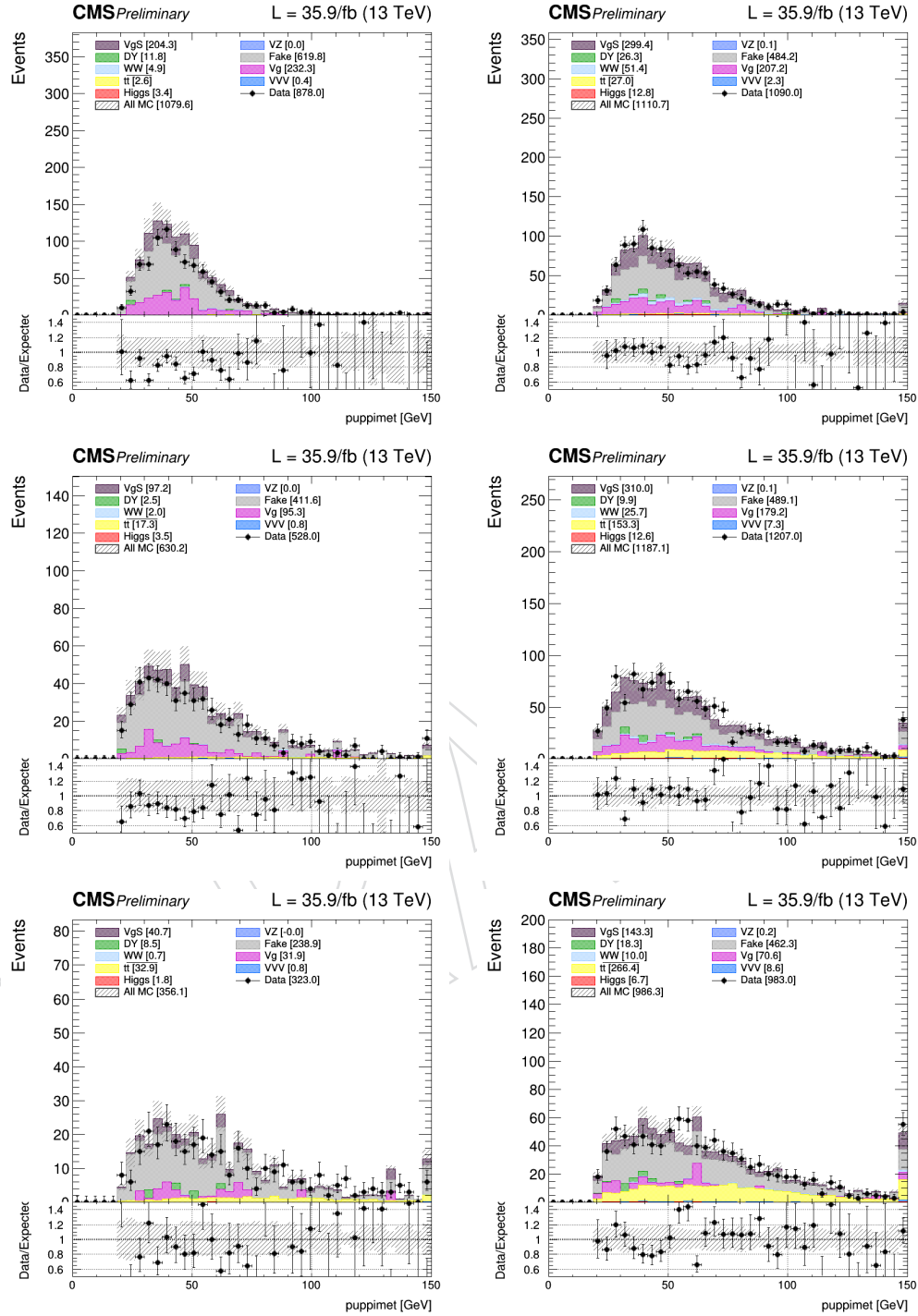


Figure 81: Various distributions at the WW selection level in the same-sign control region for  $e\mu$  events for the year 2016 and divided into low ( $< 20$  GeV, left) and high ( $\geq 20$  GeV, right) trailing lepton  $p_T$  and jet multiplicity (top:  $0j$ , middle:  $1j$ , bottom:  $\geq 2j$ ). as described in the text. Errors are only statistical.

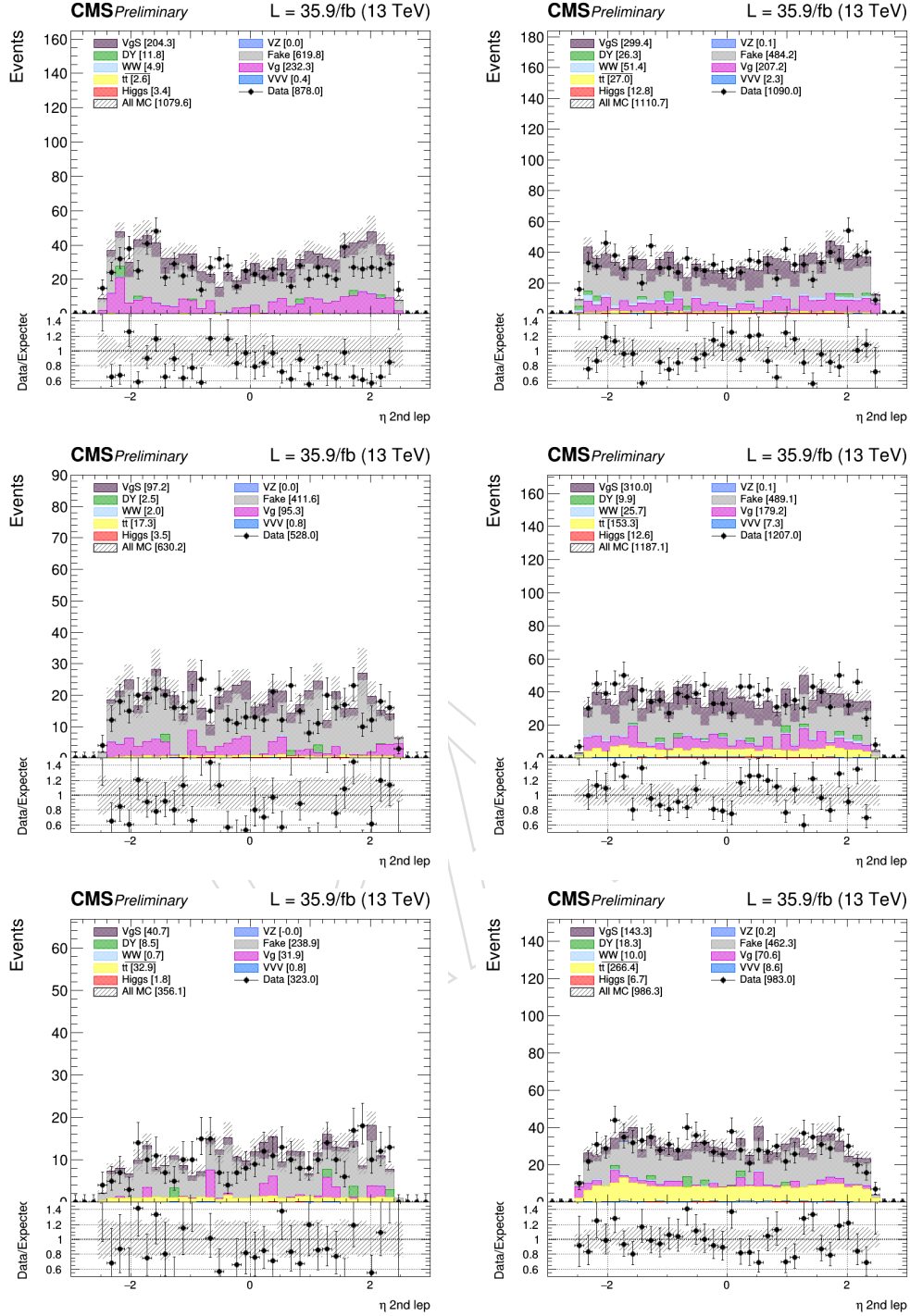


Figure 82: Various distributions at the WW selection level in the same-sign control region for  $e\mu$  events for the year 2016 and divided into low ( $< 20 \text{ GeV}$ , left) and high ( $\geq 20 \text{ GeV}$ , right) trailing lepton  $p_T$  and jet multiplicity (top: 0j, middle: 1j, bottom:  $\geq 2j$ ). as described in the text. Errors are only statistical.

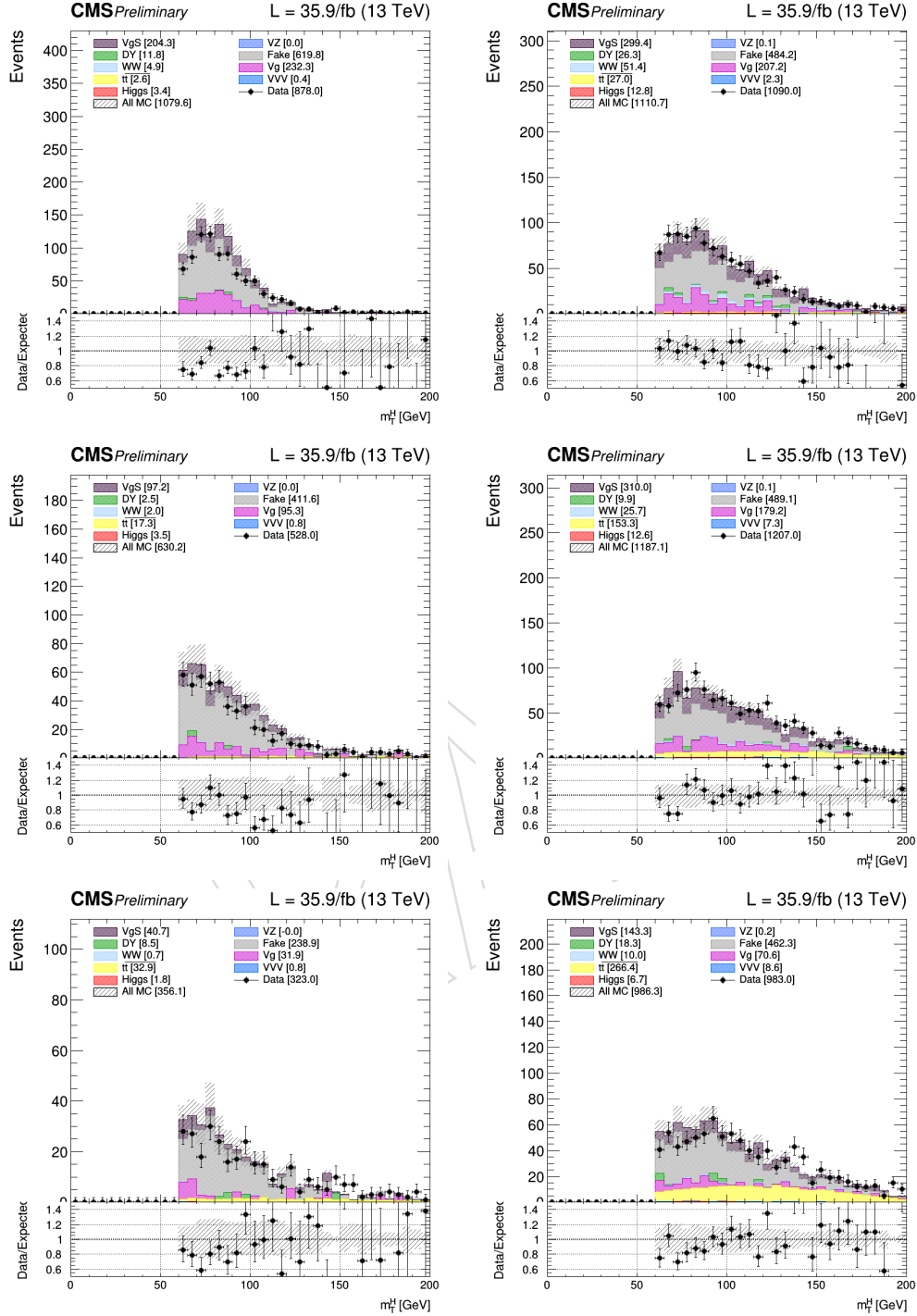


Figure 83: Various distributions at the WW selection level in the same-sign control region for  $e\mu$  events for the year 2016 and divided into low ( $< 20$  GeV, left) and high ( $\geq 20$  GeV, right) trailing lepton  $p_T$  and jet multiplicity (top: 0j, middle: 1j, bottom:  $\geq 2$ j). as described in the text. Errors are only statistical.

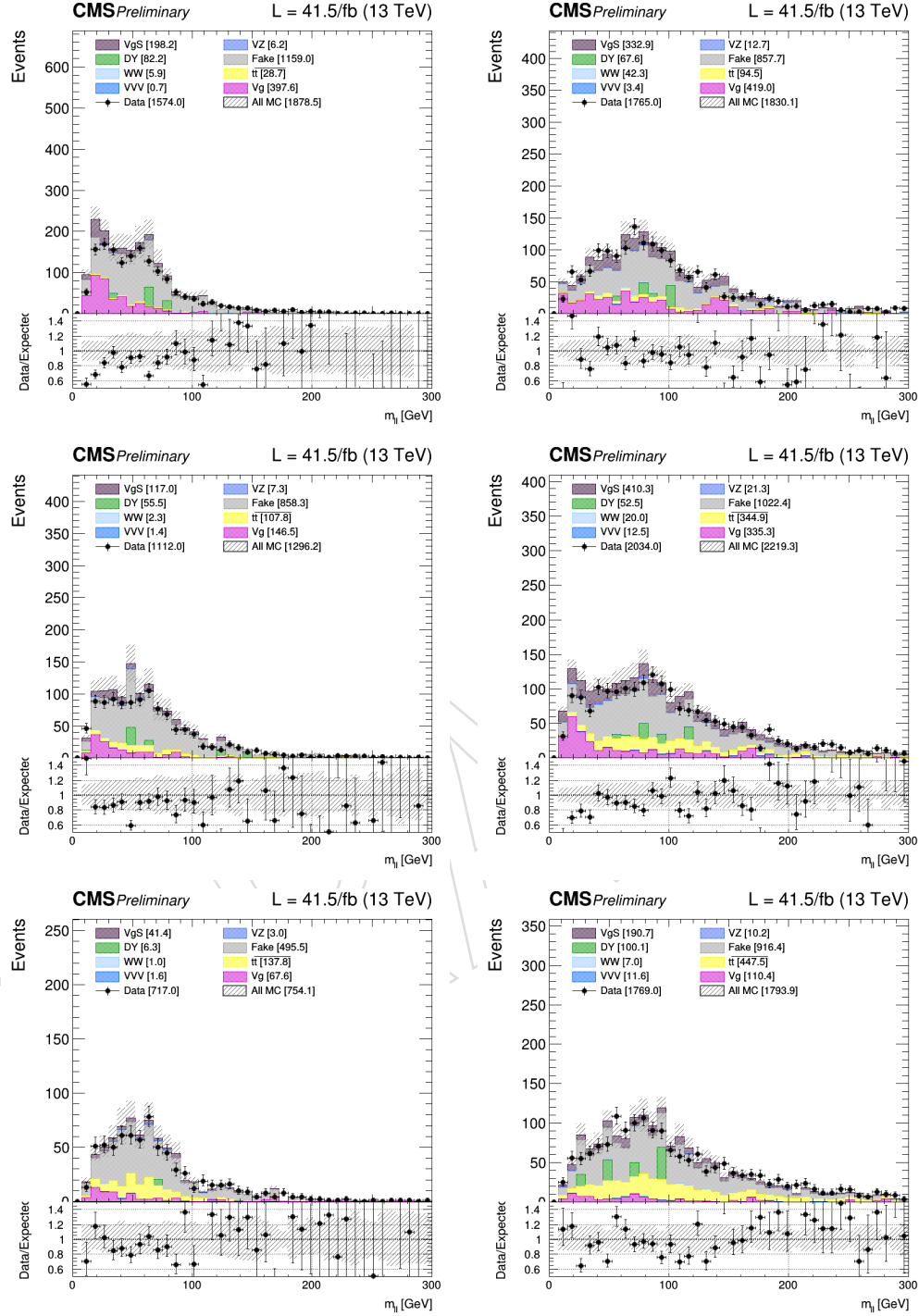


Figure 84: Various distributions at the  $WW$  selection level in the same-sign control region for  $e\mu$  events for the year 2017 and divided into low ( $< 20$  GeV, left) and high ( $\geq 20$  GeV, right) trailing lepton  $p_T$  and jet multiplicity (top: 0j, middle: 1j, bottom:  $\geq 2$ j). as described in the text. Errors are only statistical.

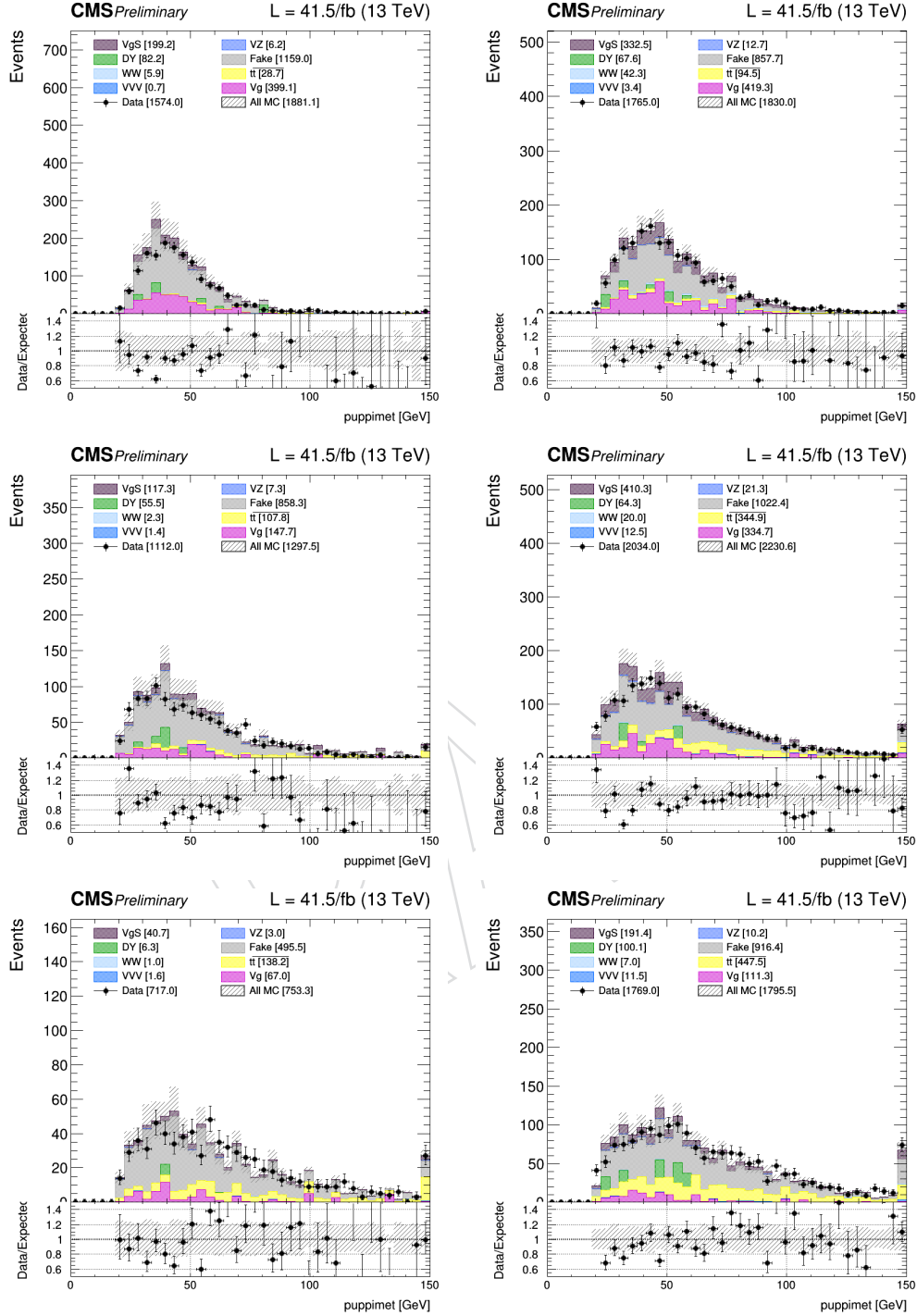


Figure 85: Various distributions at the WW selection level in the same-sign control region for  $e\mu$  events for the year 2017 and divided into low ( $< 20 \text{ GeV}$ , left) and high ( $\geq 20 \text{ GeV}$ , right) trailing lepton  $p_T$  and jet multiplicity (top: 0j, middle: 1j, bottom:  $\geq 2j$ ). as described in the text. Errors are only statistical.

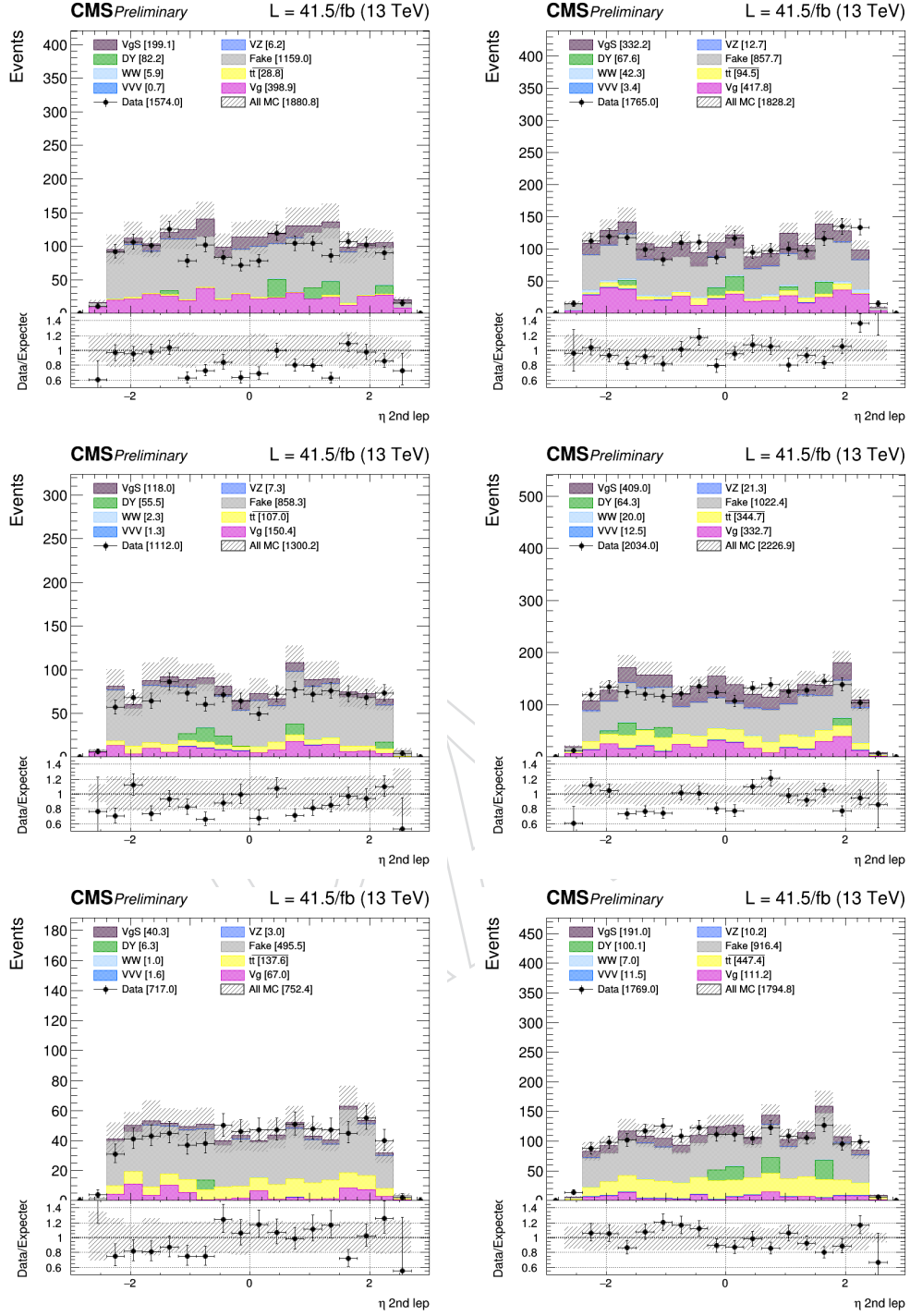


Figure 86: Various distributions at the WW selection level in the same-sign control region for  $e\mu$  events for the year 2017 and divided into low ( $< 20$  GeV, left) and high ( $\geq 20$  GeV, right) trailing lepton  $p_T$  and jet multiplicity (top: 0j, middle: 1j, bottom:  $\geq 2$ j). as described in the text. Errors are only statistical.

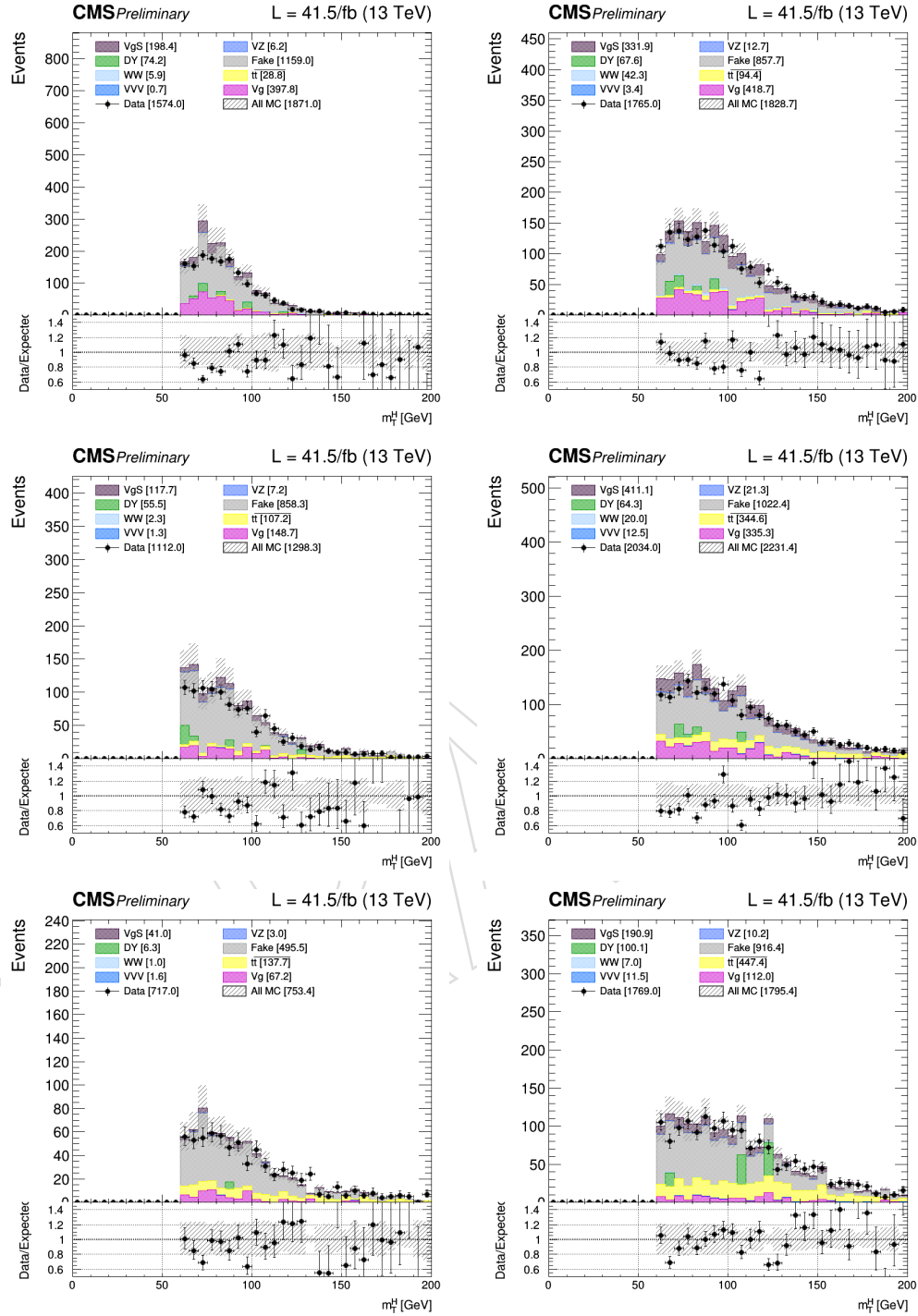


Figure 87: Various distributions at the WW selection level in the same-sign control region for  $e\mu$  events for the year 2017 and divided into low ( $< 20$  GeV, left) and high ( $\geq 20$  GeV, right) trailing lepton  $p_T$  and jet multiplicity (top: 0j, middle: 1j, bottom:  $\geq 2j$ ). as described in the text. Errors are only statistical.

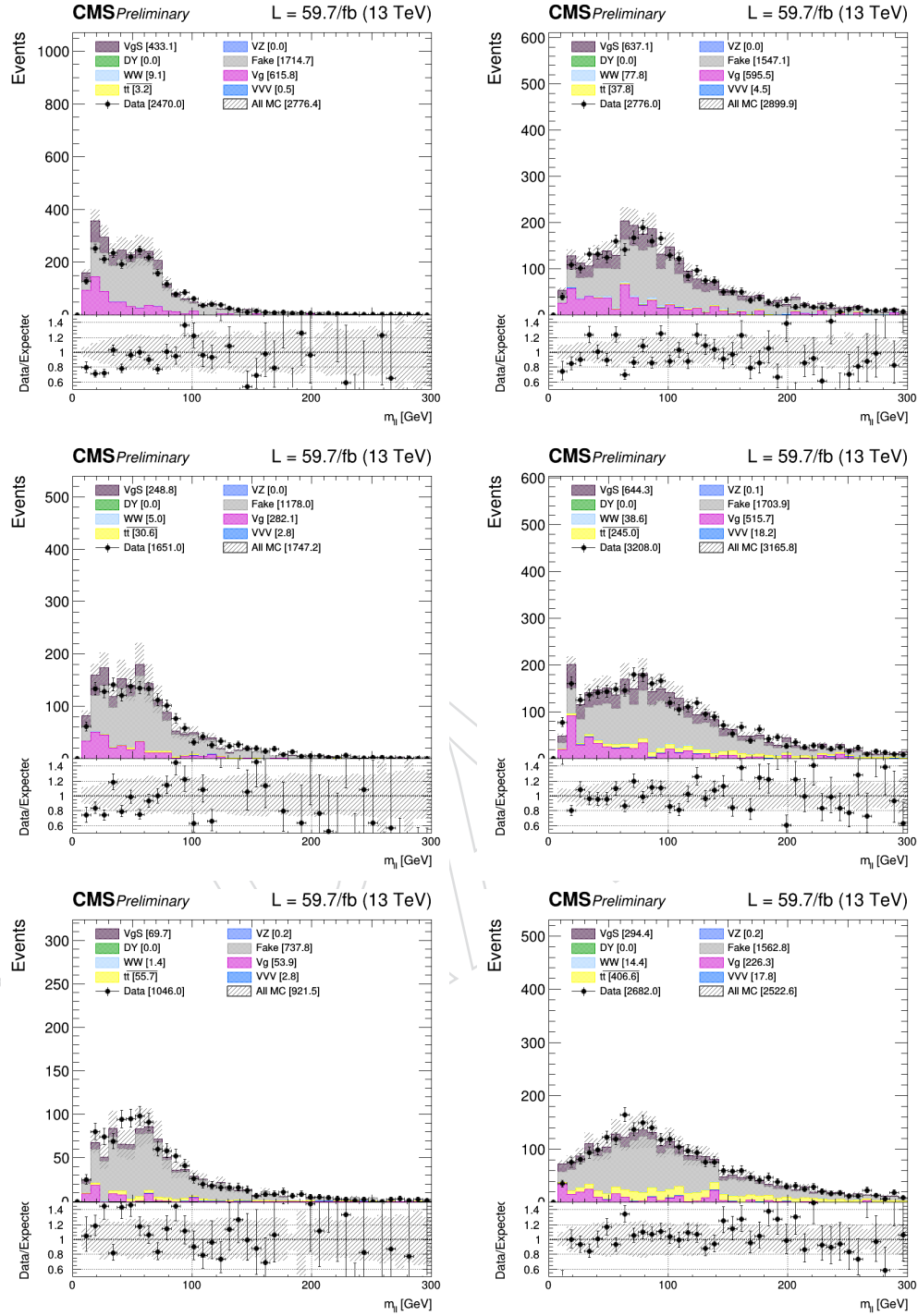


Figure 88: Various distributions at the  $WW$  selection level in the same-sign control region for  $e\mu$  events for the year 2018 and divided into low ( $< 20$  GeV, left) and high ( $\geq 20$  GeV, right) trailing lepton  $p_T$  and jet multiplicity (top:  $0j$ , middle:  $1j$ , bottom:  $\geq 2j$ ). as described in the text. Errors are only statistical.

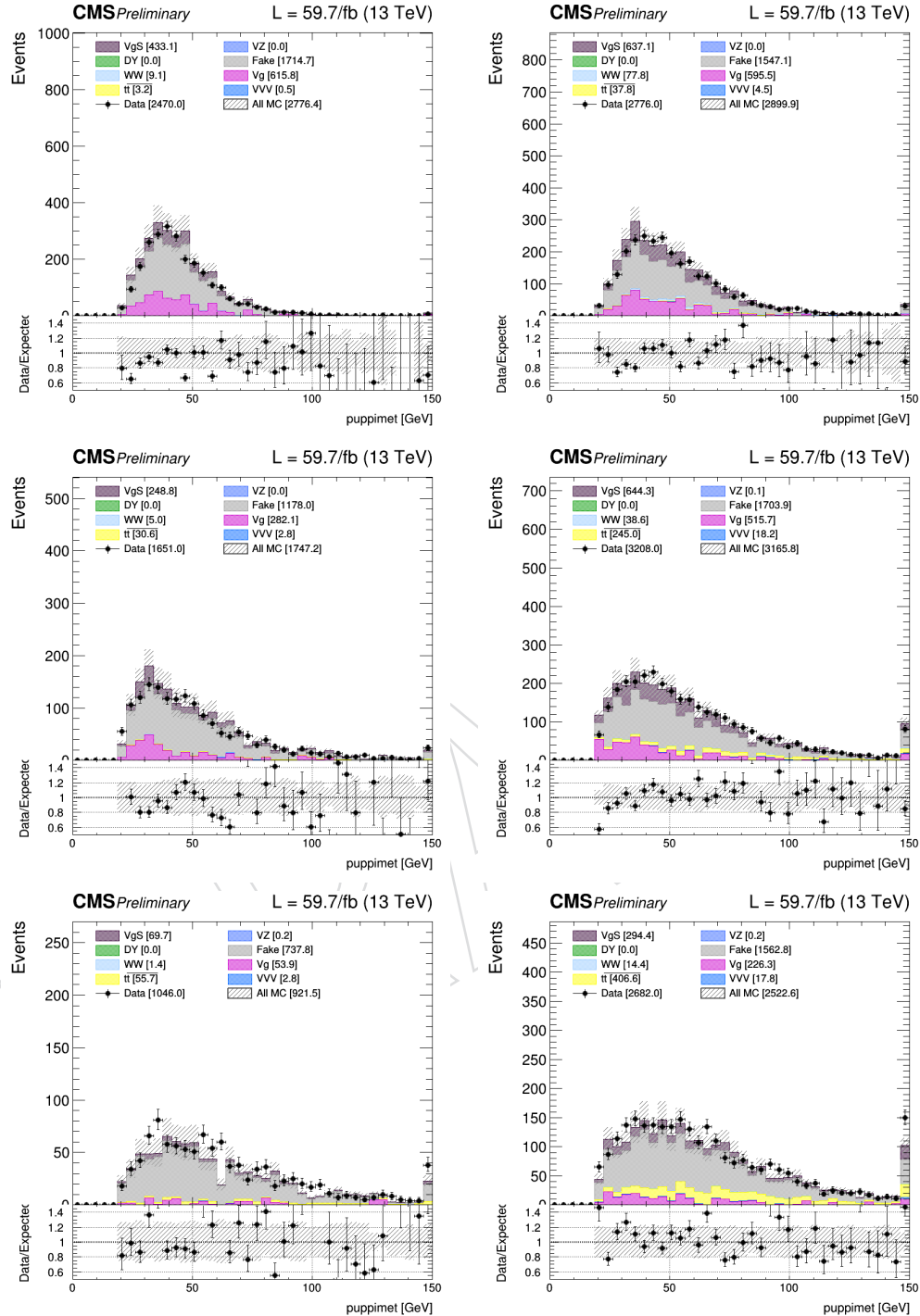


Figure 89: Various distributions at the WW selection level in the same-sign control region for  $e\mu$  events for the year 2018 and divided into low ( $< 20 \text{ GeV}$ , left) and high ( $\geq 20 \text{ GeV}$ , right) trailing lepton  $p_T$  and jet multiplicity (top: 0j, middle: 1j, bottom:  $\geq 2j$ ). as described in the text. Errors are only statistical.

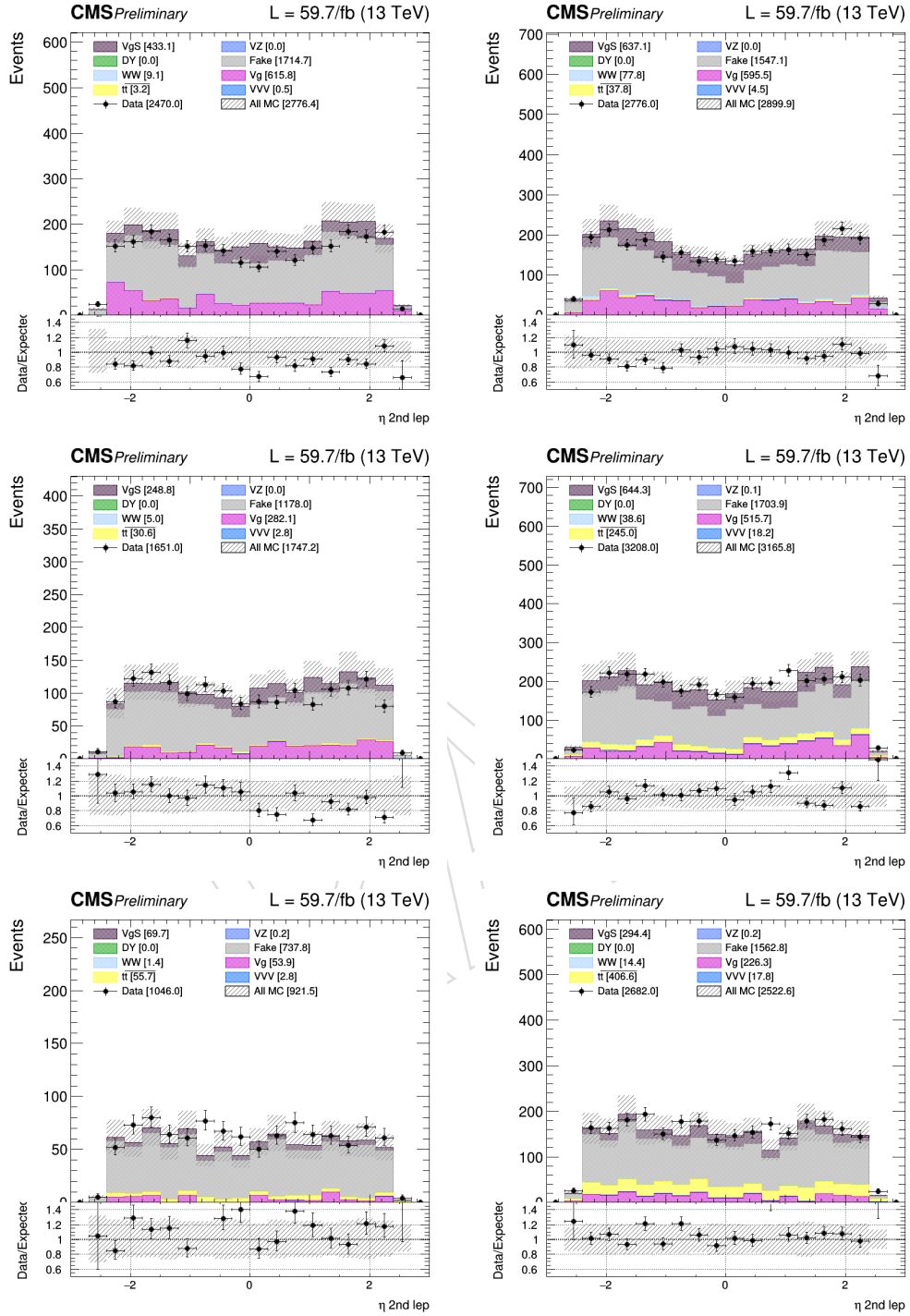


Figure 90: Various distributions at the WW selection level in the same-sign control region for  $e\mu$  events for the year 2018 and divided into low ( $< 20$  GeV, left) and high ( $\geq 20$  GeV, right) trailing lepton  $p_T$  and jet multiplicity (top: 0j, middle: 1j, bottom:  $\geq 2j$ ). as described in the text. Errors are only statistical.

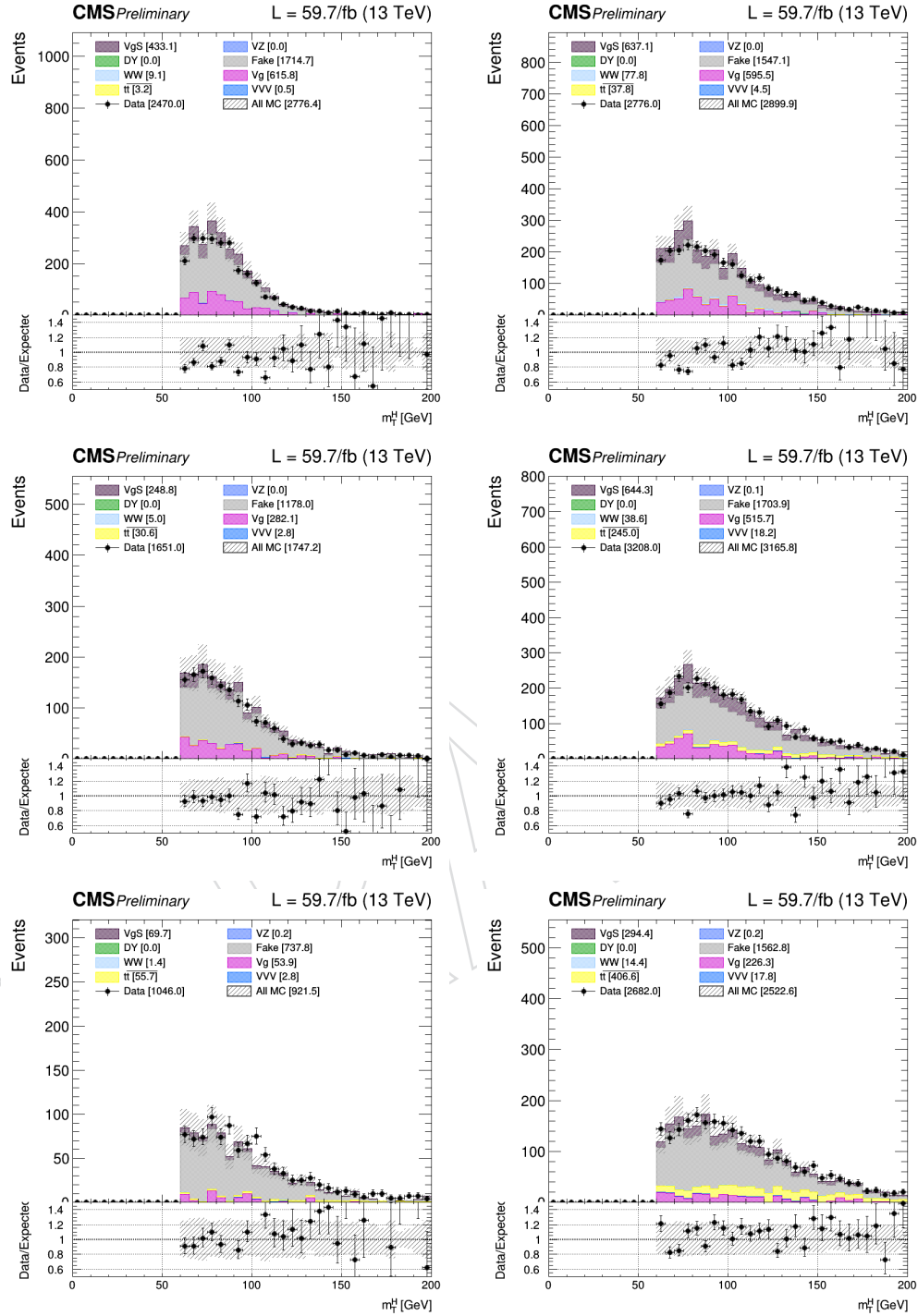


Figure 91: Various distributions at the WW selection level in the same-sign control region for  $e\mu$  events for the year 2018 and divided into low ( $< 20$  GeV, left) and high ( $\geq 20$  GeV, right) trailing lepton  $p_T$  and jet multiplicity (top: 0j, middle: 1j, bottom:  $\geq 2j$ ). as described in the text. Errors are only statistical.

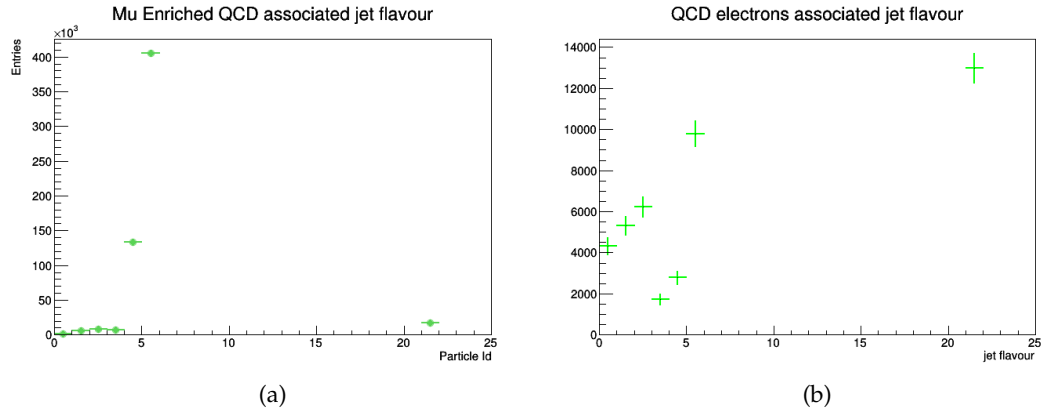


Figure 92: Flavour of the jets associated with muons (a) and electrons (b) in a QCD MC sample. The fake muons come mostly from b quark jets and the electrons from light quarks and gluons.

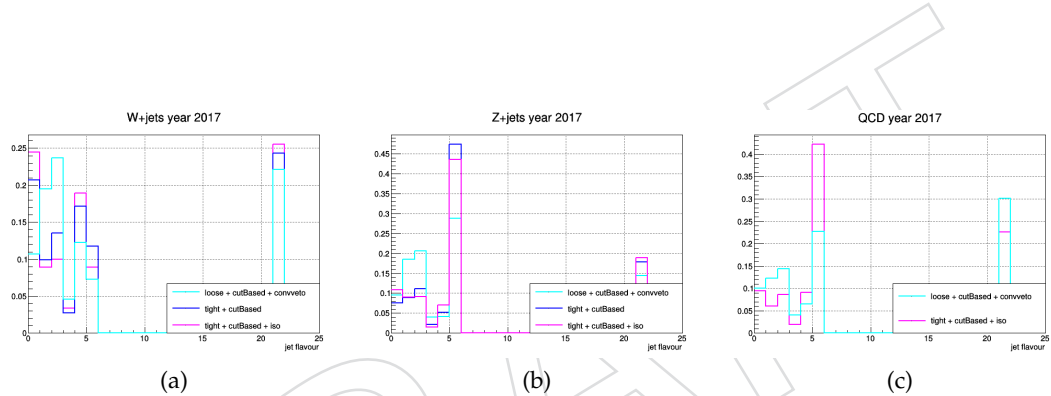


Figure 93: Associated jet flavour distributions for different working points in a W+jets MC sample (a), in a Z+jets MC sample (b) and in a QCD MC sample (c). The light blue distribution belongs to our final electron loose working point, and our choice for the tight working point is the magenta line.

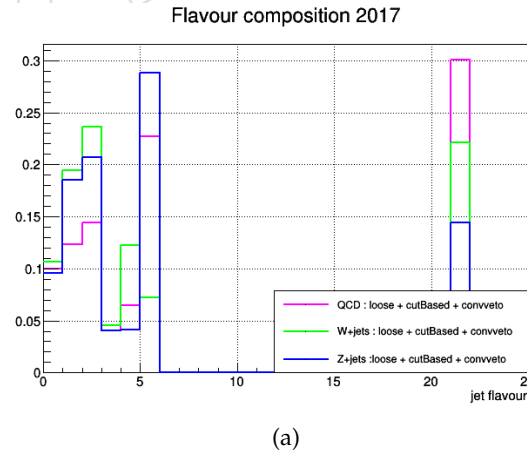


Figure 94: Comparison of the associated jet flavour distributions for the chosen loose working point in all three control regions.

Table 54: Systematics uncertainties associated to the non-prompt leptons data-driven estimation (i.e. W+jets and QCD) at WW selection cuts in the  $e\mu$  channel for the 0-,1-and 2-jet categories and for the year 2016.

	$e\mu$ 0-jet bin	$e\mu$ 1-jet bin	$e\mu$ 2-jet bin
Electron jet $E_T$	7.9/-3.2%	7.1/-2.3%	7.3/-1.9%
Electron statistical	5.2/-5.0%	4.5/-4.3%	4.9/-4.6%
Muon jet $E_T$	5.2/-1.7%	5.9/-3.4%	6.7/-6.2%
Muon statistical	1.4/-1.3%	2.0/-1.9%	2.5/-2.5%

Table 55: Systematics uncertainties associated to the non-prompt leptons data-driven estimation (i.e. W+jets and QCD) at WW selection cuts in the  $e\mu$  channel for the 0-,1-and 2-jet categories and for the year 2017.

	$e\mu$ 0-jet bin	$e\mu$ 1-jet bin	$e\mu$ 2-jet bin
Electron jet $E_T$	2.0/-1.6%	1.0/-1.3%	0.9/-0.8%
Electron statistical	10.6/-9.1%	9.9/-8.5%	9.6/-8.2%
Muon jet $E_T$	4.6/-1.5%	4.9/-3.6%	6.0/-5.8%
Muon statistical	2.5/-2.3%	3.1/-2.9%	4.0/-3.7%

Table 56: Systematics uncertainties associated to the non-prompt leptons data-driven estimation (i.e. W+jets and QCD) at WW selection cuts in the  $e\mu$  channel for the 0-,1-and 2-jet categories and for the year 2018.

	$e\mu$ 0-jet bin	$e\mu$ 1-jet bin	$e\mu$ 2-jet bin
Electron jet $E_T$	1.9/-1.5%	3.0/-1.6%	2.7/-1.7%
Electron statistical	10.4/-8.6%	10.5/-8.5%	10.5/-8.3%
Muon jet $E_T$	5.6/-1.7%	4.8/-3.7%	6.1/-6.1%
Muon statistical	2.7/-2.5%	3.5/-3.2%	4.7/-4.3%

## 850 7 Jets

851 Editors: Dennis Roy, Tomas Kello, Davide di Croce

### 852 7.1 Jet reconstruction

853 Jets are an ensemble of particles resulting from a hadronic shower. They are reconstructed as  
854 AK4 PF jets with Charged Hadron Subtraction (CHS), meaning that the jets are clustered from  
855 particle flow candidates using the anti-kT algorithm with a distance parameter of  $R = 0.4$ ,  
856 while also charged particles from non-primary vertices or pileup are removed before cluster-  
857 ing. Jet Energy Corrections (JEC), which consist of the L1FastJet, L2Relative and L3Absolute  
858 corrections on MC and also L2L3Residual corrections on data, are applied to these jets. The  
859 JECs for the different years are the following:

- 860 • 2016: Summer16\_07Aug2017\_V11
- 861 • 2017: Fall17\_17Nov2017\_V32
- 862 • 2018: Autumn18\_V8

### 863 7.2 Jet selection

864 In order to separate noise from real jets, only those jets passing tight jet ID as defined by the Jet  
865 Identification group [10] are considered. Additionally, jets with  $p_T < 50$  GeV are required to  
866 pass loose pile-up (PU) jet ID [11]. This particular choice of PU working point is a deal between  
867 the capability to reject jets from PU interactions (Figure 95 (2016), Figure 96 (2017), Figure 97  
868 (2018)) and the agreement between data and MC in the fraction of the jet veto efficiency (Fig-  
869 ure 98 (2016), Figure 99 (2017), Figure 100 (2018)).

### 870 7.3 L1 Prefire corrections

871 In 2016 and 2017 there was an issue, which would cause highly energetic readout in the ECAL  
872 endcap from jets, photons and electrons to be assigned by the L1 Trigger to the previous bunch-  
873 crossing. This is known as “prefiring”, as the Trigger is fired to the previous bunch-crossing,  
874 rather than the bunch-crossing where the highly energetic object came from. The event with  
875 interresting physics is therefore lost in data, while the issue is not reproduced in MC.  
876 To make up for this difference, a weight is applied to all events in MC, which is essentially  
877  $(1 - x)$ , where  $x$  is the probability of an event to be prefire, based on all objects that may  
878 induce the prefire. The recipe that is applied follows [12].

879 The magnitude of how much the MC (and the data) is affected by this issue has been studied.  
880 Applying the weights leads to an average loss in the event yield by about 3 % (Figure 101 as  
881 an example for DY), meaning that this is also the amount of data lost from prefire. The loss  
882 is however slightly process-dependent. For example in VBF signal events, highly energetic jets  
883 are expected in the forward direction of the detector. As a result, the total amount of VBF signal  
884 events lost is closer to 5 % (Figure 102).

885 As seen in the control regions, applying prefire corrections leads to a better data/MC agree-  
886 ment (Figure 103). In distributions of leptons or jets over  $\eta$ , it is seen that the agreement is  
887 significantly improved in the area of  $2.5 < \text{abs}(\eta) < 3.0$ .

### 888 7.4 Uncertainties

889 All of the Jet Energy Scale (JES) uncertainties are considered as a single nuisance parameter,  
890 which is applied to the  $p_T$  of each jet as a function of the jet’s  $p_T$  and  $\eta$ . The full list of uncer-  
891 tainties is given in [13].

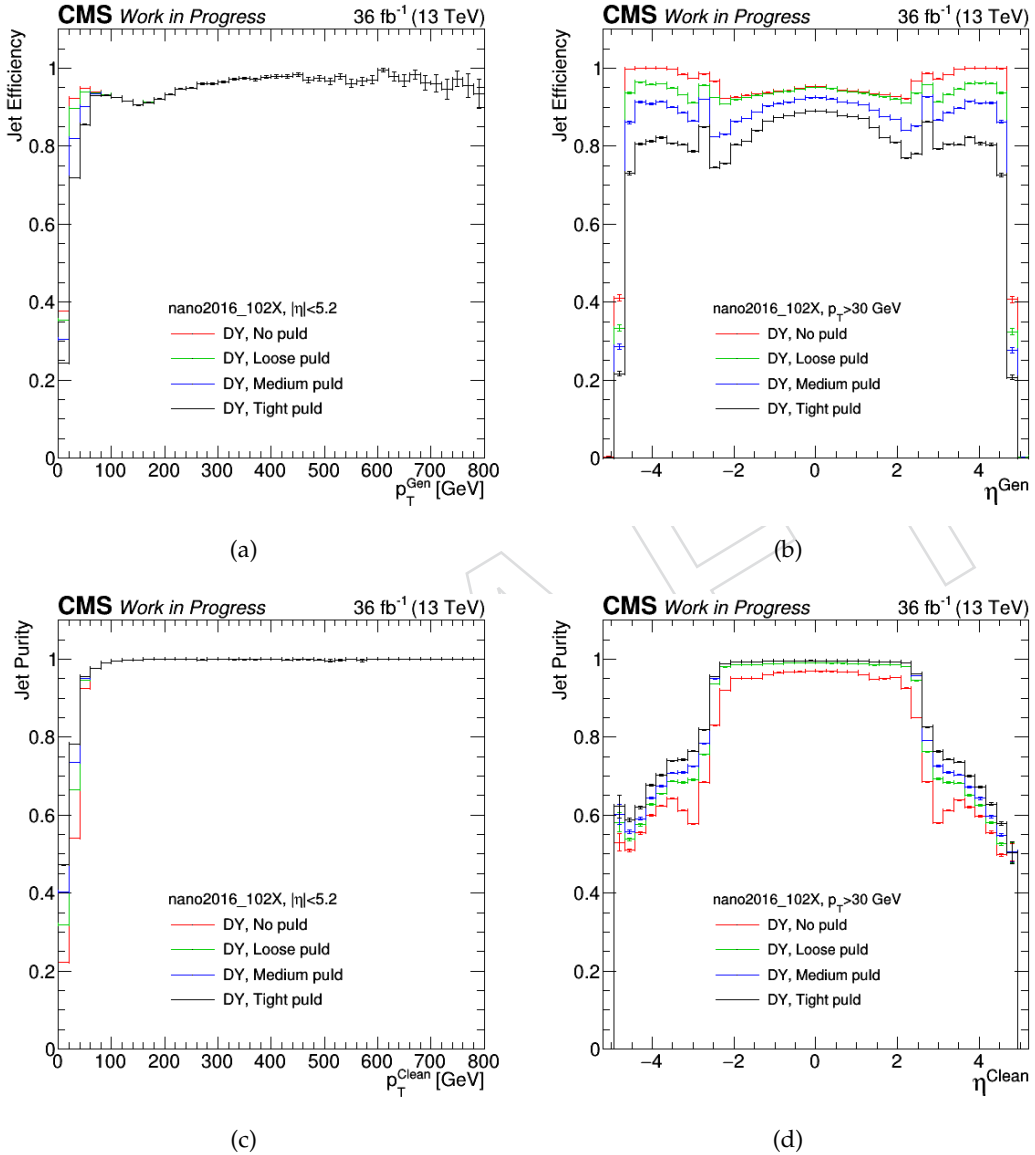


Figure 95: Comparison of the jet PU ID efficiency as a function of  $p_T$  (a) and  $\eta$  (b), and jet PU ID purity as a function of  $p_T$  (c) and  $\eta$  (d) in Drell-Yan events (2016).

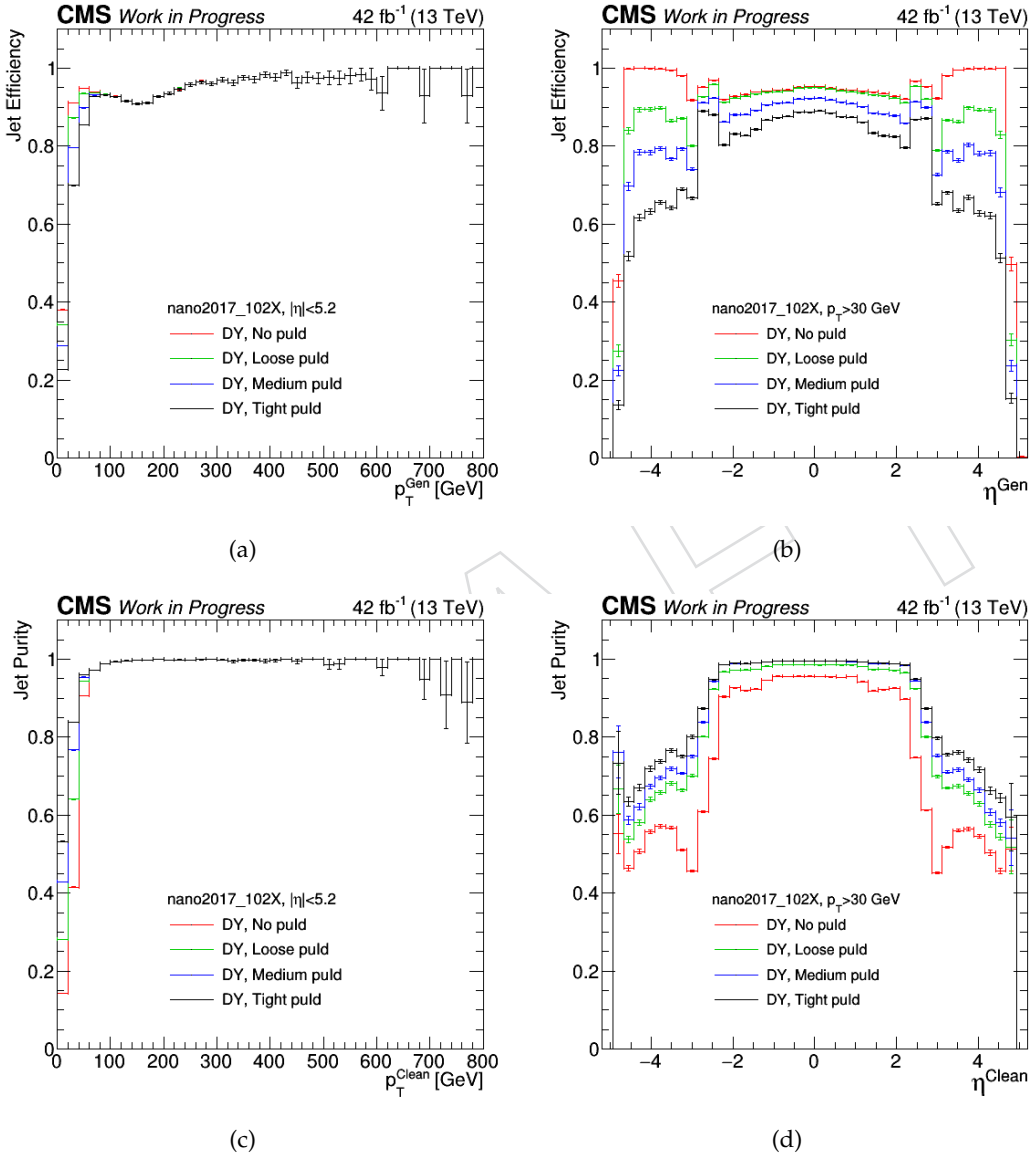


Figure 96: Comparison of the jet PU ID efficiency as a function of  $p_T$  (a) and  $\eta$  (b), and jet PU ID purity as a function of  $p_T$  (c) and  $\eta$  (d) in Drell-Yan events (2017).

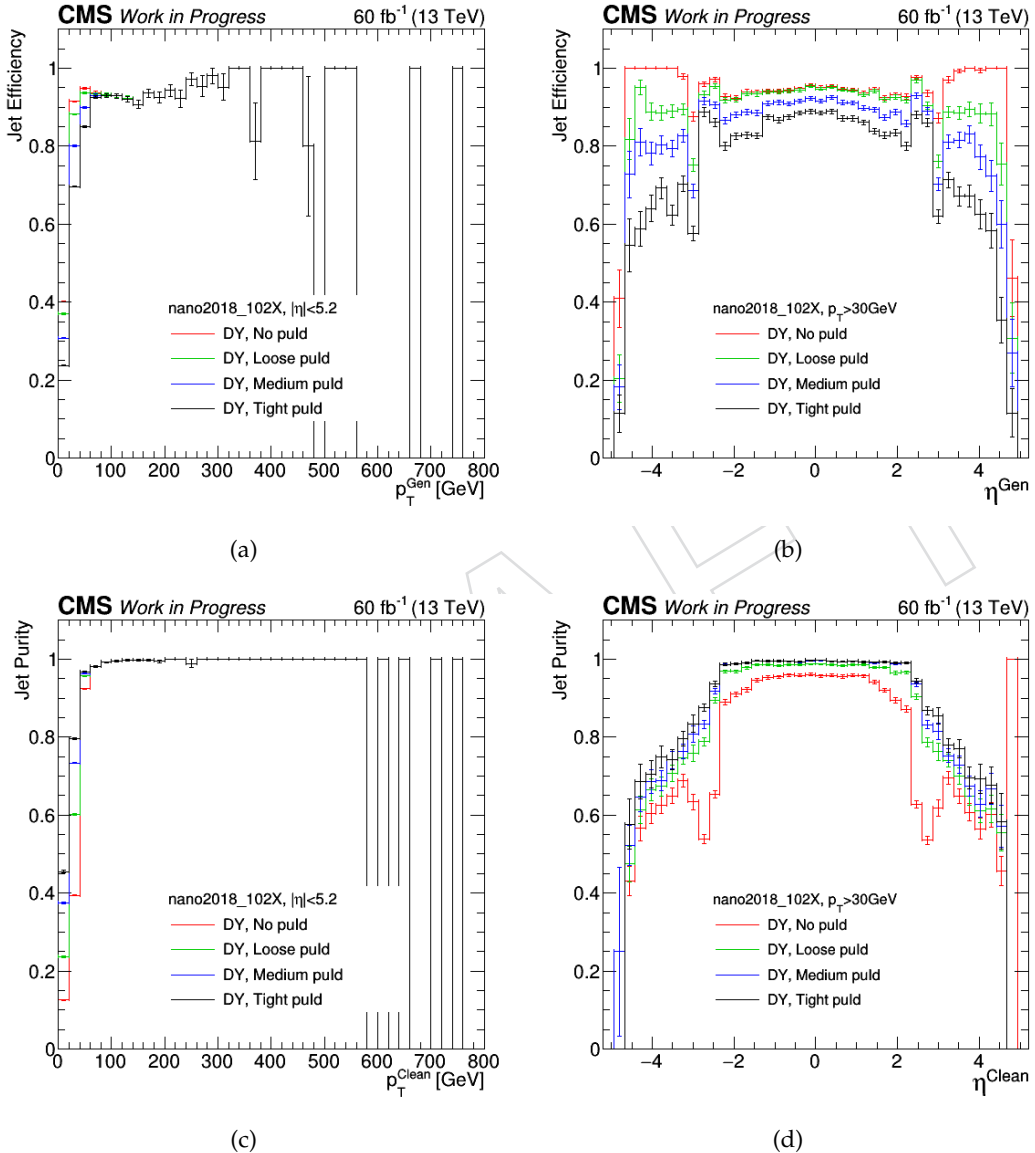


Figure 97: Comparison of the jet PU ID efficiency as a function of  $p_T$  (a) and  $\eta$  (b), and jet PU ID purity as a function of  $p_T$  (c) and  $\eta$  (d) in Drell-Yan events (2018).

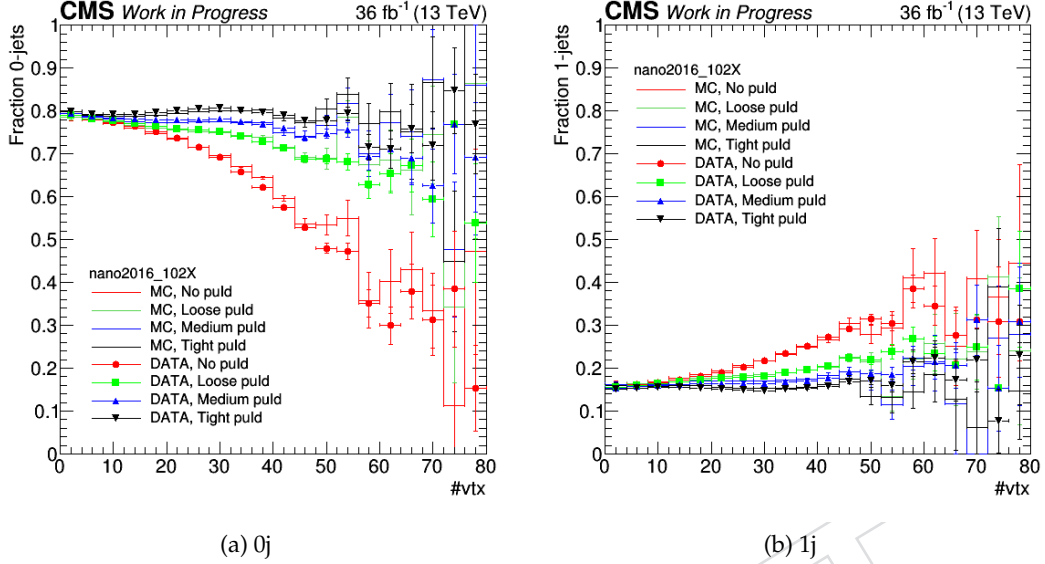


Figure 98: Fraction of the jet veto efficiency in 0-jet events (a) and 1-jet events (b), respectively, as a function of the number of vertices with tight jet ID selection in Drell-Yan events (2016) compared for different PU jet ID working points.

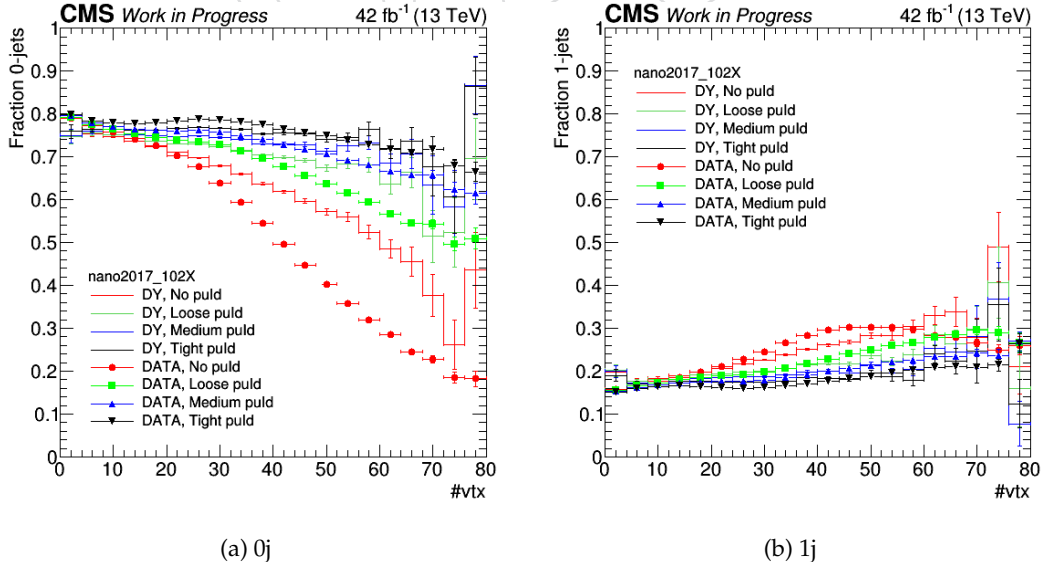


Figure 99: Fraction of the jet veto efficiency in 0-jet events (a) and 1-jet events (b), respectively, as a function of the number of vertices with tight jet ID selection in Drell-Yan events (2017) compared for different PU jet ID working points.

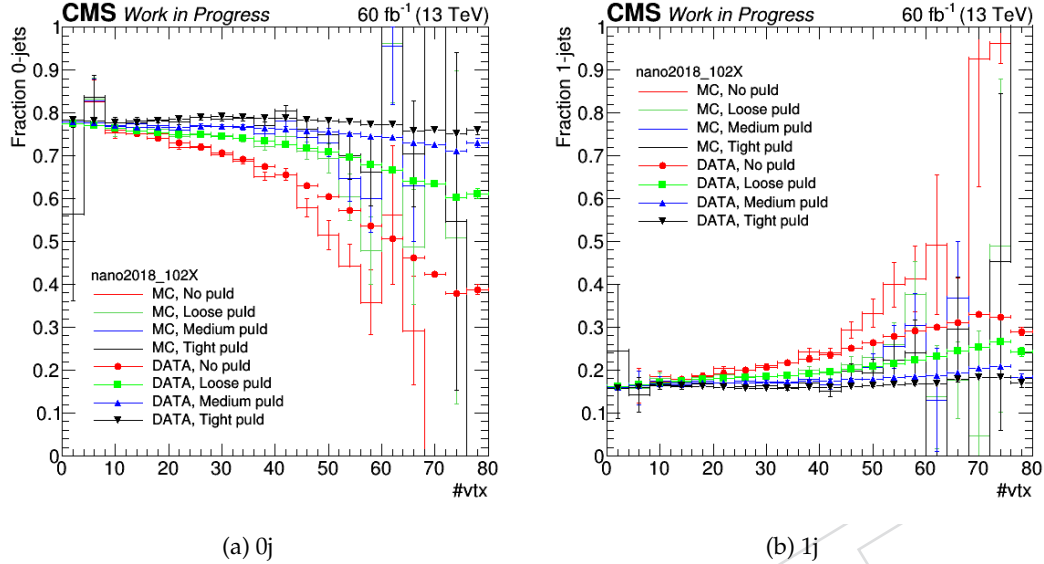


Figure 100: Fraction of the jet veto efficiency in 0-jet events (a) and 1-jet events (b), respectively, as a function of the number of vertices with tight jet ID selection in Drell-Yan events (2018) compared for different PU jet ID working points.

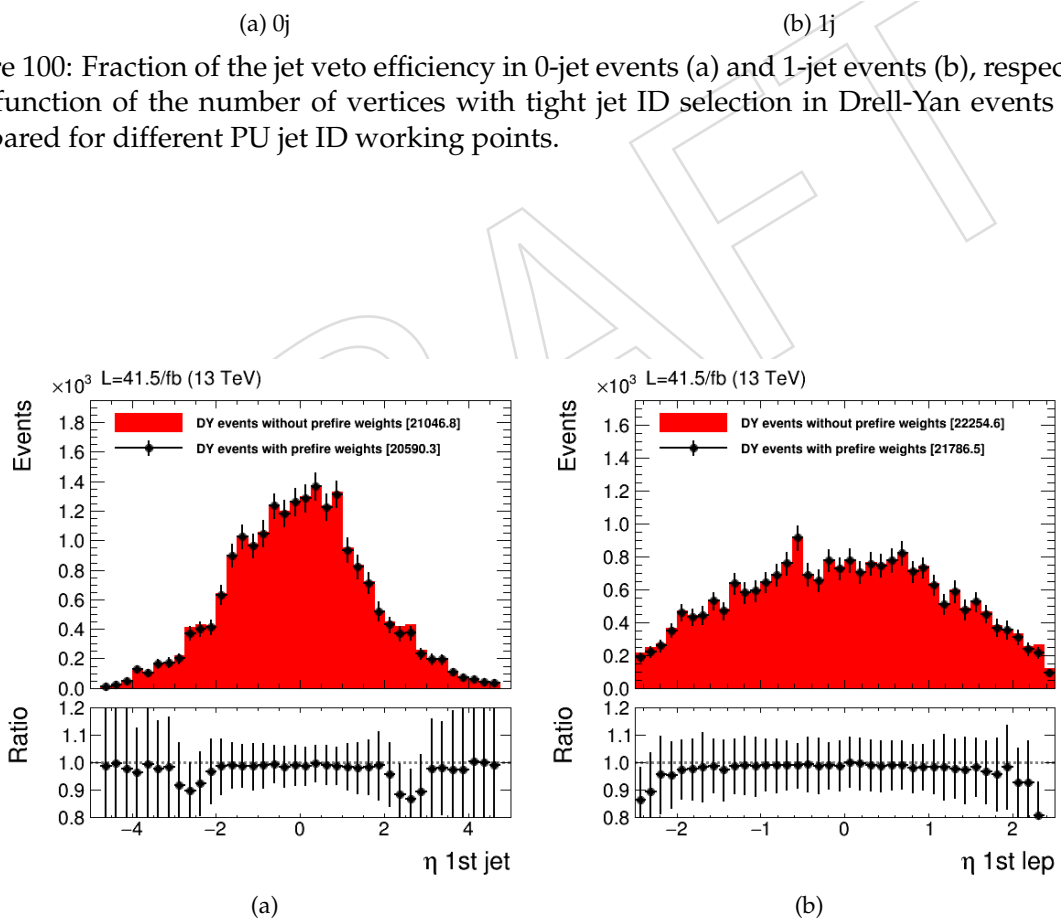


Figure 101: Visualisation of the effect induced from the prefire issue on 2017 DY samples. The histogram is the distribution given by MC samples without the prefire correction applied; The dots show the distribution with the correction applied. Distribution are shown for the  $\eta$  of the leading jet (a) and the  $\eta$  of the leading lepton (b).

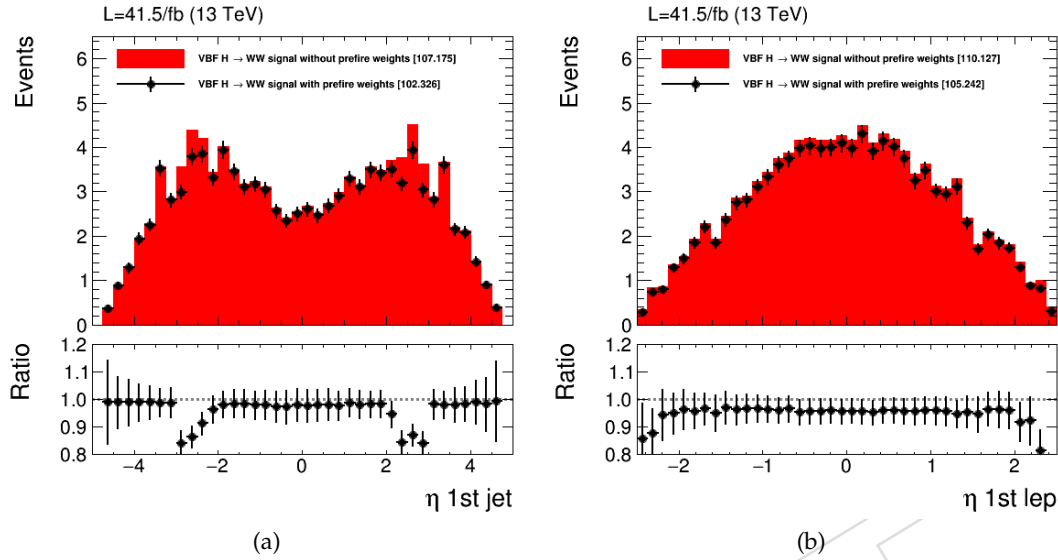


Figure 102: Visualisation of the effect induced from the prefiring issue on 2017 VBF signal samples. The histogram is the distribution given by MC samples without the prefire correction applied; The dots show the distribution with the correction applied. Distribution are shown for the  $\eta$  of the leading jet (a) and the  $\eta$  of the leading lepton (b).

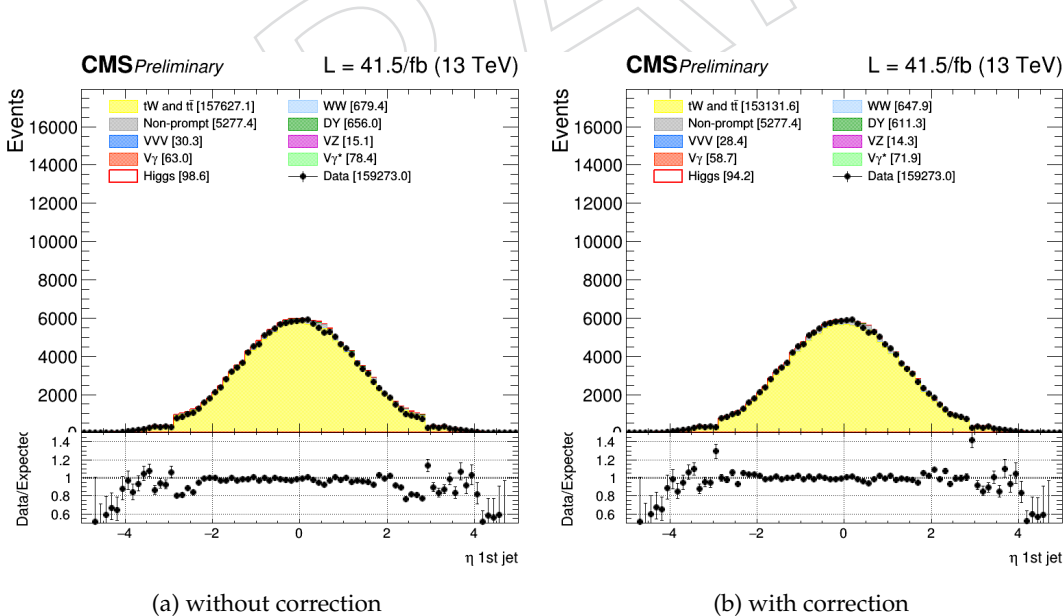


Figure 103: Visualisation of the effect induced from the prefiring issue on the 2017 Top control region with 2 jets. The distribution on the left shows the Data/MC agreement without the prefire correction applied (a) and on the right with the correction applied (b).

## 8 Missing Transverse Energy

Editors: Dennis, Jonatan, SangEun

### 8.1 MET reconstruction

The transverse missing energy (MET) is defined as the negative sum of the transverse momentum of all PF candidates in an event. In particular, the MET from the Pileup Per Particle Indetification (PUPPI) algorithm is used, as it was found to have a better resolution, as well as a better data to MC agreement.

This is illustrated in Figure 104. In 2017 data a number of problems and data/MC disagreements have been reported. For instance there is a large disagreement in fake MET distributions between data and MC, caused by the EE noise at high  $|\eta|$ . This effect is however significantly reduced for PuppiMET. Also in 2018 the agreement between data and MC is better in the tail when using PuppiMET. For 2016 there are no significant differences between PF MET and PuppiMET, therefore PuppiMET is only used for consistency between all three years.

### 8.2 MET filter

Several algorithms used to identify incorrect contributions to the MET (e.g. detector noise) are applied in the form of filters. The filters used on both data and MC for all years are:

- goodVertices
- globalSuperTightHalo2016Filter
- HBHENoiseFilter
- HBHENoiseIsoFilter
- EcalDeadCellTriggerPrimitiveFilter
- BadPFMuonFilter

Additionally the filter "eeBadScFilter" is applied for all years only on data [14].

For 2017 and 2018 the filter "ecalBadCalibFilter", which is used to filter events where fake MET exists due to bad ECAL endcap crystals, is also applied on both data and MC. The updated crystal list is used for this filter.

### 8.3 MET uncertainties

There are several sources which may cause a fluctuation on the MET. Therefore uncertainties on the MET are applied from:

- Unclustered MET
- Jet Energy Scale
- Jet Energy Resolution
- Muon  $p_T$  scale
- Electron  $p_T$  scale

The uncertainty from unclustered MET is determined by directly applying Up- and Down-shifts to the MET. The uncertainties on jets, electrons and muon are applied to the respective objects while the MET is recalculated with the same Up- and Down-variations alongside.

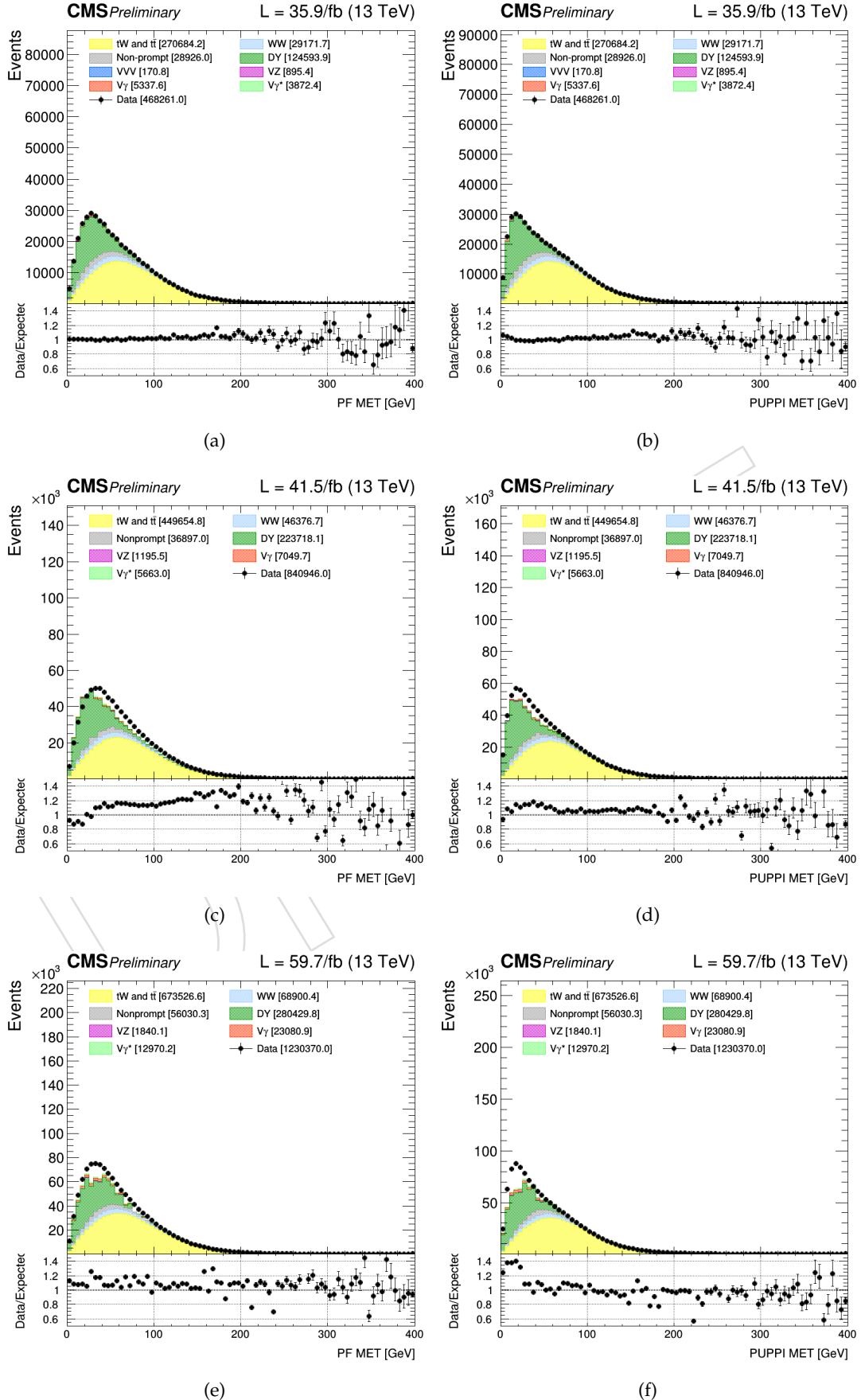


Figure 104: Inclusive distributions of PF MET (left) and PuppiMET (right) for 2016 (top), 2017 (middle) and 2018 (bottom).

## 9 Drell-Yan multivariate discriminants

Editors: D. Di Croce, X. Janssen

In order to reject the Drell-Yan (DY) background, one possibility for the HWW same-flavor (SF) final states is to add tighter cuts on  $E_T^{\text{miss}}$  and kinematics variables on top of the opposite-flavor (OF) selection. In this way, most of the signal in the SF final state is rejected due to this high background. However the selection might be not optimal as in OF. For this reason a multi-variable analysis (MVA) was performed to recover as much signal as possible while rejecting the DY.

Two different methods were applied: a Boosted Decision Tree (BDT) and a Deep Neural Network (DNN). The methods are implemented in the TMVA package.

Moreover, the training samples were selected as close as possible to the final selection:

- $p_T^\ell > 25 \text{ GeV}$  for the leading lepton and  $p_T^\mu > 13(10) \text{ GeV}$  for the trailing electron (muon);
- third lepton veto ( $p_T^3 < 10 \text{ GeV}$ );
- Z veto ( $|m_{ll} - m_Z| > 15 \text{ GeV}$ );
- b veto;
- Puppi  $E_T^{\text{miss}} > 20 \text{ GeV}$ .

In addition, the training is performed separately in each of the SF final states for each year. These SF final states are categorized as:

- 0-jet category:  $p_T^{jet_1} < 30 \text{ GeV}$ .
- 1-jet category:  $p_T^{jet_1} \geq 30 \text{ GeV}$  and  $p_T^{jet_2} < 30$ .
- 2-jets ggH tagged category:  $p_T^{jet_1} \geq 30 \text{ GeV}$ ,  $p_T^{jet_2} \geq 30$ , and  $\Delta\eta_{jj} < 3.5$  or  $\Delta\eta_{jj} \geq 3.5 + m_{jj} < 65$  or  $\Delta\eta_{jj} \leq 3.5 + 105 \geq m_{jj} < 400 \text{ GeV}$ .
- 2-jets VH tagged category:  $p_T^{jet_1} \geq 30 \text{ GeV}$ ,  $p_T^{jet_2} \geq 30$ , and  $\Delta\eta_{jj} < 3.5$  or  $\Delta\eta_{jj} \geq 3.5 + 65 \leq m_{jj} < 105 \text{ GeV}$ .
- 2-jets VBF tagged category:  $p_T^{jet_1} \geq 30 \text{ GeV}$ ,  $p_T^{jet_2} \geq 30$ ,  $\Delta\eta_{jj} \geq 3.5$  and  $m_{jj} \geq 400 \text{ GeV}$ .

In order to avoid over-training the MC samples, alternative samples have been used. The list of training samples is in Table x.

Table 57: Training samples for DYMVA

MC sample	2016	2017	2018
GluGluHToWWTo2L2Nu	AMCNLO_M125	Powheg_M125_CP5Down Powheg_M125_CP5Up	Powheg_M125_CP5Down Powheg_M125_CP5Up
VBFHToWWTo2L2Nu	M125_CUETDown M125 CUETUp	Powheg_M125_CP5Down Powheg_M125_CP5Up	Powheg_M125_CP5Down Powheg_M125_CP5Up
HWminusJ_HToWW_LNu HWplusJ_HToWW_LNu	M120 M120	M120 M120	M120 M120
DYJetsToLL <sub>M</sub> - 10to50 DYJetsToLL <sub>M</sub> - 50	NLO LO_ext1	LO_ext1	LO LO

## 9.1 DNN Training

The DNN training is performed with the PyKeras interface to Tensorflow library. The network model consist of 2 hidden layers with 512 and 256 neurons, respectively. Moreover, a 10% dropout is used between hidden layers (i.e. 10% of the nodes of the second layer are randomly disconnected at each event) to avoid overtraining. In addition, the optimizer used is Adam, and the metrics are categorical accuracy and categorical cross-entropy loss. The metric responses are cross-checked with the validation sample, which is a sub set of 30% of the training sample and it is not used for training. The training and validation samples are split in 768 batches, at each batch the internal model parameters are updated. Then, the training is performed up to 400 epochs, each epoch is a complete set of events and after an epoch the metric response is updated. However, the training is stopped after 20 epochs without validation loss improvement, also to avoid overtraining.

The variables used for the training are different for each category. For the 0-jet ggH tagged training, 21 input variables are used:

- $E_T^{\text{miss}}$  variables:
  - pf  $E_T^{\text{miss}}$ ;
  - track  $E_T^{\text{miss}}$ ;
  - suppressed PU  $E_T^{\text{miss}}$  (Puppi  $E_T^{\text{miss}}$ );
  - proj. pf  $E_T^{\text{miss}}$ ;
  - proj. track  $E_T^{\text{miss}}$ ;
  - minimum proj.  $E_T^{\text{miss}}$ ;
  - pf  $E_T^{\text{miss}}$  divided  $\sum E_T^{\text{miss}}$  ( $E_T^{\text{miss}} / \sum E_T^{\text{miss}}$ );
- kinematic variables:
  - $p_T^{ll}$ ;
  - recoil ( $p_T^{WW}$ );
  - $p_T^{jet_1}$ ;
  - $m_T^H$ ;
  - $m_T^{W_1}$ ;
  - $m_T^{W_2}$ ;
  - $u_{\perp}$ ;
  - $u_{\parallel}$ ;
- azimuthal angles differences:
  - $\Delta\phi_{l_1, E_T^{\text{miss}}}$ ;
  - $\Delta\phi_{l_2, E_T^{\text{miss}}}$ ;
  - $\Delta\phi_{ll, E_T^{\text{miss}}}$ ;
  - $\Delta\phi_{jet_1, E_T^{\text{miss}}}$ ;
  - $\Delta\phi_{ll, jet_1}$ ;
- number of primary vertices ( $n_{vtx}$ ).

For the 1-jet ggH tagged training, the  $p_T^{jet_2}$  is added in the list of training variables. While for the 2-jet ggH and 2-jet VH tagged categories, more 5 variables related to the second jet are added:

- $\Delta\phi_{jet_2, E_T^{\text{miss}}}$ ;
- $\Delta\phi_{jj, E_T^{\text{miss}}}$ ;

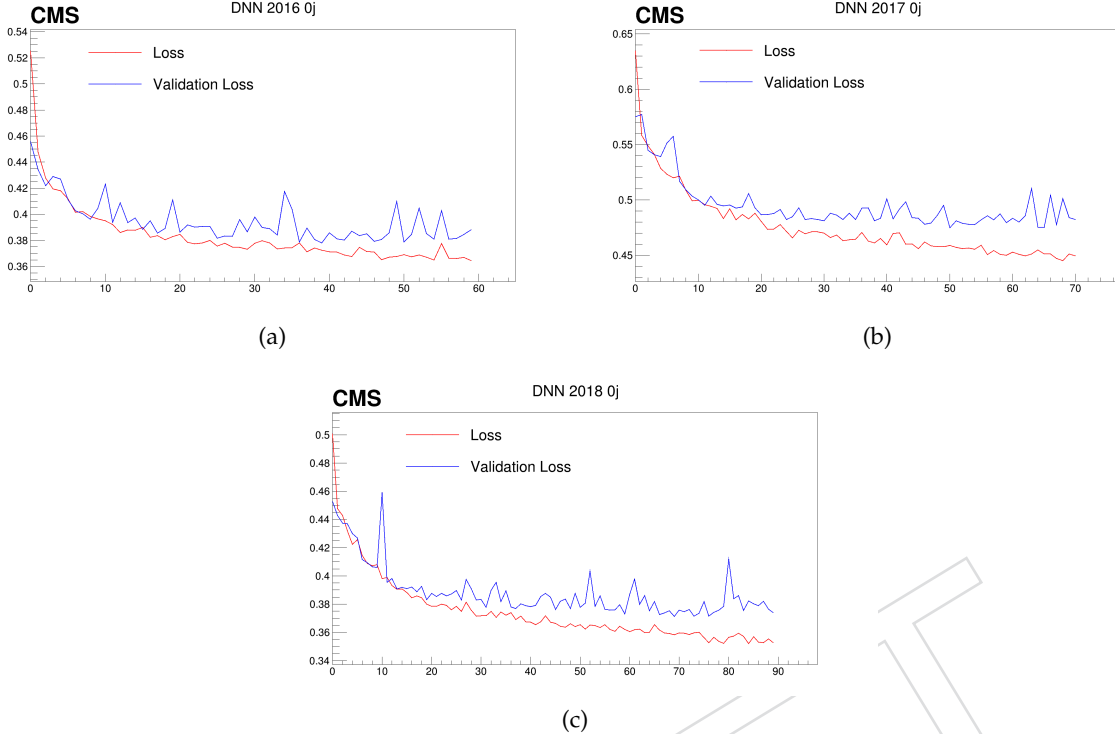


Figure 105: 0j-jet ggH tagged loss function performance in function of epochs for 2016 (left), 2017 (right) and 2018 (bottom).

- 999    •  $\Delta\phi_{ll,jet_2}$ ;
- 1000    •  $\Delta\phi_{ll,jj}$ ;
- 1001    •  $p_T^{TOT}$ ;
- 1002    •  $m_T^{TOT}$ ;

1003 And for the training of the VBF category, the centrality of the jets  $c_\eta^{jj}$  is added, totalizing 28  
1004 input variables.

1005 The loss metric performance in function of the number of epochs for each of the trainings are  
1006 in Fig. 105-109. Discrepancies between the training and validation samples of this function are  
1007 indicative of a possible overtraining. The train is stopped when the validation loss stops to  
1008 improve, to avoid the deterioration of the performance. The resulting discriminator distribu-  
1009 tions are in Fig. 110-114, there are large separation between signal and background in all the  
1010 categories. Moreover, no inconsistencies of the discriminator regarding the training and final  
1011 samples are observed, this is an important proof that the performances have no overtraining.  
1012 These variables will be called DYMVA<sub>DNN</sub> through the rest of this note.

## 1013 9.2 DYMVA<sub>DNN</sub> discriminator

1014 To check if this new variable is well describing data, it is checked the distribution in fake  $E_T^{\text{miss}}$   
1015 like events in DY SF control region: same flavor and opposite charge leptons with leading lep-  
1016 ton  $p_T > 25$  GeV, trailing electron (muon)  $p_T > 13(10)$  GeV, third lepton veto, b-veto, Z peak  
1017 events ( $|m_{ll} - m_Z| < 15$ ). The MC distribution of DYMVA<sub>DNN</sub> is not properly describing data  
1018 because in this region the  $E_T^{\text{miss}}$  input variables are not well described, too. Besides, discrep-  
1019 ances between MC/data is expected as the DY MC samples used for the training are different.

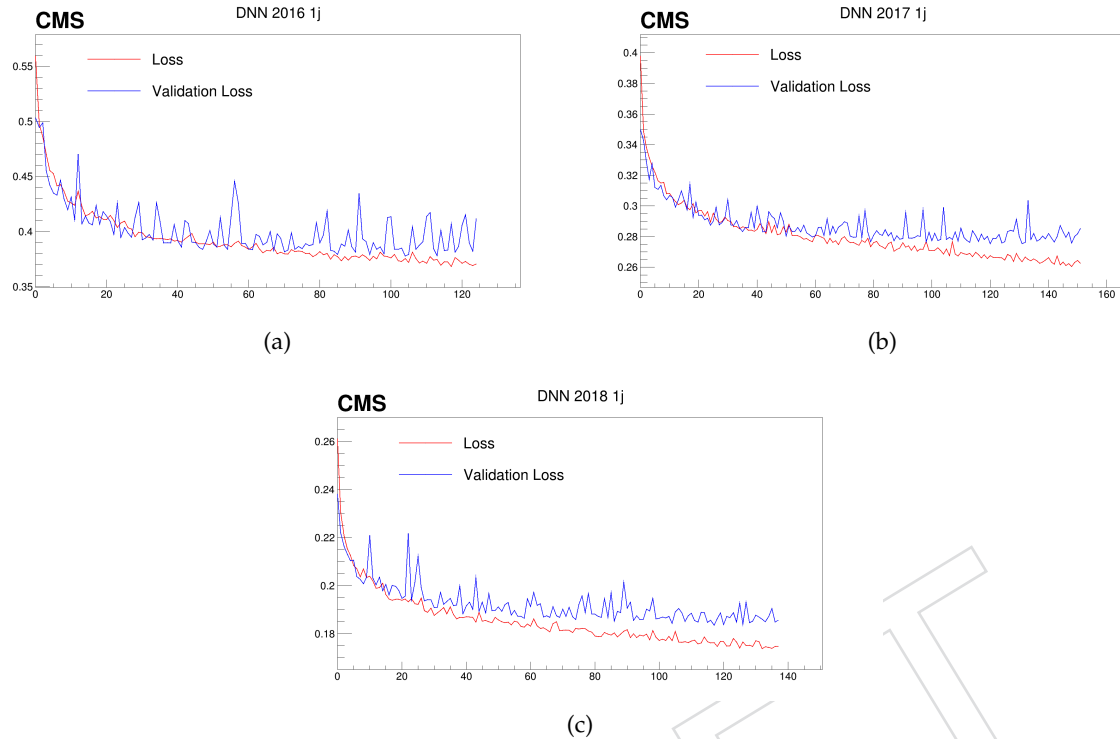


Figure 106: 1j-jet ggH tagged loss function performance in function of epochs for 2016 (left), 2017 (right) and 2018 (bottom).

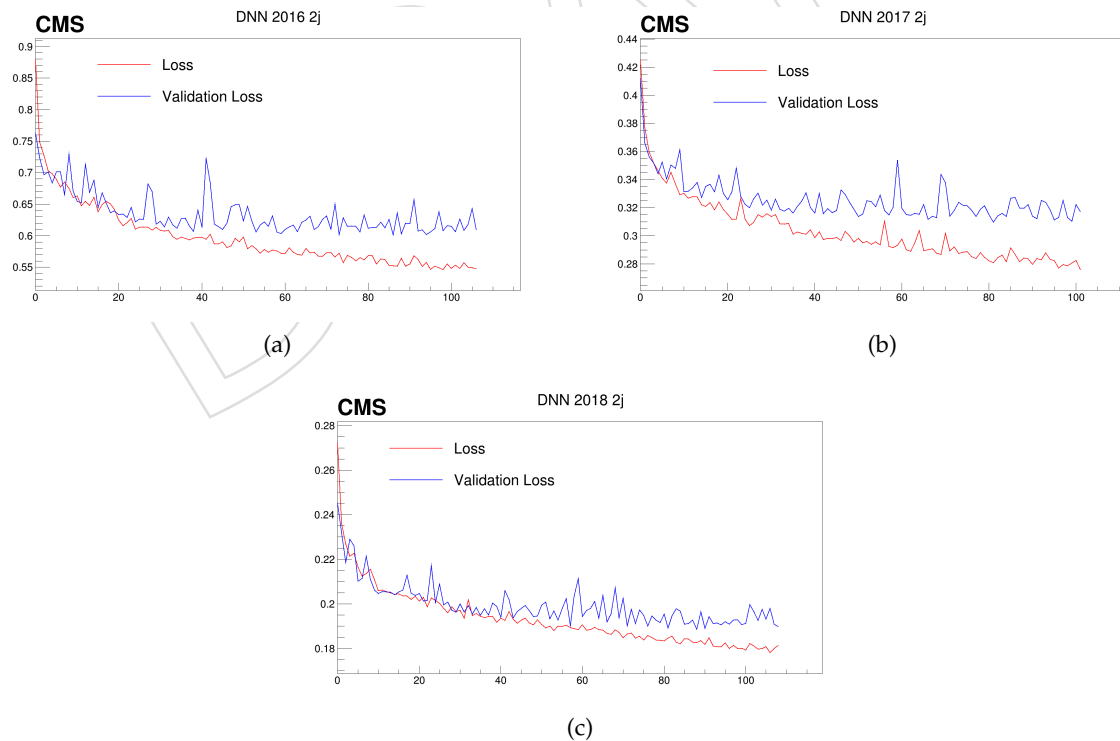


Figure 107: 2j-jet ggH tagged loss function performance in function of epochs for 2016 (left), 2017 (right) and 2018 (bottom).

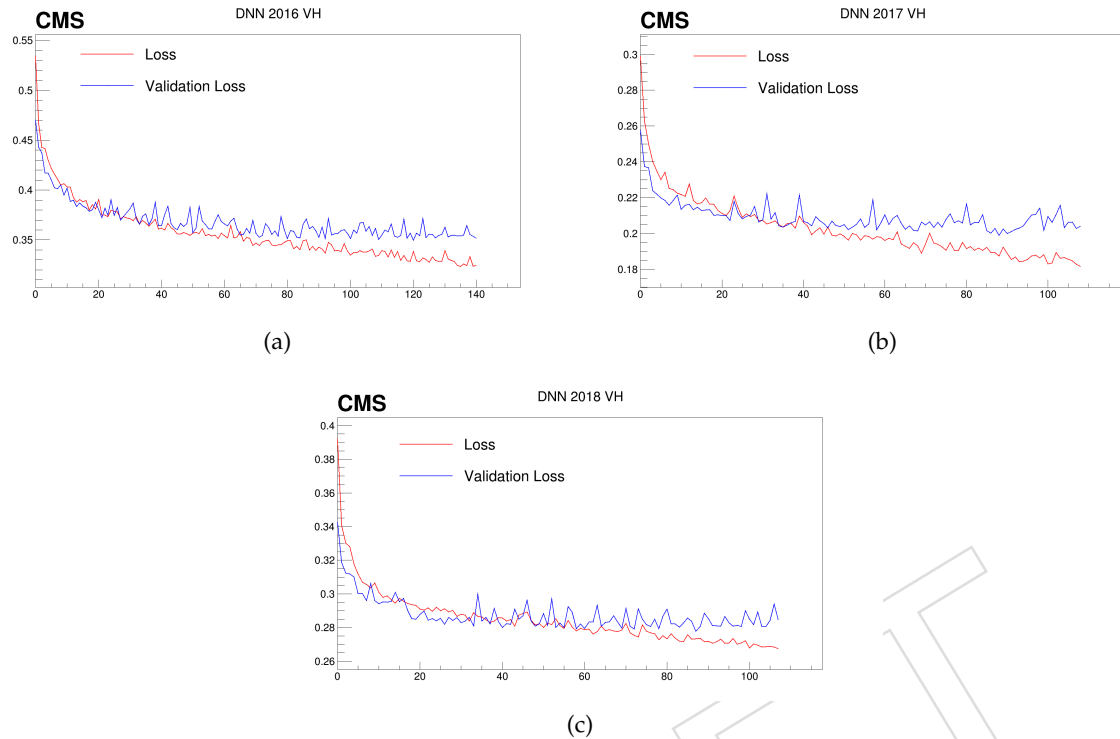


Figure 108: 2j-jet VH tagged loss function performance in function of epochs for 2016 (left), 2017 (right) and 2018 (bottom).

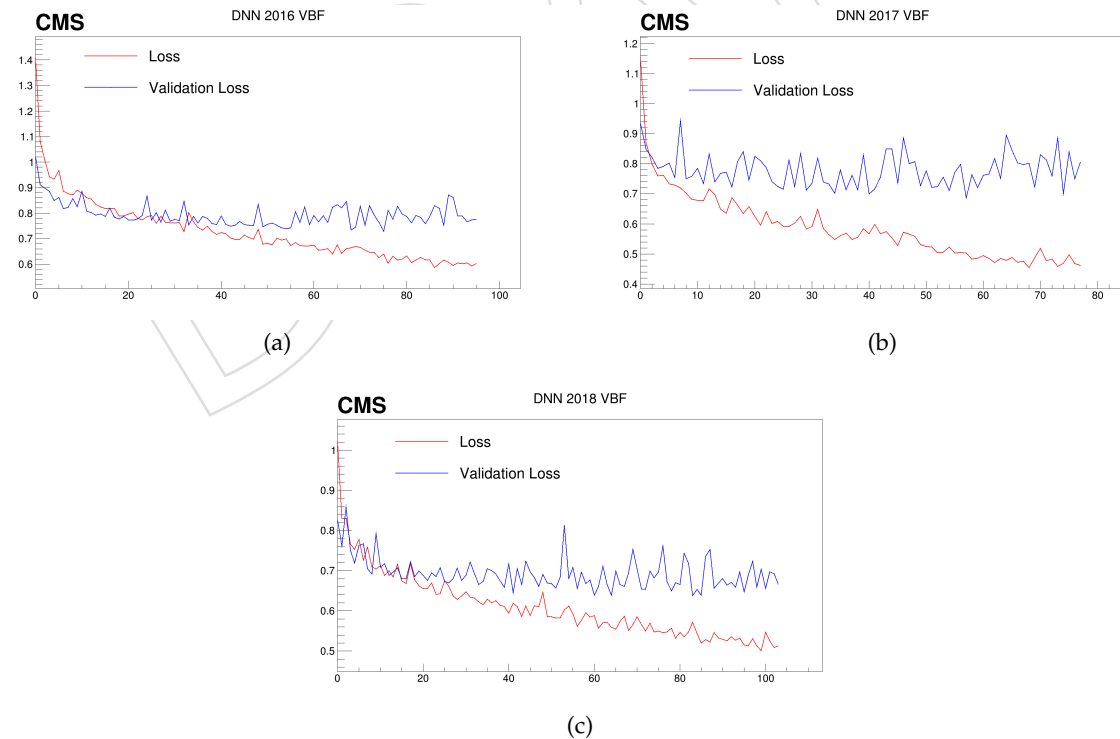


Figure 109: 2j-jet VBF tagged loss function performance in function of epochs for 2016 (left), 2017 (right) and 2018 (bottom).

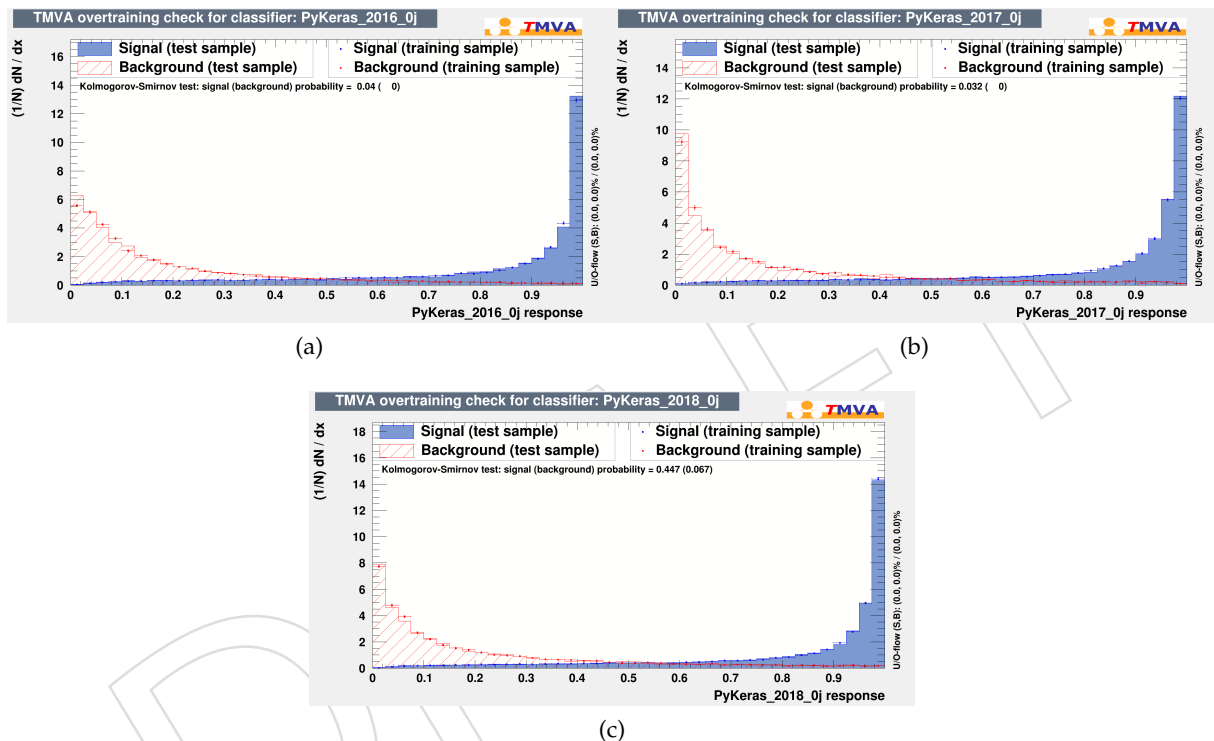


Figure 110: 0j-jet ggH tagged DYMVA<sub>DNN</sub> discriminator distribution for the three different years: 2016 (left), 2017 (right) and 2018 (bottom). The Higgs signal is in blue and DY background is in red. The histogram shows the distribution for the training sample, while the graph shows the final response from the analysis samples.

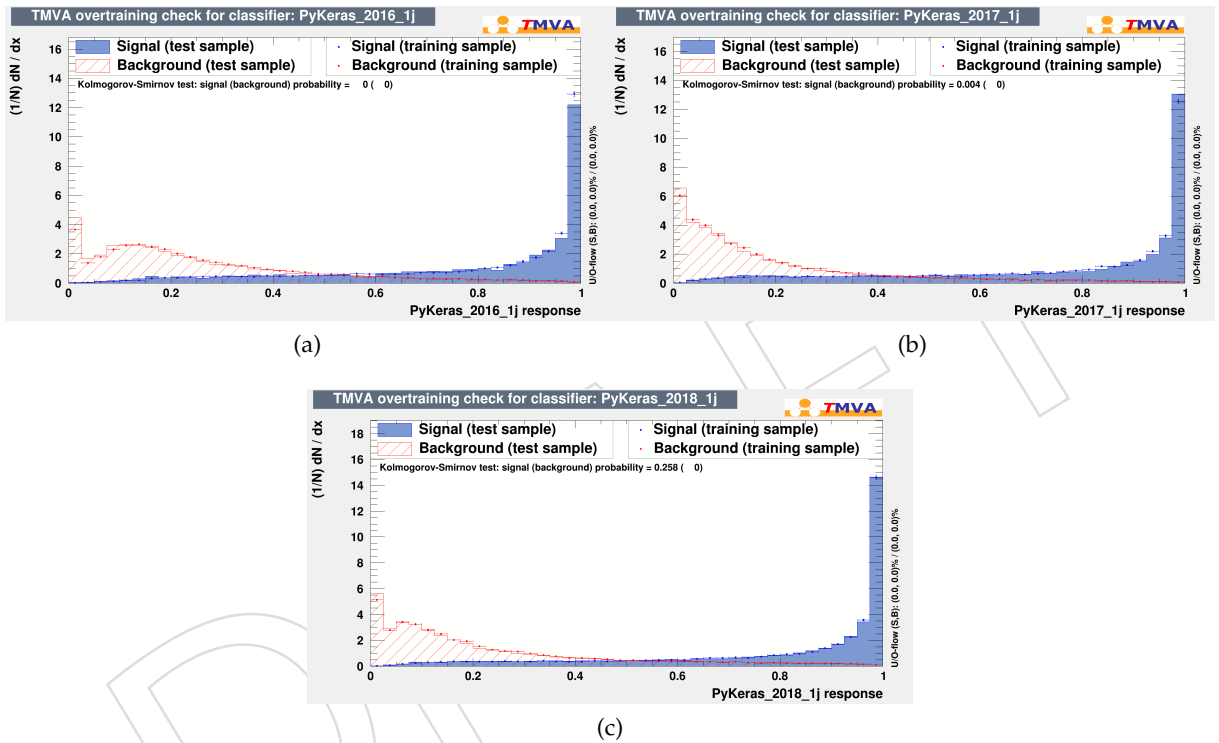


Figure 111: 1j-jet ggH tagged DYMVA<sub>DNN</sub> discriminator distribution for the three different years: 2016 (left), 2017 (right) and 2018 (bottom). The Higgs signal is in blue and DY background is in red. The histogram shows the distribution for the training sample, while the graph shows the final response from the analysis samples.

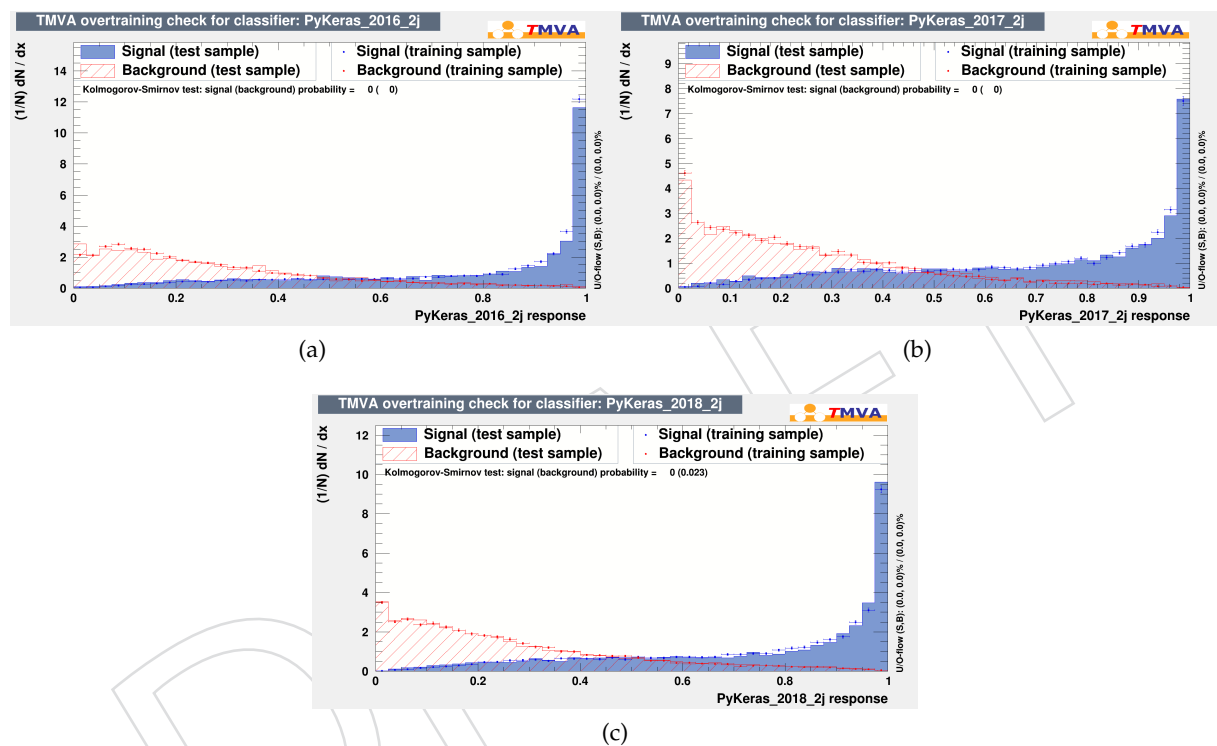


Figure 112: 2j-jet ggH tagged DYMVA<sub>DNN</sub> discriminator distribution for the three different years: 2016 (left), 2017 (right) and 2018 (bottom). The Higgs signal is in blue and DY background is in red. The histogram shows the distribution for the training sample, while the graph shows the final response from the analysis samples.

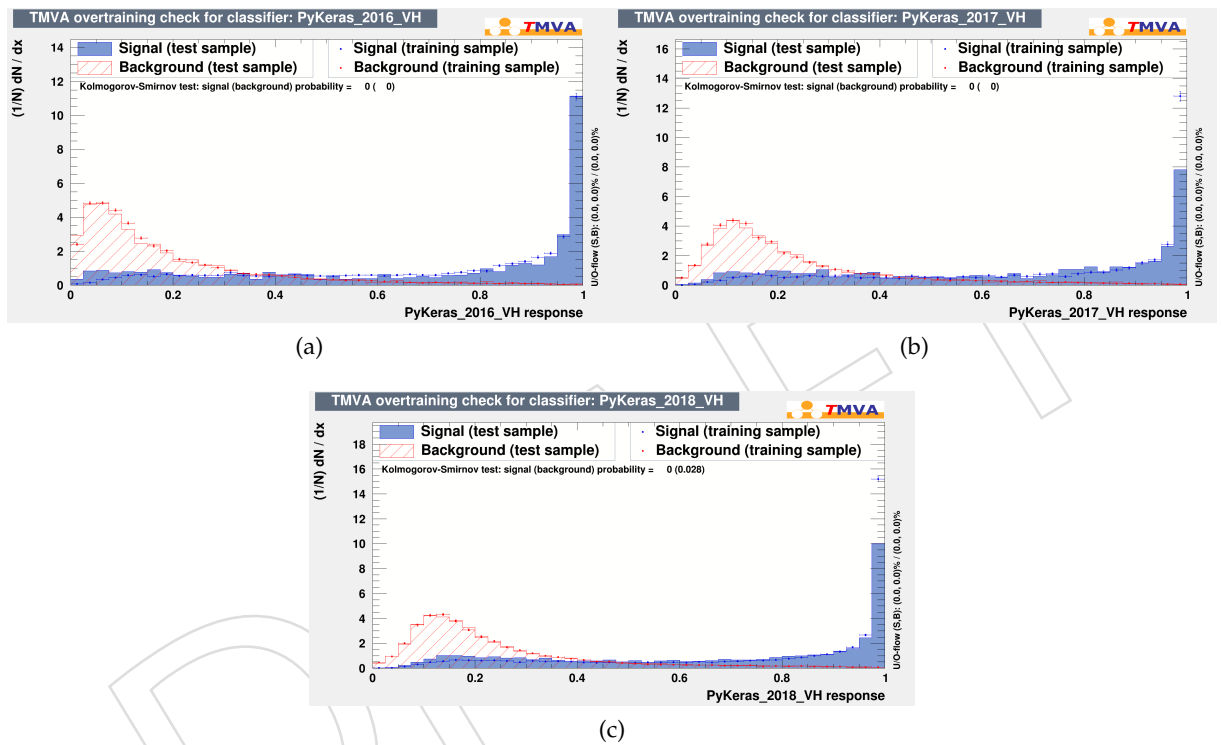


Figure 113: 2j-jet VH tagged DYMVA<sub>DNN</sub> discriminator distribution for the three different years: 2016 (left), 2017 (right) and 2018 (bottom). The Higgs signal is in blue and DY background is in red. The histogram shows the distribution for the training sample, while the graph shows the final response from the analysis samples.

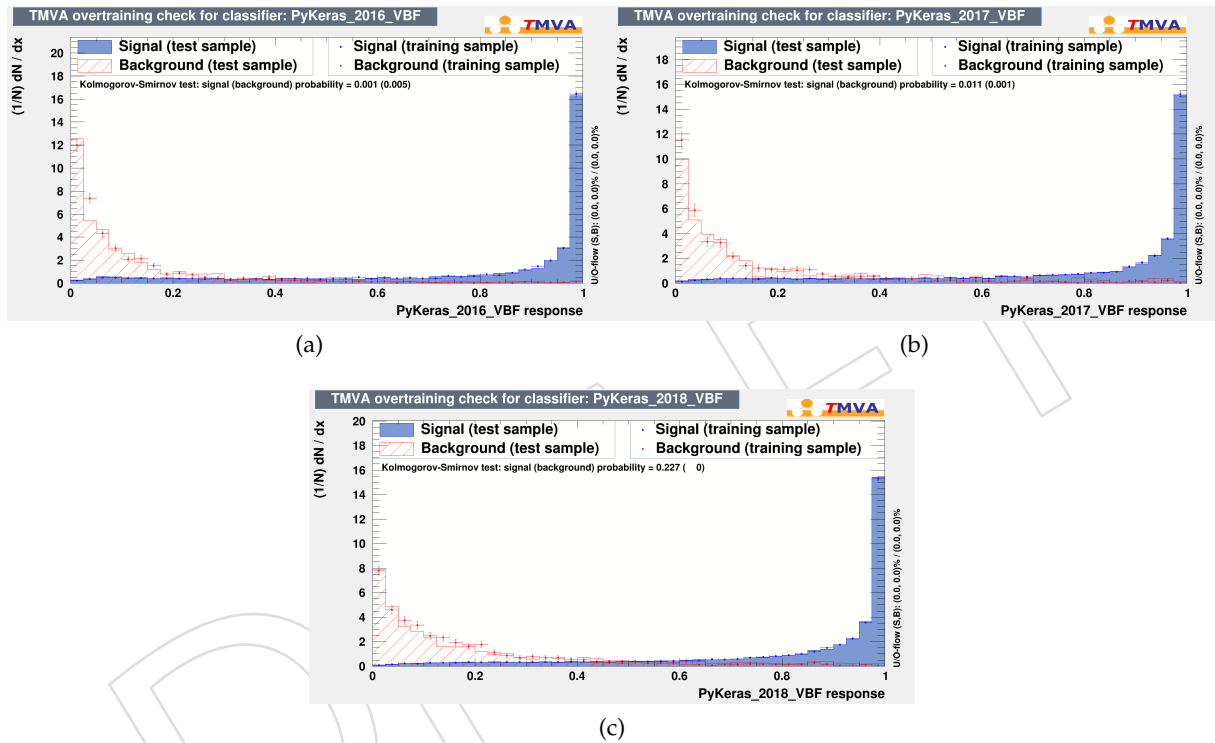


Figure 114: 2j-jet VBF tagged DYMVA<sub>DNN</sub> discriminator distribution for the three different years: 2016 (left), 2017 (right) and 2018 (bottom). The Higgs signal is in blue and DY background is in red. The histogram shows the distribution for the training sample, while the graph shows the final response from the analysis samples.

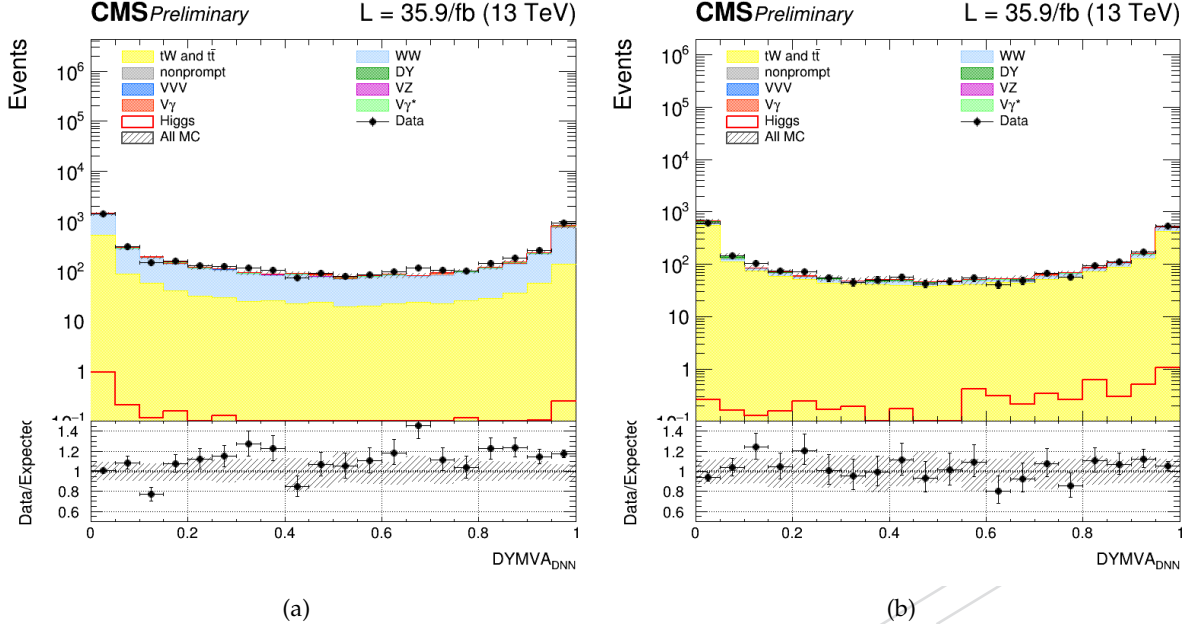


Figure 115: Distributions of the 2016 DYMVA<sub>DNN</sub> output for 0-jet ggH tagged different-flavor final state in WW CR (left) and top CR (right).

For this reason, a data-driven estimate of DY background is performed. However, the DYMVA<sub>DNN</sub> distributions are checked in real  $E_T^{\text{miss}}$  signal-like events (Fig 115-Fig 129), by looking at WW DF control region: different flavor and opposite charge leptons with leading electron (muon)  $p_T > 25(20)$  GeV, trailing electron (muon)  $p_T > 13(10)$  GeV, third lepton veto, b-veto,  $m_{ll} > 80$  GeV, and in Top DF control region: different flavor and opposite charge leptons with leading electron (muon)  $p_T > 25(20)$  GeV, trailing electron (muon)  $p_T > 13(10)$  GeV, third lepton veto, b-tag, Z-veto. In these regions, the discriminators are quite well described.

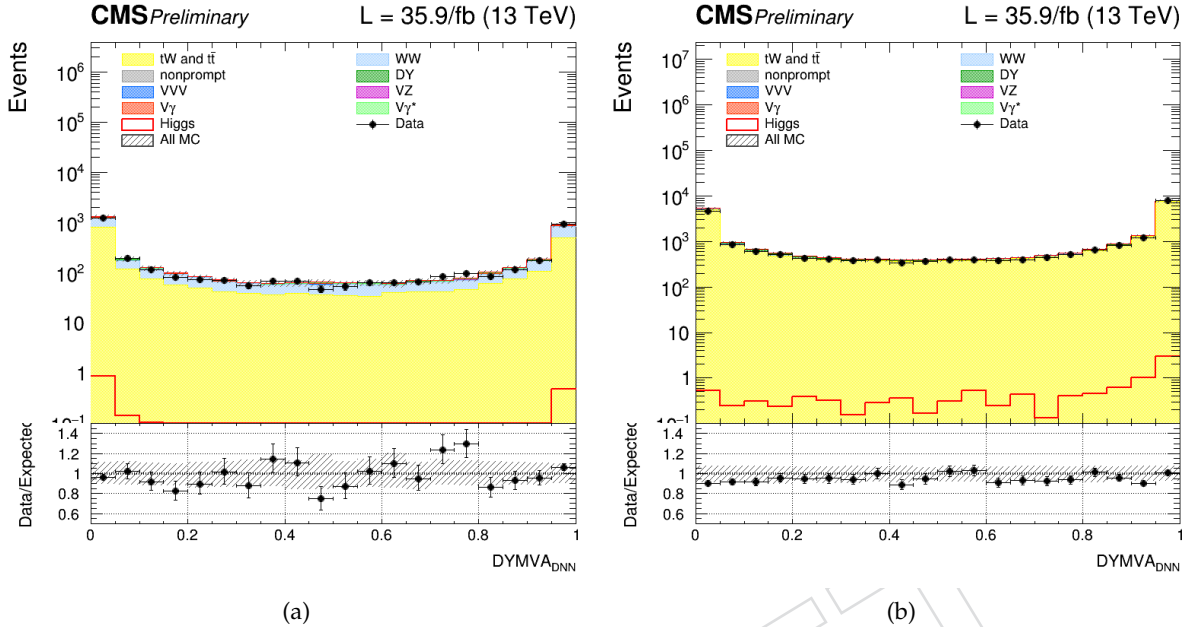


Figure 116: Distributions of the 2016 DYMVA<sub>DNN</sub> output for 1-jet ggH tagged different-flavor final state in WW CR (left) and top CR (right).

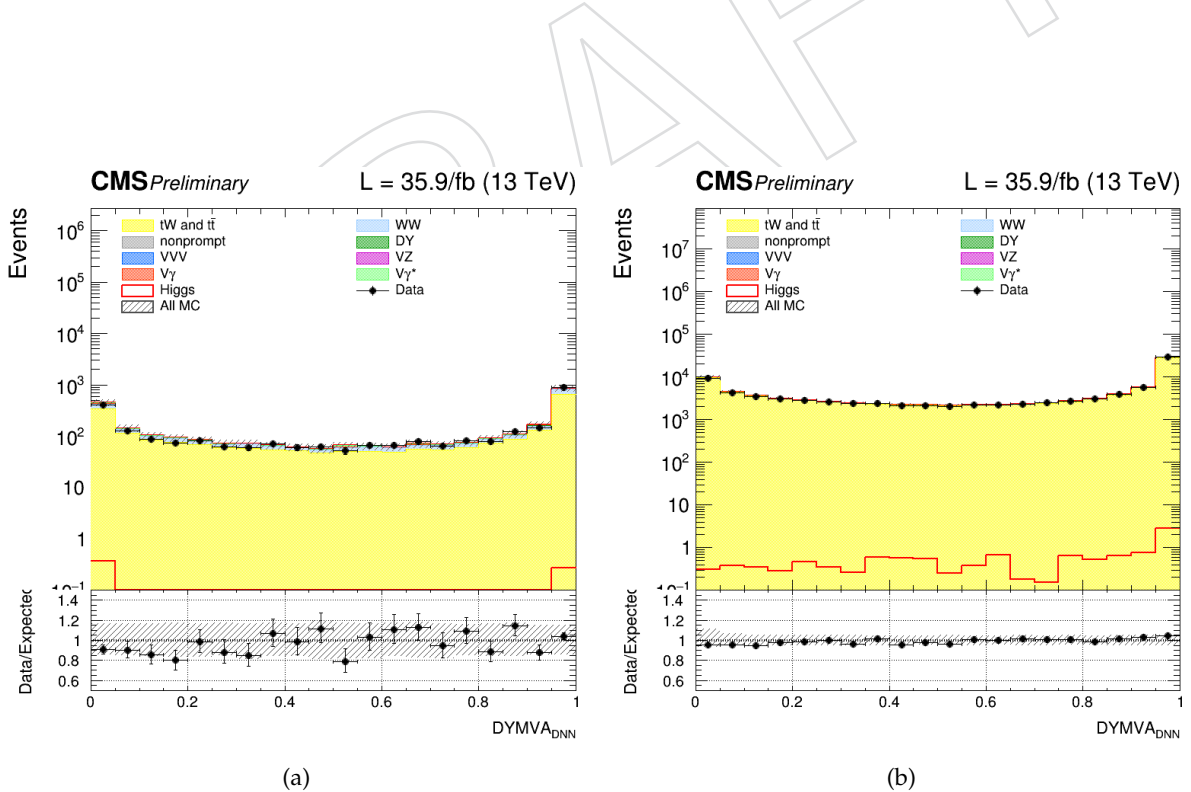


Figure 117: Distributions of the 2016 DYMVA<sub>DNN</sub> output for 2-jet ggH tagged different-flavor final state in WW CR (left) and top CR (right).

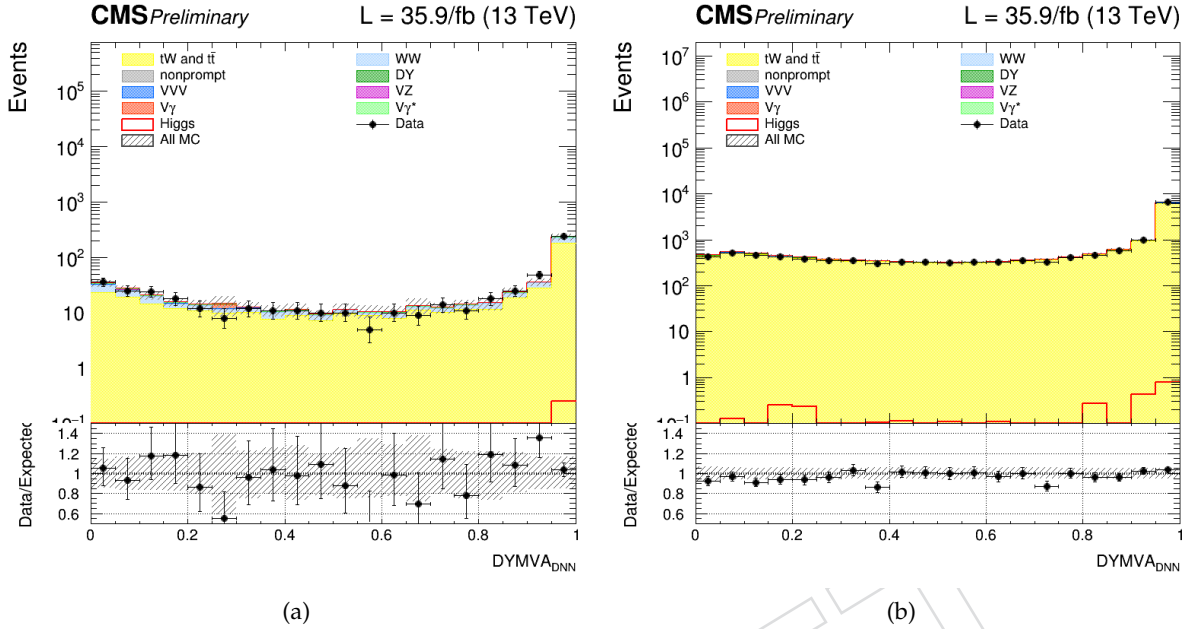


Figure 118: Distributions of the 2016 DYMVA<sub>DNN</sub> output for 2-jet VH tagged different-flavor final state in WW CR (left) and top CR (right).

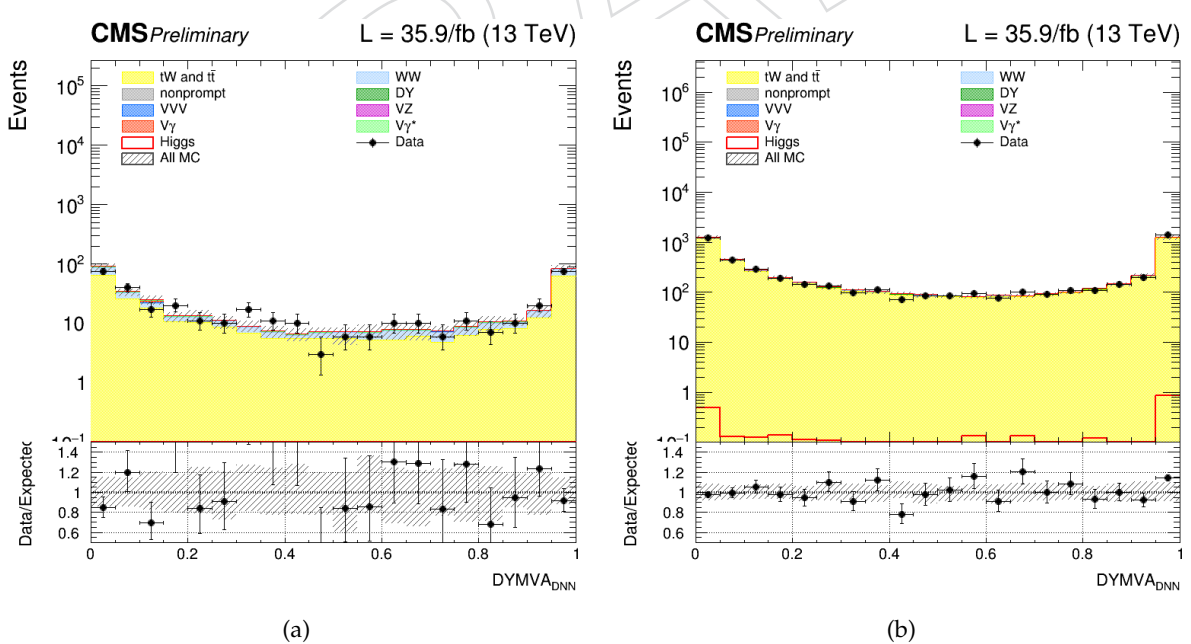


Figure 119: Distributions of the 2016 DYMVA<sub>DNN</sub> output for 2-jet VBF tagged different-flavor final state in WW CR (left) and top CR (right).

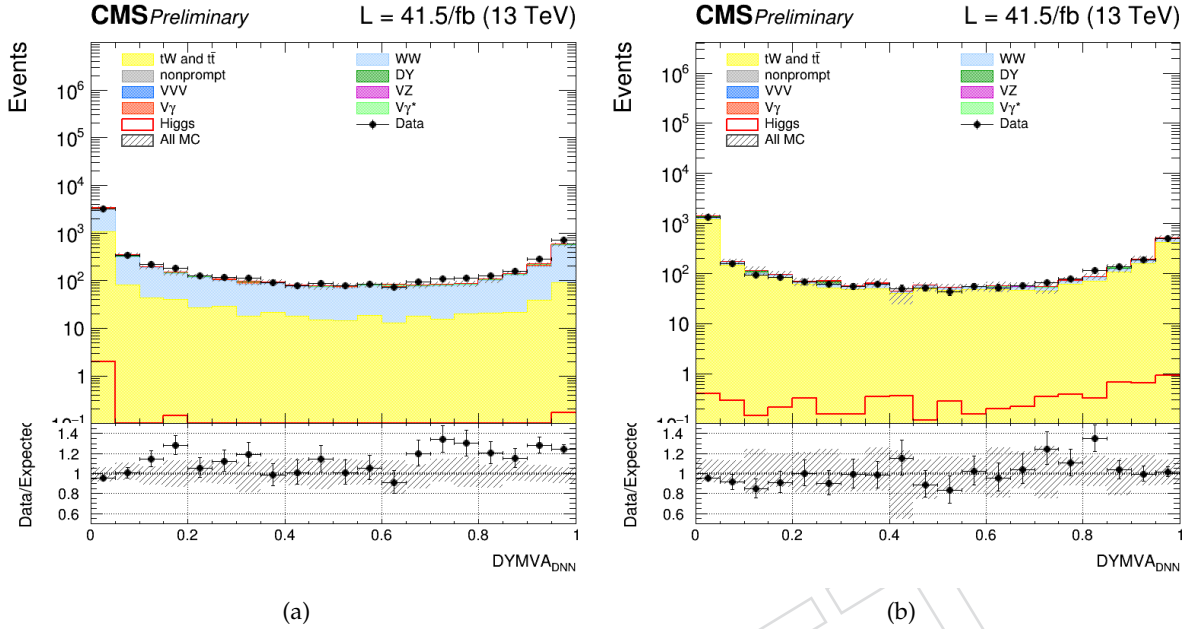


Figure 120: Distributions of the 2017 DYMVA<sub>DNN</sub> output for 0-jet ggH tagged different-flavor final state in WW CR (left) and top CR (right).

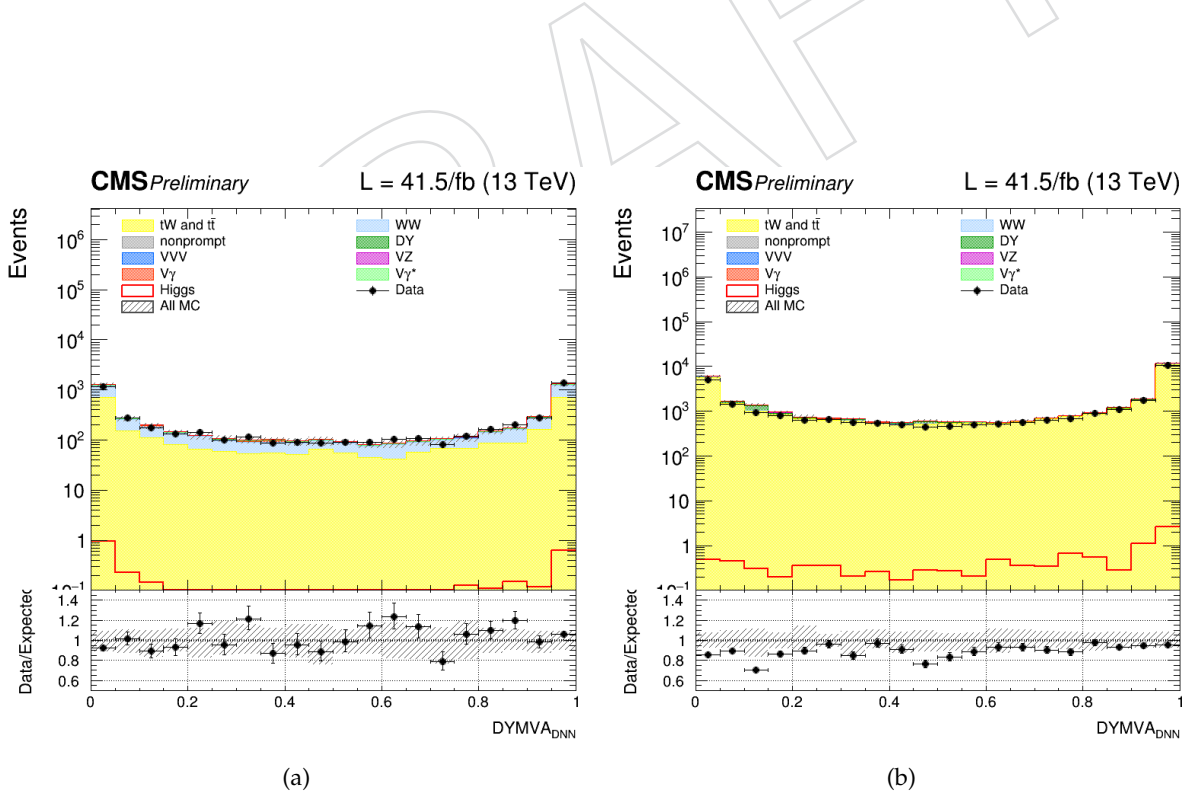


Figure 121: Distributions of the 2017 DYMVA<sub>DNN</sub> output for 1-jet ggH tagged different-flavor final state in WW CR (left) and top CR (right).

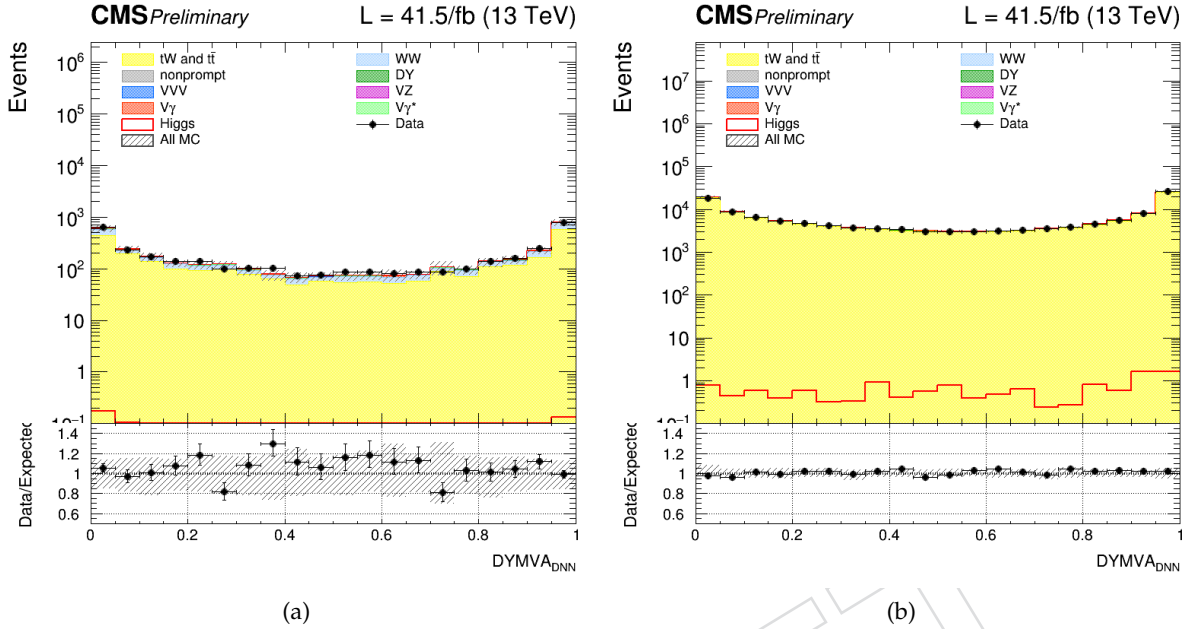


Figure 122: Distributions of the 2017 DYMVA<sub>DNN</sub> output for 2-jet ggH tagged different-flavor final state in WW CR (left) and top CR (right).

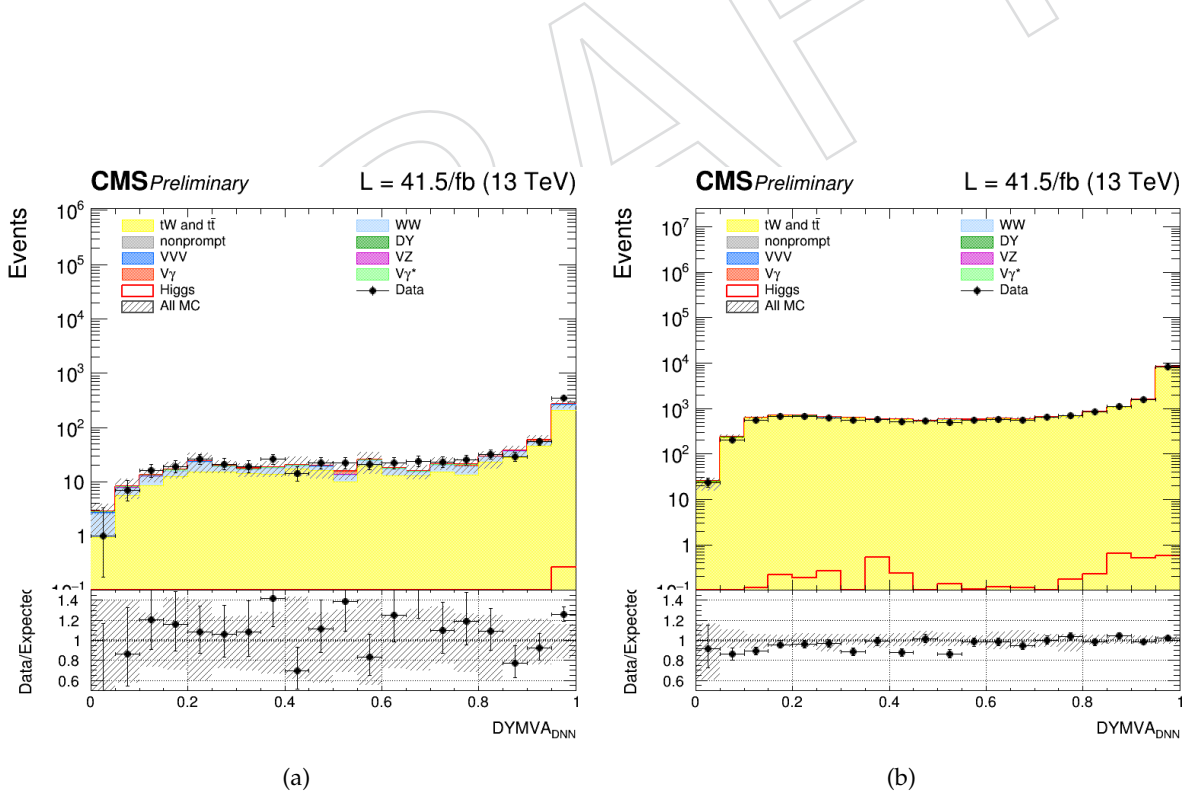


Figure 123: Distributions of the 2017 DYMVA<sub>DNN</sub> output for 2-jet VH tagged different-flavor final state in WW CR (left) and top CR (right).

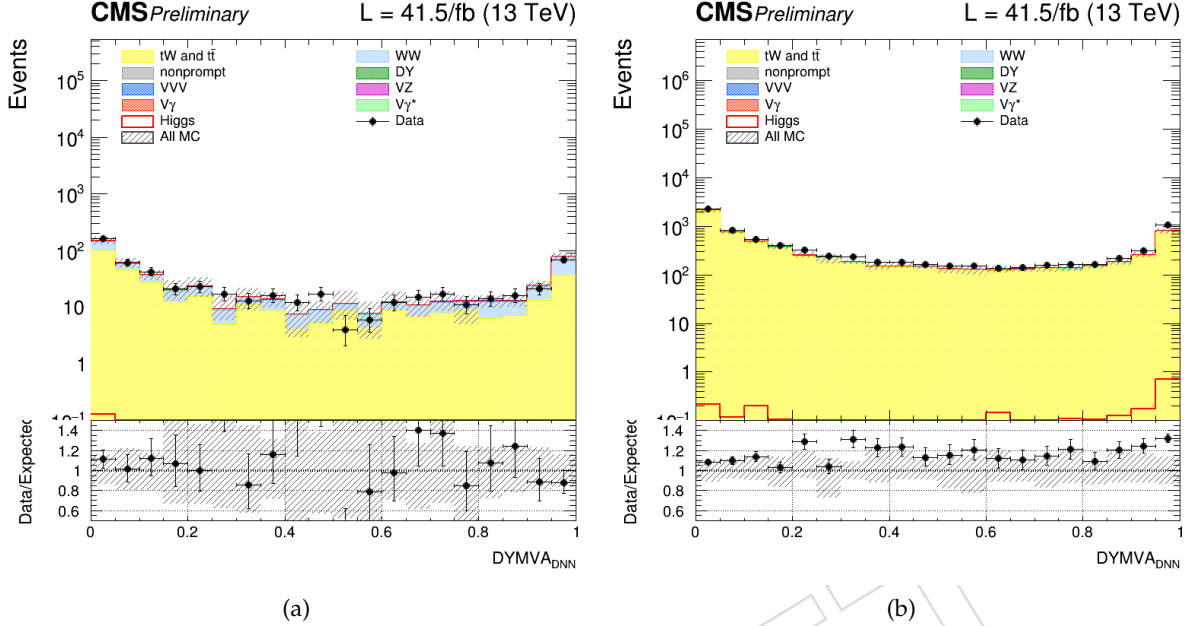


Figure 124: Distributions of the 2017 DYMVA<sub>DNN</sub> output for 2-jet VBF tagged different-flavor final state in WW CR (left) and top CR (right).

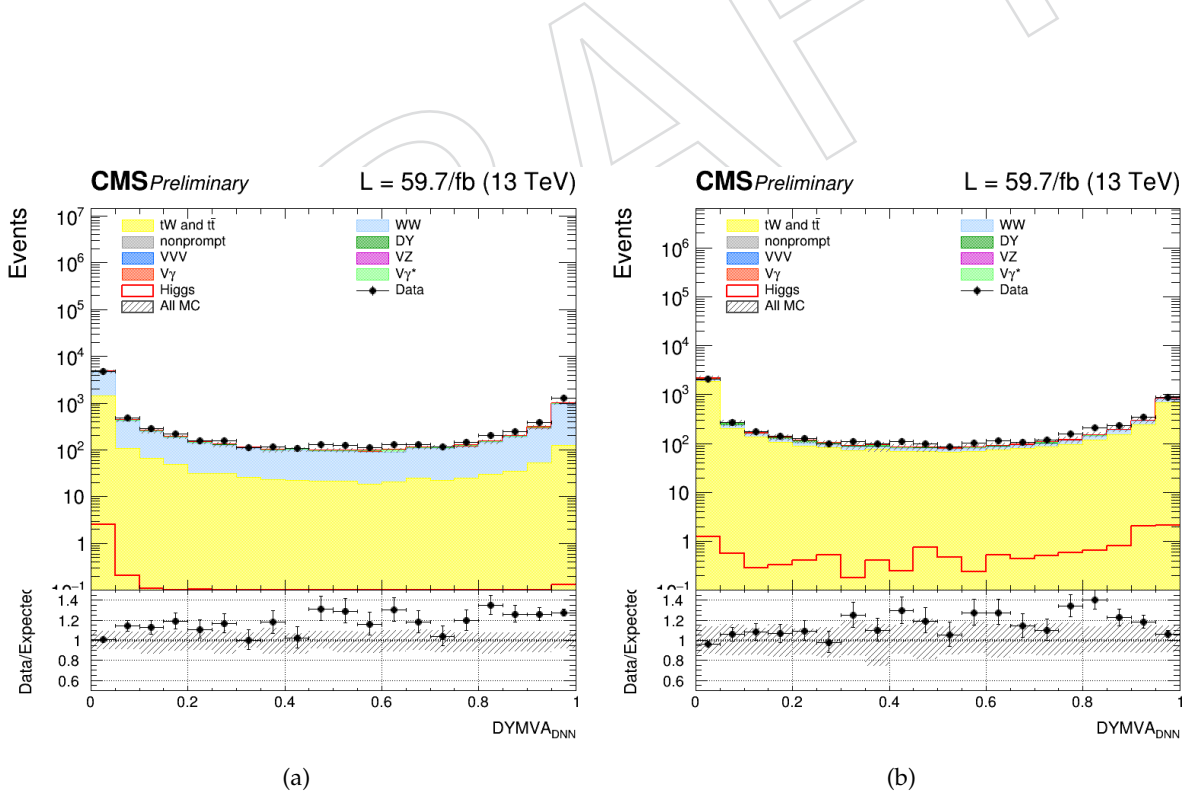


Figure 125: Distributions of the 2018 DYMVA<sub>DNN</sub> output for 0-jet ggH tagged different-flavor final state in WW CR (left) and top CR (right).

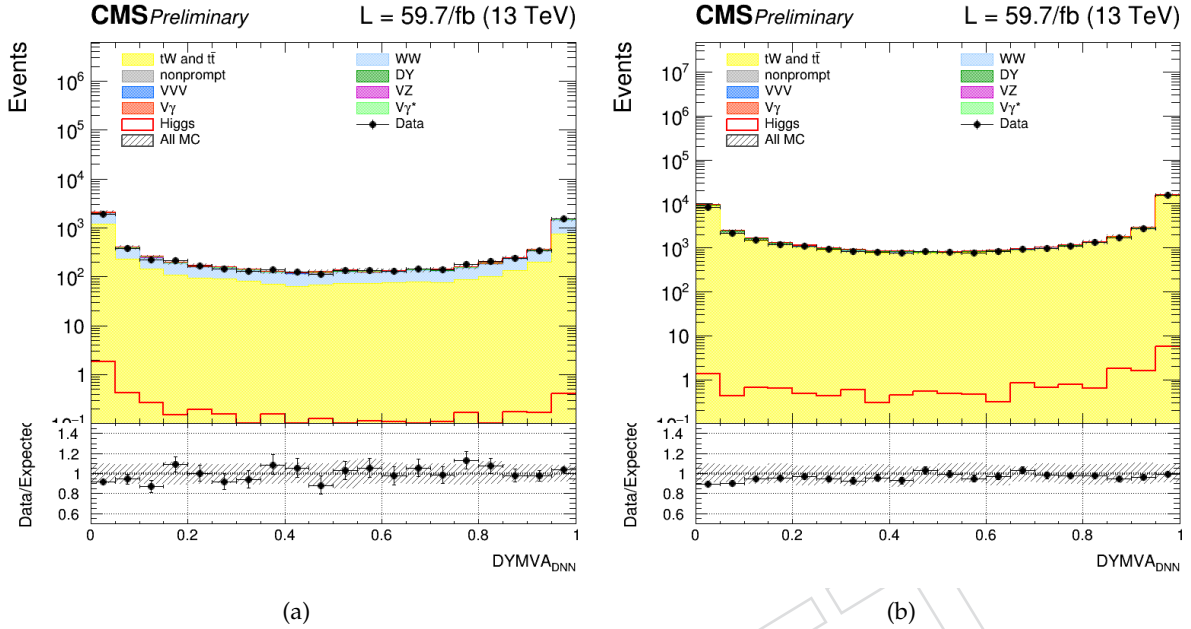


Figure 126: Distributions of the 2018 DYMVA<sub>DNN</sub> output for 1-jet ggH tagged different-flavor final state in WW CR (left) and top CR (right).

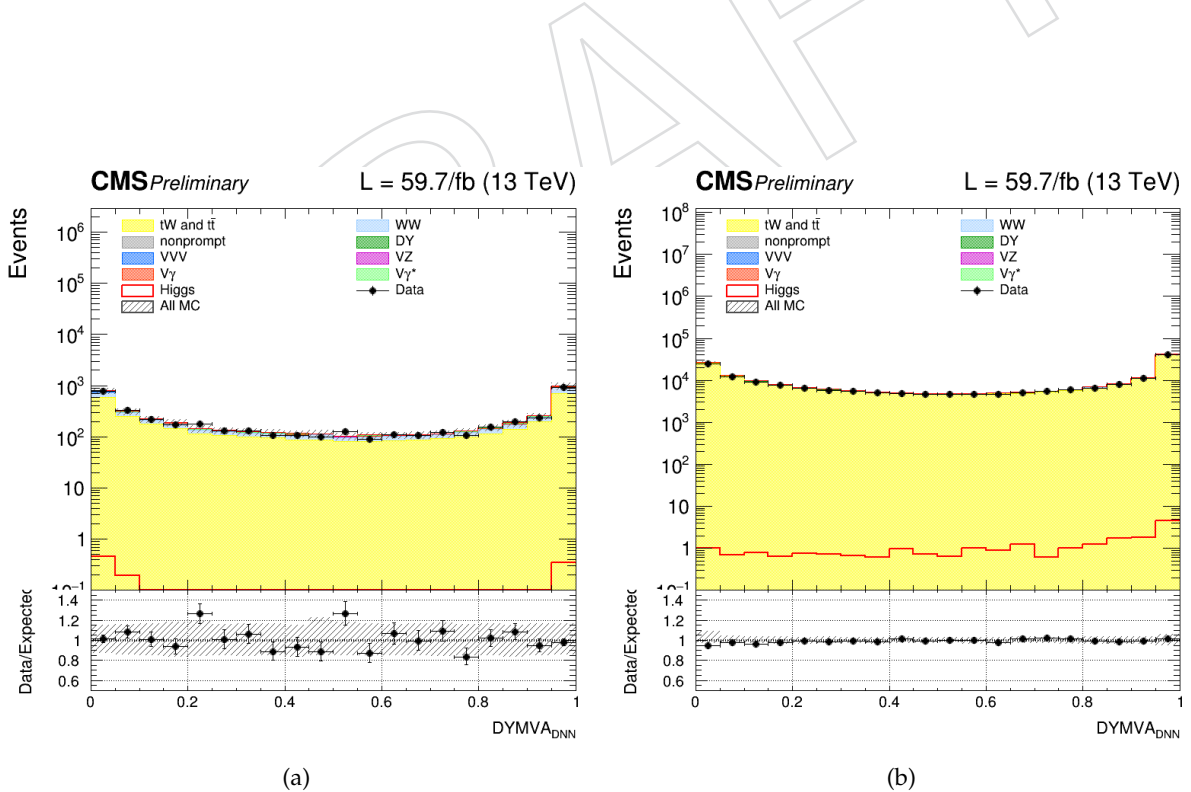


Figure 127: Distributions of the 2018 DYMVA<sub>DNN</sub> output for 2-jet ggH tagged different-flavor final state in WW CR (left) and top CR (right).

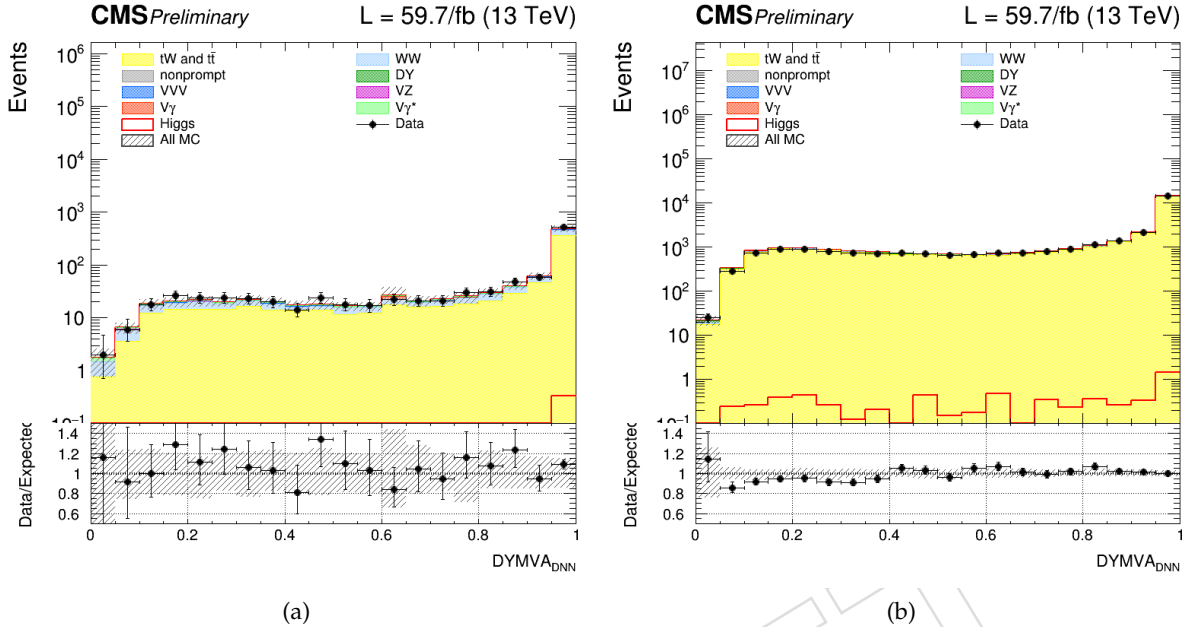


Figure 128: Distributions of the 2018 DYMVA<sub>DNN</sub> output for 2-jet VH tagged different-flavor final state in WW CR (left) and top CR (right).

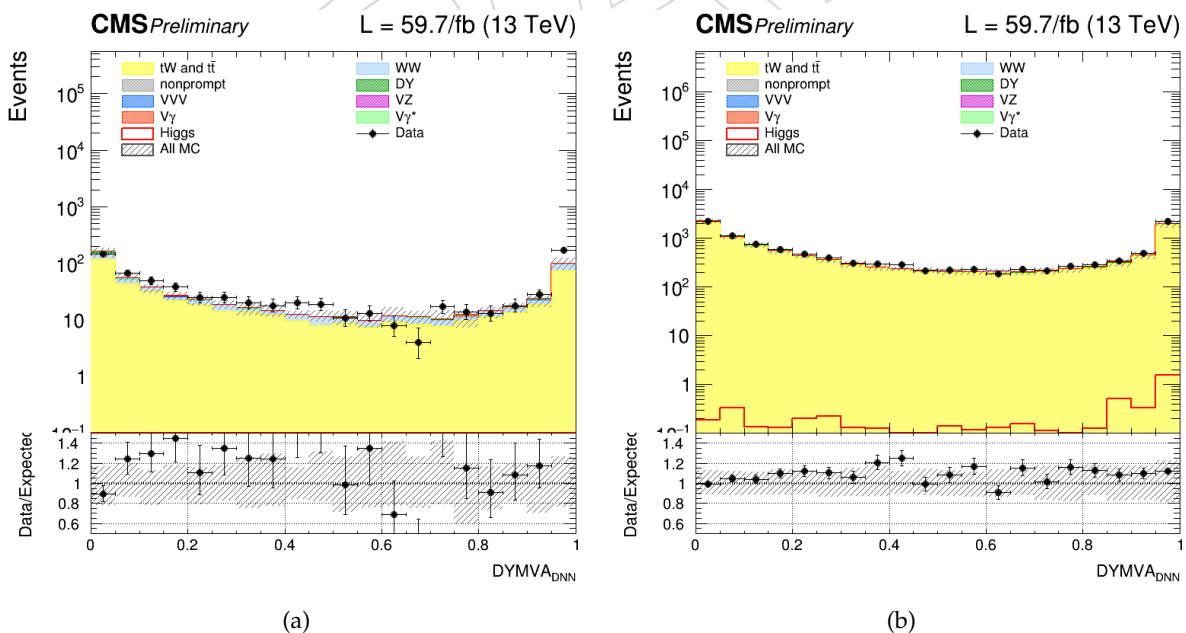


Figure 129: Distributions of the 2018 DYMVA<sub>DNN</sub> output for 2-jet VBF tagged different-flavor final state in WW CR (left) and top CR (right).

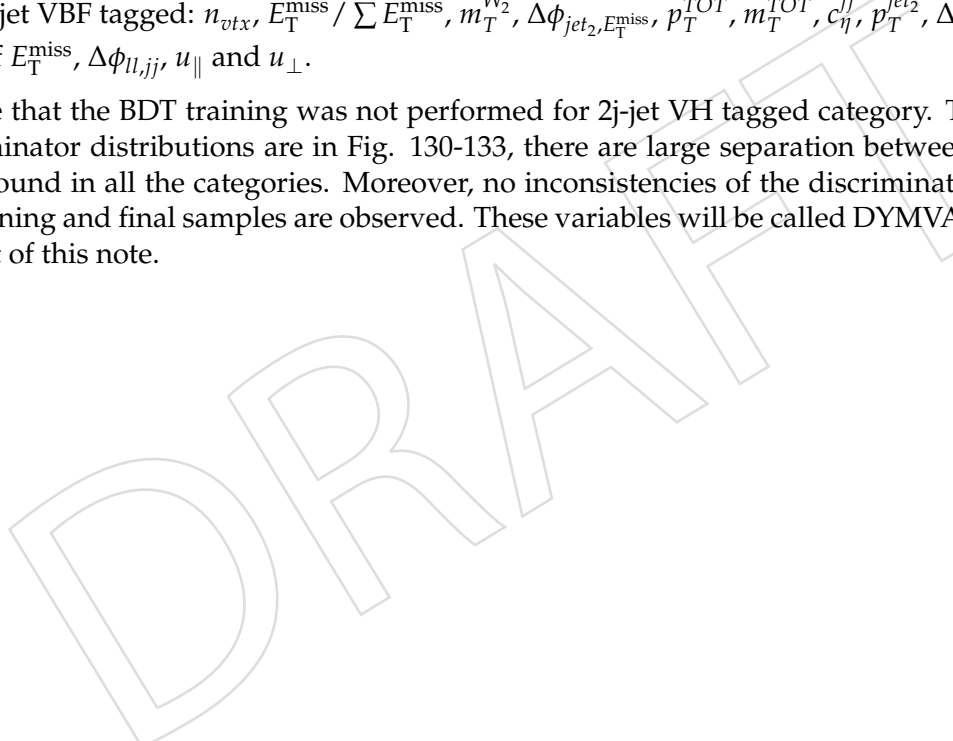
---

### 1028 9.3 BDT training

1029 For the BDT training, all the possible combinations of the previous input variables are consid-  
 1030 ered, with the maximum of 13 variables per set. These variables provide a good discrimination.  
 1031 On the other hand, the  $n_{vtx}$  variable is added in all combinations because it is useful for corre-  
 1032 lations with PU dependency. After performing the training over all possible sets, the one with  
 1033 higher ROC curve is selected. The best combinations of input variables for each category are  
 1034 the following:

- 1035 • 0-jet ggH tagged:  $n_{vtx}, p_T^{ll}, m_T^H, p_T^{jet_1}, u_{\parallel}, E_T^{\text{miss}} / \sum E_T^{\text{miss}}$ , minimum proj.  $E_T^{\text{miss}}, p_T^{WW}$ ,  
 1036 Puppi  $E_T^{\text{miss}}$ , pf  $E_T^{\text{miss}}$ ,  $\Delta\phi_{jet_1, E_T^{\text{miss}}}$  and  $u_{\perp}$ .
- 1037 • 1-jet ggH tagged:  $n_{vtx}, p_T^{ll},$  minimum proj.  $E_T^{\text{miss}}, u_{\parallel}, E_T^{\text{miss}} / \sum E_T^{\text{miss}}, m_T^{W_1}, \Delta\phi_{l_1, E_T^{\text{miss}}},$   
 1038  $\Delta\phi_{ll, jet_1}, \Delta\phi_{jet_1, E_T^{\text{miss}}}, \Delta\phi_{jet_2, E_T^{\text{miss}}},$  pf  $E_T^{\text{miss}}, m_T^H$  and  $m_T^{TOT}$ .
- 1039 • 2-jet ggH tagged:  $n_{vtx}, u_{\parallel}, m_T^H, p_T^{TOT}, u_{\perp}, \Delta\phi_{ll, jet_1}, p_T^{ll}, E_T^{\text{miss}} / \sum E_T^{\text{miss}},$  pf  $E_T^{\text{miss}}, m_T^{W_1},$   
 1040  $p_T^{jet_1}, \Delta\phi_{jj, E_T^{\text{miss}}}$  and minimum proj.  $E_T^{\text{miss}}$ .
- 1041 • 2-jet VBF tagged:  $n_{vtx}, E_T^{\text{miss}} / \sum E_T^{\text{miss}}, m_T^{W_2}, \Delta\phi_{jet_2, E_T^{\text{miss}}}, p_T^{TOT}, m_T^{TOT}, c_{\eta}^{jj}, p_T^{jet_2}, \Delta\phi_{ll, E_T^{\text{miss}}},$   
 1042 pf  $E_T^{\text{miss}}, \Delta\phi_{ll, jj}, u_{\parallel}$  and  $u_{\perp}$ .

1043 To note that the BDT training was not performed for 2j-jet VH tagged category. The resulting  
 1044 discriminator distributions are in Fig. 130-133, there are large separation between signal and  
 1045 background in all the categories. Moreover, no inconsistencies of the discriminator regarding  
 1046 the training and final samples are observed. These variables will be called DYMVA<sub>BDT</sub> through  
 1047 the rest of this note.



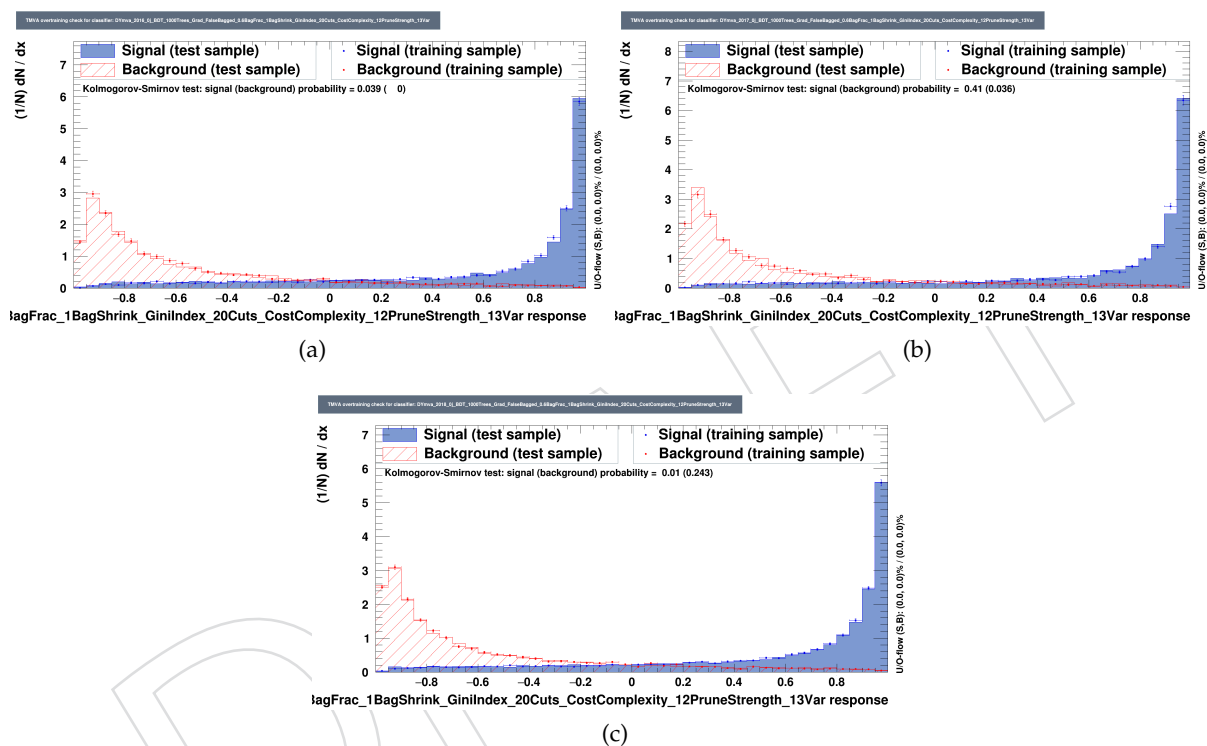


Figure 130: 0j-jet ggH tagged DYMVA<sub>DNN</sub> discriminator distribution for the three different years: 2016 (left), 2017 (right) and 2018 (bottom). The Higgs signal is in blue and DY background is in red. The histogram shows the distribution for the training sample, while the graph shows the final response from the analysis samples.

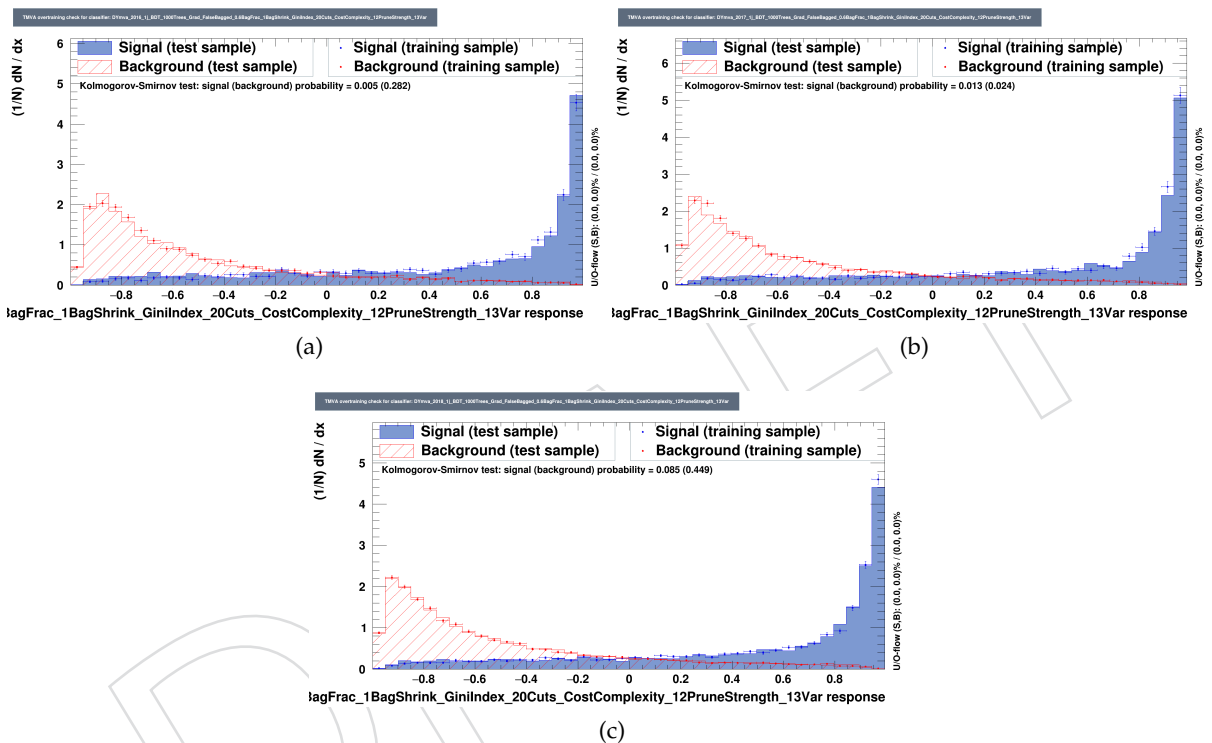


Figure 131: 1j-jet ggH tagged DYMVA<sub>DNN</sub> discriminator distribution for the three different years: 2016 (left), 2017 (right) and 2018 (bottom). The Higgs signal is in blue and DY background is in red. The histogram shows the distribution for the training sample, while the graph shows the final response from the analysis samples.

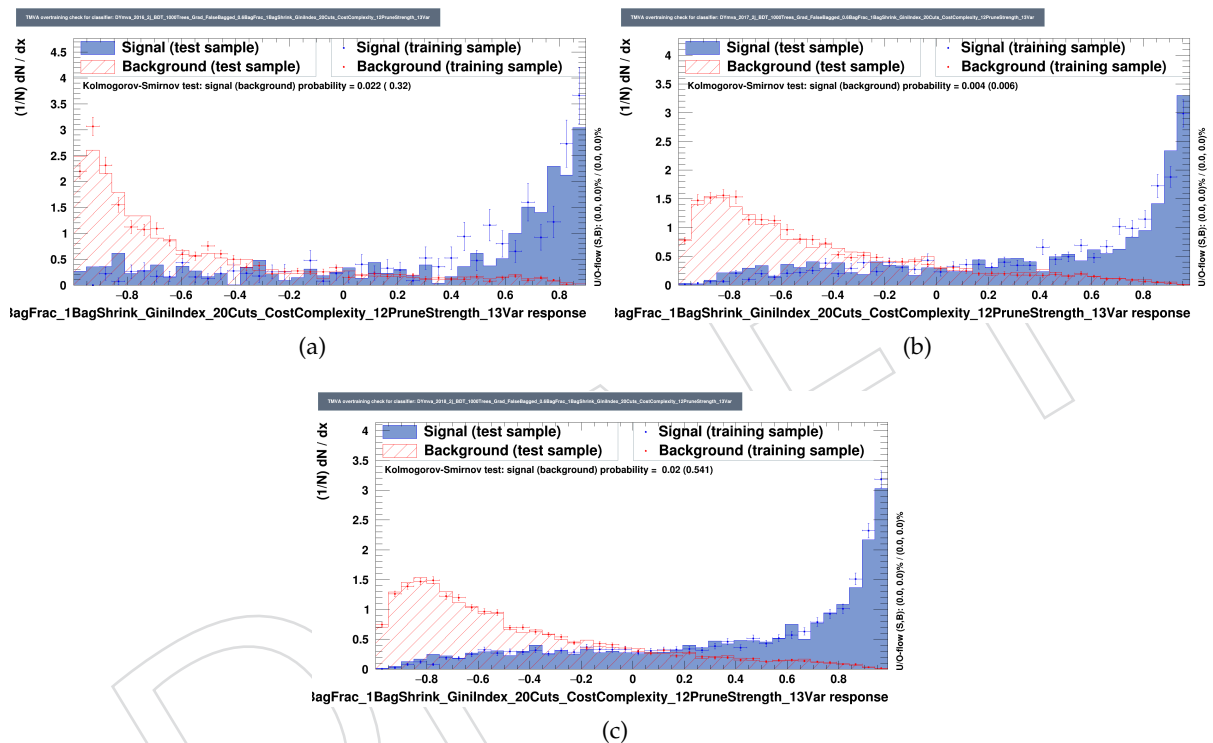


Figure 132: 2j-jet ggH tagged DYMVA<sub>DNN</sub> discriminator distribution for the three different years: 2016 (left), 2017 (right) and 2018 (bottom). The Higgs signal is in blue and DY background is in red. The histogram shows the distribution for the training sample, while the graph shows the final response from the analysis samples.

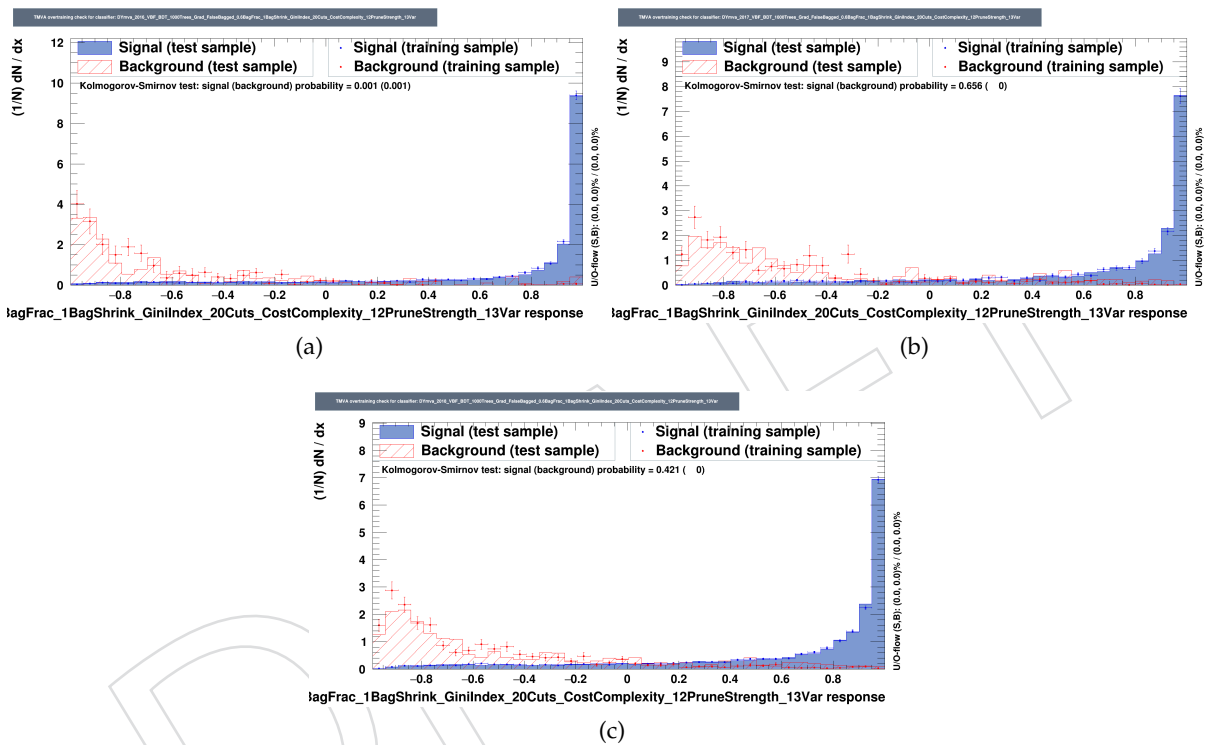


Figure 133: 2j-jet VBF tagged DYMVA<sub>DNN</sub> discriminator distribution for the three different years: 2016 (left), 2017 (right) and 2018 (bottom). The Higgs signal is in blue and DY background is in red. The histogram shows the distribution for the training sample, while the graph shows the final response from the analysis samples.

## 1048 10 Tau embedded samples

1049 Editor: Dennis Roy

### 1050 10.1 Introduction

1051 Embedded samples refer to events selected from data which are used to estimate background  
1052 from  $Z \rightarrow \tau\tau$  using a data-driven technique. It starts off with  $Z \rightarrow \mu\mu$  events being selected  
1053 from data. The two muon tracks and their calorimetry entries are removed from the event. Tau  
1054 leptons are then simulated using the same kinematics as the muons removed from the event.  
1055 These simulated taus are then embedded into the data event, such that the event now repre-  
1056 sents an  $Z \rightarrow \tau\tau$  event. A more detailed description can be found in [15].

1057 In the context of the  $H \rightarrow WW$  analysis, these samples can be used to estimate the DY back-  
1058 ground in  $e\mu$  final state channels. While the  $H\tau\tau$  group provides these embedded samples for  
1059 different final states, including those with at least one hadronically decaying tau, only those  
1060 samples which describe the process  $Z \rightarrow \tau\tau \rightarrow e\mu$  are used here.

### 1061 10.2 Scale factors

1062 While the  $H\tau\tau$  group does provide workspaces containing scalefactors for the electrons, muons  
1063 and triggers alongside the embedded samples themselves, these are based off of the working  
1064 points used  $H \rightarrow \tau\tau$  analyses, which are different than those used in  $H \rightarrow WW$  analyses.  
1065 Therefore most of the scalefactors were recomputed for the embedded samples. The only scale-  
1066 factors that were inherited from the official  $H\tau\tau$  scalefactors are those correcting for the effi-  
1067 ciency of the DoubleMuon-HLT, used during the initial selection of  $Z \rightarrow \mu\mu$  events.

1068 The scalefactors obtained from MC cannot be used for embedded samples for a number of  
1069 reasons, including that the simulation of the embedded leptons was performed in a different  
1070 geometry. In order to determine the efficiency of the Id, isolation and trigger on the embedded  
1071 leptons, a special set of samples are provided by the  $H\tau\tau$  group, where both muons from the  
1072 data events are replaced with either a pair of simulated muons or a pair of simulated electrons.  
1073 The scale factors for the electron and muon Id and isolation, as well as for the triggers, are  
1074 determined using the Tag&Probe method. Probe electrons are required to pass  $p_T > 10\text{ GeV}$   
1075 and  $|\eta| < 2.5$ . Probe muon are required to pass  $p_T > 10\text{ GeV}$  and  $|\eta| < 2.4$ , as well as to be  
1076 identified as "Tracker muons". Electrons are selected as a Tag if they pass a "Tight" working  
1077 point as they are defined in section 4. Additionally, for 2016, they must fulfill  $p_T > 35\text{ GeV}$  and  
1078 pass the HLT\_Ele27\_WPTight\_Gsf trigger. For 2017 and 2018 the tagged electrons must fulfill  
1079  $p_T > 40\text{ GeV}$  and pass the HLT\_Ele35\_WPTight\_Gsf trigger. Muons are selected as a Tag if they  
1080 pass the "TightHWW" working point as defined in section 3. They must have  $p_T > 30\text{ GeV}$   
1081 and pass the HLT\_IsoMu24 trigger in 2016 and the HLT\_IsoMu27 trigger in 2017 and 2018.

1082 Pairs of a Tag and Probe are selected by requiring that both leptons have a same flavor and  
1083 opposite sign. They must also not be within  $\Delta R < 0.5$  of each other, and the invariant di-lepton  
1084 mass of the pair must be within  $60\text{ GeV} < m_{ll} < 120\text{ GeV}$ . If there are multiple Tag and Probe  
1085 pairs identified in a single event, which may occur for example when both leptons in a pair  
1086 satisfy the requirements for being the Tag, then all pairs are considered for the determination  
1087 of the efficiency.

1088 All efficiencies of the lepton Id and isolation in data and embedded samples are determined  
1089 by checking the ratio of Probe leptons that pass the Id and the isolation requirement over all  
1090 Probes that are selected alongside a Tag. For the trigger efficiencies, it is checked whether the  
1091 Probes pass the respective legs of the electron-muon crosstriggers. For electrons, these are the  
1092 same legs as are part of the di-electron trigger HLT\_Ele23\_Ele12\_CaloIdL\_TrackIdL\_IsoVL. For  
1093 muons the legs of the di-muon trigger HLT\_Mu17\_TrkIsoVVL\_Mu8\_TrkIsoVVL do not corre-

1094 spond to the legs of the electron-muon crosstrigger. For this reason, the Probe muons instead  
 1095 pass the trigger if they pass the Mu8 leg of the di-muon trigger, as well as pass  $p_T > 23\text{ GeV}$  or  
 1096  $p_T > 13\text{ GeV}$  for the leading lepton leg or subleading lepton leg respectively. In addition, the  
 1097 muon and the L1-muon must be within  $\Delta R < 0.5$  of each other.

1098 Efficiencies are determined for different bins of  $p_T$  and  $\eta$ . The same binning is used here as for  
 1099 the MC scalefactors, which are listed in sections 3, 4 and 5. Additionally however, the embed-  
 1100 ded electron Id also requires binning dependent on  $\phi$ , and is split up into 8 bins of the same  
 1101 size between  $-\pi < \phi < \pi$ . While it is a known issue that the electron Id performs worse  
 1102 in embedded samples than in regular MC (due to the leptons being simulated in a different  
 1103 geometry, which is then translated into real geometry), it turns out that the cut-based electron  
 1104 Id has a strong impact on the electron efficiency as a function of  $\phi$ . In particular the variable  
 1105  $dEtaInSeed(\Delta\eta)$  appears to be strongly  $\phi$  dependent for the embedded electrons.

1106 In order to remove any further background events from the selected Tag&Probe pairs, a fit is  
 1107 performed over the di-lepton mass for each bin of  $p_T$ ,  $\eta$  and  $\phi$  (for electrons). The sum of two  
 1108 voigtians is used for the fit to signal. For the Id and isolation, the CMSshape function is used  
 1109 for the fit to background. For the trigger, an exponential function is used for the background  
 1110 fit. The resulting Tag&Probe efficiency is then calculated using only the passing/failing probes  
 1111 under the signal fit. Some fits are shown as an example in figures 134, 135, 136, 137, 138.

1112 Due to the additional binning over  $\phi$  for the electrons, there are a few bins where the fit does  
 1113 not work properly due to low statistics (around less than 100 events). For this reason, the fit-  
 1114 ting procedure is not used in cases where the relative uncertainty on the resulting efficiency is  
 1115 larger than 10 %. Instead the counting method is used in these bins, meaning the efficiency is  
 1116 calculated using the passing/failing probes from all events.

### 1117 10.3 Interference with other MC samples

1118 The initial events with two muons selected from data are not exclusively from Z decay pro-  
 1119 cesses. About 2 % of all events in the embedded samples originate from other processes. Some  
 1120 of these are negligible as a result of the requirements on a minimal lepton  $p_T$ . Others, such as  
 1121 Di-boson and processes involving Tops, are still relevant in the embedded samples. In order to  
 1122 avoid double-counting between these few events in the embedded samples and those as they  
 1123 are predicted from the corresponding MC samples, events from the MC samples are veto-ed if  
 1124 the two final state leptons originate from Taus. This can be determined from the generator-level  
 1125 information of the MC samples.

### 1126 10.4 Uncertainties

1127 Making use of embedded samples over MC has the advantage that the uncertainties are ex-  
 1128 pected to be much lower. The only uncertainties which need to be taken into account are those  
 1129 of the trigger efficiency, electron and muon efficiency and energy scale. Additionally, an uncer-  
 1130 tainty on the events that were removed from MC samples to avoid double-counting (Section  
 1131 10.3) is added. This is done by taking 10 % the shape of all veto-ed MC events and applying  
 1132 this as an uncertainty onto the embedded samples.

### 1133 10.5 Control regions

1134 The effect of using embedded samples to describe the DY background can be seen in figures  
 1135 139, 140, 141. While the overall normalization is not yet perfect, the uncertainties are visibly  
 1136 lower.

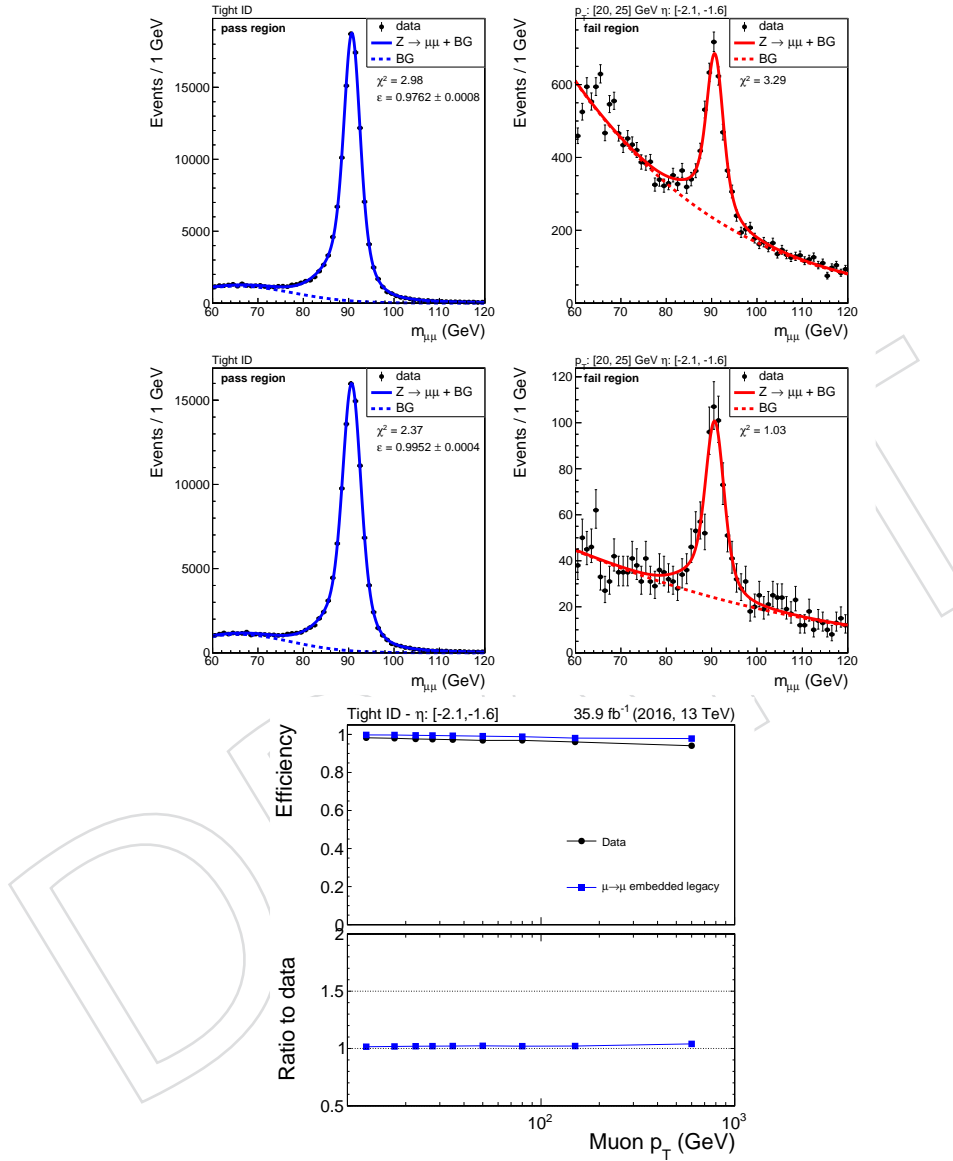


Figure 134: Tag&Probe fits for the muon ID for 2016 in the bin  $20 < p_T < 25 \text{ GeV}$  and  $-2.1 < \eta < -1.6$  for data (top) and embedded samples (middle), and the efficiencies over all  $p_T$  in this  $\eta$  bin for both data and embedded samples (bottom)

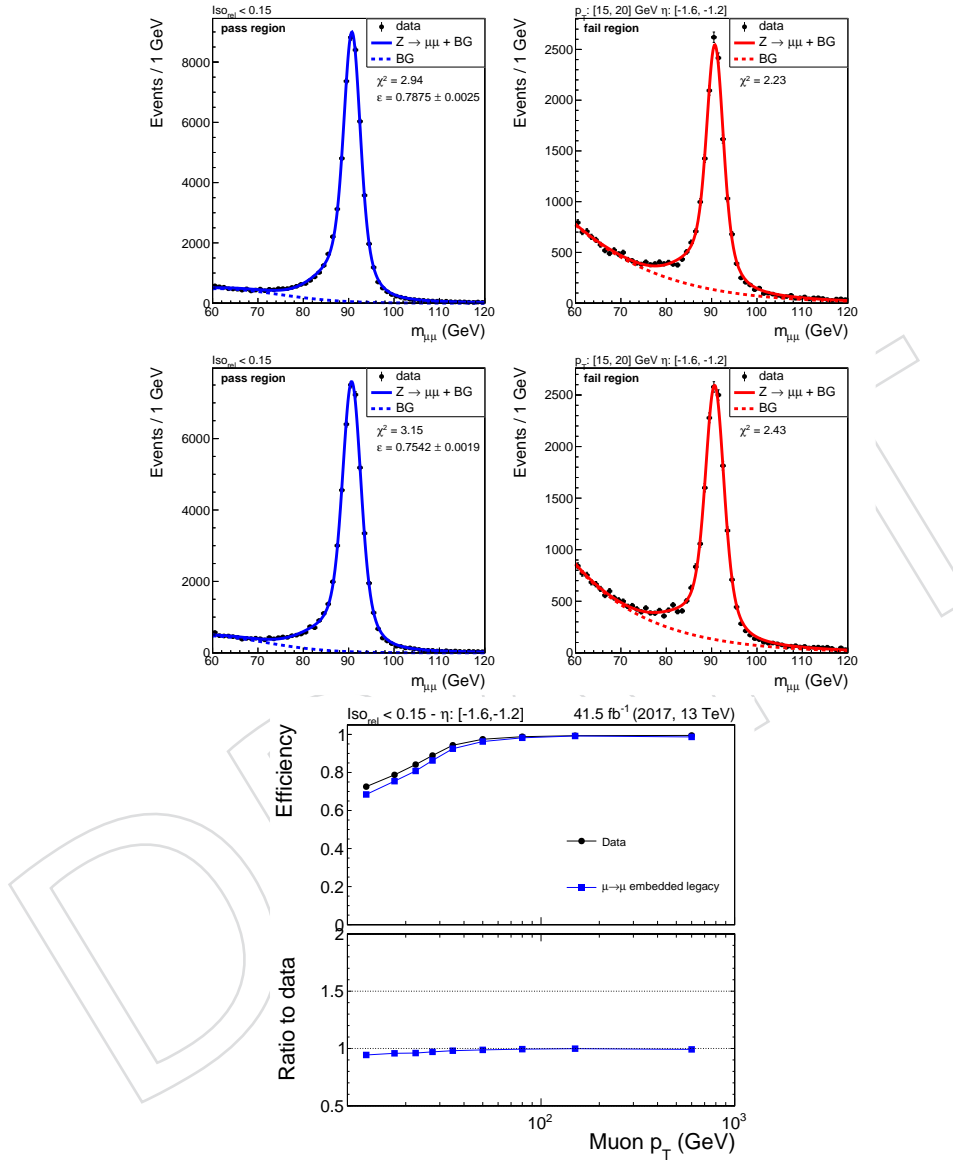


Figure 135: Tag&Probe fits for the muon Isolation for 2017 in the bin  $15 < p_T < 20 \text{ GeV}$  and  $-1.6 < \eta < -1.2$  for data (top) and embedded samples (middle), and the efficiencies over all  $p_T$  in this  $\eta$  bin for both data and embedded samples (bottom)

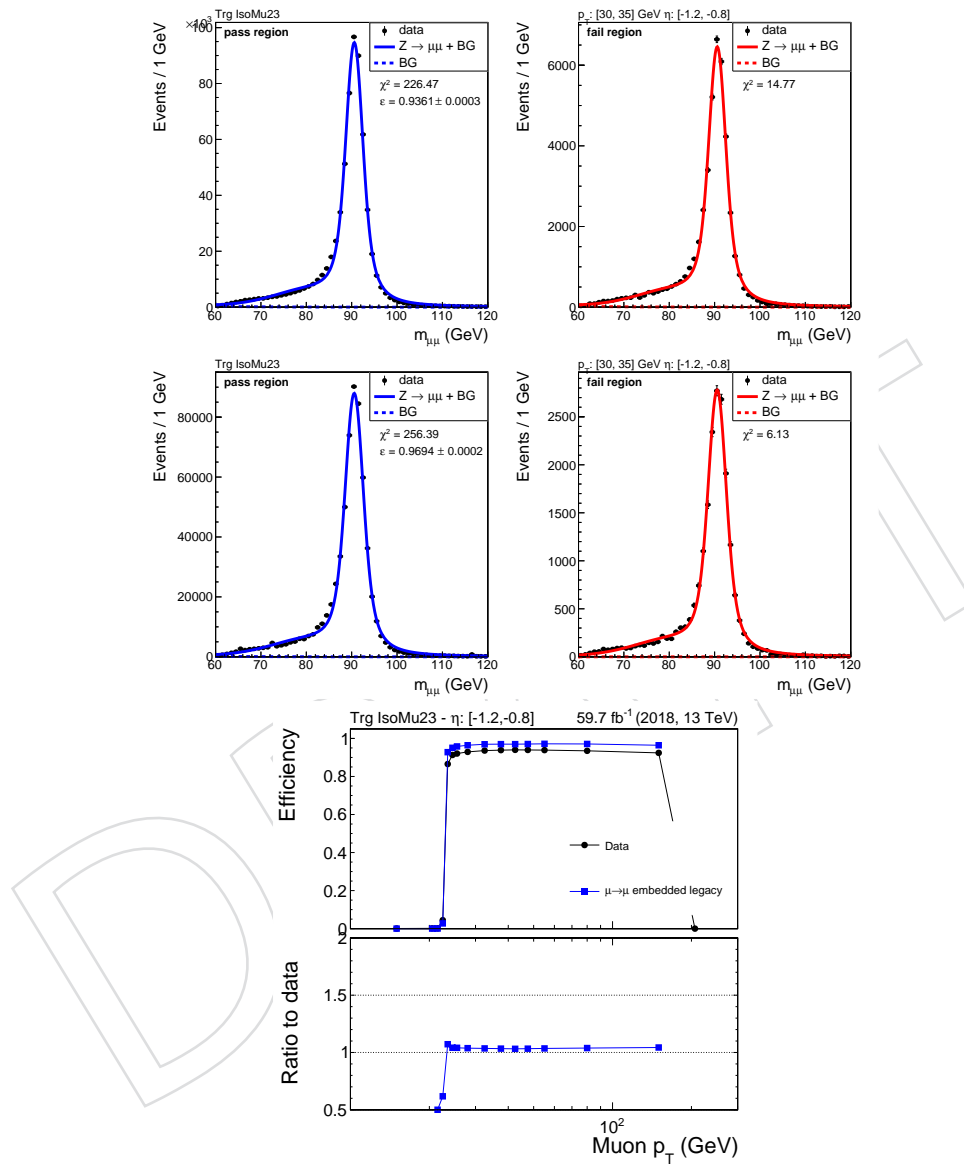


Figure 136: Tag&Probe fits for the muon 23 GeV Trigger for 2018 in the bin  $30 < p_T < 35 \text{ GeV}$  and  $-1.2 < \eta < -0.8$  for data (top) and embedded samples (middle), and the efficiencies over all  $p_T$  in this  $\eta$  bin for both data and embedded samples (bottom)

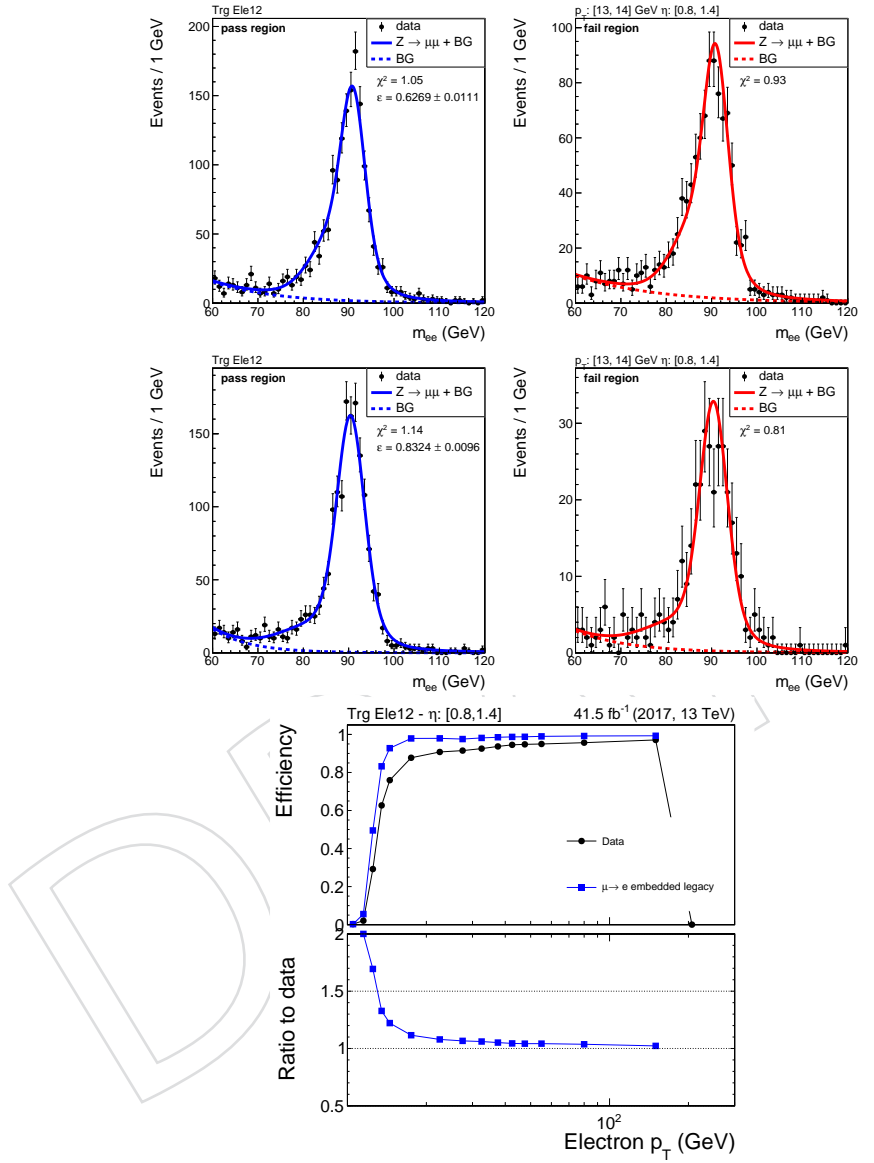


Figure 137: Tag&Probe fits for the electron 12 GeV Trigger for 2017 in the bin  $13 < p_T < 14$  GeV and  $0.8 < \eta < 1.4$  for data (top) and embedded samples (middle), and the efficiencies over all  $p_T$  in this  $\eta$  bin for both data and embedded samples (bottom)

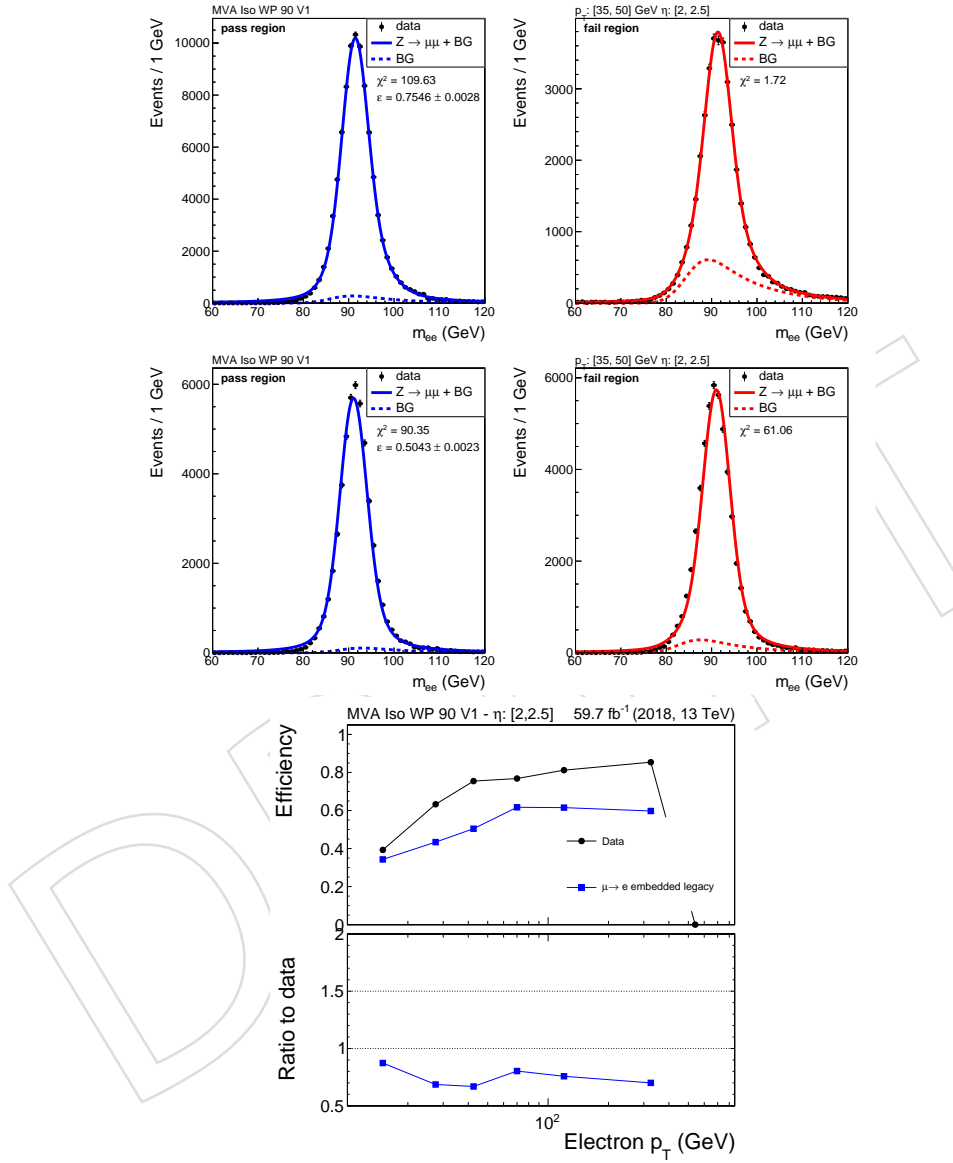


Figure 138: Tag&Probe fits for the electron ID for 2018 in the bin  $35 < p_T < 50 \text{ GeV}$ ,  $2.0 < \eta < 2.5$  and  $0 < \phi < \pi/2$  for data (top) and embedded samples (middle), and the efficiencies over all  $p_T$  in this  $\eta$ - $\phi$  bin for both data and embedded samples (bottom)

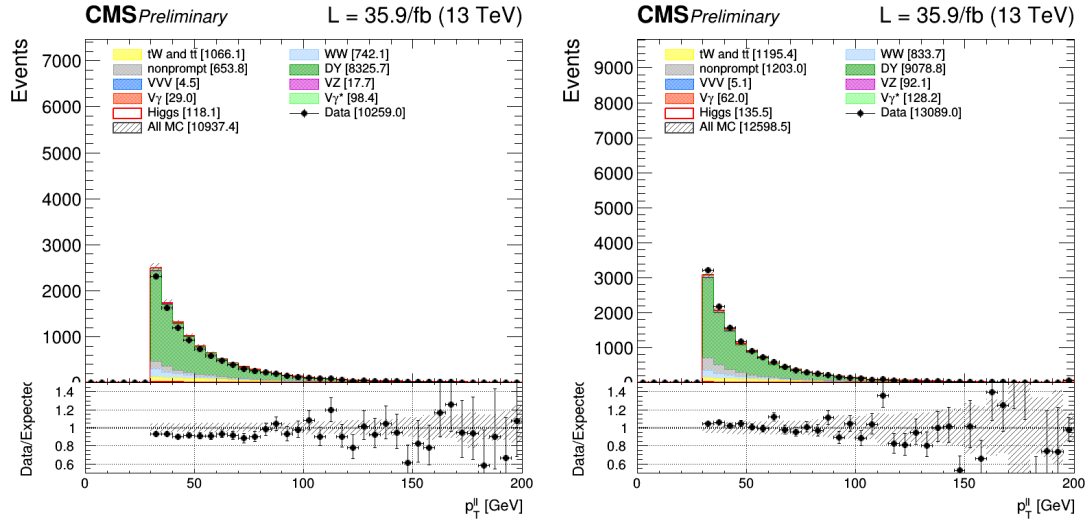


Figure 139: DY enhanced control region with 2016 data, using embedded samples describing the green DY background (left) and using regular DY MC (right)

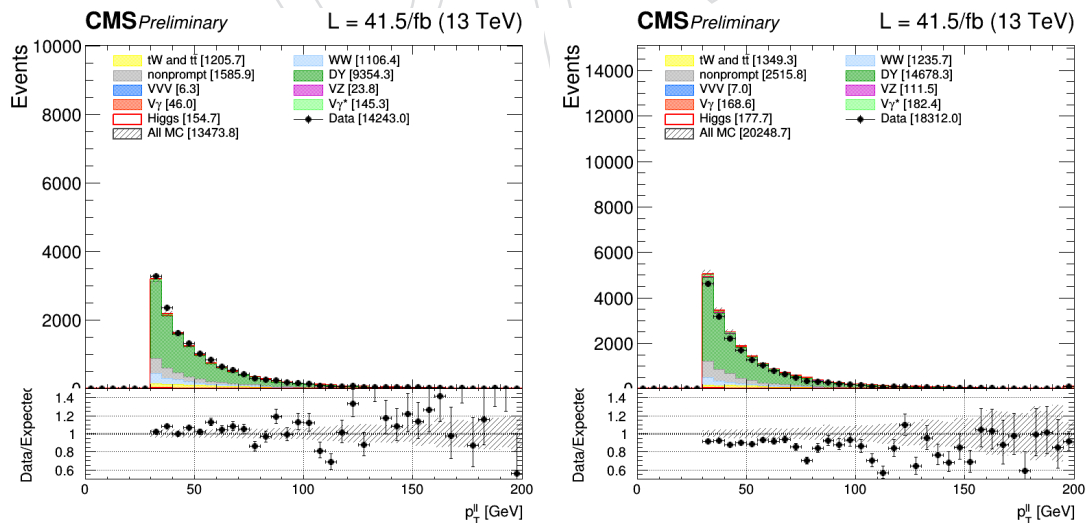


Figure 140: DY enhanced control region with 2017 data, using embedded samples describing the green DY background (left) and using regular DY MC (right)

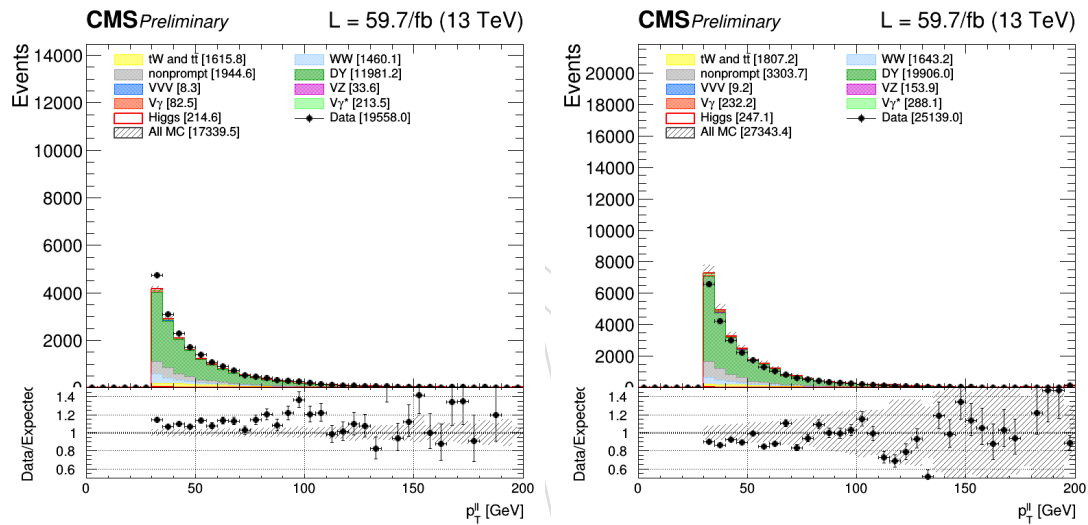


Figure 141: DY enhanced control region with 2018 data, using embedded samples describing the green DY background (left) and using regular DY MC (right)

## 1137 11 B-Tagging

1138 Editors: Lorenzo Viliani, Piergiulio Lenzi, Benedetta Camaiani

1139 An important task for analyses characterized by two W bosons in the final state is the suppression  
 1140 of the dominant top quark background. The main processes belonging to this category are  
 1141  $t\bar{t}$  production, characterized by the presence of two b jets in the final state and  $tW$  production,  
 1142 which is characterized by having only one top quark, decaying to a W and a b quark, produced  
 1143 together with a W boson.

1144 The usage of b tagging algorithms to efficiently tag jets that are likely coming from b hadron  
 1145 decays is thus a fundamental tool to reject top background events. B tagging is a reconstruction  
 1146 technique that takes advantage of the characteristic properties of b hadrons and assigns to each  
 1147 jet a “likelihood” that it contains a b hadron. The b tagging can be based on track information,  
 1148 secondary vertex information, soft lepton information or some combination of the above.

1149 A variety of b tagging algorithms based on different input information has been developed by  
 1150 CMS [? ]. A common feature is that all these algorithms produce an output discriminator which  
 1151 describes how likely it is that a given jet is actually a b-jet, *i.e.* higher is the discriminator value,  
 1152 bigger is the probability that the jet is a real b-jet.

1153 Several b tagging algorithms are provided by the BTV POG, and for each of them three values of  
 1154 the discriminator, *i.e.* working points, are provided as well. Each working point, namely loose,  
 1155 medium and tight, corresponds to a different b tagging efficiency and mistag rate. Scale factors  
 1156 for the various taggers and for each working point are provided by the BTV POG together with  
 1157 their associated uncertainties according to [? ].

1158 Alternatively, one can use data-to-simulation scale factors obtained using an iterative fitting  
 1159 technique that aims at correcting the full discriminator shape, as described in Ref. [? ]. This  
 1160 method, which is adopted in this analysis, is designed to meet the needs of analyses in which  
 1161 the full distribution of the b tagging discriminator is used, or in which the discriminator working  
 1162 point has to be tuned separately for each analysis category.

1163 The b tagging algorithms that have been tested in this study are: Combined Secondary Vertex  
 1164 V2 (CMSSW tagger name `pfCombinedInclusiveSecondaryVertexV2BJetTags`), Combined  
 1165 MVA v2 (CMSSW tagger name `pfCombinedMVAV2BJetTags`), Deep CSV (CMSSW tagger  
 1166 name `pfDeepCSVJetTags:probb + pfDeepCSVJetTags:probbb`) and Deep Flavour.  
 1167 The choice of b tagging algorithm and working point is driven by the expected significance  
 1168 obtained performing a simplified cut and count analysis. As discussed in the following, the  
 1169 algorithm providing the best significance is found to be Deep CSV, and this is the one used in  
 1170 the analysis for 2016, 2017, and 2018 data taking periods.

1171 Information regarding the discriminators are accessed using the following branches in NanoAOD  
 1172 samples from the 94X release: `Jet_btagCMVA`, `Jet_btagCSVV2`, `Jet_btagDeepB`, and  
 1173 `Jet_btagDeepFlavB`.

### 1174 11.1 B tagging algorithms performance

1175 In the  $H \rightarrow WW$  analysis it is important to suppress the contribution of top quark backgrounds,  
 1176 and this is done by applying a b-jet veto, *i.e.* by rejecting all events that contain at least one jet  
 1177 with  $p_T > 20 \text{ GeV}$  and  $|\eta| < 2.4$  passing a given discriminator working point. In order to assess  
 1178 which tagger and working point are performing better for the  $H \rightarrow WW$  analysis, the ROC  
 1179 curves for each analysis category have been constructed. The ROC curves are built using two  
 1180 simulated samples: one enriched in b flavour jets (`TTTo2L2Nu_TuneCP5_13TeV-powheg-pythia8`),

which represents the background process, and one enriched in light flavour jets (GluGluHToWWTo2L2Nu\_M125\_13TeV\_powheg2\_JHUGenV714\_pythia8), which represent the signal. These samples are used to compute the b-jet veto signal efficiency ( $\epsilon_s$ ), and the b-jet veto background rejection ( $1 - \epsilon_b$ ) for different tagger working points. The ROC curves are obtained applying a basic preselection common to  $H \rightarrow WW$  final states, defined using the following event requirements: an electron and a muon, the leading lepton with  $p_T$  greater than 20 GeV, the subleading with  $p_T$  greater than 10 GeV (13 GeV) if muon (electron). No other lepton with  $p_T$  greater than 10 GeV, dilepton invariant mass greater than 20 GeV, dilepton  $p_T$  greater than 30 GeV, Puppi MET above 20 GeV.

On top of the preselection, the events are further categorized based on the number of jets in each event. i.e. 0, 1 and 2 jets. In addition, the ROC curve has been computed also in a phase space with VBF topology, i.e. 2 jets with  $m_{jj} > 500$  GeV and  $|\Delta\eta_{jj}| > 3.5$ . In this case a VBF simulation is used as signal process (VBFHToWWTo2L2Nu\_M125\_13TeV\_powheg2\_JHUGenV714\_pythia8).

The corresponding ROC curves are shown in Fig. 142.

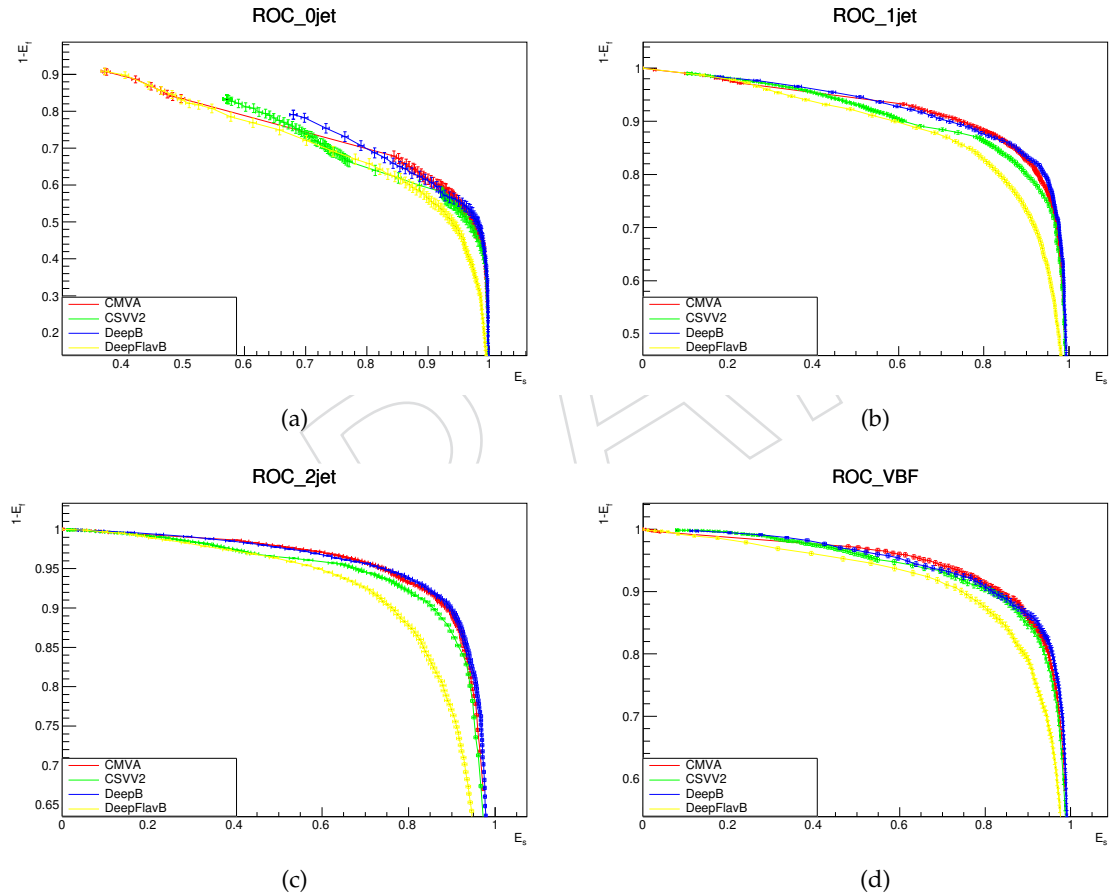


Figure 142: ROC curves for different b tagging algorithms for events with 0 jets (top left), 1 jet (top right), 2 jets (bottom left), and 2 jets with VBF topology (bottom right).

The Deep CSV algorithm (dubbed DeepB in Fig. 142) is the one providing the best performance overall. In order to assess the best working point for each category, we have computed the significance for signal events passing the b-jet veto selection as a function of the discriminator cut. The significance is calculated as  $S/\sqrt{S+B}$ , where  $S$  and  $B$  are the numbers of signal and background events passing the selection. Background processes considered in this study are obtained using top and WW (WWTo2L2Nu\_NNPDF31\_TuneCP5\_PSweights\_13TeV-powheg-pythia8)

1201 simulated samples. The significances as a function of the discriminator cut are shown in  
 1202 Fig. 143.

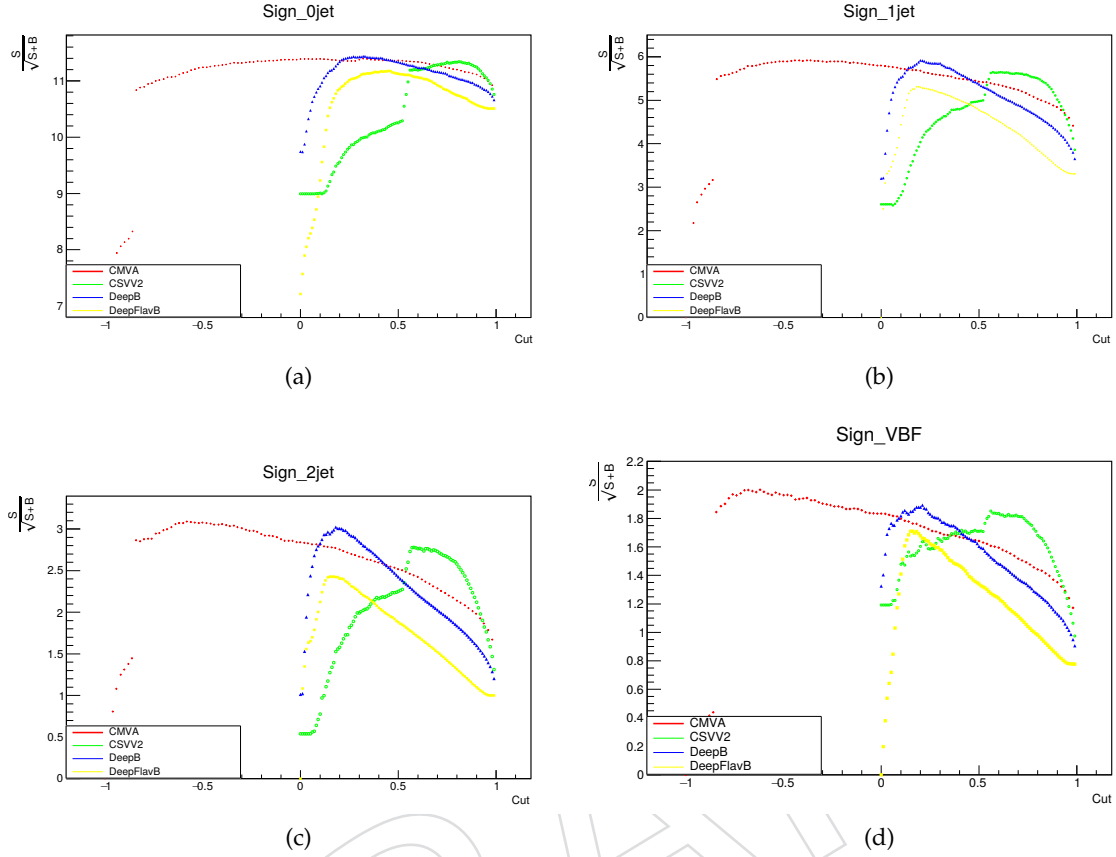


Figure 143: Significance as a function of the discriminator cut for different b tagging algorithms for events with 0 jets (top left), 1 jet (top right), 2 jets (bottom left), and 2 jets with VBF topology (bottom right).

1203 This study confirms that the Deep CSV algorithm is the one with better performance in this  
 1204 final state, and the working point corresponding to the largest significance is very close to the  
 1205 loose working point provided by the BTV POG (0.1522 for 2017 data) in all categories, which  
 1206 is the one adopted in this analysis. As a future development we will perform a more refined  
 1207 study to assess whether slightly different working points for each category could enhance the  
 1208 final analysis significance.

## 1209 11.2 Scale factors

1210 The values of the data-simulation scale factors for the various taggers are retrieved from a  
 1211 comma-separated-value file provided by the BTV POG and propagated through the NanoAOD  
 1212 format. The scale factors are provided separately for different jet flavours, i.e. b,c and udsg  
 1213 (light jets), in bins of the jet  $p_T$  and  $\eta$ , and as a function of the discriminator value itself. For  
 1214 CSVv2 and Deep CSV the  $\eta$  and  $p_T$  binning scheme is shown in [? ]. For b- and c-jets with  
 1215  $20 < p_T <= 30$  GeV the same scale factors as the ones computed at  $p_T = 30$  GeV are used, but  
 1216 doubling the associated uncertainty.

The MC events are reweighted using these scale factors and the event weights are computed according to the prescription 1d) in Ref. [? ]. For each event the weight  $w$  is computed as

follows:

$$w = \prod_i^{N_{\text{jets}}} SF_{\text{jet}_i}, \quad (7)$$

where  $i$  runs over all the jets in the event with  $|\eta| < 2.4$  and  $p_T > 20$  GeV for which b tagging is applied.

The scale factors are provided together with the following sources of systematic uncertainty:

- Jet energy scale (JES): scale factors obtained from samples with up/down shifted JES (branch names in NanoAOD: `Jet_btagSF_shape_up/down_jes`);
- Purity of the sample used to derive scale factors: varied scale factors obtained varying the light/heavy flavour composition in the sample (branch names in NanoAOD: `Jet_btagSF_shape_up/down_hf`, `Jet_btagSF_shape_up/down_lf`, `Jet_btagSF_shape_up/down_cferr1`, `Jet_btagSF_shape_up/down_cferr2`);
- Statistical fluctuations in both data and MC (branch names in NanoAOD: `Jet_btagSF_shape_up/down_hfstats1`, `Jet_btagSF_shape_up/down_hfstats2`, `Jet_btagSF_shape_up/down_lfstats2`, `Jet_btagSF_shape_up/down_lfstats2`).

The event weight corresponding to each source of uncertainty is computed in a similar way as for the nominal weight, according to Eq.(7).

As discussed in the previous section, the Deep CSV algorithm with loose working point is the one providing the largest significance. In order to check the b tagging scale factors for this algorithm, the discriminator shape obtained in MC after applying the b tagging scale factors is compared to data in a top quark enriched control region, as well as in a control region enriched in Z+jets events.

The top quark control region is defined by applying the common  $H \rightarrow WW$  preselection and requiring events with a leading jet with  $p_T$  greater than 30 GeV and a Deep CSV score above the loose working point. The Deep CSV score distribution for the subleading jet, which can be either above 30, GeV or between 20 and 30 GeV, is used to check the agreement between data and MC in this control region, and is shown in Figs. 144, 145, and 146 for 2016, 2017, and 2018 data taking periods, respectively. The Deep CSV distribution is shown in two bins: [0, WPL] (events in this bin contain non b-tagged jets) and [WPL, 1] (events in this bin contain b-tagged jets), where WPL represents the score corresponding to the loose working point. The only systematic uncertainties that are taken into account in this comparison are the ones associated to the b tagging scale factors. The WPL score is 0.2217, 0.1522, and 0.1241, respectively for 2016, 2017, and 2018 data taking periods.

Similar plots are shown in Figs. 147, 148, and 149, for a control region enriched in light flavour jets, for 2016, 2017, and 2018 data taking periods, respectively. This control region is defined by selecting events containing two same flavour and opposite charge leptons, with the same requirements in terms of  $p_T$  as the top enriched control region, but with a dilepton invariant mass between 80 and 120 GeV. This selection assures that the far major part of the events arise from the Z boson decays.

To check the agreement between data and MC in this control region, the Deep CSV score distribution for jets with  $p_T > 30$  GeV, or  $20 \text{ GeV} < p_T < 30 \text{ GeV}$ , are used, binned in the same way as for the top enriched control region.

An important remark in the evaluation of the data/MC comparisons is that the relevant aspect in the comparison is not the normalization, but rather the flatness of the data/MC ratios. The

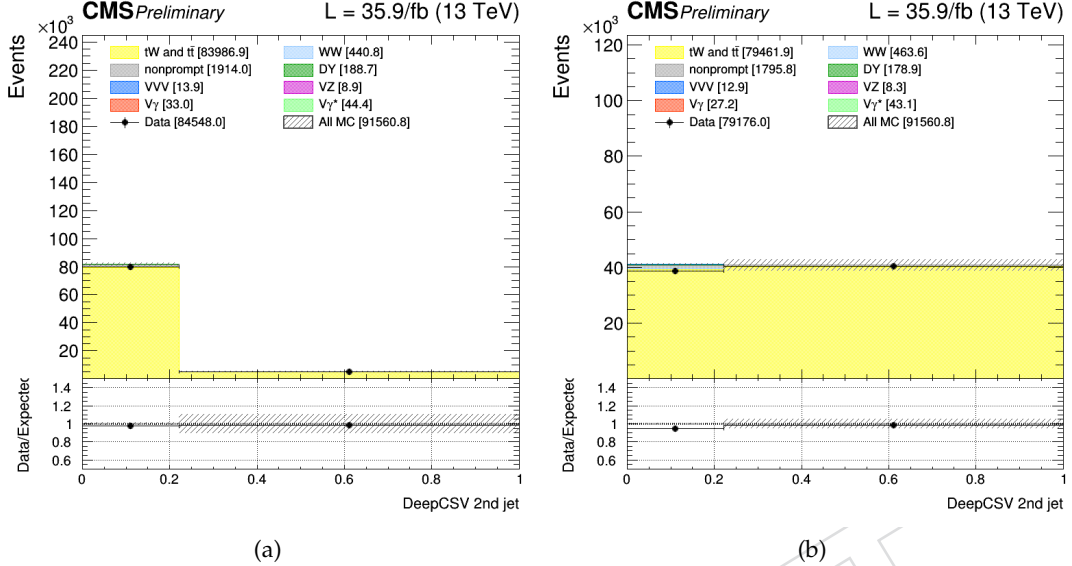


Figure 144: Deep CSV discriminator for jets above 30 GeV (a) and between 20 and 30 GeV (b) in a top enriched control region, after applying the scale factors, for 2016 data taking. The systematics band comprises only the uncertainties related to the b tagging scale factors.

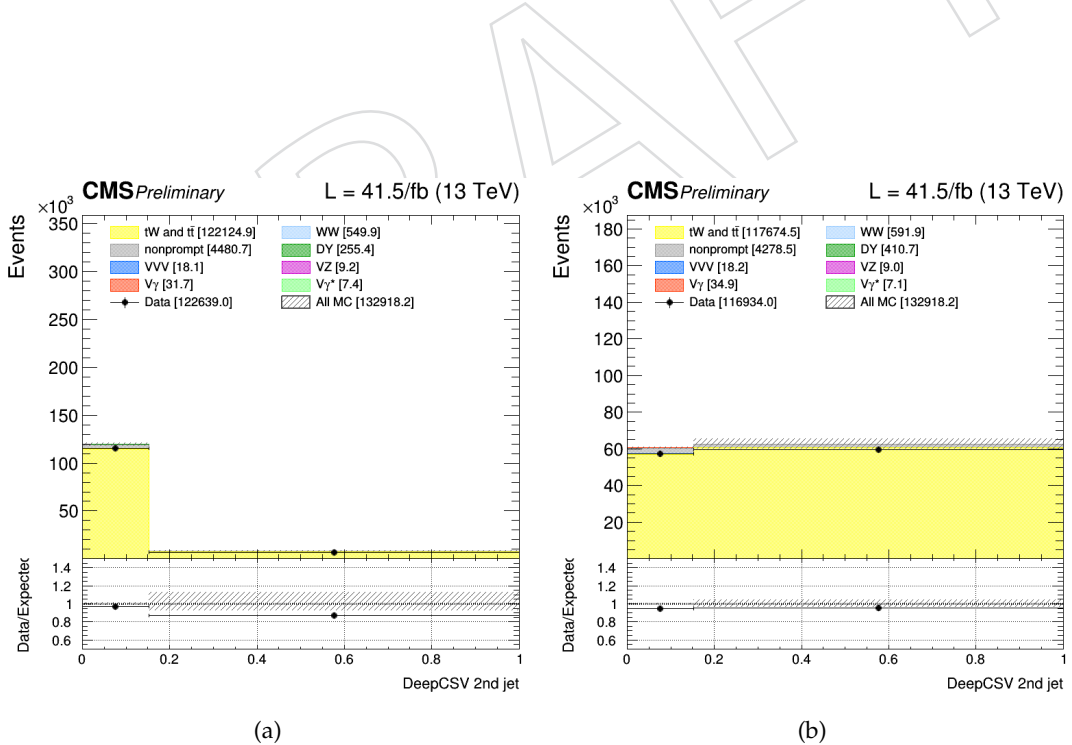


Figure 145: Deep CSV discriminator for jets above 30 GeV (a) and between 20 and 30 GeV (b) in a top enriched control region, after applying the scale factors, for 2017 data taking. The systematics band comprises only the uncertainties related to the b tagging scale factors.

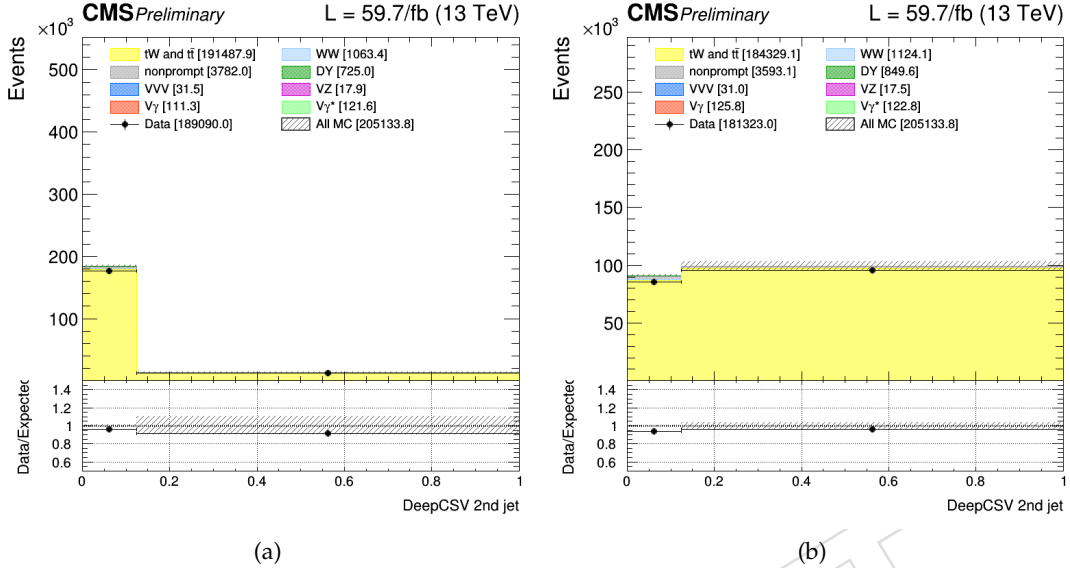


Figure 146: Deep CSV discriminator for jets above 30 GeV (a) and between 20 and 30 GeV (b) in a top enriched control region, after applying the scale factors, for 2018 data taking. The systematics band comprises only the uncertainties related to the b tagging scale factors.

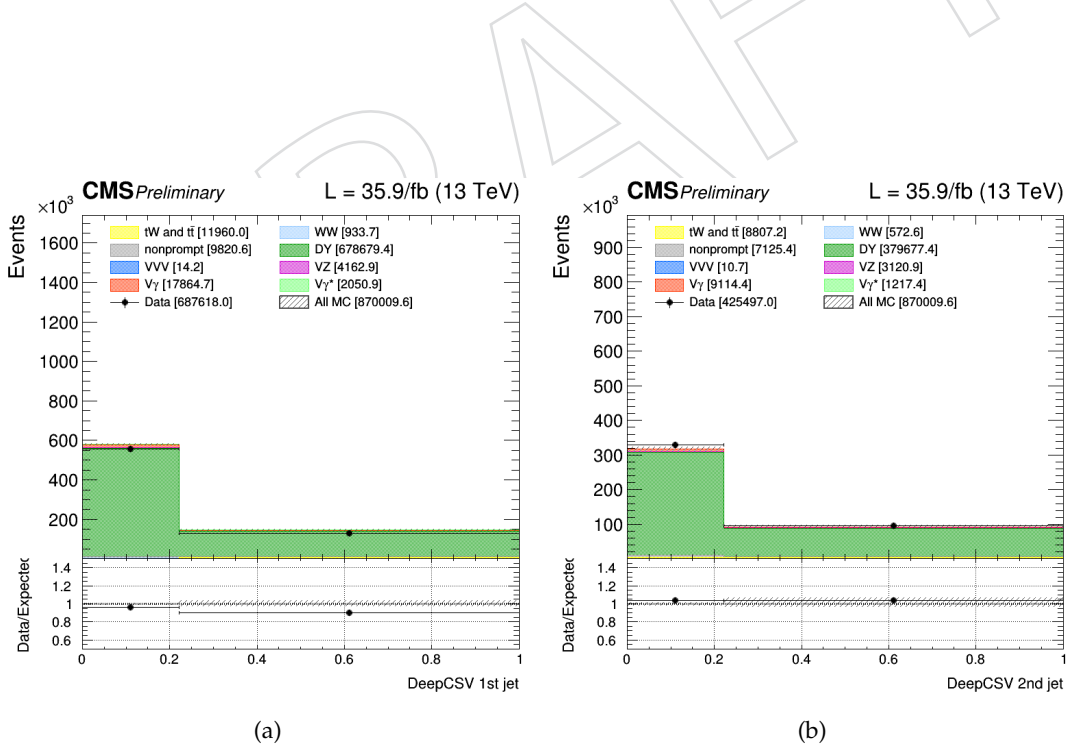


Figure 147: Deep CSV discriminator for jets above 30 GeV (a) and between 20 and 30 GeV (b) in a Z enriched control region, after applying the scale factors, for 2016 data taking. The systematics band comprises only the uncertainties related to the b tagging scale factors.

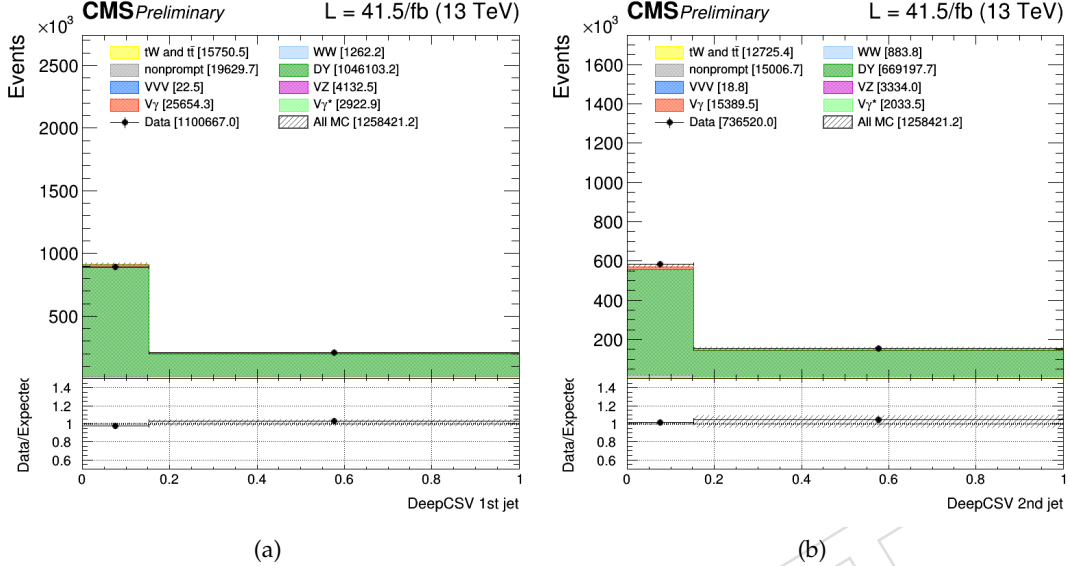


Figure 148: Deep CSV discriminator for jets above 30 GeV (a) and between 20 and 30 GeV (b) in a Z enriched control region, after applying the scale factors, for 2017 data taking. The systematics band comprises only the uncertainties related to the b tagging scale factors.

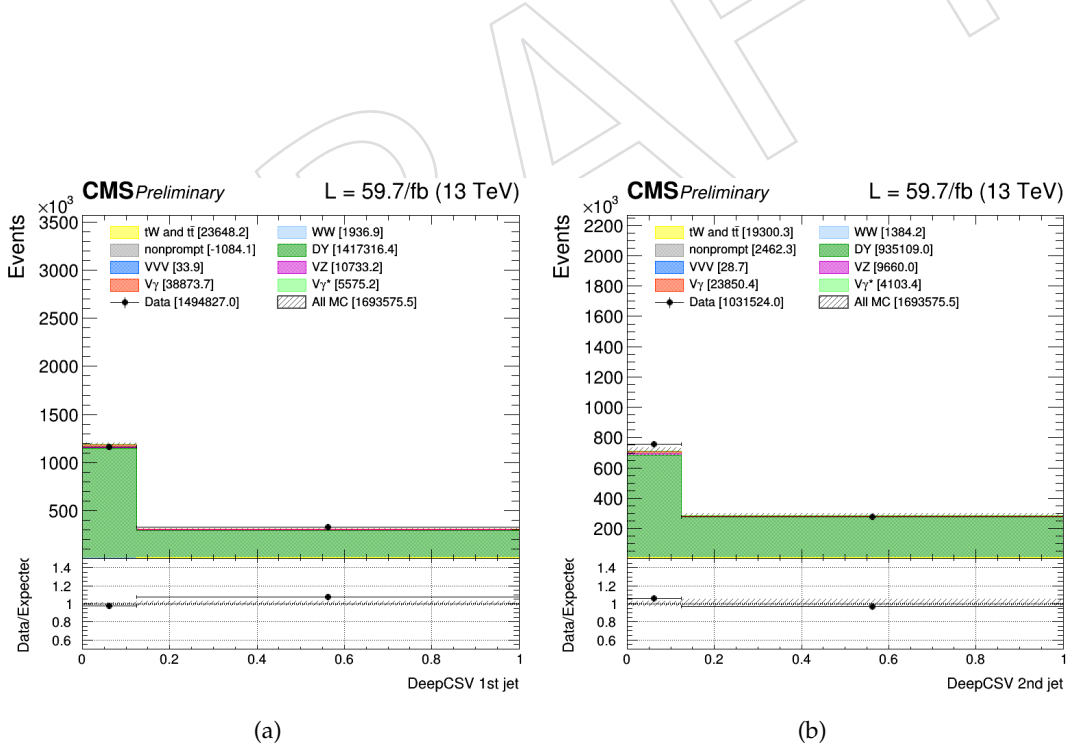


Figure 149: Deep CSV discriminator for jets above 30 GeV (a) and between 20 and 30 GeV (b) in a Z enriched control region, after applying the scale factors, for 2018 data taking. The systematics band comprises only the uncertainties related to the b tagging scale factors.

1258 overall normalization of the  $t\bar{t}$  and DY backgrounds will be fixed by a dedicated data driven  
1259 normalization technique, while what is relevant here is that the fraction of events above or  
1260 below the b-tagging cut is well under control.

DRAFT

---

## References

- [1] "Muon POG reference efficiencies for Run-II".  
<https://twiki.cern.ch/twiki/bin/view/CMS/MuonReferenceEffsRun2>.
- [2] "Muon POG standard selections for Run-II".  
<https://twiki.cern.ch/twiki/bin/view/CMS/SWGuideMuonIdRun2>.
- [3] N. Adam et al., "Generic tag and probe tool for measuring efficiency at cms with early data", *CMS Note* **2009/111** (2009).
- [4] "Muon POG tag and probe tool for Run-II".  
<https://twiki.cern.ch/twiki/bin/viewauth/CMS/MuonTagAndProbeTreesRun2>.
- [5] "Muon ID, isolation and trigger efficiencies for Run2016 with HWW selections".  
[https://github.com/latinos/TagAndProbeLepton/tree/master/Muons/plot\\_tnp/Eff.txt](https://github.com/latinos/TagAndProbeLepton/tree/master/Muons/plot_tnp/Eff.txt).
- [6] A. Bodek et al., "Extracting Muon Momentum Scale Corrections for Hadron Collider Experiments", *Eur. Phys. J. C* **72** (2012) 2194,  
doi:10.1140/epjc/s10052-012-2194-8, arXiv:1208.3710.
- [7] "Rochester Correction". <https://twiki.cern.ch/twiki/bin/view/CMS/RochcorMuon>.
- [8] CMS Collaboration, "Computing the contamination from fakes in leptonic final states", *CMS Physics Analysis Note* **CMS-AN-10-261** (2010).
- [9] CMS Collaboration, "Data driven estimates of non-prompt leptons background for the higgs bos on decaying to ww and ww cross section in the leptonic final state measurements", *CMS Physics Analysis Note* **CMS-AN-13-184** (2013).
- [10] "Jet Identification for the 13 TeV data Run2017".  
<https://twiki.cern.ch/twiki/bin/viewauth/CMS/JetID>.
- [11] "Jet identification in high pile-up environment".  
<https://twiki.cern.ch/twiki/bin/viewauth/CMS/PileupJetID>.
- [12] "Reweighting recipe to emulate Level 1 ECAL prefiring".  
<https://twiki.cern.ch/twiki/bin/viewauth/CMS/L1ECALPrefiringWeightRecipe>.
- [13] "Jet energy scale uncertainty sources".  
<https://twiki.cern.ch/twiki/bin/viewauth/CMS/JECUncertaintySources>.
- [14] "MET Filter Recommendations for Run II".  
<https://twiki.cern.ch/twiki/bin/view/CMS/MissingETOptionalFiltersRun2>.
- [15] CMS Collaboration, "An embedding technique to determine  $\tau\tau$  backgrounds in proton-proton collision data", *JINST* **14** (2019) P06032,  
doi:10.1088/1748-0221/14/06/P06032, arXiv:1903.01216.